Università degli Studi Roma Tre

Roma Tre

**Department of Industrial, Electronic,**
**and Mechanical Engineering**

Ph.D. Program in “Industrial and Mechanical Engineering”
Cycle XXXVIII

# Research and development of design tools and methods for Additive Manufacturing: virtual prototyping and artificial intelligence

Disciplinary scientific area:
IIND-03/B

| Ph.D. Supervisors: | Ph.D. Candidate: |
|---|---|
| **Prof. Paolo Cicconi** | **Michele Trovato** |
| **Prof. Alessandro Giorgetti** | |

PhD coordinator:
**Prof. Ornella Chiavola**

# Abstract

The Industry 4.0 revolution promotes the integration of computers and control systems into manufacturing processes. Additive Manufacturing technologies are a key part of Industry 4.0 because they align with the industrial revolution's essential principles of connectivity, flexibility, and integration with Artificial Intelligence. Additive methods enable high personalisation and flexibility, allowing on-demand creation of customised items without the lengthy and costly retooling required by traditional methods. Additive Manufacturing promotes innovation by enabling rapid prototyping and shortening the time to market for new products. Its digital nature permits direct compatibility with other Industry 4.0 technologies, such as the Internet of Things and Digital Twins.

Design for Additive Manufacturing is a field of study that focuses on reducing errors and costs in additive projects from the early design phases. This approach is a crucial practice for avoiding failures and enhancing 3D part quality by optimising the part geometry in function of the manufacturing process and boundary conditions. One of the main advantages of Additive Manufacturing, and particularly the Laser-Powder Bed Fusion process for metals, is its ability to produce highly complex geometries. These intricate shapes can justify the higher cost of metal Laser-Powder Bed Fusion components, compared to traditional manufacturing. Although research continues to improve part quality, reducing porosity, surface roughness, and geometric or dimensional deviations, further studies are needed to fully understand the mechanical performance of such complex geometries under loads.

Using a Design for Additive Manufacturing technique, the designer can minimise wasting raw materials and time, resulting in higher performance and printability. The additive process diffusion is slowed down, especially for metals, by the high cost and low repeatability of results. The application of Machine Learning methods in the Additive Manufacturing field is already well-documented in the literature, showing various application levels. Among the most studied are geometric optimisation (Topological Optimisation, Generative Design, Lattice Structures, etc.), process parameter optimisation, and production process control practices. Industry 4.0 delivers vast volumes of data that can be used as training material for a Machine Learning system, creating a direct connection between these two worlds.

This thesis proposes a method that combines Artificial Intelligence techniques, advanced CAD modelling, and virtual prototyping into Design for Additive Manufacturing workflows to enhance the integration of these innovative technologies with classical design techniques.

**Keywords:** Design for Additive Manufacturing; Laser-Powder Bed Fusion; Machine Learning, Machine Learning applications for Design for Additive Manufacturing.

# Contents

# List of Figures

# List of Tables

# List of Abbreviations

| | |
|---|---|
| 3D | Three Dimensional |
| ADE | Automatic Data Extraction |
| AI | Artificial Intelligence |
| Al-Cu | Aluminium-Copper |
| Al-Si-Mg | Aluminium-Silicium-Magnesium |
| AM | Additive Manufacturing |
| API | Application Programming Interface |
| BJT | Binder Jetting |
| B-Rep | Boundary Representation |
| CAD | Computer-Aided Design |
| CAE | Computer-Aided Engineering |
| CT | Computed Tomography |
| DED | Direct Energy Deposition |
| DfAM | Design for Additive Manufacturing |
| DoE | Design of Experiments |
| DT | Decision Tree |
| DTE | Decision Tree Evaluation |
| E% | Elongation % |
| EBM | Electron Beam Melting |
| EOC | Environmental Operating Conditions |
| FDM | Fused Deposition Modelling |
| FEM | Finite Element Method |
| FAHP | Fuzzy Analytical Hierarchy Process |
| GA | Genetic Algorithms |
| GD | Generative Design |
| GD&T | Geometric Dimensioning and Tolerancing |
| HIP | Hot Isostatic Pressing |
| HS-Al | High Strength Aluminium |
| ICE | Internal Combustion Engines |
| KB | Knowledge Base |
| LD | Lightweight Design |
| LoF | Lack of Fusion |
| L-PBF | Laser-Powder Bed Fusion |
| LS | Lattice Structures |
| MAE | Mean Absolute Error |
| MEX | Material Extrusion |
| MJT | Material Jetting |
| ML | Machine Learning |
| MPI | Mechanical Performance Index |
| MSE | Mean Squared Error |
| NN | Neural Network |
| PA12 | Polyamide 12 |
| PBF | Powder Bed Fusion |
| RE | Reverse Engineering |
| RL | Reinforced Learning |
| RF | Random Forest |
| SC | Shape Complexity |
| SCI | Shape Complexity Index |
| SDK | Software Development Kit |
| SHL | Sheet Lamination |
| SL | Supervised Learning |
| SLM | Selective Laser Melting |
| SLS | Selective Laser Sintering |
| SO | Shape Optimization |
| SS | Stainless Steel |
| STL | Stereolithography |
| TO | Topology Optimization |
| TPMS | Triply Periodical Minimal Surface |
| UL | Unsupervised Learning |
| UTS | Ultimate Tensile Stress |
| VD | Volume Density |
| VPP | Vat Photopolymerization |
| YS | Yield Stress |

# Introduction

The work presented in this thesis has been conducted in Rome, Italy, at Roma Tre University, within the Department of Industrial, Electronic and Mechanical Engineering, in the scientific area of Design Tools and Methods (S.C. IIND-03B), including a period of study abroad at Loughborough University, within the Design School, UK. During the PhD, the integration between the Design for Additive Manufacturing discipline and Machine Learning techniques was analysed. During the three months at Loughborough University, the relationship between geometric complexity and the mechanical properties of 3D printed metal parts was studied.

The union of the industrial and digital worlds has led to the definition of Industry 4.0, where the integration of computers and control systems coexist with the manufacturing process. One of the primary revolutions in Industry 4.0 is the diffusion of Additive Manufacturing (AM) technologies. The design process for these technologies is entirely digital, from the early design phase to the final sending of the file to the printer and correlated part quality inspection. Design for Additive Manufacturing (DfAM) is the branch of study that specialises in minimising the defects and costs of these technologies. DfAM is a fundamental practice to avoid errors and reduce the waste of raw materials and time, improving the 3D part quality and the entire production process of the component. Machine Learning (ML) is the sector of Artificial Intelligence (AI) that deals with creating algorithms that learn how to improve the performance of a system based on the acquired data. In the AM and DfAM sector, the usage of ML includes various application levels; among the most relevant, it is possible to identify geometric optimisation practices (Topological Optimisation, Generative Design, Lattice Structures, etc.), cost prediction, selection of process parameters, control of the production process, and other applications. Industry 4.0 provides a large amount of data, often utilised as training data for a Machine Learning system, creating a direct connection between these two worlds.

One of the main advantages of AM, particularly in the Laser-Powder Bed Fusion (L-PBF) process for metals, is its ability to manufacture highly complex geometries. These intricate shapes can justify the use of L-PBF over traditional manufacturing techniques, even though L-PBF costs are higher. While research is improving the final quality of parts, referring to porosity, roughness, and geometric and dimensional tolerances, further studies are necessary to gain a complete understanding of the real mechanical performance of these complex geometries under loads.

The application of ML in AM and DfAM is slowed down by various issues, mostly related to data problems such as non-homogeneity, gaps, and data quality. The data can be obtained from multiple sources, such as physical tests, AM simulations, and sensors (non-homogeneity). AM process-related issues, such as accuracy, repeatability, and distortion, can compromise data quality. The data takeover can be expensive, in the case of 3D metal printing, due to the high cost related to powders and machines, and the high computational cost due to simulations of complex physical problems. Another issue can be associated with the model variety. The AM processes enable printing of complex geometries, introducing a large model variety that complicates the ML training phase.

The objective of this thesis is to provide a method for enhancing the usage and diffusion of AM technologies, with the support of advanced design tools such as virtual prototyping, optimisation methods, and ML predictive models. The focus is on the design of parts realised by Laser-Powder Bed Fusion (L-PBF), which guarantees better mechanical performance, part quality, and dimensional and geometrical tolerances for metal-printed parts.

To establish this challenging research scope, a systematic research approach has been defined since the beginning of the work, and four main objectives were determined to achieve these tasks (Table 1).

*Table 1. Research Objectives and Sub-Objectives*

| **Objectives** | **Description** |
|---|---|
| Obj. 1 | Study of the state of the art on DfAM and ML |
| Sub-obj. 1.1 | Study of design optimisation Methods for AM, considering constraints related to the L-PBF process. |
| Sub-obj. 1.2 | Study of support structures and lattice structures. |
| Sub-obj. 1.3 | Simulation and modelling of the printing process, including techniques for cost and processing time estimation. |
| Sub-obj. 1.4 | Study of ML algorithms, focusing on Supervised Learning methods, for correlating ML and DfAM |
| Obj. 2 | Definition of the DfAM method and software platform, including CAD/CAE tools. |
| Sub-obj. 2.1 | Definition of rules for the Design for Additive Manufacturing. |
| Sub-obj. 2.2 | Definition of analysis models to be used in simulations, with implementation of analytical models for rapid estimation of time and costs. |
| Obj. 3 | Experimentation with AI tools to support the early stages of design. |
| Sub-obj. 3.1 | Definition and classification of input and output parameters. |
| Sub-obj. 3.2 | Training of ML models to estimate the outputs of the print design. |
| Obj. 4 | Case studies and validation: Critical analysis and validation of results. |
| Sub-obj. 4.1 | Additive design of metal components for the automotive and related sectors, with the support of printing simulations. |
| Sub-obj. 4.2 | Use of AI tools in the initial design phase, to be applied to different case studies |

The first objective regards an in-depth study of the state of the art on DfAM and ML. The DfAM includes part geometry optimisation methods and the analysis of the orientations and the necessary support structures. The second one concerns the DfAM method and software platform, including CAD/CAE tools. The third one analyses the geometric, technical, and economic parameters useful as input for ML methods in the experimentation of AI tools. The fourth objective validates the process through case studies regarding the additive design of metal components, with related AM process simulations.

The remainder of the thesis includes, in Chapter 1, a description of the state of the art, starting with the description of AM, describing its potential and current limitations, focusing on the L-PBF process; DfAM and its relevance to reduce errors during and after the printing phase; and a brief description of ML and its application in the AM and DfAM sectors. Chapter 2 illustrates the proposed methodology. Chapter 3 analyses the effect of shape complexity on the mechanical performance of the L-PBF aluminium alloy. Chapter 4 shows some applications of the design optimisation methods for the L-PBF process. Chapter 5 presents the ML-trained models used to validate the proposed approach. Finally, Chapter 6 ends with a discussion section and conclusions.

# 1 Research Background

## 1.1 Industry 4.0

The Fourth Industrial Revolution, also known as Industry 4.0, is an emerging but consolidated approach that incorporates technological advancements in industrial manufacturing. Cloud computing, Cyber-Physical Systems, and the Internet of Things are technologies helping industries become more autonomous, efficient, and customisable. Industry 4.0 refers to a new industrial revolution changing how manufacturing operations are controlled due to the merging of physical and digital areas. Some of the technologies that promote this innovation are Cloud Computing, Big Data, Artificial Intelligence (AI), Cyber-Physical Systems, Digital Twins, Internet of Things, etc. (Figure 1). Thanks to fundamental concepts and characteristics such as Interoperability, Virtualisation, Real-time capacity, Service orientation, Modularity, etc., manufacturing organisations can participate in the transition to Industry 4.0 [1].

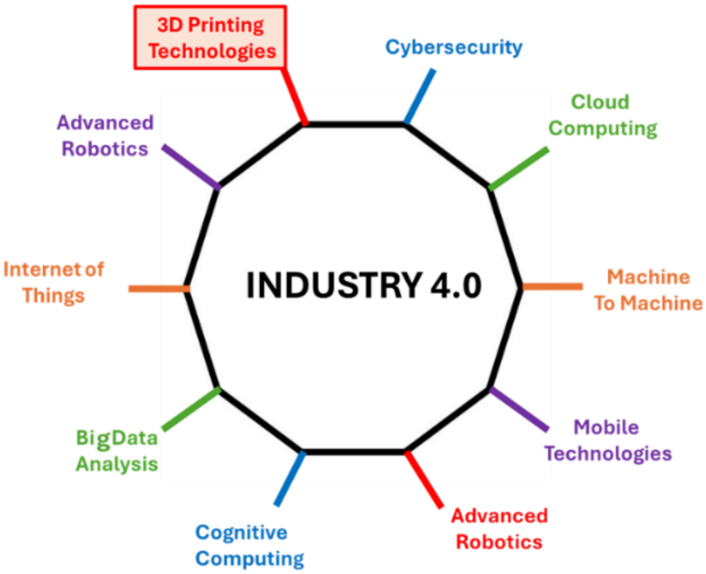

*Figure 1. Technologies for Industry 4.0.*

AM is considered one of the pillars of this industrial revolution, as it aligns with the core principles of this industrial revolution: connectivity, flexibility, and integration with AI. The additive processes enhance personalisation and flexibility, enabling on-demand production of highly customised products without the lengthy and expensive retooling required by traditional manufacturing. AM accelerates innovation by promoting rapid prototyping and reducing the time to market for new products. Its digital nature allows direct interoperability with other Industry 4.0 technologies, such as the Internet of Things and Digital Twins [2]. Innovative 3D printers may provide real-time data feedback, assisting maintenance and process optimisation. Moreover, AM facilitates the decentralisation of manufacturing, delegating smaller enterprises to produce goods closer to the end consumer. This approach can reduce transportation costs and minimise environmental impact since digital files can be shared and printed locally, streamlining supply chains.

## 1.2 Additive Manufacturing

AM is defined by ISO/ASTM 52900:2022 as the process of adding material to produce parts from 3D CAD models, usually layer by layer. The AM process is opposed to traditional processes such as subtractive and formative manufacturing [3]. Following the above-mentioned standard, seven categories of production processes are identified to realise an object from a 3D CAD model; these AM processes are Binder jetting (BJT), Directed energy deposition (DED), Material extrusion (MEX), Material jetting (MJT), Powder bed fusion (PBF), Sheet lamination (SHL), and Vat photopolymerization (VPP). The PBF process for metal parts is generally Laser PBF (L-PBF), also called Selective Laser Melting (SLM). Figure 2 provides a brief description of these production processes.

BJT deposits a liquid binding agent onto a bed of powder (such as metal, sand, or ceramics), bonding the material selectively without using heat during printing; the green bodies thus created need to undergo heat treatment. DED uses focused thermal energy (typically a laser, electron beam, or plasma arc) to melt material as it is being deposited, often through a nozzle; this method is suited for repairing or adding features to existing metal components. MEX involves forcing a thermoplastic or composite material through a heated nozzle, which moves in a pattern to create each layer; it's widely used in desktop 3D printing through Fused Deposition Modelling (FDM). MJT works similarly to inkjet printing, where droplets of photopolymer or wax are deposited layer by layer and cured with UV light, allowing for high-detail and multi-material parts. PBF uses thermal energy, such as a laser or electron beam, to selectively fuse powdered material spread in thin layers; common methods include SLS (Selective Laser Sintering) for polymers and SLM (Selective Laser Melting) or EBM (Electron Beam Melting) for metals. SHL builds parts by stacking and bonding sheets of material, such as metal, paper, or polymer, using adhesives or ultrasonic welding, and then cutting each layer to shape. Finally, VPP uses a vat of liquid photopolymer resin that is selectively cured by a light source, typically a laser or projector, to solidify the resin layer by layer, as seen in technologies like SLA (stereolithography).

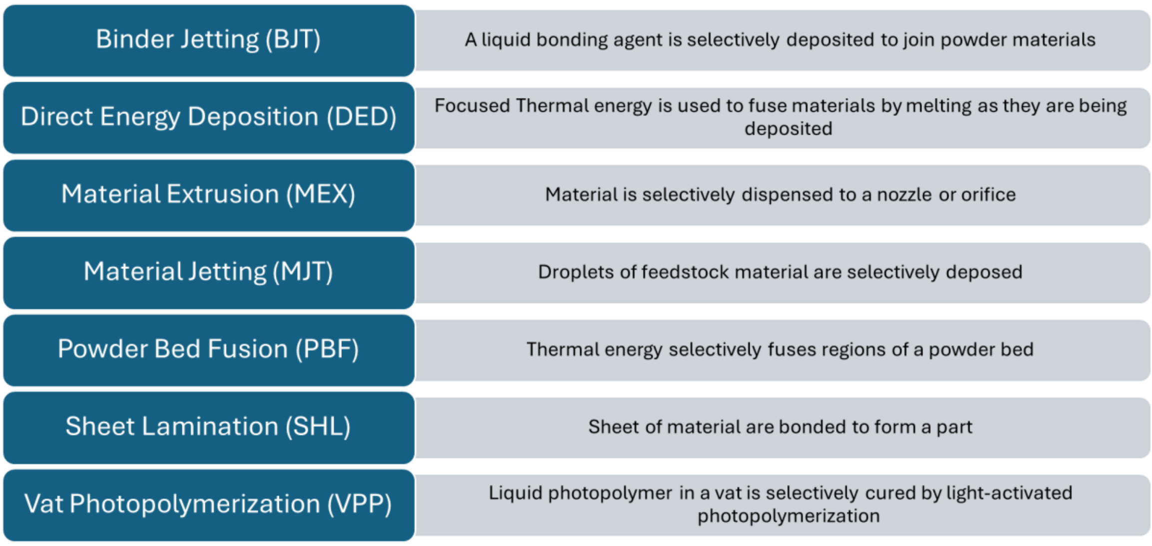

| | |
|---|---|
| Binder Jetting (BJT) | A liquid bonding agent is selectively deposited to join powder materials |
| Direct Energy Deposition (DED) | Focused Thermal energy is used to fuse materials by melting as they are being deposited |
| Material Extrusion (MEX) | Material is selectively dispensed to a nozzle or orifice |
| Material Jetting (MJT) | Droplets of feedstock material are selectively deposed |
| Powder Bed Fusion (PBF) | Thermal energy selectively fuses regions of a powder bed |
| Sheet Lamination (SHL) | Sheet of material are bonded to form a part |
| Vat Photopolymerization (VPP) | Liquid photopolymer in a vat is selectively cured by light-activated photopolymerization |

*Figure 2. Outline of AM processes.*

### 1.2.1 Additive Manufacturing Benefits

AM technologies present a wide range of advantages that have positioned them as profitable techniques in sectors such as aerospace, automotive, healthcare, and consumer products. One of the main strengths is the design flexibility and freedom, which accelerates product development by supporting rapid prototyping with iterative refinement, enhancing innovation, and reducing development risks. Another significant benefit of AM is its capacity for product customization. These technologies allow the efficient production of tailored components in small batches or unique items. AM enables new design possibilities that can be resumed through four types of complexity: form, hierarchical, material, and functional complexity [4]. Form complexity refers to the ability to fabricate highly intricate and freeform geometries. Unlike conventional manufacturing, AM enables the production of complex shapes, such as internal channels or lattice structures, with reduced additional costs or tooling. This leads to benefits such as lightweighting, improved performance, and reduced part count. Hierarchical complexity describes the possibility to control geometry across multiple length scales, from macro to micro-level features. This enables the creation of multi-scale designs, improving properties such as strength-to-weight ratio, energy absorption, and surface functionality. Material complexity is the ability to vary materials or material properties within a single component. AM supports multi-material fabrication and functionally graded materials, allowing designers to optimize local properties (e.g., stiffness, thermal resistance), resulting in enhanced performance and reduced need for assembly. Functional complexity refers to the ability to integrate multiple functions into a single component. These features, such as structural support, heat transfer, fluid flow, and even embedded mechanisms, can be combined within one part rather than being designed separately. This capability enables significant benefits, allowing part consolidation, reducing the number of components in an assembly, and simplifying manufacturing and assembly time and cost. Functional integration can enhance performance; for example, internal cooling channels can be directly embedded within load-bearing structures, improving thermal efficiency without increasing size or weight. Improvements in part design lead to more efficient, compact, and lightweight systems, which are particularly valuable in industries such as aerospace, biomedical, and automotive engineering.

By facilitating custom production, AM challenges economies of scale [5]. Material efficiency is also an essential characteristic of AM. These technologies minimise material waste compared to subtractive manufacturing methods such as milling or machining. Furthermore, certain additive processes allow for the integration of multiple materials within a single build, creating functionally graded components with enhanced mechanical, thermal, or electrical performance [6]. The adoption of AM also offers the potential to streamline supply chains. Instead of maintaining extensive physical inventories, manufacturers can employ digital inventories and produce parts on demand in a few hours. This capability not only reduces warehousing and logistics costs but also improves responsiveness to fluctuating demand. Moreover, the possibility of localised production mitigates reliance on global supply chains and contributes to shorter lead times and lower transportation-related emissions [7]. Furthermore, AM holds considerable promise in maintenance and spare parts provision. By enabling the on-demand fabrication of replacement components, the technology reduces the need for long-term inventory management, a benefit particularly relevant in cases where original tooling is obsolete or unavailable [8].

Lightweighting is probably the most relevant advantage of these technologies, particularly within transport industries. AM allows the realisation of structurally efficient components that reduce weight without compromising strength or durability. These advancements directly contribute to energy efficiency, as lighter parts cut down fuel consumption and operating costs in both automotive and aerospace applications [9]. Sustainability considerations also favour the adoption of AM. Its inherent material efficiency, potential use of recycled or bio-derived feedstocks, and capacity for localised production contribute to reduced environmental impacts compared to conventional approaches. The possibility of closed-loop systems, where materials can be reclaimed and reused, aligns well with global efforts to advance sustainable manufacturing practices.

The combination of mass customisation, distributed production, and enhanced product functionality challenges traditional industrial paradigms and positions AM as a critical enabler of the next generation of engineering and product development.

### 1.2.2 Additive Manufacturing Materials

AM processes utilise a wide range of materials tailored to the specific process and the application of the 3D-printed object. In MEX, thermoplastic polymers such as PLA, ABS, PETG, and nylon are commonly used due to their ease of melting and resolidifying, making them suitable for rapid prototyping and functional parts. Some thermoplastics are also reinforced with carbon or glass fibres to improve strength and stiffness. High-performance thermoplastics like PEEK, PEI, and PPSU require specialised 3D printers with higher chamber and nozzle temperatures. In VPP and MJT, the primary materials are liquid photopolymers that cure when exposed to UV light. These resins can be engineered for a range of properties, from flexibility to high heat resistance, but they generally remain more brittle than thermoplastics [10]. PBF and BJT utilise powdered materials, which can include metals such as stainless steel, titanium, aluminium, nickel-based alloys, and cobalt-chrome. These are especially common in aerospace, automotive, and medical applications due to their high strength and durability. Non-metallic powders, such as polymers and ceramics, are also used for both functional and decorative parts [11]. In DED, metal wires or powders are the main feedstock, typically like those used in welding or PBF, and are selected based on the need for structural integrity, corrosion resistance, or thermal performance. SHL processes involve bonding layers of material such as paper, polymer films, or metal sheets, which are then cut to shape. Table 2 reports some AM commercial materials and their process.

The choice of material in AM depends on factors such as mechanical performance, thermal resistance, biocompatibility, appearance, and cost, with ongoing research continually expanding the range of usable materials.

*Table 2. Some AM commercial materials are classified by AM processes* [12][1].

| Material | MEX | VPP | MJT | PBF | BJT | SHL | DED |
|---|---|---|---|---|---|---|---|
| ABS (Acrylonitrile Butadiene Styrene) | x | | | | | | |
| Polycarbonate | x | | | | | | |
| PC/ABS Blend | x | | | | | | |
| PLA (Polylactic Acid) | x | | | | | | |
| PEI (Polyetherimide) | x | | | | | | |
| Acrylics | | x | x | | | | |
| Acrylates | | x | x | | | | |
| Epoxies | | x | x | | | | |
| Polyamide (Nylon) 11 and 12 - Neat | | | | x | | | |
| Polyamide (Nylon) 11 and 12 - Glass-filled | | | | x | | | |
| Polyamide (Nylon) 11 and 12 - Carbon-filled | | | | x | | | |
| Polyamide (Nylon) 11 and 12 - Metal (Al) filled. | | | | x | | | |
| Polyamide (Nylon) 11 and 12 - Polymer-bound | x | | | | | | |
| Polystyrene | | | | x | | | |
| Polypropylene | | | | x | | | |
| Polyester ('Flex') | | | | x | | | |
| PEEK (Polyether ether ketone) | x | | | x | | | |
| Thermoplastic polyurethane (Elastomer) | x | | | | | | |
| Chocolate | x | | | | | | |
| Paper | | | | | | x | |
| Aluminium alloys | | | | x | x | x | x |
| Co-Cr alloys | | | | x | x | | x |
| Gold | | | | x | | | |
| Nickel alloys | | | | x | x | | x |
| Silver | | | | x | | | |
| Stainless steel | | | | x | x | x | x |
| Titanium, commercial purity | | | | x | x | x | x |
| Ti-6Al-4V | | | | x | x | x | x |
| Tool steel | | | | x | x | | x |

## 1.3 Additive Manufacturing Economic Impact

The AM economic impact is influencing production costs, business models, supply chains, and market dynamics across industries. AM reduces the cost of prototyping, eliminating the need for expensive tooling and moulds. This aspect reduces the starting barriers for small firms and startups, enabling them to compete with established manufacturers through faster product development and lower capital expenditure. The acceleration of prototyping and the reduced time-to-market enhance competitiveness and innovation [13].

AM also modifies supply chains. Its ability to produce parts on demand diminishes the necessity of large inventories and global shipping, leading to reductions in warehousing and logistics costs. This concept of “digital inventory” allows companies to store designs virtually and manufacture components when and where they are needed. Moreover, localised production reduces lead times and transportation costs, which is particularly valuable in industries with highly complex global supply networks [14].

Traditional subtractive manufacturing often produces significant waste, while AM can minimise excess by building parts layer by layer. This not only reduces the cost of raw materials but also aligns with sustainability goals. In sectors such as aerospace, automotive, and healthcare, AM

---

[1] Bourell, D., Kruth, J. P., Leu, M., Levy, G., Rosen, D., Beese, A. M., & Clare, A. (2017). Materials for additive manufacturing. CIRP Annals, 66(2), 659–681. https://doi.org/10.1016/j.cirp.2017.05.009

enables lightweighting, customisation, and functional integration, which can generate long-term economic benefits [15].

However, the economic impact is not uniformly positive. AM technologies still face challenges related to production speed, reliability, scalability, and material costs, which limit their competitiveness in high-volume manufacturing. In addition, industries and labour markets must adapt to the displacement of certain jobs while simultaneously creating demand for new skills in design, digital manufacturing, and materials science [16].

Overall, the economic impact of additive manufacturing is based on its ability to reduce costs, optimise supply chains, enable innovation, and support more sustainable and localised production models. While its potential is most visible in high-value, low-volume sectors, continued technological advancements could expand its influence into mass production.

## 1.4 Laser-Powder Bed Fusion Process

This thesis is specifically focused on the L-PBF process (Figure 3), also called Selective Laser Melting (SLM). Compared with other metal 3D printing processes, L-PBF can provide metal 3D parts with medium-fine surface roughness and tolerances. This AM process is based on the fusion of thin layers of metal powders (30 – 50 μm) through the thermal energy provided by a laser source [17].

The mechanical properties of materials can be reduced by process defects related to non-homogeneity in thermal distribution, a bad range of powder granulometry, porosity, and wrong energy source parameters set-up [18]. The thermal gradient generates a residual stress state that can lead to geometrical distortion and part failure, such as distortion, delamination, or cracking [19]. The thermal gradient can also compromise the fatigue assessment, which is also affected by surface roughness, porosity, and residual stress [20]. To achieve a high density compared to parts fabricated by foundry, the metal powder particles should be completely melted [21, 22]. Defects related to porosity, residual stresses [23], dimensional tolerancing [24], balling [25], and roughness are directly related to process control (temperature, environment measurements, chemical analysis) and material properties [26]. Compressive strength, elastic modulus, porosity, and surface roughness can be improved by heating treatments that are able to increase the microstructural performance of the materials, reducing issues related to fusion porosity, balling effect, and entrapped gas pores and shrinkage [27, 28].

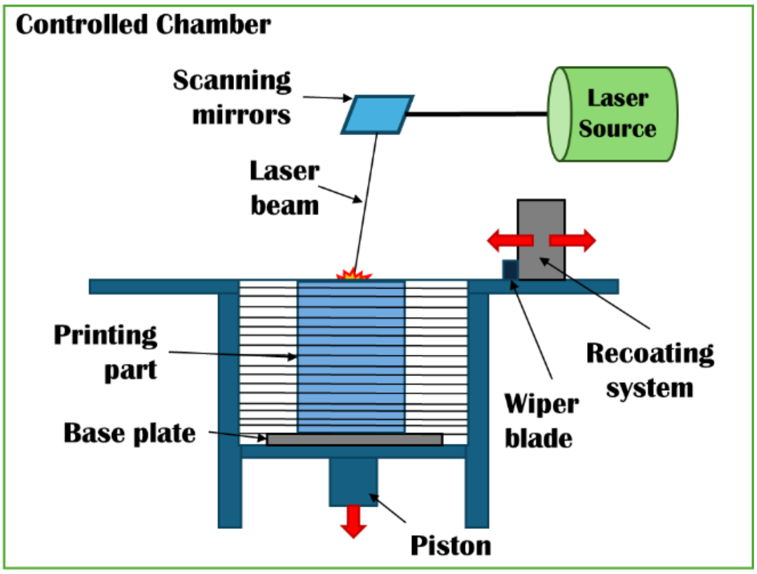

*Figure 3. L-PBF operating scheme [29][2].*

Table 3 lists the main variables that influence the L-PBF process for metals. It categorises these variables into two groups: powder properties and process parameters. The powder properties include factors such as particle shape, particle size and distribution, chemical composition, thermal conductivity, melting temperature, and absorptivity or reflectivity of the atomised metal alloy. These properties affect how the powder melts and solidifies. The process parameters refer to the operational and environmental settings that control the manufacturing process, including laser power, scanning speed, hatching distance, protective atmosphere of the building chamber, laser beam radius, laser type, layer thickness, scanning strategy, building orientation, gas flow, and bed temperature. Together, these parameters and powder properties determine the quality, microstructure, and mechanical performance of the fabricated metal parts [30].

*Table 3. Some of the main L-PBF process parameters and Powder Properties.*

| **Process Parameters** | | **Powder Properties** |
|---|---|---|
| Laser power | Gas flow | Particle shape |
| Layer thickness | Protective atmosphere | Particle size and distribution |
| Scanning speed | Bed temperature | Chemical composition |
| Hatching distance | Laser Beam radius | Melting temperature |
| Scanning strategy | Laser type | Thermal conductivity |
| Building orientation | | Absorptivity/Reflectivity |

Equation 1 describes the Energy Density factor ($E_d$); it represents the amount of laser energy delivered to a specific volume or area of the powder bed ($J/mm^3$). It is a key parameter that influences melting behaviour, part density, and surface quality.

$$E_d = \frac{P}{v \cdot h \cdot t} \tag{1}$$

---

[2] Trovato, M., Belluomo, L., Bici, M., Prist, M., Campana, F., & Cicconi, P. (2025). Machine learning in design for additive manufacturing: A state-of-the-art discussion for a support tool in product design lifecycle. The International Journal of Advanced Manufacturing Technology, 137(5–6), 2157–2180. https://doi.org/10.1007/s00170-025-15273-9

Where $P$ is the laser power ($W$), $v$ is the scanning speed ($mm/s$), $h$ is the hatch spacing ($mm$), and $t$ is the layer thickness ($mm$). This combined parameter is often used to compare different printing setups, given that $E_d$ strongly influences density, microstructure, mechanical properties, surface quality, and defects of metal parts. For example, for the printing of pure Nickel, with the $E_d$ increase, many pores appear inside the grains, and the grains grow along the building direction, pores gradually disappear after undergoing remelting at the edges of the melting tracks [31]. For example, for the AlSi10Mg alloy, the relationship between internal porosity and $E_d$ is shown in Figure 4. The internal porosity first decreases and then increases with the increase of $E_d$. It is relatively small when the energy density is between 35 $J/mm^3$ - 45 $J/mm^3$ [32].

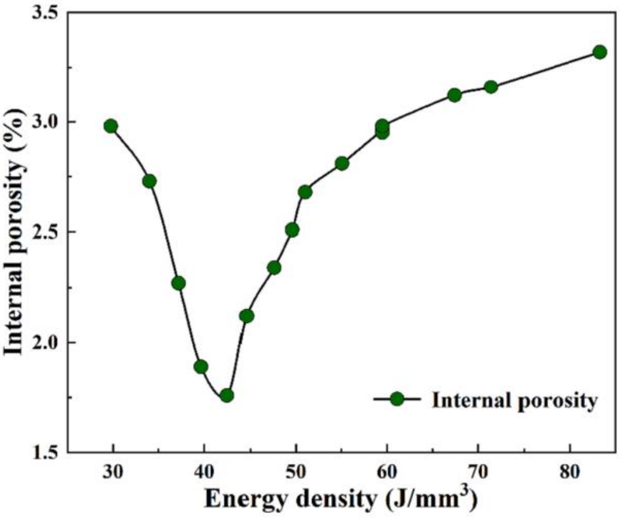

*Figure 4. Influence of Energy density in the AlSi10Mg alloy [31][3].*

### 1.4.1 L-PBF Materials

Conventional bulk materials produced through casting or forging generally exhibit equiaxed grains, providing uniform mechanical properties in all directions. In contrast, L-PBF parts have a distinct microstructure characterised by fine, columnar grains aligned with the build direction due to rapid cooling and directional heat flow during the layer-by-layer process. Porosity levels in bulk materials are typically very low after processes like forging or rolling, as these methods consolidate the material. L-PBF parts, however, usually contain between 0.1% and 1.0% porosity in the as-built state, caused by incomplete melting or trapped gas. Full densification often requires post-processing, such as hot isostatic pressing (HIP) [33].

While conventional materials are largely isotropic, L-PBF parts tend to show moderate to significant anisotropy, with mechanical properties varying by direction and generally higher strength along the vertical (Z) axis [34].

Surface finish also differs significantly. Machined bulk materials have smooth surfaces, while L-PBF parts are much rougher, with typical roughness values of 5–20 µm Ra. This makes post-processing, such as machining or polishing, necessary for functional or aesthetic requirements [35].

---

[3] Li, D., Zhang, X., Qin, R., Xu, J., Yue, D., & Chen, B. (2023). Influence of processing parameters on AlSi10Mg lattice structure during selective laser melting: Manufacturing defects, thermal behavior and compression properties. Optics &amp; Laser Technology, 161, 109182. https://doi.org/10.1016/j.optlastec.2023.109182

These factors strongly affect fatigue strength. Polished bulk materials exhibit reliable fatigue performance, whereas L-PBF parts have lower fatigue strength in the as-built condition. To improve this, HIP treatment combined with surface finishing is commonly applied, reducing internal defects and enhancing durability.  Table 4 lists the main application areas of different metals and their alloys used in the L-PBF process. Alloys must be selected based on their properties and mechanical performance requirements in specific applications [36].

*Table 4. Common AM alloys and their application [36][4].*

| **Application Area** | **Aluminium** | **Maraging steel** | **Stainless steel** | **Titanium** | **Cobalt chrome** | **Nickel super alloys** | **Precious metals** |
|---|---|---|---|---|---|---|---|
| Aerospace | X | | X | X | X | X | |
| Medical | | | X | X | X | | X |
| Energy, oil and gas | | | X | | | | |
| Automotive | X | | X | X | | X | |
| Machinability and weldability | X | | X | X | X | X | |
| Corrosion resistance | | | X | X | X | X | |
| High temperature | | | X | X | | X | |
| Tools and Moulds | | X | X | | | | |
| Consumer products | X | | X | | | | X |

The most common titanium alloy is Ti6Al4V. L-PBF parts exhibit higher tensile and yield strengths than the bulk material due to fine microstructures formed by rapid solidification, although ductility is slightly reduced. With optimised parameters and post-processing, such as HIP or heat treatments, density and mechanical performance approach or exceed those of wrought materials [37]. Inconel 718 is a high-strength, corrosion-resistant nickel-based superalloy used in extreme temperature environments. The as-built material shows comparable or even superior tensile strength to conventionally produced alloys, while maintaining excellent yield strength and elastic modulus. However, ductility is somewhat lower in the as-built state and improves after post-processing [38]. The 316L stainless steel produced by L-PBF demonstrates slightly higher strength than its bulk counterpart, attributed to fine-grain structures, while retaining good ductility and density [39]. AlSi10Mg shows a significant increase in tensile and yield strength due to rapid solidification and refined microstructure, though its ductility is initially low in the as-built condition. Heat treatment or annealing helps improve ductility [40].

### 1.4.2 L-PBF Process Simulation Methods

Due to the high cost of the L-PBF process, different simulation methods have been developed to predict the thermo-mechanical behaviour of the metal 3D printing process [41]. As described in Figure 5, these simulation methods can be classified into micro-scale [42], hybrid micro-scale, meso-scale [43], thermo-mechanical, thermo-fluids dynamics, and inherent strain-based methods [44]. These methods investigate different aspects of the AM process, such as analysis of the melt-

---

[4] du Plessis, A., Razavi, N., Benedetti, M., Murchio, S., Leary, M., Watson, M., Bhate, D., & Berto, F. (2022). Properties and applications of additively manufactured metallic cellular materials: A review. Progress in Materials Science, 125, 100918. https://doi.org/10.1016/j.pmatsci.2021.100918

pool geometry, the induced porosity and roughness, the micro-structural formation, etc. [45]. Micro and meso-scale methods are suitable to analyse the behaviour from micro-structure to molten pool; however, the elevated computational cost and time limit their application in the simulation of a full 3D component. The other methods are suitable to analyse the mechanical behaviour of a full 3D part while printing; however, they are less precise.

Due to its relevant computational efficiency, the inherent strain-based method is one of the most used simulation methods for evaluating the 3D printing of metal parts with L-PBF. This method consists of two phases: the first one realises a thermo-mechanical simulation on a micro-scale specimen to compute the plastic strain tensor (calibration phase), the second one applies the resulting plastic strain tensor to an actual component and performs a linear elastic analysis [46]. Instead of simulating every single laser scan and thermal cycle, which would be computationally expensive, this method simplifies the process by focusing on the mechanical effects of the thermal history rather than explicitly modelling the full transient thermal behaviour. In the L-PBF process, localised heating from the laser causes rapid melting and solidification, leading to steep thermal gradients. These gradients induce non-uniform expansion and contraction, generating plastic strains that remain locked into the material after cooling, known as inherent strains. The key idea of the inherent strain method is to predefine these strains and apply them directly to the model, treating them as an input rather than calculating them through detailed thermal-mechanical coupling [47]. During the simulation, the build process is represented layer by layer. Instead of modelling heat transfer, each new layer is assigned a predefined inherent strain in specific directions, typically longitudinal, transverse, and occasionally vertical. The mechanical solver then calculates the resulting deformations and stresses caused by the accumulation of these strains. This approach significantly reduces computational time and resources while still capturing the essential mechanical effects of the L-PBF process [48].

However, the inherent strain-based method shows several limitations related to calibration required, no coupling with thermal simulations, and different simplifications related to fixed inherent strain values, time-dependent phenomena not considered, nonlinear effects not considered, etc. This method can provide an average prediction of residual stress and deformations in metal AM, with results mostly affected by the calibration data.

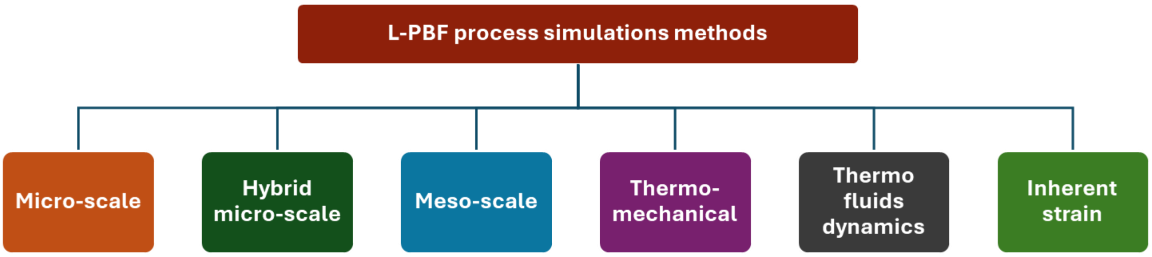

*Figure 5. L-PBF process simulation methods.*

## 1.5 Design for Additive Manufacturing

Design for Additive Manufacturing (DfAM) is the branch of engineering design studies that analyses how to realise defectless components, from the early design phases to the quality inspection of 3D printed components [49]. DfAM can be seen as a solution for the drawbacks in AM. The early design phase in mechanical design is the initial stage where the fundamental ideas and direction of a product are defined. At this stage, the study focuses on understanding the problem and the constraints (cost, size, materials, standards); concept generation, brainstorming multiple possible solutions and design approaches; preliminary evaluation, comparing concepts based on feasibility, performance, and their simplicity; basic calculations and sketches, rough models, hand calculations, and simple simulations to test ideas. The goal is not detailed accuracy, but to explore options and choose the best overall concept before investing time in detailed design. Decisions made here have the biggest impact on the cost, performance, and success of the final product [50].Despite the significant advantages related to the possibility of realising free-form and complex geometries, several manufacturing constraints are present. For the L-PBF process, several constraints are related to manufacturing limits, including minimum wall thickness, minimum and maximum hole clearance, dimensional accuracy, and surface roughness. Other drawbacks are limiting the industrial widespread of this 3D printing process, such as the necessity of support structures, the necessity of post-processing operations, high building time for large-sized components, limited dimensions of the building chamber, and the high cost associated with the process and raw materials [51]. Figure 6 illustrates an Ishikawa diagram that displays parameters affecting the final part quality in the L-PBF process, highlighting the complexity of this manufacturing process [52].

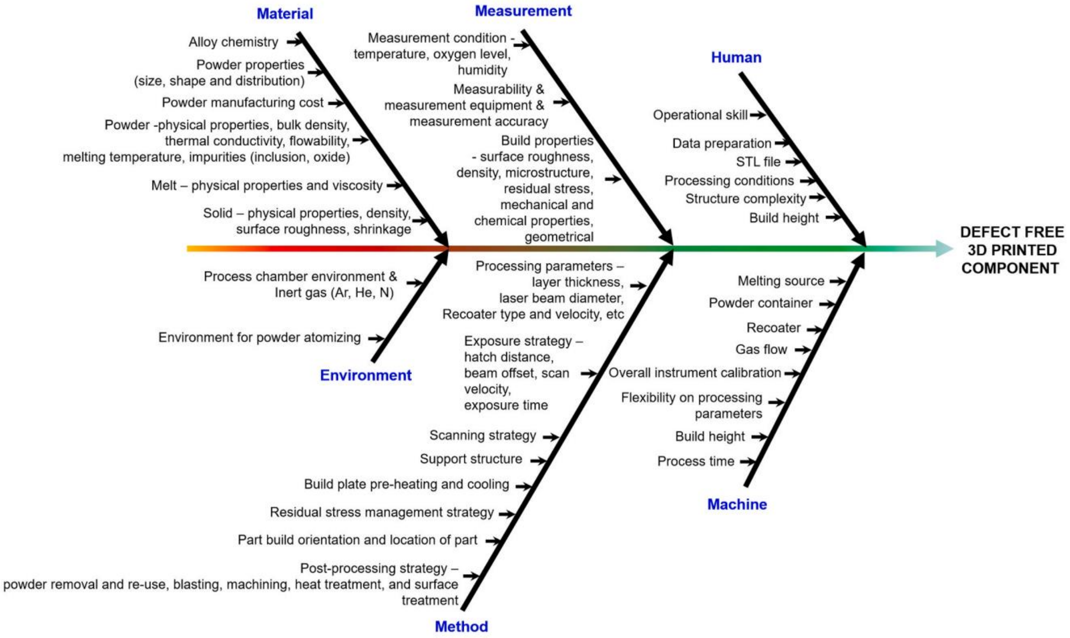

*Figure 6. Ishikawa diagram presenting the factors that influence part quality in the L-PBF process* [52][5].

---

[5] Kotadia, H. R., Gibbons, G., Das, A., & Howes, P. D. (2021). A review of Laser Powder Bed Fusion Additive Manufacturing of aluminium alloys: Microstructure and properties. Additive Manufacturing, 46, 102155. https://doi.org/10.1016/j.addma.2021.102155

Using a DfAM approach, the designers can study the design constraints related to the 3D printing process during the early design phases [53]. The use of DfAM aims to prevent multiple iterations during the design process and avoid high costs and material consumption while realising the parts [54]. Figure 7 illustrates some of the common L-PBF process geometrical constraints. DfAM activities also include the design of the support structures, which are necessary to support overhanging surfaces in additive processes [55]. The support structures allow parts to be correctly built [56]; however, they must be designed to be accessible, heat-dissipating, lightweight, and load bearing [57,58]. Geometric Dimensioning and Tolerancing (GD&T) is essential information in mechanical drawing. The desired functional behaviour of a mechanical component is respected only when the specific geometrical tolerances are verified [59]. However, one of the main issues of the L-PBF process is the presence of geometric distortions in the built part. These distortions can compromise the GD&T check and even fail the 3D printing process [60]. DfAM tools can improve the definition of geometry and parameters to achieve optimised results. For example, Das et al. [61] have studied a methodology to consider GD&T specifications while optimising the build orientation of an AM part, defining a relationship between tolerance errors and build orientation. This study also proposes the development of a tool to automatically retrieve the tolerance specifications from the 3D CAD annotations using the Application Programming Interface (API) libraries of the employed CAD software. The support structures are necessary to orient the part when printing. The orientation should consider the best trade-off between production time, cost, removability, and accuracy [62]. However, while supports reduce the risk of distortion when printing, their volume increases the processing time in printing and post-processing operations.

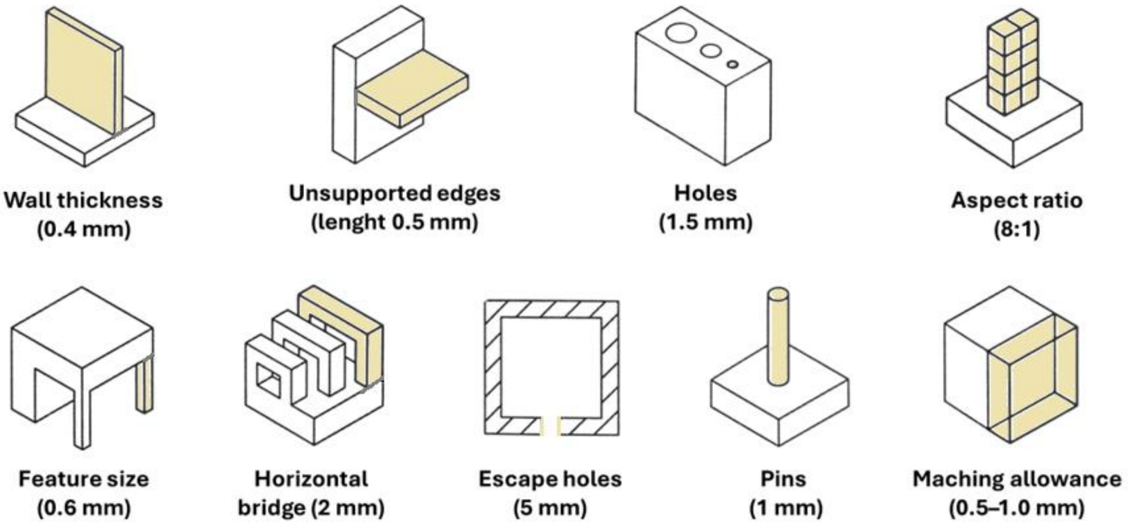

*Figure 7. Common values for some L-PBF constructive constraints* [63][6].

Figure 8 illustrates an example of a DfAM workflow. The user, following the main phases, could have a structured approach that could help avoid errors. The process begins by defining the

---

[6] Redwood, B., Schöffer, F., & Garret, B. (2017). *The 3D printing handbook: Technologies, design and applications*. 3D Hubs B.V. ISBN 978-90-827485-0-5.

reference model, then it continues with the application of one or more optimisation practices and ends with the simulations of the AM process.

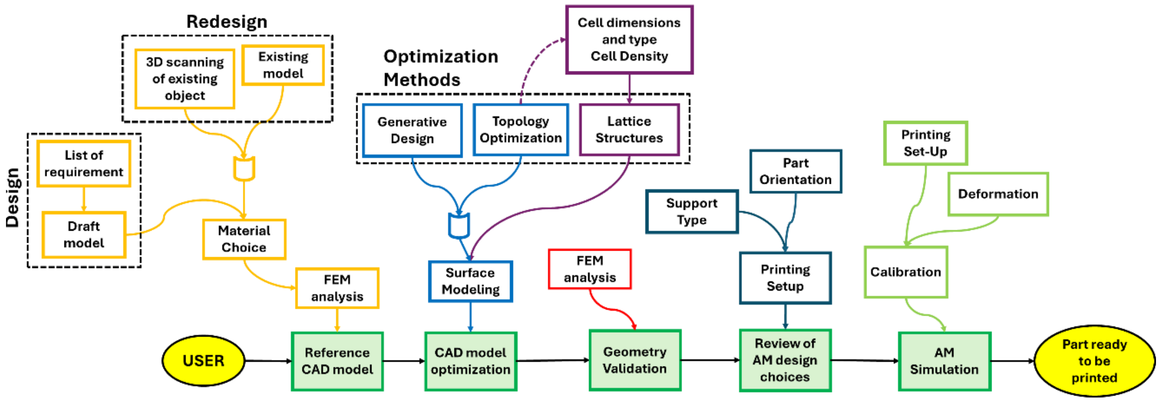

*Figure 8. Example of DfAM workflow [64]*[7].

## 1.5.1 Reference CAD Model

A starting CAD model to be used as a reference is necessary to begin a design activity for AM. If the part already exists, the CAD file could be available. Otherwise, a draft model can be modelled using CAD software. This reference model will be a conceptual model to be used in the early design phases. If a physical part exists but the CAD model is not available, the modelling phase can be supported by reverse engineering techniques. To successfully perform a 3D acquisition of a real component, it is necessary to follow some steps: Data acquisition or measurement, using various measurement technologies such as CMMs, optical or laser scanners, structured light, CT, to capture the physical object geometry; mesh generation, converting raw data into a usable geometric (triangular surface mesh or point cloud); surface fitting, turning mesh into meaningful features (planar, cylindrical, conical, free-form) so that simpler underlying surfaces can be fitted; model construction, constructing a B-rep model (faces, edges, vertices) that represents solid [65].

To start with the design activity, the mechanical behaviour of the reference CAD model must be evaluated. Generally, Finite Element Methods (FEM) tools are used to simulate mechanical behaviour. This phase requires the definition of the material properties and boundary conditions, such as operative temperature, loads, constraints, etc. The results of the numerical analysis give information about the distribution of stress and deformation on the reference model, highlighting the areas to be improved. The analysis of the results is an essential phase to define the objective functions for the optimisation analysis.

## 1.5.2 Topology Optimisation Methods

Lightweight Design (LD) is a relevant engineering discipline focused on reducing the mass of products and structures while maintaining or improving their performance and functionality. Two main reference points are fundamental in this discipline: the concept of material design, particularly

---

[7] Trovato, M., Vigna, A., Cicconi, P., Belluomo, L., Bici, M., & Campana, F. (2025). Analyzing Tools and Methods in Design for Additive Manufacturing: Workflow and Test Cases. Computer-Aided Design and Applications, 1125–1135. https://doi.org/10.14733/cadaps.2025.1125-1135

from the perspective of material replacement and the strategic utilisation of lightweight alloys and other advanced materials; and the structural optimisations, which permit the optimisation of material distribution, placing it where it is needed. The primary goal of LD is to achieve weight reduction; for example, in the automotive sector, this objective enhances energy efficiency in passenger cars, thereby reducing energy consumption and improving performance. This also leads to the possibility of reducing the environmental impacts of vehicles and increasing the payload capacity [66]. One of the most relevant options for lightweighting is the use of performance materials, which offer high strength-to-weight ratios and stiffness-to-weight ratios. These materials can be metal alloys or composites.

In the case of metal alloys, AM processes demonstrate the potential to utilise metal powders such as AlSi10Mg, Ti6Al4V, Inconel 625 and 718, and 316L. However, the design phase should consider that the mechanical properties of 3D printed parts are usually different from those of their commonly manufactured counterparts; even post-treatments can increase their mechanical behaviour. 3D parts show an anisotropic behaviour concerning the z-axis of the 3D printer.

Analysing the interaction between materials, mechanical behaviour, and mass distribution is a complex process that requires specialised tools and methods. In this context, Structural Optimisation methods are powerful tools used in engineering design to improve the performance of components or structures. These methods aim to find the optimal design configuration that satisfies boundary conditions and objectives such as minimising weight or maximising stiffness. They also consider constraints such as mass limits, geometrical limits (including volume, symmetry, and thickness), and manufacturing constraints such as the overhang angle for AM processes. The primary structural optimisation categories are Topology Optimisation, Shape Optimisation, Generative Design, Parametric Optimisation, and Lattice Structures (Figure 9). These structural optimisation methods enable engineers to design lighter, stronger, and more efficient products across various industries, including aerospace, automotive, medical devices, and consumer goods. Following, these practices are briefly described.

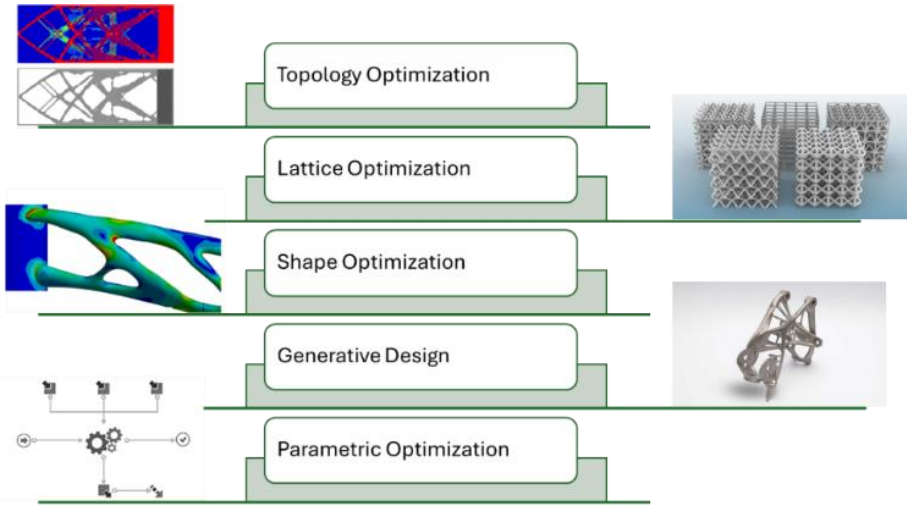

*Figure 9. Geometry Optimisation Methods.*

#### 1.5.2.1 *Topological Optimisation*

Topology Optimisation (TO) aims at defining the optimal material distribution within a given design space, for a given set of loads, boundary conditions, constraints, and performance requirements. Many algorithms have been developed to achieve this scope; the most widely used are the SIMP (Solid Isotropic Material with Penalisation) and the LSM (Level Set Method) [67].

In the SIMP method, a density value between 0 and 1 is assigned to each mesh element, and a threshold value. The shape of the component is obtained by leaving elements with a density value above the threshold value. To have intermediate densities toward 0 or 1, the material stiffness is interpolated using a penalised relation (Equation 2)

$$E(\rho) = \rho^p E_0 \tag{2}$$

where $\rho$ is the density, $E_0$is the Young's modulus of solid material, and $p > 1$is the penalisation factor (commonly $p = 3$) [68]. Figure 10 shows the Normalized Young's modulus $\frac{E(\rho_e)}{E_0}$ trend as a function of the element density $\rho_e$ depending on the penalization factor $p$.

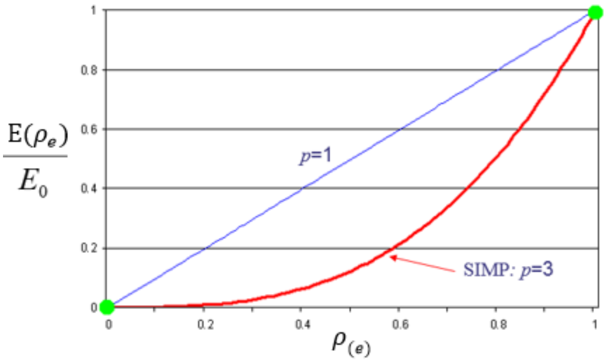

*Figure 10. Normalized Young's modulus* $\frac{E(\rho_e)}{E_0}$*as a function of the element density* $\rho_e$ *depending on the penalization factor* $p$.

In the LSM, a function $\phi(x)$, defined on the finite element mesh, represents an isosurface. The domain is defined based on the value of $\phi(x)$ (Equation 3).

$$\begin{cases} \phi(x) > 0 : x \in \Omega/\partial\Omega \\ \phi(x) = 0 : x \in \Omega \\ \phi(x) < 0 : x \in \mathrm{D}/\Omega \end{cases} \tag{3}$$

where, $\mathrm{D}$ is the design domain; $\Omega$ is the material region, $\partial\Omega$ is the boundary and $\mathrm{D}/\Omega$ is the region with no material. The level set equation (Equation 4) determines the dynamic behaviour of the boundary [69]. Figure 11 show a domain representation.

$$\frac{\partial\phi}{\partial t} = v_n|\nabla\phi| \tag{4}$$

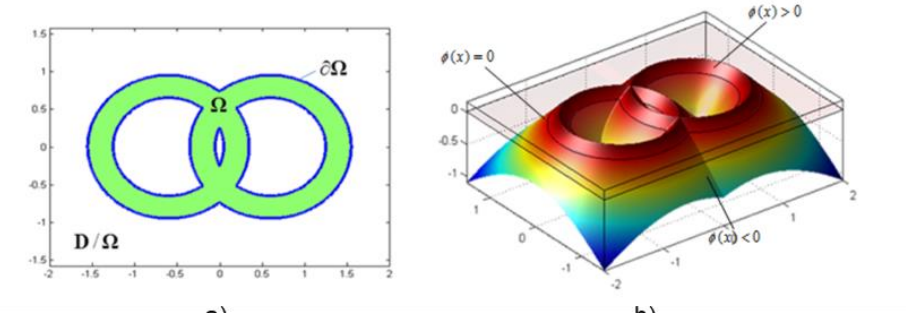

a) b)

*Figure 11. Level set representation of a domain: a) the material domain $\Omega$ and its boundary $\partial\Omega$; b) the level set function $\phi(x)$with regions where $\phi(x) > 0$, $\phi(x) = 0$, and $\phi(x) < 0$.*

### 1.5.2.2 Lattice Structures

Lattice Structures (LS) are defined as geometrical repetitive structures that infill a determined volume. They are used for lightweight purposes, enhancing stiffness relative to mass, energy absorption, and increasing surface area. They are suitable for realization by AM processes and can be easily applied to the 3D model, as described mathematically by equations. LS can be classified as heterogeneous or homogeneous depending on the relative cell density and dimensions, as well as Strut-Based (Fig. 12 a-e) or Triply Periodical Minimal Surface (TPMS) (Fig. 12 f-h), depending on the starting cell geometry.

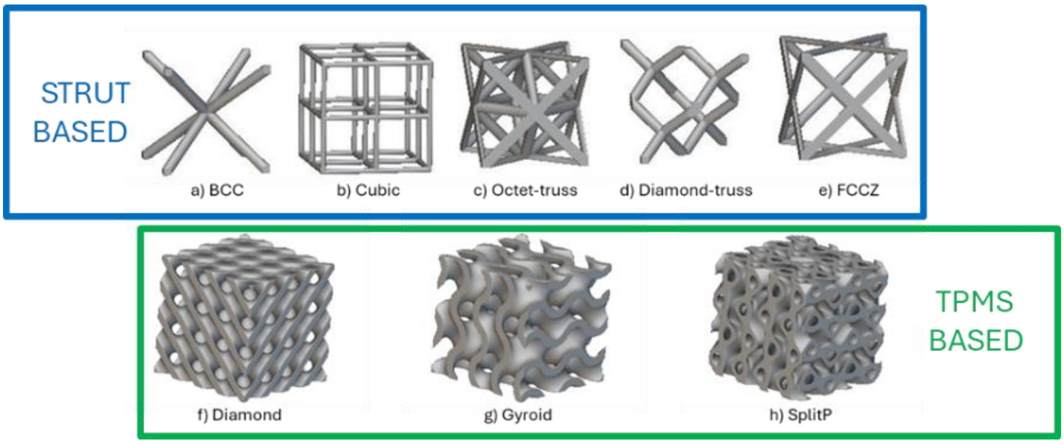

*Figure 12. Examples of Strut-based Lattice Structures (a-e) and TPMS Lattice Structures (f-h)*

They are defined parametrically by determining the unit cell parameters, which depend on the unit cell type. They are especially suited to reduce density and obtain the desired component properties. The main drawbacks of the applications are that the expected resistance is not linear with the relative density of the lattice due to stress concentration, and, depending on the selected material, the component's mechanical properties may vary. Therefore, it is common practice to validate the structure before realization. Multi-graded LS types can locally vary the lattice characteristics and therefore enable the design of components with specific local properties; they are often associated with the result of a TO when it yields a density map.

The Maxwell number $M$ (Equation 5) is a parameter used to characterize the structural behaviour of strut-based framework:

$$M = s - 3n + 6 \tag{5}$$

where $s$ is the number of struts and $n$ is the number of nodes for the single cell. When $M < 0$, the structure lacks enough struts to balance external forces without creating moments at the nodes, inducing bending stresses in the struts. When $M \geq 0$, the external loads are supported entirely through axial tension and compression in the struts, these systems are therefore stretch dominated [70]. TPMS are generated from mathematical equations that define the $U = 0$ isosurface, which separates the solid and void regions of the structure. Their mechanical properties can be tailored by adjusting parameters such as periodicity and relative density. The periodicity is determined by the k-values ($k_x$, $k_y$, $k_z$), calculated using Equation 6, where $n_i$ is the number of cell repetitions in the x, y, or z directions, and $L_i$ is the total size of the structure along that axis. The variable *t* is used to modify the relative density:

$$k_i = \frac{2\pi n_i}{L_i}\ (i = x, y, z) \tag{6}$$

Compared to strut-based lattices, TPMS structures offer advantages in manufacturability. In L-PBF, strut-based lattices are limited by the inclination angles of their struts. TPMS geometries overcome this issue because their surfaces change inclination smoothly, allowing each layer to be supported by the one below, enhancing printability [71]. Table 5 reports some topology isosurface formulas of common TPMS structures.

*Table 5. Topology Isosurface Formulas for TPMS structures.*

| **TPMS** | **Formula** |
|---|---|
| Schoen Gyroid | $U_G = \cos(k_x x)\sin(k_y y) + \cos(k_y y)\sin(k_z z) + \cos(k_z z)\sin(k_x x) - t$ |
| Schwartz Diamond | $U_D = \sin(k_x x)\sin(k_y y)\sin(k_z z) + \sin(k_x x)\cos(k_y y)\cos(k_z z) + \cos(k_x x)\sin(k_y y)\cos(k_z z) + \cos(k_x x)\cos(k_y y)\sin(k_z z) - t$ |
| Neovius Surface | $U_N = 3[\cos(x) + \cos(y) + \cos(z)] + 4\cos(x)\cos(y)\cos(z)$ |

One of the main parameters used for unit cell optimization is Relative Density ($\rho_{rel}$), defined as the ratio between the density of the lattice material ($\rho^*$) and the density of the solid material (bulk) ($\rho_s$) of the individual cell (Equation 7).

$$\rho_{rel} = \frac{\rho^*}{\rho_s} \tag{7}$$

. The Gibson-Ashby model describes the mechanical property of lattice and TPMS structures, which depends on relative density. It uses power-law relationships between the effective properties of the lattice and those of the solid material it's made of. The Gibson–Ashby model provides a scaling law to predict how stiffness and strength decrease as a lattice becomes lighter. Equations 8 and 9 describe the relationships between elastic modulus and yield strength, respectively.

$$\frac{E^*}{E_s} = C_1\left(\frac{\rho^*}{\rho_s}\right)^{n_1} \tag{8}$$

$$\frac{\sigma^*}{\sigma_s} = C_2(\frac{\rho^*}{\rho_s})^{n_2} \tag{9}$$

Where $E^*$ is the effective Young's modulus of the lattice, $E_s$is the Young's modulus of solid material, $\sigma^*$is yield strength of the lattice, $\sigma_s$is yield strength of the solid material, and $C_1$, $n_1$, $C_2$, and $n_2$ are empirical constants depending on lattice geometry [72].Table 6 reports some lattice and TPMS applications with their desired properties.

*Table 6. Some Lattice and TPMS applications with relative desired properties* [36][8].

| Application | Desired Properties |
|---|---|
| Lightweight Structures | High Specific Stiffness; High Specific Strength |
| Biomedical Implants | Tuned mechanical properties to match desired mechanical properties |
| Crashworthiness, Packaging, Shock Absorption | High energy absorption |
| Vibration Control | High mechanical loss/damping coefficient; High specific natural flexural vibration frequencies |
| Electrodes, Catalysts, Heat Pipe Wicks | High Surface/Volume ratio |
| Thermal Insulation | Low Thermal Conductivity; Low Specific Heat |
| Heat Exchanger | High Thermal Diffusivity: Low Differential Thermal Expansion; |
| Thermal Control / Hydrogen Storage Tanks | Controlled thermal conductivity; High surface area |
| Acoustic Absorption | High sound-absorption coefficient |
| Support Structures and Infill in AM, Buoyancy | Low density |

#### *1.5.2.3 Generative Design*

Generative methods make their most significant impact during the product development cycle, particularly in the conceptual design phase. They enable the creation of organic geometries that extend beyond the limitations set by designers, who are often influenced by their prior experiences. With advances in AI algorithms, the availability of computing power, the rise of AM techniques, and the development of new materials, a gradual increase in this innovative design approach is observed.

Generative Design (GD) methodologies utilise algorithmic approaches to automatically correlate requirements and constraints of the design project with the design space of possible design solutions [73]. GD approaches use several algorithms and tools to create design variants and to explore a vast solution space. They can generate numerous design variations based on input criteria such as objective functions, constraints, parameters, and performance criteria. Popular GD algorithms are Genetic Algorithms (GA), inspired by natural selection, that use mutation, crossover, and selection to evolve better designs over generations; TO; Shape Grammars, rule-based systems that iteratively apply design rules to generate complex shapes or architectural layouts; L-systems, recursive algorithms used to mimic natural growth patterns, and ML models [74]. The GD result is a set of possible solutions for the individual problem. The designer's role will then be to qualitatively and quantitatively evaluate these solutions, depending

---

[8] du Plessis, A., Razavi, N., Benedetti, M., Murchio, S., Leary, M., Watson, M., Bhate, D., & Berto, F. (2022). Properties and applications of additively manufactured metallic cellular materials: A review. Progress in Materials Science, 125, 100918. https://doi.org/10.1016/j.pmatsci.2021.100918

on the objectives set, choosing the one that best meets those objectives deemed the overall optimum for solving that specific problem. Figure 13 reports a set of GD possible solutions for the same case study.

*Figure 13. Examples of different solutions obtained with a GD method*[9].

### *1.5.2.4 Parametric Design*

Parametric design is a method in which geometry and form are defined by parameters and rules rather than fixed dimensions. By changing input parameters such as length, angle, or density, designers can quickly generate and explore variations of similar models, which are referred to as a family of parts. This approach, combined with GA, is widely used for searching optimal solutions, where performance (e.g., strength, weight, stiffness) can be optimised by adjusting geometrical parameters [75].

The GA exploits the process of natural selection, in which the fittest individuals have a higher chance of surviving, procreating, and passing on their advantageous traits to the following generation. Over multiple generations, the algorithm explores the solution space and converges toward optimal or near-optimal solutions. Starting from an initial population (individuals), GA evaluates the fitness score of the objective functions, quantifying the solution's quality. Subsequently, GA selects from the current population to serve as parents for the next generation and performs crossover and mutation, creating a new population. GA repeats the evaluation, selection, crossover, mutation, and replacement until a satisfactory solution is found. The best individuals represent the optimised solutions to the problem. In the proposed test case, the individuals are the combinations of the design parameters. The best individuals are the parameter configurations that maximise the fitness score [76].

### *1.5.2.5 Shape Optimisation*

The Shape Optimisation (SO) approaches use morphing optimisation technologies to manipulate solid parts by altering node positions. The part shape is represented by the mesh; a low mesh quality may lead to inaccurate approximation errors in the case of excessive deformation from the

---

[9] Solanki, C. (2019, July 10). *Generative design for components in the automotive industry*. Autodesk Fusion 360 Blog. https://www.autodesk.com/products/fusion-360/blog/generative-design-for-components-in-the-automotive-industry/

starting shape, due to the mesh's non-dynamicity. The starting shape is modified by updating the position of the mesh vertices using the shape perturbation $\theta^*$ as described in Equation 10 [77]:

$$x_i^{n+1} = x_i^n + \theta^*(x_i^n) \tag{10}$$

where $x_i^{n+1}$ is the position vector of vertex $i$ at the new shape, $x_i^n$ is the position vector of vertex $i$ at the current shape.

### 1.5.3 Support Structures and Part Orientation

In L-PBF, both the orientation of the part and the design of the support structures have a significant impact on the final quality, mechanical behaviour, and efficiency of the process.

The orientation of a part determines its positions and inclinations with respect to the build plate. This factor directly affects surface quality, dimensional accuracy, and mechanical properties. Surfaces facing upward generally exhibit better surface finish, while downward facing or overhanging regions tend to be rougher due to partially melted powder adhering to the surface and the presence of burrs related to the detachment of the supports. Parts oriented vertically often have higher dimensional accuracy, whereas horizontal or angled features are more prone to distortion due to uneven cooling and residual stresses. Orientation also influences mechanical anisotropy, as L-PBF parts typically exhibit stronger bonding on the XY plane, resulting in lower strength along the Z direction. Moreover, the build orientation affects production time and cost; minimising build height can reduce printing time and overall energy consumption [78].

Support structures play a complementary role by providing stability during the fabrication process. They support overhanging sections, prevent collapse, and help dissipate heat away from critical areas, thereby reducing residual stresses and warping. Supports also help maintain geometric accuracy and protect the part from recoater forces [79]. However, they increase material consumption, printing time, and post-processing effort since they must be removed after the build. Improperly designed supports can even cause distortion or surface damage during removal [80].

In practice, orientation and support design must be optimised together. The goal is to choose an orientation that minimises the need for supports while maintaining adequate thermal management, mechanical integrity, and surface quality. Simulation and optimisation tools are often used to find the balance between manufacturability, cost, and performance.

## 1.6 Machine Learning

In 1959, Arthur Samuel described ML as the “field of study that gives computers the ability to learn without being explicitly programmed” [81]. ML is a discipline of AI that enables a system to learn by training from a dataset obtained from various sources rather than following a pre-programmed technique [82].

The algorithms used in ML are based on activation functions and the assignment of weight factors for each input variable to analyse data and find hidden connections among them. The final objective is the prediction of future events or scenarios that are unknown [83]. The approaches can be classified into Supervised Learning (SL), Unsupervised Learning (UL), and Reinforcement Learning (RL), as described in Figure 14.

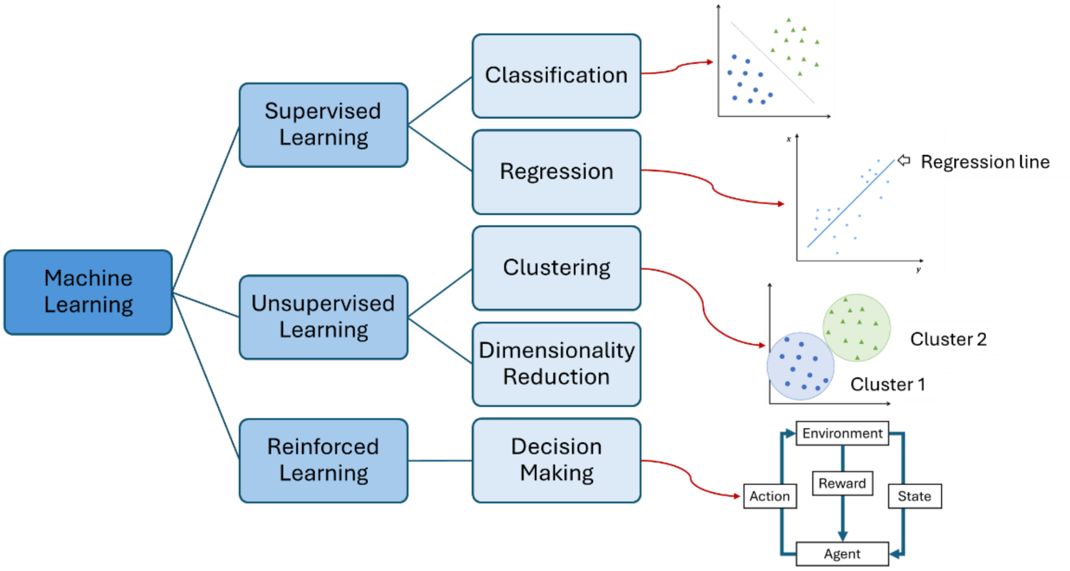

*Figure 14. ML Classification scheme [84]*[10].

### 1.6.1 Supervised Learning

SL algorithms are trained using a dataset with known input $x$ and output $y$ pairs. In training, the algorithm extracts the associations between independent attributes and a designated dependent attribute to develop a prediction model [85]. Indeed, the model can make predictions of unknown output values from a new set of input data. The performance depends on the size and variance of the training dataset to achieve better generalisation and greater predictive power for new datasets [83]. Decision Trees, Naive Bayes, Support Vector Machines, and Neural Networks (NNs) are some of the most widespread supervised ML algorithms.

The SL goal is to identify the function $f : x \rightarrow y$, the classifier, from a training dataset, composed of pairs of (input, output) points. Usually, $y \in \mathbb{R}$ for regression problems, and $y_i$ is discrete for classification problems. The first hypothesis is that training data is created independently and identically from an unknown but fixed joint probability distribution function $P(x,y)$. The learning objective is to identify the function $f$ that attempts to simulate the dependency encoded in $P(x,y)$ between the input $x$ and the output $y$. The second one is the concept of error or loss to measure the agreement between the prediction of $f(x)$ and the desired output $y$. The loss function is used to evaluate the prediction error; the choice of the Loss function $L(f(x),y)$ depends on the learning problem being solved. The Loss function $L$ leads to the definition of the risk for a function $f$, called generalisation error (Equation 11).

$$R(f) = \int L(f(x),y)dP(x,y) \qquad (11)$$

The learning problem is expressed as a minimisation of $R$ for any classifier $f$.[85]

Tables 7 and 8 describe the most used algorithms for classification and regression problems, highlighting their successful applications in the AM field.

---

[10] Trovato, M., Amicarelli, M., Prist, M., & Cicconi, P. (2025). A Neural Network-Based Approach to Estimate Printing Time and Cost in L-PBF Projects. Machines, 13(7), 550. https://doi.org/10.3390/machines13070550

*Table 7. Classification Techniques and AM Applications [84][11].*

| Model | When to Use | AM Applications |
|---|---|---|
| Support Vector Machine (SVM) | SVM is effective in solving classification problems involving datasets with numerous features, especially when using the kernel trick to handle complex, non-linear decision boundaries. It performs well on small datasets, especially when classes are separable. | Print success estimation, defect detection, process optimisation, and material property analysis [86] |
| Decision Tree (DT) | DT can be useful for datasets with numerical and categorical features and can handle nonlinear decision boundaries. DT performs optimally with small to medium-sized datasets and can also be used with imbalanced data. However, it is susceptible to overfitting, particularly when the tree becomes excessively deep. | Defect classification, process parameter optimisation, print quality analysis, and manufacturability prediction [87]. |
| Random Forest (RF) | RF excels at handling datasets with numerous features and complex nonlinear interactions. | Image-based porosity classification [88]. |
| K-Nearest Neighbours (KNN) | KNN does not assume any predefined distribution for the underlying data. It is non-parametric and suitable for datasets with arbitrary distributions. It works well with numerical and categorical features. It requires careful tuning and can be computationally intensive for large datasets. | Surface roughness prediction [89] |
| Naive Bayes (NB) | NB performs effectively with relatively small datasets, with good results for text classification or categorical data. The algorithm functions optimally with clean, noise-free datasets, and it can handle imbalanced data by estimating class probabilities. | Defect classification, material composition analysis, printability prediction, and anomaly detection [90]. |
| Convolutional Neural Networks (CNN) | CNNs excel at automatically learning spatial hierarchies of features, making them suitable for datasets with strong local patterns or visual characteristics. They are ideal for large datasets because they can generalise well. | Quality and process control [91]. |
| Recurrent Neural Network (RNN) | RNNs are designed to handle sequential data, making them suitable for datasets with critical temporal or sequential dependencies. RNNs are effective for datasets where the current input is influenced by previous states, allowing the model to capture dynamic patterns over time. | Process monitoring, fault detection over time, predictive maintenance, and real-time monitoring [92]. |

*Table 8. Regression Techniques and AM Applications [84][12].*

| Model | When to Use | AM Applications |
|---|---|---|
| Linear Regression (LR) | LR works best with numerical datasets that are well-structured, clean, and free from significant outliers. The method is sensitive to extreme values and unsuitable for datasets with strong non-linear patterns. It performs well with small to moderately sized datasets. | Process parameter optimisation [93]. |
| Polynomial Regression (PR) | PR is particularly suitable for small to moderately sized datasets where polynomial terms of the independent variables can approximate the non-linearity. This method works best when the dataset is clean and free | Process parameter modelling and optimisation [94]. |

---

[11] Trovato, M., Amicarelli, M., Prist, M., & Cicconi, P. (2025). A Neural Network-Based Approach to Estimate Printing Time and Cost in L-PBF Projects. Machines, 13(7), 550. https://doi.org/10.3390/machines13070550

[12] Trovato, M., Amicarelli, M., Prist, M., & Cicconi, P. (2025). A Neural Network-Based Approach to Estimate Printing Time and Cost in L-PBF Projects. Machines, 13(7), 550. https://doi.org/10.3390/machines13070550

|  |  |  |
|---|---|---|
|  | from outliers, as higher-degree polynomials are sensitive to noise and overfitting. |  |
| Support Vector Regression (SVR) | SVR excels with small to moderately sized datasets, especially when the data has many features, and the relationships are non-linear. SVR can capture intricate, non-linear. SVR is sensitive to noise and outliers. | Real-time monitoring for defect detection [95]. |
| Gradient Boosting Machines (GBM) | GBMs are well-suited for moderately sized datasets with diverse feature types, including numerical and categorical variables. GBR performs well even with noisy data or datasets with missing values, as the boosting mechanism reduces bias and variance. | Melt pool shape prediction with process parameters data [96]. |
| Deep Neural Networks (DNN) | DNNs excel in scenarios with high-dimensional data and multiple features, especially when sufficient labelled data is available to train the network effectively. They perform best with clean, well pre-processed datasets, as they are sensitive to noise and can overfit smaller datasets without proper regularisation techniques, such as dropout or weight decay. | Print time prediction, defect severity estimation, material property, and multi-parameter optimisation [97]. |
| Recurrent Neural Network (RNN) | RNN is ideal for datasets with ordered structures, such as sensor data, production logs, process monitoring logs, or sequential datasets. The model requires large, clean, sequential datasets to learn effectively, as they are sensitive to noise and data quality. | Time-series prediction for print times, process monitoring and optimisation, fault prediction, and tracking of material property evolution [98]. |

#### *1.6.1.1 Artificial Neural Networks*

ANNs take inspiration from the functioning of biological mechanisms in the human brain, made up of a very large number of interconnected neurons. Each neuron is a single cell that elaborates a single task, such as the response to a specific input signal [99]. An ANN has three fundamental parts: node character, network topology, and learning rules. Node character defines how input signals are processed by the node, such as the activation function, the number of inputs and outputs associated with a single node, and the weight associated with each input and output. Network topology maps the connections and the organisation between nodes. Learning rules determine how the weights are initialised and adjusted [100].

Figure 15(a) shows the structure of a basic node with inputs, weights, and outputs. The nodes are organised into *layers* and column vectors of the node. There are three types of layers, such as the input layers, the hidden layers, and the output layers (Figure 15(b)). Designing the network topology means defining the dimensions (number of nodes and layers) and the connection paths among the nodes [100].

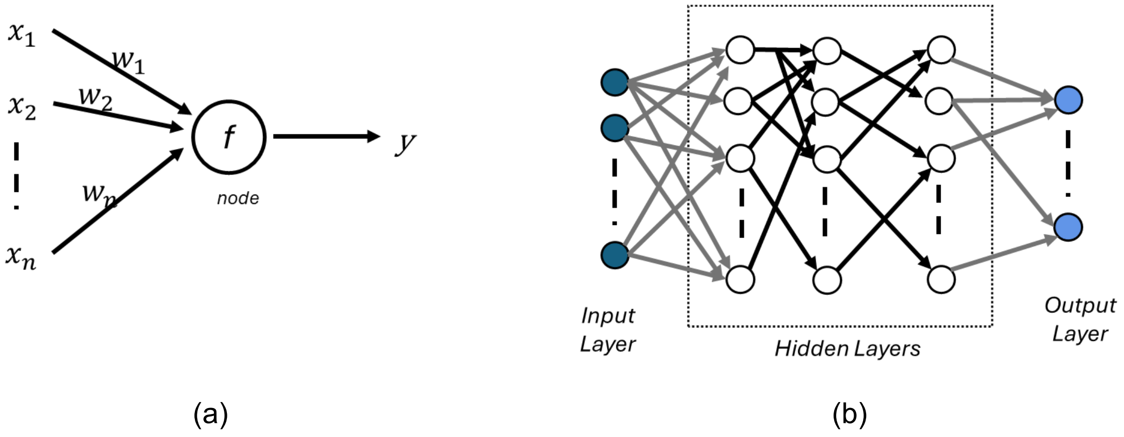

*Figure 15. (a) ANN Activation node; (b) ANN Operating Scheme.*

Each node elaborates multiple inputs $x_i$ pre-multiplied by weights $w_i$. When the sum of the weighted inputs exceeds the threshold value $T$, the node computes the input signal through a transfer function $f$ and sends the output signal $y$ to the neighbouring nodes (Equation 12). The transfer function $f$ can be a Binary Step Function, Linear, Sigmoid, Tanh, ReLU, Leaky ReLU, Parametrised ReLU, Exponential Linear Unit, Swish, or SoftMax [56].

$$y = f\left(\sum_{i=0}^{n} w_i x_i - T\right) \tag{12}$$

During the training phase, the weights are optimised to obtain the desired output values. The weights are adjusted to minimise the error between the network and experimental outputs. Different types of networks require different learning processes. In each data-driven analysis, the dataset with the input data must be sufficiently large. Data sources can be filled with both real experiments and virtual analysis. The use of simulations in data collection can reduce the time and cost in the training phase; however, the accuracy of the simulations affects the ML result.

### 1.6.2 Unsupervised Learning

UL algorithms are used to learn how to represent input patterns using statistical methods from a dataset [101], without using explicit target outputs associated with each input [102]. UL methods are classified as clustering and dimensionality reduction algorithms, such as K-Means Clustering and Principal Component Analysis. UL methods are essential components of any data science or ML workflow. UL approaches are commonly used in ML pipelines to do data exploration, visualisation, feature engineering, preprocessing, and data preparation. However, UL can be a relevant technique for making new data-driven discoveries from unlabelled data. Major unsupervised tasks include clustering to discover group structures, graphical models to discover relationships, anomaly detection to discover informative outliers, and dimension reduction to discover low-dimensional latent subspaces that capture major patterns in high-dimensional data [103]. The main UL algorithms are the Apriori, the ECLAT, the Frequent Pattern Growth, Clustering using K-Means, and Principal Components Analysis. The Apriori algorithm was created with data mining in mind; it can be used to extract data from databases with many transactions. ECLAT is a data mining technique that acquires element groups and locates frequent items. Because the Apriori technique employs a horizontal data structure, it must repeatedly scan the database to identify frequently occurring objects. ECLAT has a vertical approach and is quicker because it only needs to search the database once. The k-means clustering technique organises components into groups according to their similarity. The key is to find the cluster centroids, which are K centres. After presenting a new data point, the algorithm uses metrics such as Euclidean distance to determine which cluster the data point belongs to. The centroids are computed using the K-means clustering approach, which iterates until the optimal centroid is found. Principal Components Analysis is an algorithm for decreasing dimensionality of large data sets by reducing many variables into a smaller group while preserving most of the data information in the "large set."[104].

### 1.6.3 Reinforced Learning

RL proposes a solution to the problem of learning from interaction with an environment to achieve a specific goal. RL methods are usually applied in autonomous robots and control system applications. The learner is the decision-maker and is called the Agent. Everything outside the Agent is the Environment. Agent and Environment continually interact. The Agent selects the actions, and the Environment responds by presenting new situations to the Agent and giving Rewards. The Agent must maximise the Reward values. Generally, Rewards are special numerical values (i.e. 0 and 1) and represent the goal of the RL problem. As described in Figure 16, the RL approach is a closed-loop method because the learning system's actions influence its later inputs [105]. In this loop, the Policy defines the learning Agent's way of behaving at a given time [106].

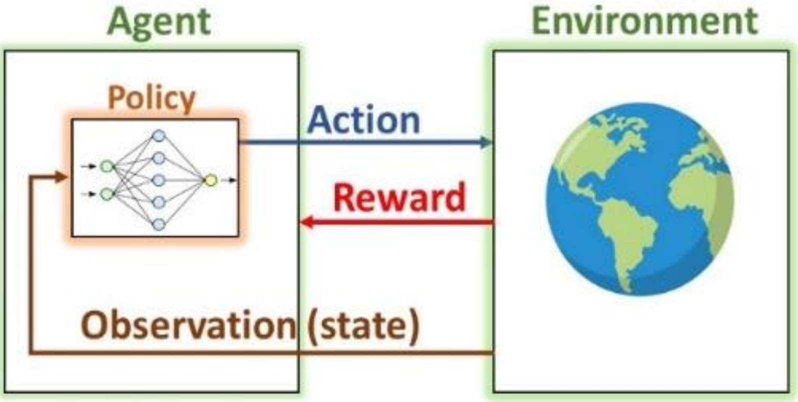

*Figure 16. A simplified Reinforced Learning scheme: the Agent explores the space of possible strategies and receives feedback (Reward) related to the choices made.*

Formally, RL can be described as a Markov decision process, which consists of a set of states $S$, plus a distribution of starting states $p(\boldsymbol{s}0)$; a set of actions $A$; transition dynamics $T(\boldsymbol{s}_{\boldsymbol{t}+\boldsymbol{1}}|\boldsymbol{s}_{\boldsymbol{t}}, \boldsymbol{a}_{\boldsymbol{t}})$ that map a state-action pair at time $t$ onto a distribution of states at time $t + 1$; an immediate/instantaneous reward function $R(\boldsymbol{s}_{\boldsymbol{t}+\boldsymbol{1}}|\boldsymbol{s}_{\boldsymbol{t}}, \boldsymbol{a}_{\boldsymbol{t}})$ ; and a discount factor $\gamma \in [0,1]$, where lower values place more emphasis on immediate rewards. In general, the policy $\pi$ is a mapping from states to a probability distribution over actions $\pi: S \rightarrow p(A = \boldsymbol{a} \mid S)$ . If the Markov decision process is episodic, i.e., the state is reset after each episode of length *T*, then the sequence of states, actions, and rewards in an episode constitutes a trajectory or rollout of the policy. Every rollout of a policy accumulates rewards from the environment, resulting in the return $R = \sum_{t=0}^{T-1} \gamma^r r_{t+1}$. The goal of RL is to find an optimal policy $\pi^*$ that achieves the maximum expected return from all the states (Equation 13) [107].

$$\pi^* = \underset{\pi}{argmax}\, \mathrm{E}[(R|\pi)] \tag{13}$$

### 1.6.4 ML Implementation

Figure 17 illustrates an ML implementation workflow as a step-by-step process for developing, deploying, and maintaining the system. It begins with the problem definition and identification of the success metrics that will be used to measure performance, such as accuracy or precision. Once the problem is clear, data is collected and carefully inspected to understand its structure, quality, and overall characteristics. After data collection, the data is split correctly into training, validation, and test sets to ensure unbiased model evaluation. The next step is data cleaning and preprocessing, which involves handling missing values, removing duplicates, managing outliers, scaling features, encoding categorical variables, and performing feature engineering. With clean and prepared data, the model selection and training phase begins, where appropriate algorithms are chosen and trained using the training dataset. Following training, hyperparameter tuning is performed to optimise the model's performance, achieving optimal results in terms of metrics. The tuned model is then evaluated and validated using the validation set to check its accuracy and ensure it generalises well without overfitting. Once the evaluation confirms the model's effectiveness, it is possible to finalise and package it, preparing it for production use. The model is then deployed into a production environment, where it is continuously monitored to track its performance and detect any issues or data deviation from the starting point.

Finally, the workflow concludes with maintenance, which involves regularly updating and retraining the model as new data becomes available or when its performance begins to degrade. This complete cycle ensures that ML models remain accurate, reliable, and scalable over time.

*Figure 17. Practical workflow for ML implementation*

## 1.7 Machine Learning Applications in Design for Additive Manufacturing

The literature identifies numerous ML applications in the AM context. These applications can be divided into three levels: the Geometrical Design Level, the Process Configuration Level, and the Process Monitoring Level, also known as the "in situ" monitoring Level. Other ML applications include cost estimation, material development, and printability prediction. Figure 18 shows this classification grouped in ML applications for AM and DfAM. Starting from the ML usage in AM, two levels can be identified: the Material Development Level and the Process Monitoring Level. The first level involves the development of metal and composite materials using ML methods [108]. The second level, Process Monitoring, regards the real-time control of the printing process. SL algorithms are often used to classify and recognise issues during the printing phase. The possibility of checking the quality of the printed part during the process and modifying the process parameters to achieve better results makes this level relevant to the industrial world. Different methods, including image-based, optical-based, and acoustic-based techniques, are employed for monitoring the printing phase [109].

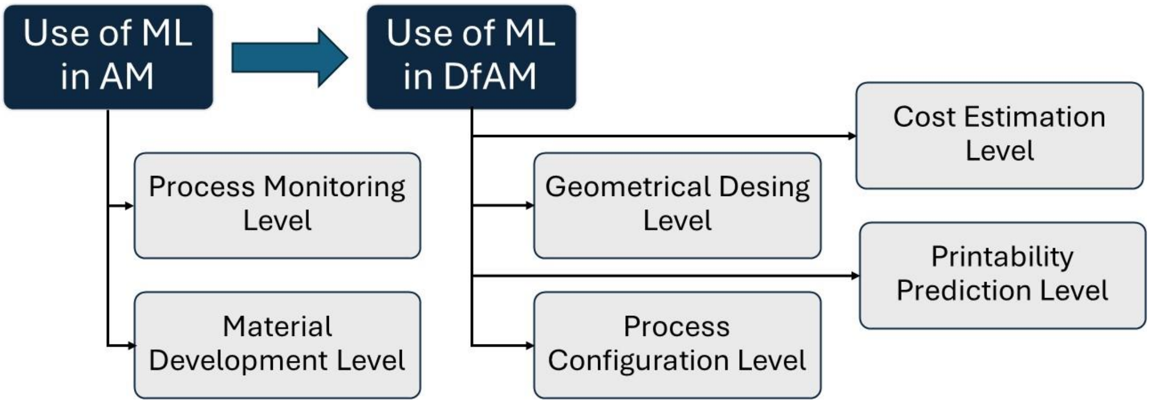

*Figure 18. ML applications in AM and DfAM.*

### 1.7.1 Geometrical Design Level

The goal of the first application level, the Geometrical Design, is the design optimisation with respect to the product's functionalities, considering that geometry has a relevant effect not only on the final weight but also on the achievement of the design requirements. According to the most recent literature analysis, AI may support the Geometrical Design level in many ways that pertain to TO and GD. To satisfy the project's requirements, custom micro- and meso-structures can be realised using ML algorithms [82]. ML algorithms are applied where geometrical optimisations are necessary, not just in additive design [110, 111].

TO optimise geometry, removing unnecessary volume from the design space that must be connected to the non-design space, definable as the geometrical space where the design boundary conditions are applied or where functional volumes and/or surfaces must be present. Using methods such as SIMP [112] or Level Set Methods [113], the optimal volume distribution is obtained by solving an FEA-based minimization problem. In [114], the actual limits of TO are discussed, and ML applications to overcome them are reviewed; Machine Learning TO is presented as a set of strategies to enhance TO, given its high computational costs. Computational costs are due to the large number of variables that are related to the FEA mesh and the iterations necessary to converge. Other efforts may be related to the computation time to evaluate objective functions. GAN-based solutions are reported to bypass iterations [115, 116]; other approaches use CNN to achieve a one-step TO through objective function and sensitivity metamodeling, so that FEA may be bypassed [117-119]. Unfortunately, this kind of approach reduces the accuracy of the result, due to a lack of physical soundness and case sensitivity. By combining TO and Long Short-Term

Memory Networks, Kallioras et al. [120] created a GD framework that incorporates ML into the GD process. The use of TO can also involve the existing mechanical components' redesign, focusing on innovating old parts to achieve better performance and lightweight. A workflow is proposed in [121], starting from Reverse Engineering (RE) and arriving at the quality check of the printed part, it passes through the intermediate phases of TO and printing. In [122], the TO is integrated with an AM knowledge Base that considers AM constraints, supports, and orientation to redesign an automotive connecting rod. In [123], a CAD-based workflow has been proposed to achieve a lightweight design using lattice structures, considering the phases from RE to design optimisation. In [124], researchers use a TO approach as a concept design tool for modelling the inner frame of an ancient bronze statue.

ML applications for generating meta-materials based on lattice structures seem to be a more mature field of applications in terms of accuracy and validation of the results. In this case, geometric variables describe the unit cell via CAD parametrisation at a mesoscale level. Design requirements and constraints are the mechanical properties that are requested at the macroscale (such as stress-strain law, energy absorption, and deformation/compliance) [125]. These provide specific limits to the design space, which is often related to 2D cells, so that ML may be successfully applied without the limitation derived from complex TO, which is confined to a single cell. The macroscale evaluation of the mechanical behaviour is usually investigated by homogenization or FEA. In [126], GAN is applied to optimise lattice geometry with respect to mechanical properties. AM components have been tested to validate the results. Researchers in [127] optimised and tested multi-material gyroid structures developed by ML, adopting a data-driven design model. Mechanical properties can be described with good accuracy to determine the optimal relative density and PLA/TPU ratio by interpolation, so that ML may be accurately trained. From the trained NN, new design solutions were explored and validated. Després et al. [128] supported the creation of optimised micro-lattice structures for AM applications using an NN approach. To create new microstructures, they used GA and FEM tools to assess the relative mechanical properties. A similar strategy was adopted by Alejandrino et al. [129]; they realised a supervised NN trained with FEM simulations. They also studied an NN method for designing lattice structures that produce optimised patterns. [130-137] also confirm the achievement of good results for this kind of application.

GD aims to provide design alternatives autonomously to optimise a design problem according to its requirements and constraints. Some authors study GD approaches to develop a general procedure in agreement with design science theory [138-140]. Proper parametric CAD approaches or TO may explore design variants according to a modular approach that reflects the functional analysis of the part/assembly. Model updates from concept to executive design may be performed, including new details and evaluation criteria as demonstrated through the case study of the crank, in which three different manufacturing processes, including AM, are investigated.

In [141] and [142], the GD via RL is defined as a sequential process suitable for proposing different alternatives starting from TO. The wheel design test case demonstrated how the GAN-based approach may guarantee diversity in the topology variant definition, considering also computational efforts through NN modelling. A review of the generative product design systems created since 1998 is provided in [143] to identify important methodologies and trends. Systems are examined based on their main objectives, requirements, generative methods, design phase, type of generation (automatic or interactive), and the number of design options. After the variant generations, CAE simulations may be adopted to move towards product-process design with the help of multicriteria analysis that can be assisted by ML. Many examples of this are present in the literature [144-148], supported by the adoption of TO and AM pre-processing tools in many CAD-CAE software (e.g. Altair Hyperworks, CREO PTC, Autodesk FUSION 360, N-Topology, …). Examples and case studies are devoted to demonstrating the capability of variant generation and the aid provided by the automation of the multicriteria assessment of the peculiar problem. Unfortunately, the selection of the proper ML approach and the peculiarity of the physical description of the design problems do not allow a proper evaluation of the maturity of the solutions yet. Table 9 reports some papers that show the use of ML in the Geometrical Design Level. They are classified by algorithm, application, and methodology description, and main features.

*Table 9. Examples of ML applications in the Geometrical Design Level [29][13].*

| Ref. | Algorithms | Application | Methodology description and main features |
|---|---|---|---|
| [110] | Fuzzy NN, GA | TO | A system to provide automatic design and rapidly obtain a product form and its corresponding image; using NN to correlate input form parameters and a series of adjectival image words, and GA is to search for a near-optimal design. |
| [111] | PPO, NN | TO | RL-based GD process, with reward functions for maximising the diversity of TO designs. |
| [112] | WGAN, CNN | TO | GAN generates an optimal topology for a given boundary condition and optimisation settings. CNN provides the corresponding design variables and optimisation conditions. |
| [116] | cGAN, U-SE-ResNet | TO | Definition of a data-driven topology optimisation model called TopologyGAN. |
| [117] | CNN | TO | Using a 48x16 pixel resolution dataset, CNN substitutes the FEM process to calculate compliances. |
| [118] | SOLO, DNN | TO | SOLO integrates DNN with FEM calculations. A DNN substitutes the objective as a function of design variables. |
| [119] | SCA, FFNN, CNN | TO | SCA is used to develop a material behaviour database. FFNN makes predictions of mechanical responses. CNN is used to identify if damage has occurred on the microscale and penalise the design accordingly. |
| [120] | SIMP, LSTM | TO | GD framework, called MLGen, integrates several methods to deliver automatically generated shapes using TO (SIMP), LSTM, image filtering and metaheuristics. |
| [126] | GAN | Lattice Opt. | GAN model to create lattice structures with a high strength-to-weight ratio. |
| [127] | NN | Lattice Opt. | A data-driven inverse design model developed for multi-material gyroid structures. Starting from the fabrication of multi-material gyroid structures, an NN was trained to find the relationship between mechanical properties and design parameters. |
| [128] | GA, Encoder, Decoder | Lattice Opt. | ML framework for analysis and design of micro-lattices. An encoder and decoder are responsible for the analysis and design of micro-lattices generated by a GA. The Mechanical properties are evaluated by FEA. |
| [129] | NN, SCG | Lattice Opt. | The 3D coordinates of the infill pattern are extracted as the input of the NN model. The optimisation technique of SCG is the algorithm used to train the FFNN. |
| [130] | ANN-LM, k-fold | Lattice Opt. | ANN-LM used to predict the energy absorption of the lattice structure with parameters such as overlapping area, wall thickness, and size of the unit cell. The k-fold cross-validation |

---

[13] Trovato, M., Belluomo, L., Bici, M., Prist, M., Campana, F., & Cicconi, P. (2025). Machine learning in design for additive manufacturing: A state-of-the-art discussion for a support tool in product design lifecycle. The International Journal of Advanced Manufacturing Technology, 137(5–6), 2157–2180. https://doi.org/10.1007/s00170-025-15273-9

| | | | |
|---|---|---|---|
| | | | technique was applied in the training phase to get the best training results. |
| [131] | ML | Lattice Opt. | ML approach to predict the mechanical properties of G-Lattices under defined loading conditions. Training data is generated through a sampling technique. Voxelized data is employed as ML feature vectors for predicting properties determined by FEA. |
| [132] | GD Method | Lattice Opt. | The GD method is used to investigate the structural topology of the original geometry under tensile loading conditions. |
| [133] | NN–GO | Lattice Opt. | The shape of the lattice beam is investigated using a deep learning approach with high-order Bézier curves. This is then combined with NN–GO adaptive method for the generation of superior lattice structures. |
| [134] | CNN, QSGS, RGGM, LBM | Lattice Opt. | The thermal conductivity of composite materials is predicted using a CNN. Digital images are generated using the QSGS method and the RGGM to model the microstructure of the composites.  LBM is used to predict the thermal conductivities. |
| [135] | Bayesian optimization | Lattice Opt. | Computational framework that leverages Bayesian optimisation to identify configurations with increased uniaxial effective elastic stiffness and plastic or buckling strength. |
| [136] | LR, PR, DT, RF, ANN | Lattice Opt. | The Mechanical Stiffness of Lattice Structure-Based Polymer Foam is predicted using various ML algorithms. ML results are analysed to identify the most efficient ML method. |
| [137] | DT, LR, RF, GBR | Lattice Opt. | ML approach to optimise the design of honeycomb, lattice, and gyroid infill structures in 316L steel fabricated using L-PBF technology. ML is used to predict maximum stress while defining the infill parameters such as wall thickness, orientation, shape, etc. |
| [141] | RL, PPO | GD | This study proposes an RL-based GD process, with reward functions that maximise the diversity of topology designs. GD is a sequential problem of finding the optimal design parameter. PPO is used as the learning framework. |
| [142] | GAN | GD | The proposed framework integrates TO and generative models (GANs) in an iterative manner to explore new design options. Anomaly detection can evaluate the novelty of generated designs, thus helping designers choose among design options. |
| [144] | GAN, Convolutional Autoencoder, | GD | A deep learning-based CAD/CAE framework is used in the conceptual design phase for generating 3D CAD models to be evaluated. |
| [145] | Autodesk Fusion 360® algorithm | GD | The GD method is used for optimising customised structures used in Cultural Heritage applications. |
| [146] | TO (SIMP) | GD | An iterative and automated GD method, based on Python scripts, to optimise the multi-material distribution of components. Possibility to change the target volume and the space distribution related to each material during the optimisation workflow. |
| [147] | Autodesk Fusion 360® algorithm | GD | A generative approach for the optimisation of a static structural design problem. |
| [148] | Matlab PDE, FEA iteratively | GD | A forceflow-based TO process is explained in detail and extended with a PDE function to use as a GD tool. |

### 1.7.2 Process Configuration Level

The second level, Process Configuration, involves the selection of the process parameters and the powder spreading characterisation with its optimisation. Due to the numerous and complex parameters, this level is crucial for metal AM processes [149]. The selected AM technique and the specific 3D printer affect and sometimes determine the process parameters such as laser power, layer thickness, powder size and distribution, scanning strategies, etc. These process parameters hugely impact the mechanical properties of the component, such as surface roughness, porosity, density, fatigue strength, etc. [150]. The quality of the finished part is influenced by the uniformity of powder spreading [151]. Inadequate powder spreading can introduce defects or lead to issues like warping or swelling [152]. The AM printing phase's success depends on the component's final mechanical properties.

The definition of the support structures and selecting the part's best orientation also concern the Process Configuration Level. The support structures allow the surfaces with critical overhang angles to be printed [153]. Against the high thermal gradients, the supports can reduce deformation and residual stress while optimising the thermal dissipation. The supports must be lightweight and easily removable to minimise the scraps. The quantity and extension of the overhang surfaces to be supported are influenced by the part orientation. Moreover, 3D printing cost and time are highly affected by the choice of part orientation and supports. In this context, ML can support the definition of the parameters related to supports and part orientation. A GA has been used in [154] to find the optimum of different conflicting objective functions among the solutions belonging to the Pareto front; the objective functions regard the minimisation of the support structure volume and the building time. Estimation methods are developed for computing the amount of support structure and the build time.

Regression methods are well used in the literature to study the process parameters for metal AM processes. For example, a Back Propagation Neural Network (BP-NN) with one hidden layer was used in [151] to optimise the spreading parameters. The main objective of this study focuses on the part porosity and roughness. In this study, simulations were proposed to feed the training phase. Tapia et al. also investigated porosity prediction for SLM processes [155]. To correlate porosity with process parameters, they first created a Gaussian regression model, followed by the implementation of a Bayesian inference framework to estimate statistical model parameters. Finally, the porosity of the printed part was predicted using the Kriging method. Ren et al. used a Gaussian regression model to select the optimal laser power value to maintain a constant melt-pool size [156]. While keeping the other process parameters constant, they used two input variables: laser power and thermal history.  Baldi et al. [157] used regression methods to predict the melt pool morphology for Inconel 718, constructing a printability map for this material as a function of layer thickness and building platform temperature.

Focusing on the prediction of the part density, Gor et al. [158] investigated ML methods like ANN, K-nearest neighbour, support vector machine, and linear regression for objects printed in 316L stainless steel. The parameters examined in this study have to do with the build chamber, laser system, hatch spacing, layer thickness, and scanning speed. Porosity, defects, roughness, and density all have an impact on the fatigue response. Zhang et al. [159] studied the high-cycle fatigue life of 3D printed materials. The method chosen for processing and post-processing can alter this mechanical property. To predict the high-cycle fatigue life of stainless steel 316L parts, they used a neuro-fuzzy-based ML method.

Regression and classification methods were also combined in the literature. Kappes et al. proposed a regression and classification approach, using a Random Forest Network (an SL method), to link the process variables to the part's final microstructure [160]. They studied parameters such as part orientation, the amount of recycled powder, heat treatment, laser power, laser speed, laser spot, and contour overlap. The objective of this study was to predict defects in L-PBF processes. These studies highlight that the most popular algorithms for predicting the parameters involved in AM processes are SL methods. The literature demonstrates various regression techniques with fruitful outcomes. Table 10 reports some papers that show the use of ML in the Process Configuration Level. They are classified by algorithm, input, output, and material.

*Table 10. Examples of papers that use ML in the Process Configuration Level [29]*[14]*.*

| Ref. | Material | Algorithm | Input | Output |
|---|---|---|---|---|
| [151] | Ti-6Al-4V | BPNN | Diameter, Length, Translation speed, and Rotation speed of the spreader | Roughness, porosity |
| [154] | / | GA | Orientation, Support Volume | Orientation to optimise the amount of support structures and building time. |
| [155] | SS 17-4 PH | spatial GPR, Bayesian | Laser power, Scanning speed | Porosity |
| [156] | Inconel 625 | GPR, CFHOC | Laser power | Melt-pool size |
| [157] | Inconel 718 | Regression Methods | Laser Power, Scanning Speed, Layer Thickness, Building Platform Temperature | Printability map of the material |
| [158] | SS 316L | ANN, KNN, SVM, LR | Laser Power, Scanning Speed, Hatch Spacing, Layer Thickness | Density |
| [159] | SS 316L | ANFIS | Processing/post-processing parameters and tensile properties | High-cycle fatigue life prediction |
| [160] | Inconel 718 | RFN | Part location, Orientation, Recycled powder | Porosity (keyhole and lack of fusion) |
| [161] | SS 316L | Surface GP | Laser power, Scanning speed, Laser beam size | Depth of the melt pool |
| [162] | Ti-6Al-4 V | SVM | Lack of fusion population, size, location, and morphology of defects | Fatigue life |
| [163] | SS 316L | ANN, RFN, SVM | Laser power, Scan speed, Hatch space, Powder layer thickness | CDM-based fatigue life prediction |
| [164] | Inconel 718 | PR, SVR, DT, EGB | Post-processing parameters | Corrosion behaviour |

### 1.7.3 **Cost Estimation Level**

Most of the cost of a mechanical product depends on the design phase. The cost analysis considers the entire production cycle of the component, including the material cost, the process cost, and, sometimes, the disposal cost. While the cost related to traditional processes is well known in the literature, the cost analysis of Metal AM parts is still a challenging topic. In the Metal AM context, the analytical approach for the cost analysis could be replaced by ML methods due to the complexity of the process and the number of parameters involved. However, a few papers deal with ML for the cost estimation in SLM processes.

The approach developed in analytical tools provides the calculation of material cost, machine cost, operator cost, and cost related to energy consumption (Equation 14). Maintenance and administrative costs can also be considered [165].

$$C_{TOT} = C_{Equipment} + C_{Material} + C_{Labour} + C_{Energy} \tag{14}$$

---

[14] Trovato, M., Belluomo, L., Bici, M., Prist, M., Campana, F., & Cicconi, P. (2025). Machine learning in design for additive manufacturing: A state-of-the-art discussion for a support tool in product design lifecycle. The International Journal of Advanced Manufacturing Technology, 137(5–6), 2157–2180. https://doi.org/10.1007/s00170-025-15273-9

In (14), $C_{Equipment}$ is the equipment investment cost, $C_{Material}$ is the material cost, $C_{Labour}$ is the operator's cost, and $C_{Energy}$ is the energy cost.

Analysing the ML cost estimation methods for mechanical components, Manuguerra et al. [166] defined an ML approach for parametric cost estimation of axisymmetric components. Through performance indicators, they compared and evaluated five algorithms: Generalised Linear Model, Deep Learning, Decision Tree, Random Forest, and Gradient Boosted Trees. They identified many independent parameters necessary for a prediction model.

For 3D printed parts, Rudolph et al. [167] analysed different statistical-based methods for an automated and self-learning calculation for metal L-PBF, given a part's CAD data, using the prediction of capacity utilisation and the prediction of part build height as input in the regression model. Chan et al. [168] used the similarities of the 3D geometry of parts and printing processes to identify relevant features. They used different ML algorithms for dynamic clustering, LASSO, and elastic net regressions to predict the cost based on historical data. Another example of ML applications for cost estimation in AM has been proposed by Sharma et al. [169], realising a fuzzy set-based cost model. Initially, they developed a deterministic cost model, and then they converted it to a fuzzy set-based model by considering uncertainty in building time estimation and cost components.

Actually, few ML studies focus on the cost estimation for metal 3D printing. One of the reasons could be the difficulty of achieving a cost dataset. However, there is a high interest in this topic because the high 3D printing cost is one of the main factors that limit the use of AM in the industry.

### 1.7.4 Process Monitoring Level

The Process Monitoring Level is also called the In Situ Monitoring phase. This level concerns the real-time control of the 3D printing process through sensors [170]. The process monitoring and possible parameter corrections can significantly cut down the time and cost of the printed parts. Cracks, delamination, distortion, rough surfaces, lack of fusion, porosity, foreign inclusions, and process instability (keyhole, balling) are just a few of the processing-related errors that afflict the metal AM process. These defects are typically caused by the layer-by-layer material deposition process [171]. They are related to a high number of internal or external factors. Sensors can recognise potential critical situations, and ML can help reducing faults in 3D printing. On the other hand, the traditional approach uses the operators' experience to detect and avoid fabrication defects.

There are numerous ways to control the 3D printing process, monitoring the construction of each layer. The most common ML approaches used in the literature include the Image-based approach, the Acoustic emission, the Optical emission, and the Sensor signal-based approach. The Image-based approach analyses the layer-wise surface using photos from cameras to spot defects and lacks. Utilising spectral convolutional NNs, the Acoustic Emissions approach is based on the energies of the narrow frequency bands. The analysis of spectroscopy emissions during the process is called optical emission. This approach has been used for a long time to comprehend physical mechanisms [172]. The signals consist of melt pool profiles, intensity, plume, and spatter signatures. The fourth method for process monitoring is the sensor signal-based approach, which combines acoustic, optical, infrared, and multi-sensor signals. All these techniques are used to train ML algorithms for Process Monitoring.

SL algorithms are frequently used in Image-based monitoring methods for classification and recognition issues, using high-speed cameras and algorithms such as Deep Convolutional Neural Networks [173] and SVM [174]. UL methods can also be used for Image-based applications. In [175], images from Near-Infrared (NIR) cameras are used to monitor processes in real-time and identify melted states during the SLM process.

SL and UL methods are also used to analyse and interpret the dataset of Acoustic Emission methods. Mohammadi et al. proposed an approach using various ML techniques [176]. To match the acoustic signal with the defect type, a supervised deep-learning neural network was used after a hierarchical K-means clustering to label the data. The dataset was decreased using a Principal Component Analysis. To facilitate the detection of defects, the Gaussian Mixture Model was used. They also used a Variational Auto-Encoder approach to obtain a general feature of the signal that could be an input for the classifier. In [177], a sensitive acoustic emission sensor is used to differentiate acoustic features of different quality using an ML algorithm called Spectral Convolutional NN.

Table 11 reports some works that show the use of ML in the Process Monitoring Level for the L-PBF process. They are classified by algorithm, sensors and input features, output, and material.

*Table 11. Examples of papers that use ML in the Process Monitoring Level [29][15].*

| Ref. | Process | Material | Algorithm | Sensors and Input Features | Output |
|---|---|---|---|---|---|
| [173] | L-PBF | Inconel 718 | Bi-stream DCNN | Image feature learning and feature fusion. | Pattern defective condition |
| [174] | L-PBF | SS 316 L | CNN, SVM | Images of the melt pool, plume, and spatter | Quality anomalies identification |
| [175] | L-PBF | SS 304 L | DBN | NIR camera. | Plume and spatter signatures |
| [176] | L-PBF | H13 tool steel | hierarchical K-means, DNN, PCA, GMM, VAE | AE sensor, elastic waves | Anomaly detection |
| [177] | L-PBF | SS 316 L | Spectral CNN | FBG sensor to detect the airborne AE signals, | Quality monitoring |
| [178] | L-PBF | Hastelloy-X | K-means, SOM | Co-axial photodiode, melt pool light intensity. | Porosity detection (LoF) |
| [179] | L-PBF | AlSi10Mg. | Mapping algorithm | High-speed Camera, melt pool light. | Melt pool variations linked to pores |
| [180] | L-PBF | SS 316 L | CNN, LSTM | AE sensor, photodiode detectors: BR, Visible, IR | Keyhole, conduction mode, LoF monitoring |
| [181] | L-PBF | SS 316L,<br>CuSn8,<br>Inconel 718 | CNN (1 model for 3 materials) | AE features | Keyhole, conduction mode, LoF monitoring |
| [182] | L-PBF | SS 304 | DBN | AE signals | Quality monitoring |
| [183] | L-PBF | Ti-6Al-4V | LENSP realised with MLP, SOM, SOEDNN, FGA | Melt pool images | Costs of the spatial distribution of defects |

---

[15] Trovato, M., Belluomo, L., Bici, M., Prist, M., Campana, F., & Cicconi, P. (2025). Machine learning in design for additive manufacturing: A state-of-the-art discussion for a support tool in product design lifecycle. The International Journal of Advanced Manufacturing Technology, 137(5–6), 2157–2180. https://doi.org/10.1007/s00170-025-15273-9

| | | | | | |
|---|---|---|---|---|---|
| [184] | L-PBF | Inconel 718 | GMM | Data from photodiode, UTS | Certification of AM builds |
| [185] | L-PBF | Inconel 625 | SGTA for multidimensional signals | SWITC, HSVC, photodetector | Different thermal signatures during overhang melting |
| [186] | L-PBF | SS GP-1 | SVM | DSLR, high-resolution 3D CT scan data. | Defect detection strategy |
| [187] | L-PBF | Inconel 718 | SIFT, HOG, SS, SVM | High-speed camera | Monitor melt pool geometry |
| [188] | L-PBF | SUS316L | DNN | dichroic mirror, galvanometer scanner, F-theta lens, and a high-speed camera | relations between melt-pool images and laser powers |

### 1.7.5 Parameter Analysis

As highlighted in the previous paragraphs, many parameters can affect the 3D printing results. The parameters can be classified into many categories, such as design, manufacturing, and monitoring parameters. Figure 19 highlights some of the most applied configuration setups used in literature to build, train, tune, and use an ML method to optimise the DfAM process.

Starting from the printing set-up, relevant parameters for the success of metal 3D printing are the type of supports, the orientation of the part, and the limit overhang angle selection. Analysing the manufacturing parameters, the most used are the scan speed, the laser power, the powder morphology and dimension, the layer thickness, the path pattern, and the overlapping rate. The most practised ML methods are supervised methods such as the ANN, the CNN, the SVM, and the GPR. Finally, considering the monitoring phase, some of the main parameters are the melt pool morphology, the porosity, the high-cycle fatigue life, the roughness, and the tensile test.

For example, Giorgetti et al. [189] characterise the printability of the Inconel 718 alloy through the melt pool morphology, realising the alloy printability map as a function of printing process parameters. The printability map guarantees a dense and defect-free material by locating the ideal melting point of the powder. In [190], Magana-Carranza et al. analyse the effects of process parameters such as scan strategies, laser power, point distance, and materials on the residual forces due to thermal gradient during the L-PBF process.

Applying an ML method gives the possibility to extend the process analysis and improve the decision-making process; it allows the study of complex multi-parameter and multi-objective systems that are not possible to study with traditional techniques. Di Angelo et al. in [191] describe which parameters influence the search for the optimal build direction, which affects part quality, surface quality, support structure, build time, manufacturing cost, and mechanical properties. The paper also analyses the optimisation techniques adopted to identify the optimal solution to the problem. In [192], Jayapal et al. realise a multi-criterion decision-making process to correlate geometric complexity, cost–benefit, and the additional cost associated with support structures using a fuzzy power Maclaurin symmetric mean operator for metric aggregation. The build orientations are also studied in [193], the paper applies a hierarchical clustering algorithm to divide facets of the design model in standard tessellation language format into different clusters. The final set of alternative build orientations is generated by combining and refining the alternatives from all clusters.

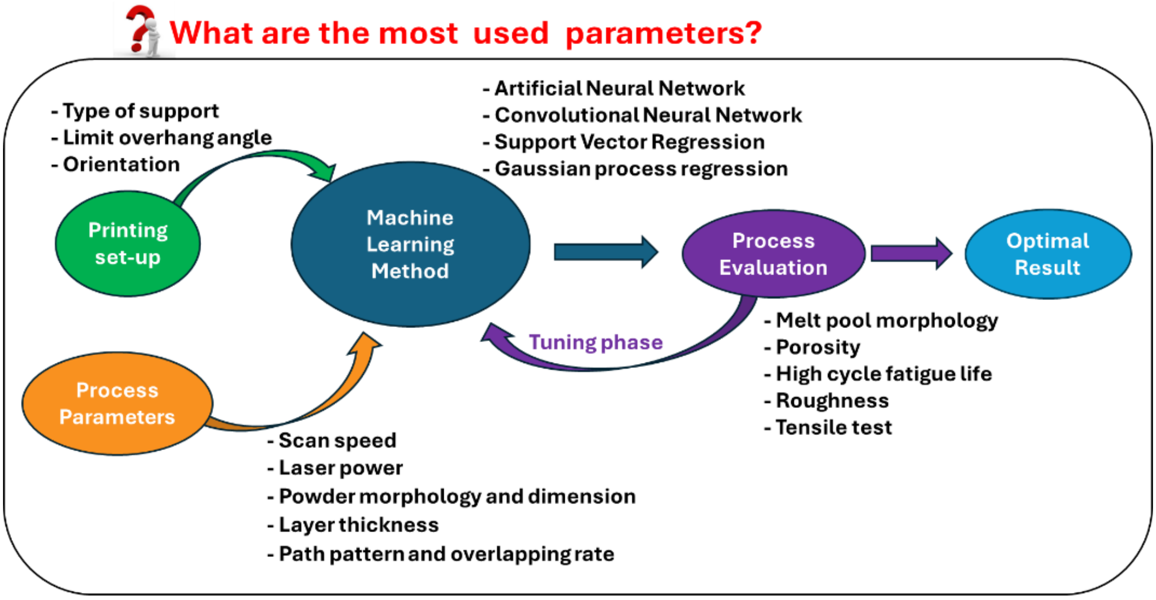

*Figure 19. Most Used Parameters for applying ML in the DfAM field [29][16].*

Analysing the current state of the art, it is possible to deduce that ML applications for AM and DfAM are focused on a single level of applications, without interactions between different levels (these levels are formerly known as Geometrical Design, Process Configuration, Cost Estimation, Process Monitoring). These interactions could improve the results of using ML models by considering parameters from different levels in a single analysis. It would be possible to obtain an ML model able to help the designers from the early design phase of the product to the control of the manufacturing process, arriving at the quality check of the part.

---

[16] Trovato, M., Belluomo, L., Bici, M., Prist, M., Campana, F., & Cicconi, P. (2025). Machine learning in design for additive manufacturing: A state-of-the-art discussion for a support tool in product design lifecycle. The International Journal of Advanced Manufacturing Technology, 137(5–6), 2157–2180. https://doi.org/10.1007/s00170-025-15273-9

# 2 Method

The objective of this thesis is to enhance industrial AM implementation through the research and development of advanced tools and methods based on virtual prototyping methods and AI techniques. Being AM a pillar of Industry 4.0, enhancing the usage of AM techniques will promote efficiency, flexibility, and innovation in manufacturing, driving the transition toward smarter, data-driven, and sustainable production systems.

Virtual prototyping methods are exploited in the product development process to design and validate new components using CAD and CAE software. Nowadays, these tools are necessary in mechanical and industrial engineering due to their wide range of applications and the optimal performance they achieve in terms of accuracy and reliability.

AI techniques are increasingly being integrated into industrial workflows, offering new perspectives for automation, decision-making, and optimisation. In this context, the thesis highlights the valuable synergy between AI and industrial manufacturing, with a particular focus on how ML methods can support AM design processes. These techniques can be used to assist in the design of innovative components, enable adaptive process control, and optimise process parameters based on predictive insights. By connecting AI and AM, the work aims to contribute to the creation of intelligent, adaptive systems that could improve production quality and resource efficiency.

As described in the introduction chapter, the research is structured around four main phases that progressively build toward the overall goal of developing a comprehensive framework for AI- and simulation-driven AM design. The first step focused on studying the state of the art in DfAM, emphasising design optimisation methods specifically tailored to the constraints of L-PBF processes. The second step involves defining a DfAM methodology that specifies design rules for AM to support simulation activities. The third step explores the application of ML tools to assist in the initial phases of product design. This involves defining and classifying input and output parameters relevant to the printing process, followed by the training of ML models able to estimate key outputs related to the final print design. Such predictive models can significantly improve design decision-making, reduce trial-and-error iterations, and enhance the efficiency of AM workflows. Finally, the fourth step concerns the validation of the developed methods and tools through a series of case studies. These include the additive design of metal components for the automotive and related industries. Additionally, ML-based tools are developed during the early design phase across different case studies, assessing their robustness and general applicability.

To identify an approach for enhancing industrial AM implementation, this thesis defines an overall method for including ML into AM and DfAM workflows. The possible ML applications can be various; each application level requires different tools and algorithms. Usually, different tools and algorithms must be combined to identify the method that can achieve the desired objectives. Figure 20 shows the proposed approach to guide designers in selecting and using ML tools in AM and DfAM. It can be divided into two macro areas.

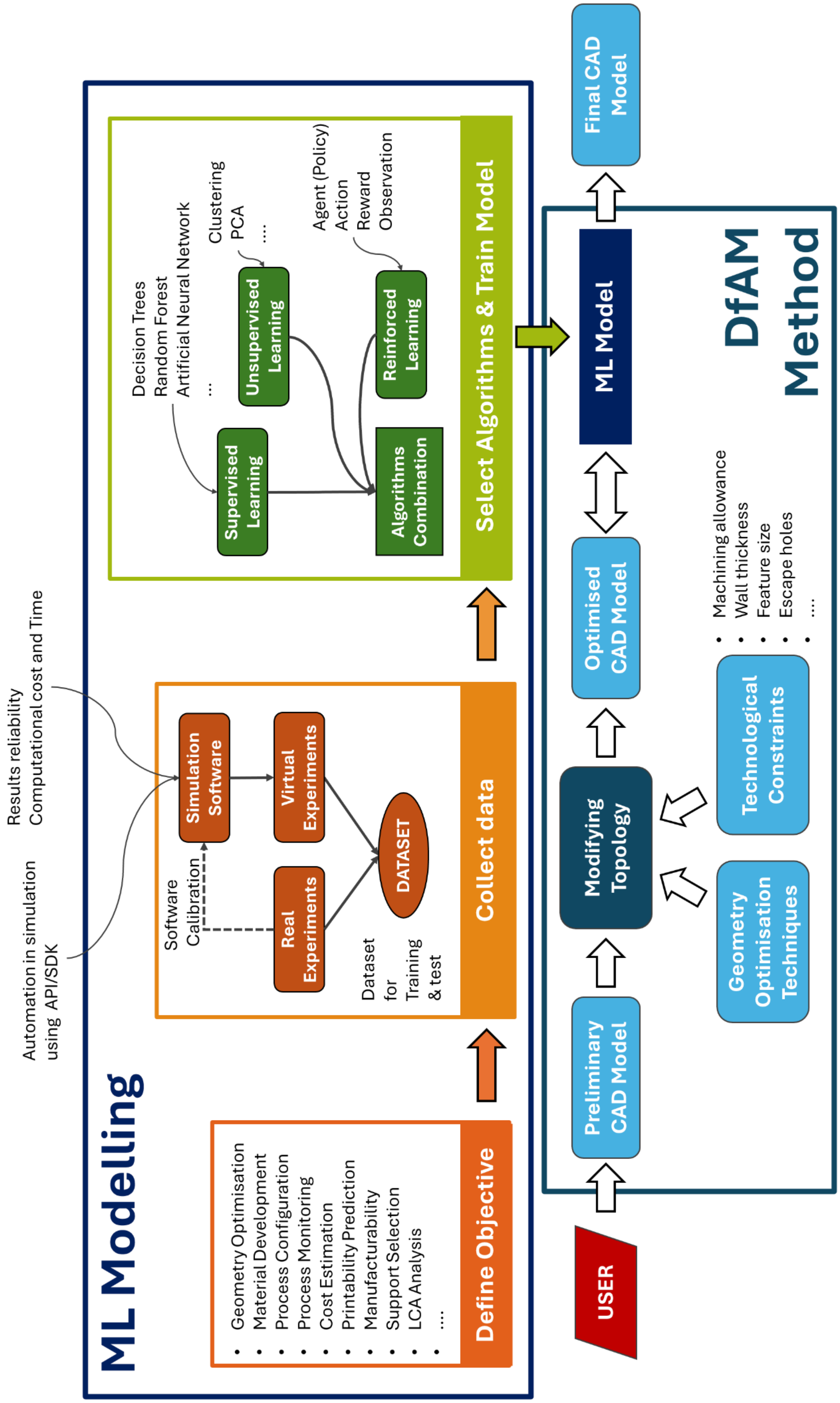

*Figure 20. Proposed Approach.*

The first area, called ML Modelling, concerns the definition of the ML model objectives, the collection of data to build the necessary dataset, the selection of a suitable algorithm or combination of algorithms, and the training and testing of the ML model. Once the ML model is trained, it can be introduced in a “classical” DfAM workflow. The second area regards the inclusion and the use of the ML model in the design approach. The ML model must be coherent with the CAD model under study; given the multitude of production technologies, process parameters, and theoretically infinite types of geometries, actually, it is impossible to train an ML model that is generic and not specific to a case study.

Each macro area can be divided into sub-steps. For the ML modelling area, the first step is the definition of the ML model objectives, which are the desired outputs, and how these objectives must be utilised. The objectives may relate to Geometry Optimisation, Material Development, Process Configuration, Process Monitoring, Cost Estimation, Printability prediction, Manufacturability support, LCA Analysis, etc.

After defining the objectives, it is crucial to transform and analyse the dataset by selecting the appropriate ML method and its corresponding algorithm, or a combination of algorithms. The ML approach chosen may involve supervised, unsupervised, or reinforcement learning algorithms or a mix of these. The choice of ML type can influence how the dataset is constructed. For example, SL methods require labelled data; consequently, the dataset must contain pre-classified examples. UL methods do not require labels and operate solely on the raw data features. Models that rely on numerical features necessitate the conversion or encoding of textual variables. Methods such as NN may demand substantially larger datasets compared to alternative approaches. Scale-sensitive techniques (e.g., SVM or k-NN) require the data to be normalised or standardised.

The second step concerns the building of the dataset. A coherent dataset construction is fundamental to obtaining a valid result that reflects the desired objectives. Creating a large dataset with sufficient elements for reliable results can be very long and expensive. It is possible to make the dataset using both real and virtual experiments. When conducting actual experiments, it is essential to consider the 3D printing cost, time, and machine availability. In the case of virtual experiments, factors such as the reliability of the results (which depend on the software and settings used) and computational time should be considered. The simulation software must be calibrated by the results obtained from real experiments.

Selecting an ML algorithm, or a combination of algorithms, requires careful attention to the nature of the task, the structure of the data, and the practical constraints involved. The process begins with identifying whether the goal involves predicting known outcomes or uncovering latent patterns, which determines the use of supervised or unsupervised methods. The volume, quality, and type of data must also be considered, since some approaches require large datasets, while others perform adequately with fewer observations. Additional factors such as computational resources, the need for interpretability, and acceptable model complexity help narrow the options. In many situations, combining multiple algorithms through ensemble techniques provides more reliable performance, provided that the selected methods complement one another and align with the requirements of the task. Training a ML model begins with assembling and cleaning a dataset that accurately represents the task. The data is then split into training, validation, and test subsets to allow learning, tuning, and evaluation. Features may require preprocessing, such as encoding categorical values or normalising numerical variables, depending on the chosen algorithm. A suitable model is selected and initialised, after which the training subset is used to adjust the model's parameters through an optimisation procedure. Performance is monitored on the validation subset to fine-tune hyperparameters and prevent overfitting. Once the model achieves satisfactory results, final performance is assessed on the test subset to ensure that the trained model generalises to new, unseen data.

Once the ML system is ready, it can be used to predict the study's objective on data outside of the original dataset.

The second area, the DfAM method area, integrates the previously developed ML model into the optimisation process. The workflow starts with the realization of a preliminary CAD model that satisfies requirements and boundary conditions. The CAD model first undergoes a topology-modification stage, which is driven by geometry-optimisation techniques and by technological constraints. Geometry optimisation techniques are often oriented towards achieving lightweight design through algorithmic methods such as topology optimisation, generative design, parametric optimisation, or shape optimisation, etc. The use of lattice structures, such as Strut-based or TPMS, combined with algorithmic methods, is also used for this purpose. The technological constraints depend on the AM process considered; for example, for the L-PBF process of metal powders, these constraints can be the necessity of machining allowances for further post-processing operations, the minimum wall-thickness or feature sizes, and the necessity of an escape-hole for powder removal, and others.

The geometries obtained with the application of optimisation methods and lattice structure, are associated to high shape complexity. It is relevant to correlate shape complexity to the overall part quality and mechanical performance. Despite the shape complexity offering a significant advantage for achieving tailored component performance, designers must use it with attention due to the fluctuating material performances when shape complexity increases. From a sustainability perspective, the strength of AM lies in its material usage; AM processes can produce parts with fewer waste materials compared to traditional manufacturing techniques. The scraps produced are due to the necessary support structures and sieving operations in powder processes. The efficiency of an AM component can be directly correlated to its quantity of material used; complex and lightweight geometries aim to exploit material usage, looking for increasingly challenging components. Designing complexity in AM, particularly for L-PBF process, may appear advantageous due to potential material reductions. However, studies are necessary to determine whether increased complexity in parts improves material effectiveness in terms of mechanical performance.

These inputs guide the generation of an optimised CAD model, which is then exchanged with the trained ML model. The ML system analyses the optimised geometry, refines it based on previously learned patterns, and returns improved design suggestions. This iterative interaction between topology modification and ML refinement ultimately produces a final CAD model tailored for the requirements of AM.

Examples of the applications and capabilities of this method are discussed in Chapters 4 and 5. Chapter 4 presents four lightweight design optimisation case studies for the automotive industry. Specifically, three different connecting rods for internal combustion engines and a lower arm for a McPherson suspension system were analysed with the aim of reducing overall weight while maintaining performance and meeting technical requirements.

Chapter 5 focuses on three ML applications developed for the DfAM field. In this chapter, three SL models were developed and tested on a parametric dataset to assess the effectiveness of the proposed method for mechanical components manufactured using the L-PBF process. Based on geometric features automatically extracted from CAD files, together with AM simulation data, the first model estimates the printability of a part using threshold values for stress and deformation; the second model predicts the required printing time; and the third model estimates the overall component cost through a cascade of three neural networks.

# 3 Shape Complexity and Mechanical Performance in L-PBF Process

The work described in this chapter was analysed during a three-month visit to the Design School at Loughborough University (UK), using experimental data. This section investigates the impact of Shape Complexity (SC) on the mechanical properties of additively manufactured Al-alloy specimens produced with the L-PBF process, starting from simpler shapes in Al-Si-Mg and Al-Cu alloys and progressing to higher complexity. The results aim to support the industrial adoption of High-Strength Aluminium (HS-Al) alloys, enabling the development of innovative, high-value, lightweight components. Studying printed specimens can help reduce future defects, promote sustainable “first-time-right” production with lower waste and resource use, and increase cost-effectiveness, making L-PBF more attractive to industry.

From a sustainability perspective, the strength of AM lies in its material usage; AM processes can produce parts with less waste than traditional manufacturing techniques [194]. The scraps produced are due to the necessary support structures and sieving operations in powder processes. The efficiency of an AM component can be directly correlated to its quantity of material used; complex and lightweight geometries aim to exploit material usage, looking for increasingly challenging components. Designing complexity in AM, particularly for the L-PBF process, may appear advantageous due to potential material reductions [195]. However, further studies are necessary to determine whether increased complexity in parts improves material effectiveness in terms of mechanical performance. It is relevant to assess whether the mechanical performance of materials benefits from high shape complexity. Given the multitude of factors involved, such as different materials (aluminium, maraging steel, stainless steel, titanium, nickel superalloys, precious metals, etc.), various types of lattice structures (struts, TPMS), and their diverse applications (heat exchangers, shock absorbers, acoustic absorbers, and biomedical implants, etc.); it is not feasible to establish a single guideline for design. Moreover, FEA solvers often struggle with small geometries, particularly in lattice structures. Simulations can be costly in terms of computational resources and time, and the resulting data may not always be reliable.

## 3.1 Shape Complexity

The shape of a component strongly influences the cooling rate and energy density during laser scanning. Variations in thickness, intricate features, larger surface area, internal cavities, and the orientations of the part with respect to the laser direction vary the amount of material near the heat source, and consequently, the cooling behaviour.

The Shape Complexity Index (SCI) is a numerical measure useful to estimate the overall geometry of a component. It describes the complexity of a part referred to a simple reference shape, such as a cube, sphere, or cylinder. SCI definitions vary by context, but higher values generally indicate more complex parts.

Valentan et al. [196] proposed a model that exploits STL file metrics, geometric partitioning, and expert-based rules to quantify complexity and assist in selecting suitable manufacturing processes. They convert a CAD model into its STL representation, extract geometric measures, subdivide space, analyse problematic orientations, and then combine those into a complexity score to guide process decisions. Pradel et al. [197] investigated how SC affects build time and material consumption in the material extrusion process, defining the SC as the ratio of surface area to volume of the bounding box of the part. More geometrically complex variants can require longer build times and higher material usage than simpler variants, related to the necessity of the numerous support structures. Greco et al. [198] realised a method for complexity evaluation, based on geometrical, manufacturing, assembly, and disassembly complexities into a unified Product Complexity Index. Matoc et al. [199] introduced a hybrid framework to define an AM Complexity Index tailored to VAT photopolymerization processes, combining an expert-based weighting method with machine learning to calibrate, validate, and refine the metric. The framework aims to support decisions during early design stages for VPP parts. Slama et al. [200] defined a method to determine whether a part is more suitable for AM or traditional manufacturing, defining a complexity measure method and a threshold value. This SCI is based on six factors: volume, surface, thickness, internal curves, surface type, and curve type ratios. The volume ratio (Equation 15.1) represents the ratio of the removed volume to the volume of the bounding box. The surface ratio (Equation 15.2) represents the ratio of the cube surface to the part surface with an equivalent volume. The thickness factor (Equation 15.3) is presented as the ratio of the minimal to maximal thicknesses of the part. The internal curves ratio is described in Equation 15.4, where the $S_i$ factor is the number of internal curves. The surface type ratio is described in Equation 15.5. Types of surfaces are divided into classes, and a numerical coefficient $\alpha_i$is assigned to each class, reflecting the manufacturing complexity of the surface class. $S_i$ is the number of surfaces of class $i$. A similar classification has been performed for curves. Types of curves are classified, and a numerical coefficient $\alpha_i$ is assigned to each curve class, reflecting the manufacturing complexity of the curves. $C_i$ is the number of surfaces of class i. Equation 15.7 describes the proposed methodology; the final $SCI$ is a linear combination of the coefficients described above.

$$V_r = \frac{V_s}{V_{box}} = \frac{V_{box} - V_{part}}{V_{box}} = 1 - \frac{V_{part}}{V_{box}} \tag{15.1}$$

$$S_r = = 1 - \frac{S_{cube}}{S_{part}} = 1 - \frac{6(V_{part})^{\frac{2}{3}}}{S_{part}} \tag{15.2}$$

$$T_r = = 1 - \frac{T_{min}}{T_{max}} \tag{15.3}$$

$$Ic_r = \ln\left(\frac{Ic}{2} + 1\right) \tag{15.4}$$

$$St_r = \sum_{i=1}^{10} \alpha_i \ln(S_i + 1) \tag{15.5}$$

$$Ct_r = \sum_{i=1}^{8} \alpha_i \ln(C_i + 1) \tag{15.6}$$

$$SCI = \sum_{j=1}^{6} C_j \tag{15.7}$$

### Shape Complexity in L-PBF

Moving from general SC definitions to L-PBF-specific considerations, several defects arise that influence manufacturability and overall quality of 3D printed parts. It is usual to associate the Strut-based structures and the TPMS (Section 1.5.2.2) with a high SC level.

Alsalla et al. [201] evaluated how cellular lattice structures (gyroid type) made of stainless steel 316L via L-PBF perform in terms of fracture toughness and tensile strength. Specifically, they analysed the effect of building direction. The lattice structures exhibited meaningful tensile strength and fracture toughness in lattice form. They highlighted that build orientation affected mechanical properties, though they reported that the predictions from the Gibson–Ashby type models were not much different from their measured values.

Referring to more general geometries, different studies have been conducted to identify and correlate geometrical features with part quality and mechanical behaviour of L-PBF printed parts.

Carrozza et al. [202] investigated how different titanium alloys perform when built via L-PBF in geometries with complex features such as thin walls and hollow channels. They analysed geometrical compliance, how well the built part matches the design, porosity and internal defects, and microstructure and hardness. They found correlations between geometry (feature size) and defects and microstructure. As the dimensions of wall width and channel diameter decrease, the numbers and sizes of defects increase, resulting in harder process behaviour. The study emphasises that there are material-specific and geometry-specific limits (thicknesses, overhangs, internal channels) that must be considered.

Bushra et al. [203] studied how specific geometric features influence part quality, specifically distortion, and used this knowledge to develop data-driven design guidelines for AM by identifying geometric features that contribute to higher part distortion. The method uses an axisymmetric-geometry dataset and FEM simulation outputs for distortion evaluation.

Deep et al. [204] developed a numerical framework for the preliminary evaluation of manufacturability for geometrically complex parts in the L-PBF process, with a particular focus on the layer thickness process parameter. The authors quantified how geometrical complexity (non-standard shapes, thin walls, etc.) impacts manufacturability, in terms of build time, productivity, linking it to the layer thickness (as a controllable process parameter) to manufacturability outcomes and explore the trade-off between quality and productivity. They define a model of manufacturability as a function of building rate efficiency and geometrical complexity of the part.

*Manufacturability = Build rate efficiency (considering layer thickness) × Part geometrical complexity*

## 3.2 Aluminium Alloys with L-PBF

Al-alloys are a sustainable material thanks to being fully recyclable and can be reprocessed indefinitely [205]. Reprocessing infrastructures are also widely available. Al is also a non-critical material, and Al natural reserves are planned to last for hundreds of years at the current consumption levels [206]. L-PBF Aluminium alloys are appreciated for their low density, high strength-to-weight ratio, and corrosion resistance, but they present challenges due to high thermal conductivity and susceptibility to hot cracking. Alloys with high silicon content, such as AlSi10Mg and AlSi12, are the most used because silicon improves fluidity, which reduces cracking during the printing phase. These alloys are suitable for complex geometries and offer a good balance of strength and ductility [207]. High-strength aluminium alloys can be used in L-PBF, but they are more difficult to process and require careful control of laser parameters, build orientation, and sometimes preheating to minimise residual stress and cracking. Post-processing, including stress relief and heat treatment, is often necessary to achieve optimal mechanical properties [208].

Alloys made with the L-PBF method are known to suffer metallurgical and surface defects, including porosity (keyhole and gas), cracks, and a lack of fusion [209]. These imperfections have a negative impact on mechanical properties by increasing microstructural irregularity and stress concentration [210]. As a result, numerous ways for minimising the faults of L-PBF metals are continually being researched, studying process parameter effects and post-processing treatments. Solution and precipitation hardening heat treatment have been investigated in several studies to determine the effect of L-PBF Al alloy precipitation hardening and pore decreasing control [211].

### 3.2.1 Al-Si-Mg Alloys

The Al-Si-Mg alloys belong to the Al-Si-Mg system, and their typical chemical composition consists of 9.0–11.0% silicon, 0.25–0.45% magnesium, less than 0.25% iron, and small traces of copper, manganese, zinc, and titanium, with aluminium as the balance. The AlSi1Mg hypoeutectic alloy was originally developed for casting, but it has spread in L-PBF applications due to its high silicon content, which enhances laser absorptivity, reduces thermal expansion, and improves melt pool fluidity. These characteristics help minimise residual stresses and prevent cracking during the printing process [212]. Applications include aerospace, automotive, and general engineering components such as brackets, housings, heat exchangers, heat sinks, lightweight enclosures, tooling inserts, and prototypes [213].

In terms of mechanical properties, parts made from L-PBF Al-Si-Mg achieve a density of approximately 99.5% of the theoretical value [214]. In their as-built condition, the tensile strength $\sigma_t < 450\ MPa$ and the yield strength $\sigma_y \cong 230\ to\ 300\ MPa$, and the elongation is between 3% and 6% [215, 216]. After heat treatment, such as T6 aging, the tensile strength typically decreases to between 320 and 420 MPa, the yield strength ranges from 220 to 280 MPa, and the elongation increases to about 8% to 12% [217, 218].

### 3.2.2 Al-Cu Alloys

Aluminium-Copper (Al-Cu) alloys are a commonly used material in the automotive, aerospace and marine industries thanks to their good mechanical properties-to-density ratio, excellent corrosion resistance, full recyclability, and relatively low cost [219].

The design opportunities L-PBF combined with the properties of Al-Cu could transform many industries through the development of advanced engineering applications such as high-efficiency heat exchangers, energy storage, and lightweight components [220]. The distinctive properties of Al-Cu combined with AM’s unique opportunities provide significant scope for advancing engineering applications such as lightweight components for automotive and aerospace, energy storage for renewable resources and heat exchangers. Enabling the capitalisation of AM opportunities, such as shape complexity, personalisation, on-demand production, and meta-materials with Al-Cu, will open great opportunities for the development of these industries.

Al-Cu and the shape complexity provided by L-PBF can enable a sustainable alternative to composite materials for advanced lightweight applications. Al-Cu has not been widely adopted in L-PBF due to crack formation during the laser melting process [221]. The production of Al-Cu components in L-PBF has been hindered by micro-crack and void formation during the laser process. This cracking mechanism arises during the melt pool solidification when the thin liquid film that forms on the grain boundaries cannot accommodate the solidification shrinkage. Furthermore, Al-Cu might contain volatile alloying elements such as Zn, Mg, and Li, which can evaporate during the L-PBF process, causing a modification of the chemical composition and consequently of the micro-structure and properties of the material [222]. Different types of metals can be processed with L-PBF, but there are still significant challenges to achieving defect-free components with Al-Cu. Until now, how the design of an Al-Cu component impacts the formation of defects, and the quality of printing has never been studied. Researchers have explored process parameters and new Al alloys with moderate success but have neglected how component geometry affects the mechanical properties, formation of voids and grain structure. Shape plays a crucial role in L-PBF as it can significantly affect the cooling rate and energy density during laser scanning [223].

## 3.3 Material Selection Methods

Quantitative methods have been developed to support designers in material selection to meet objectives such as weight reduction, performance enhancement, and cost control in engineering design. The choice of material is closely linked to the intended function of the component being considered. Numerous material properties can influence the final decision. For instance, density and cost are general properties, while elastic modulus, yield strength, ultimate strength, failure strength, and compressive strength are mechanical properties. Additionally, melting point, glass transition temperature, and thermal expansion are examples of thermal properties. Material selection is often constrained by the manufacturing process and the material's ability to be processed effectively. In the case of the L-PBF process for metals, the choices are often limited by the alloys' printability and the availability of metal powders in the market.

Material property charts, also known as Ashby charts, are graphical tools used to compare and analyse the properties of engineering materials to aid materials selection. Each chart plots one material property against another one, typically on logarithmic scales, so materials with similar characteristics occupy distinct regions on the graph. These charts provide a visual overview of the performance and trade-offs among different material classes such as metals, polymers, ceramics, composites, and foams [224].

Rao [225] proposed a structured method to select appropriate materials for a component by combining graph-theoretic concepts with matrix modelling. The idea was to represent the relationships among design criteria and feasible materials using a directed graph, where nodes represent criteria and materials, and links convey influence or preference relations. From the digraph, a relationship matrix is derived and then manipulated to evaluate how well each material satisfies the network of design criteria. Chatterjee et al. [226] presented a systematic framework for selecting materials in engineering design when multiple conflicting criteria must be considered. They apply two multi-criteria decision-making methods to a set of alternative materials evaluated on several criteria. They used the compromise ranking method, known as the VIKOR method, and the outranking method, called ELECTRE. They first identify relevant criteria and weight their importance, then build decision matrices of alternatives against criteria, and apply both methods to demonstrate how they rank the materials. Jahan et al. [227] improved the VIKOR method with a new normalisation scheme handling benefit, cost, and target criteria, yielding more realistic material. Through several case studies, they demonstrated that the revised method provides accurate and realistic rankings of materials by reflecting practical design requirements. Anojkumar et al. [228] investigated the use of several multi-criteria decision-making techniques to choose appropriate materials for piping systems within the sugar industry. The authors defined relevant material properties (cost, corrosion resistance, mechanical strength, ease of maintenance, service life, etc.), assigned weights to these criteria, and then applied a set of different methods to rank candidate materials. Their comparative analysis shows how different methods can yield different rankings; how sensitive the rankings are to the criteria weights and method chosen.

## 3.4 Experimental Approach

This study applied the following methodology. First test samples with different degrees of SC were designed using computational design. These samples were produced using L-PBF in both Al-Cu and Al-Si-Mg alloys, and the tensile strength of the samples was tested. Finally, the tensile test results were analysed and integrated with internal porosity measurements.

### 3.4.1 Design of the Test Specimens

One key advantage of the L-PBF process is the possibility to realise complex geometries, such as lattices or TPMS structures, that are difficult or impossible to manufacture conventionally. However, achieving the geometric and dimensional tolerances required in mechanical applications remains a major challenge.

This study aims to explore how the shape of a component could affect its mechanical performance while keeping its volume and cross-section constant. The work started with simple geometric designs (called No complexity) and created two increasing design variants. The following sections outline the methods used to modify the shape complexities. Figure 21 reports the main dimensions, expressed in millimetres, of the no-complexity specimens used in this study. The Type 0 (Figure 21a) specimen has a 6 mm thickness and has been printed in Al-Si-Mg alloy. The Type 1 (Figure 21b) specimen has a 3 mm thickness and has been realised in Al-Si-Mg and Al-Cu alloys.

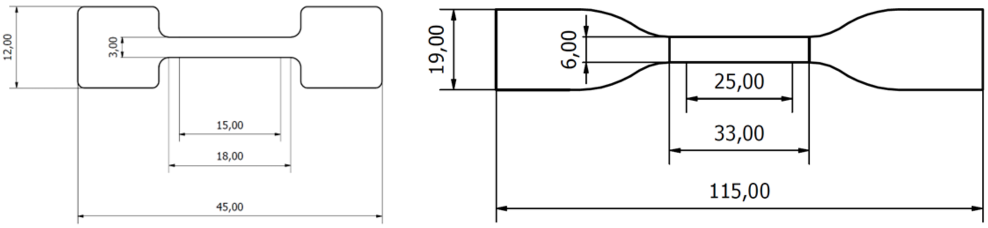

(a) (b)

*Figure 21. No complexity specimens' dimensions: (a) Type 0 specimen has a 6 mm thickness; and (b) Type 1 specimens has a 3 mm thickness.*

### 3.4.2 Type 0 Complexity Design

Figure 22 shows CAD models of the Type 0 specimens with growing shape complexity. The CAD model (a) refers to the No-Complexity model, the CAD model (b) is associated with the low-complexity model, and the CAD model (c) represents the high-complexity specimen. All these models have the same volume. The central part initially measures 3 mm in width, divided into three rods, each 1 mm in length, for the low-complexity model, and divided into six rods, each 0.5 mm in length, for the high-complexity model.

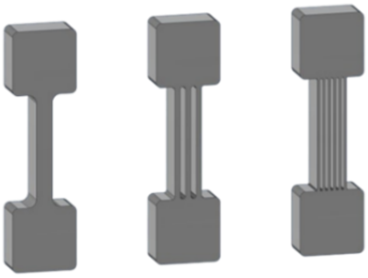

(a) (b) (c)

Figure 22. Design complexity Type 0 sample: (a) No complexity; (b) Low Complexity; (c) High Complexity.

### 3.4.3 Type 1 Complexity Design

Following the criteria of constant volume and cross-section, a method to construct variable complexity lattice structures has been realised. Maintaining constant volume, a higher shape complexity is due to a higher number of unit cells, which involves a significant increase in surface area (Figure 23).

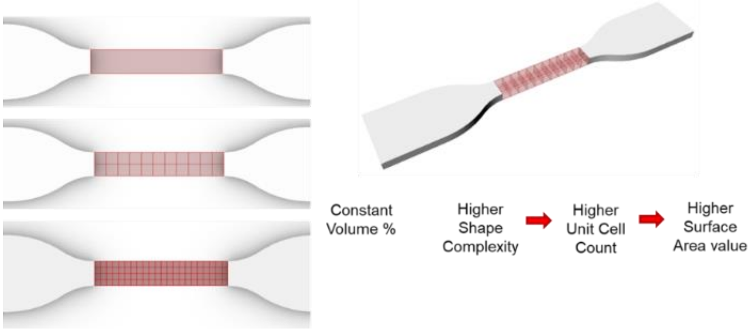

*Figure 23. Increasing complexity scheme for the type 1 specimens.*

Figure 24 schematically describes the steps used to realise the lattice cells, with a Grasshopper code. The first step determines the volume of an individual unit cell and, consequently, the maximum strut length. The second step defines the volume ratio, which splits the space between the nodes and the struts. In the third step, the spherical node radius is calculated, and in the fourth step, the strut length to join spheres is determined. Finally, in the fifth step, the script can automatically output a unit cell with suitable strut and node dimensions.

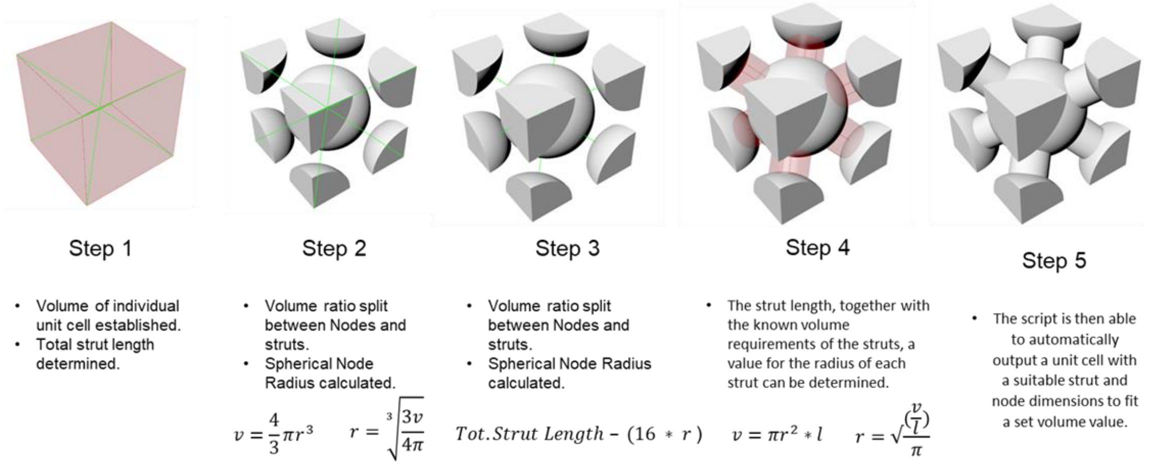

*Figure 24. Grasshopper script workflow used to generate lattice geometry.*

Figure 25 illustrates the final lattice geometries generated with the Grasshopper script. Figure 26 and Table 12 help understand the concept of constant cross-section in the built lattice geometries; as a plane moves along the direction of the tensile test, the surface area remains constant. Figure 27 presents the nomenclature that will be adopted in the following sections.

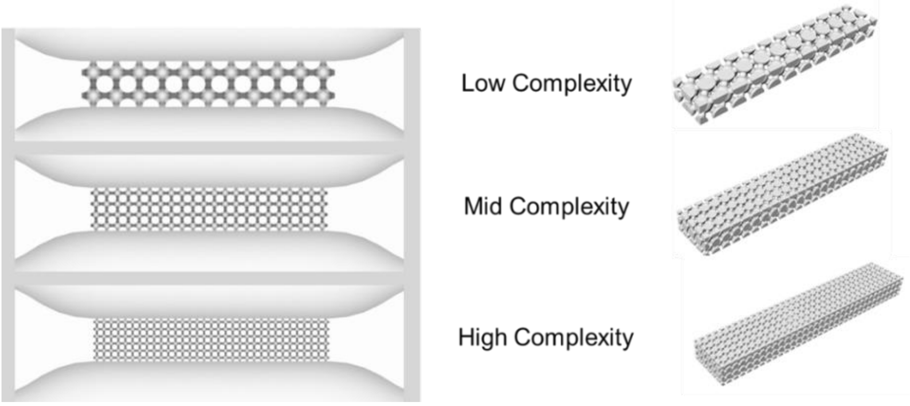

*Figure 25. Lattice geometries obtained with the grasshopper script.*

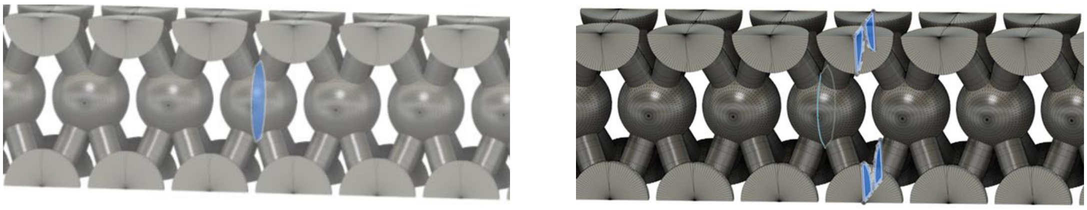

Cross-Section 1 Location

Cross-Section 2 Location

*Figure 26. Two different cross-sections for type 1 specimens.*

*Table 12. Cross-Section surface area values.*

| Sample Type | Cross-Section 1 [mm$^2$] | Cross-Section 2[mm$^2$] |
|---|---|---|
| Low Complexity | 5,87 | 5.79 |
| Mid Complexity | 7.89 | 7.86 |
| High Complexity | 7.90 | 7.91 |

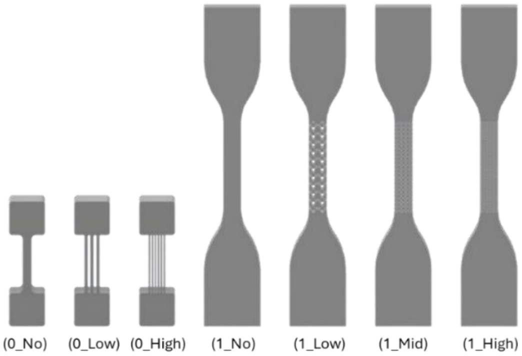

*Figure 27. Nomenclature used for the 3D printed specimens with increasing complexity.*

### 3.4.4 Shape Complexity Evaluation

A python code, exploiting the numpy-stl 3.2.0 open-source library, has been used to automatically extract data such as volume, surface area, bonding box dimensions, etc., from the STL files.

Table 13 reports the specimens' data and calculation of the $A/V$ and $A/VBbox$ ratios, where $A$ is the surface area, $V$ is the volume, and $VBbox$ is the volume of the bounding box. Table 14 exhibits the six factors (volume, surface, thickness, internal curves, surface type, and curve type) of the Slama et al. [200] approach previously described in Section 3.1 and reports the final value, called here $SC\_total$.

*Table 13. Specimens' data and calculation of the $A/V$ and $A/VBbox$ ratios.*

| Name | Area [mm^2] | Volume [mm^3] | Boundary box [mm^3] | Ratio A/V [1/mm] | Ratio A/VBbox [1/ mm] |
|---|---|---|---|---|---|
| 0_No | 1458,170 | 2107,32 | 3240 | 0,692 | 0,450 |
| 0_Low | 1959,480 | 2099,5 | 3240 | 0,9333 | 0,605 |
| 0_High | 2714,840 | 2097,46 | 3240 | 1,2943 | 0,838 |
| 1_No | 3899,130 | 4511,87 | 6555 | 0,8642 | 0,595 |
| 1_Low | 4522,490 | 4223,12 | 6555 | 1,0709 | 0,690 |
| 1_Mid | 5775,790 | 4223,12 | 6555 | 1,3677 | 0,881 |
| 1_High | 7028,980 | 4223,12 | 6555 | 1,6644 | 1,072 |

*Table 14. Shape complexity evaluation for the method proposed by Slama et al.*

| Name | Vr | Sr | Tr | Icr | Str | Ctr | $SC\_total$ |
|---|---|---|---|---|---|---|---|
| 0_No | 0,350 | 0,324 | 0,933 | 0,000 | 7,536 | 10,311 | 19,454 |
| 0_Low | 0,352 | 0,498 | 0,978 | 0,693 | 7,720 | 10,594 | 20,835 |
| 0_High | 0,353 | 0,638 | 0,989 | 1,253 | 7,910 | 10,844 | 21,986 |
| 1_No | 0,312 | 0,580 | 0,974 | 0,000 | 7,536 | 10,071 | 19,473 |
| 1_Low | 0,356 | 0,653 | 0,992 | 2,918 | 15,854 | 21,298 | 42,072 |
| 1_Mid | 0,356 | 0,729 | 0,996 | 5,421 | 25,544 | 31,285 | 64,330 |
| 1_High | 0,356 | 0,777 | 0,997 | 6,804 | 31,083 | 36,815 | 76,831 |

Three SC indices have been compared and analysed to evaluate which one better describes the complexity of geometries under study. The first one, $Ratio\ A/V$, and the second one, $Ratio\ A/VBbox$, are quick to calculate; they show analogous trends, given that the volumes and the bounding box volumes of the specimen are quite similar. The third one, the $SC\_total$, is not designed to evaluate lattice or TPMS structures and requires some time for counting internal cavities, curves, and surfaces. The $SC\_total$ index emphasizes the presence of lattice cells in the specimens, clearly differentiating the Type 1 samples from the Type 0 ones. Furthermore, this method reports equal values for no-complexity samples. Figure 28 displays the SC indices values for each specimen.

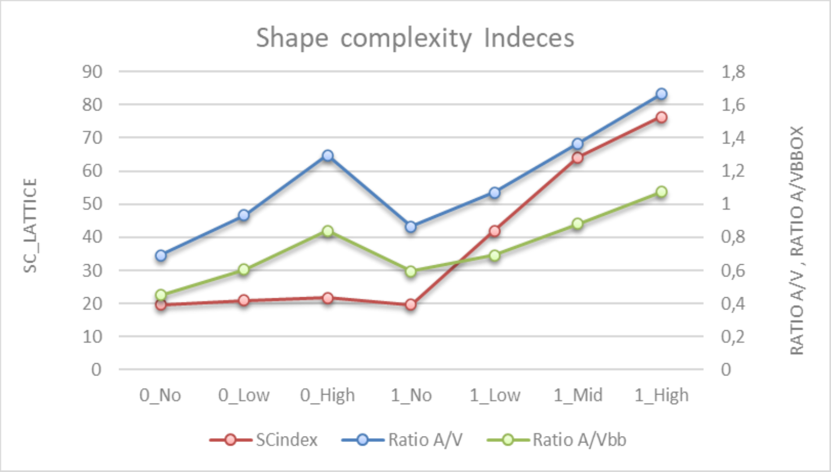

*Figure 28. Shape Complexity Indices values.*

## 3.5 Production of the Samples

### 3.5.1 Materials

In the following sections, the term "Al-Si-Mg" specifically refers to the AlSi10Mg alloy, which is an aluminium casting alloy. AlSi10Mg is widely used in AM because it provides high corrosion resistance, low density, and moderate mechanical strength in the final components. The AlSi10Mg alloy has been supplied by AM powder vendor EOS[17]. Table 15 presents the powder characterisation of the AlSi10Mg alloy used to manufacture Type 0 and Type 1 specimens.

When Al-Cu is mentioned, it refers to the A205 alloy. A205 is a lightweight aluminium powder derived from the patented A20X™ alloy developed by AMT Ltd. The high cooling rates achieved during L-PBF produce a dense, crack-free, non-dendritic microstructure, resulting in excellent high-temperature performance and fatigue resistance. The A205 alloy has been provided by AM powder dealer Eckart[18]. Table 15 also displays the powder characterisation of the A205 alloy used to manufacture Type 1 specimens.

---

[17] EOS GmbH – Electro Optical Systems. Retrieved December 17, 2025.. EOS Aluminium AlSi10Mg material data sheet. Retrieved from https://www.eos.info/metal-solutions/metal-materials/data-sheets/mds-eos-aluminium-alsi10mg

[18] Eckart. (n.d.). Additive manufacturing metal powders. Retrieved January 9, 2025, from https://www.eckart.net/en/lp-additive-manufacturing-metal-powders

*Table 15. Al-Si-Mg and Al-Cu alloy compositions (wt.-%).*

|  | **Al** | **Si** | **Mg** | **Fe** | **Ti** | **Zn** | **Pb** | **Mn** | **Cu, Ni, Sn** | **Others, each** | **Others max.** |
|---|---|---|---|---|---|---|---|---|---|---|---|
| Al-Si-Mg (AlSi10Mg) | Bal. | 9,0-11,0 | 0,2–0,45 | ≤0,55 | ≤0,15 | ≤0,10 | ≤0,03 | 0,20–0,45 | ≤0,05 each | ≤0,05 | ≤0,15 |
| Generic particle size distribution | 25 - 70 µm |  |  |  |  |  |  |  |  |  |  |

|  | **Al** | **Cu** | **Mg** | **Ag** | **Ti** | **B** | **Si** | **Fe** | **Others, each** | **Others max.** |
|---|---|---|---|---|---|---|---|---|---|---|
| Al-Cu (A20X®) | Bal. | 4.2 - 5.0 | 0.2 - 0.33 | 0.6 - 0.9 | 3.00 - 3.85 | 1.25 - 1.55 | 0.1 max. | 0.08 max. | 0.08 max. | 0.17 max. |
| Generic particle size distribution | 20 - 63 µm |  |  |  |  |  |  |  |  |  |

### 3.5.2 Metal Specimens Production

The samples were produced using a Dentas Arrow 3D laser metal printer LMP200 at the University of Maribor. The process parameters used are listed in Table 16, obtaining Energy density of 172,3 J/mm$^{3.}$

*Table 16. Process parameters for L-PBF process.*

| **Parameter** | **Laser Power** | **Scanning Speed** | **Hatch Spacing** | **Layer Thickness** | **Energy Density** |
|---|---|---|---|---|---|
| Value | 190 W | 450 mm/s | 0.049 mm | 0.050 mm | 172,3 J/mm$^3$ |

The scanning strategy employed for producing the samples followed a checkerboard pattern, with the scanning direction rotated by 60° for each successive layer. The samples were fabricated using support bars that were at least 2 mm thick, while no supports were included within the cellular structures. Figure 29 shows the print orientation used for the Type 1 Al-Si-Mg and Al-Cu specimens.

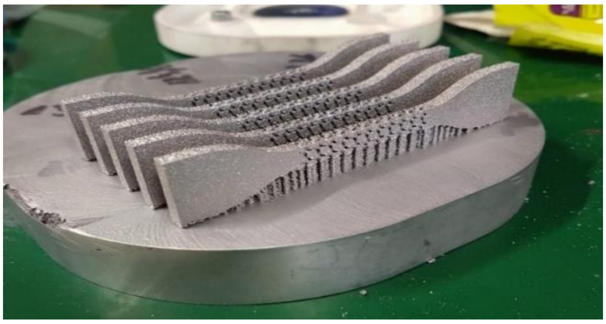

*Figure 29. Print orientation for Al-Si-Mg and Al-Cu specimens.*

Upon completion of the fabrication process, the supports were removed by breaking them off the surface of the samples. Any partially melted or adhered powder particles were subsequently eliminated using sandblasting. Figure 30a shows the Al-Si-Mg and Al-Cu Type 1 specimens, while Figure 30b displays the Al-Si-Mg Type 0 specimens.

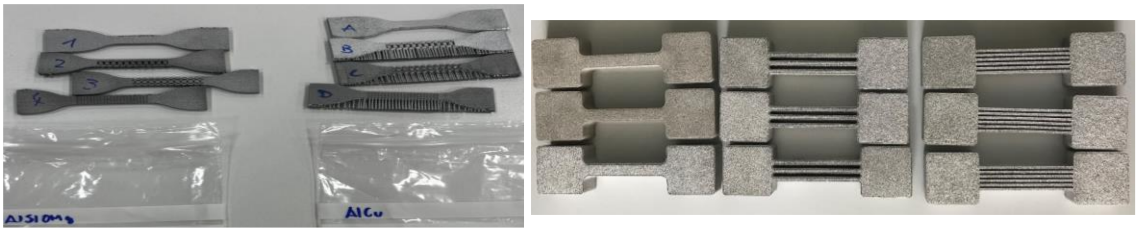

(a) (b)

*Figure 30.(a) Al-Si-Mg and Al-Cu Type 1 specimens; (b) Al-Si-Mg Type 0 specimens.*

Maintaining the same process parameters, scanning strategy, orientations, and cleaning and preparation steps for all specimens reduces the randomness in the results due to variations in influencing parameters.

## 3.6 Analysis

### 3.6.1 Tensile Strength of the Samples

A tensile test is a fundamental method used to evaluate the mechanical performance of a material by measuring its response to an applied tensile load. In this test, a specimen is mounted in a testing machine that applies an increasing uniaxial tension, typically at a constant speed, until fracture occurs. The applied force and the corresponding elongation are continuously recorded to generate a stress–strain curve. From this curve, key mechanical properties such as Young's modulus, yield strength, ultimate tensile strength, ductility, and toughness can be determined.

The tensile strength test was carried out on a Lloyds LR50K Universal Materials Testing Machine. The test constant speeds used are $1\ mm/min$ for Type 0 specimens and $10\ mm/min$ for Type 1 specimens. All tensile tests were conducted on as-fabricated specimens, without any post-processing except for the removal of excess metal powders. Figure 31 shows an example of the tensile test conducted for this work.

*Figure 31. Example photo of a tensile test experiment.*

Figures 32 and 33, together with Table 17, describe the data obtained from the tensile tests of Type 0 – Al-Si-Mg specimens. Figure 32 shows Strass-Strain diagrams across the test repetitions, Table 17 reports the mean values, and Figure 33 shows histograms and trends of the mean values. The 0_no specimens present more stable trends (orange lines) with respect to 0_Low (green lines) and

0_High (light blue lines). The Ultimate Tensile Stress (UTS) and the Yield Stress (YS) of the no-complexity samples are compatible with those reported in the literature.

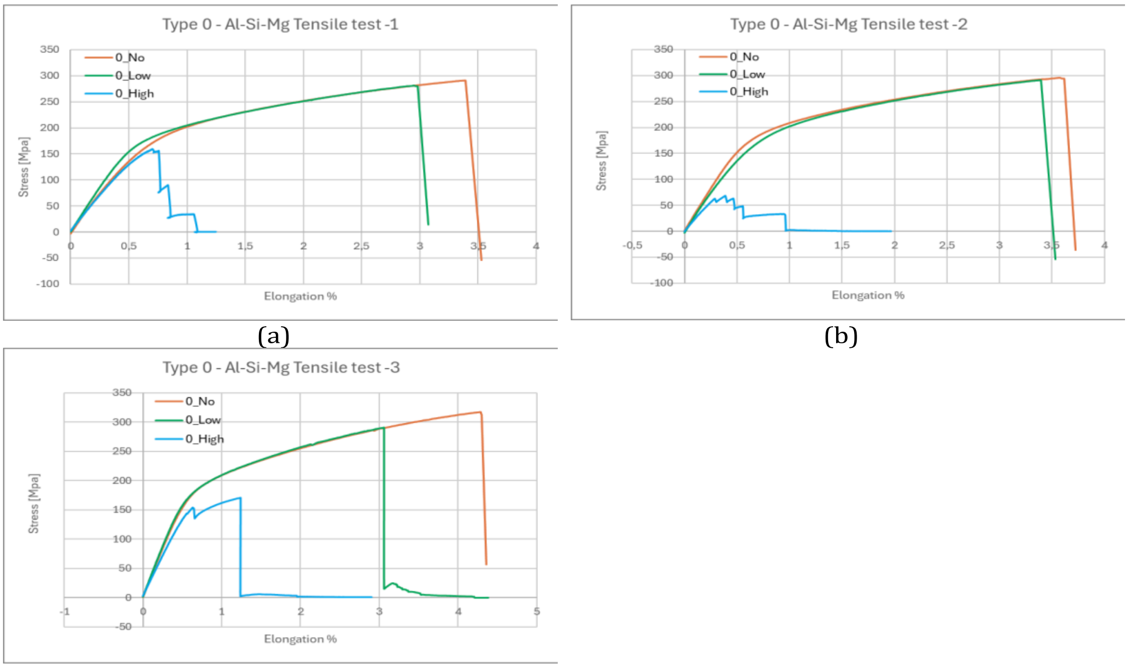

(a) (b)

(c)

*Figure 32. Stress-Strain diagrams for Type 0 - Al-Si-Mg specimens; (a) first repetition, (b) second repetition, (c) third repetition.*

*Table 17. Type 0- Al-Si-Mg specimens tensile tests mean values results.*

| Specimen | UTS (MPa) | YS (MPa) | Elongation % |
|---|---|---|---|
| 0_No | 301,44 | 153 | 3,77 |
| 0_Low | 288,93 | 148 | 3,33 |
| 0_High | 132,56 | 96 | 1,10 |

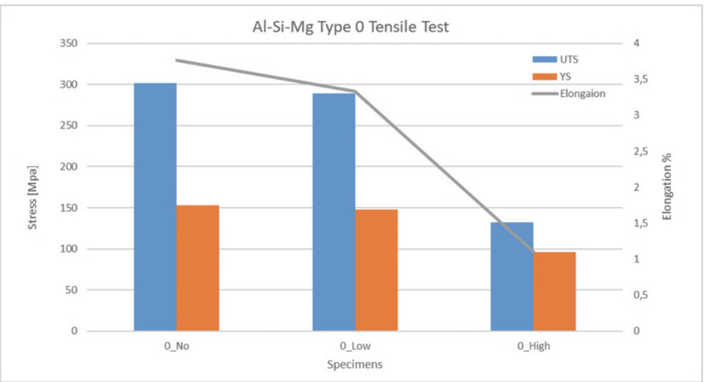

*Figure 33. Type 0- Al-Si-Mg specimens tensile tests mean results.*

Figures 34 and 35, along with Table 18, present the data from the tensile tests conducted on Type 1 – Al-Si-Mg specimens. The elongation value for 1_Low (the first repetition) was excluded from the mean calculation because it is significantly higher than the others, exceeding 50 instead of about 10 in the other experiments.

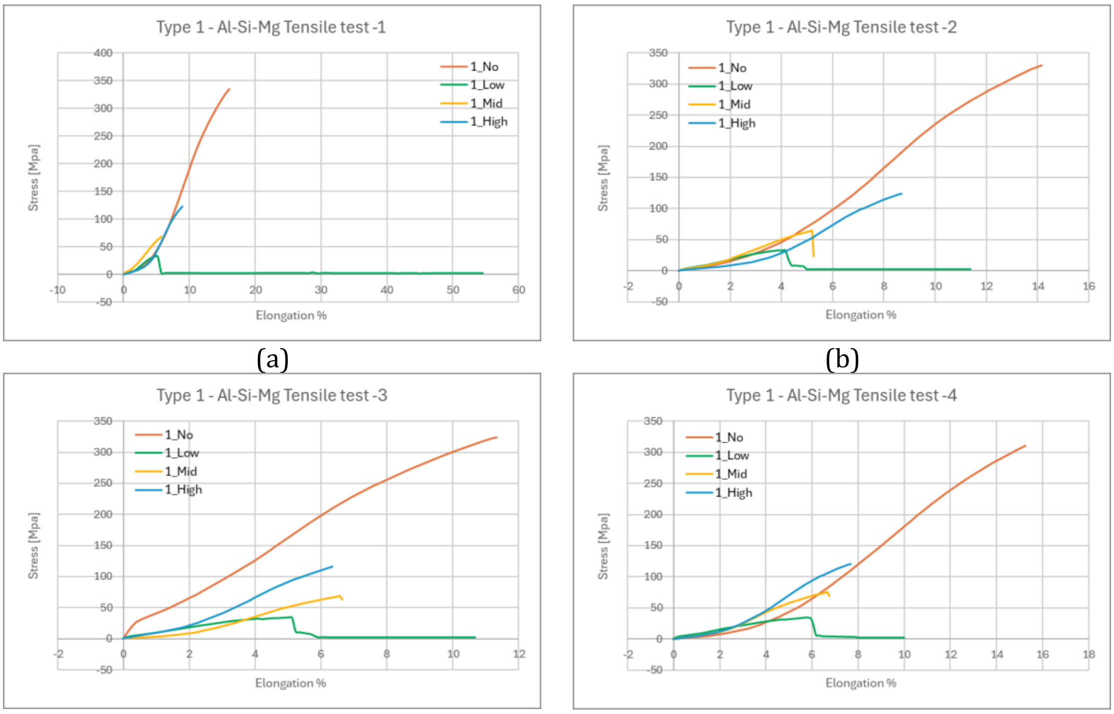

(a) (b)

(c) (d)

*Figure 34. Stress-Strain diagrams for Type 1 - Al-Si-Mg specimens; (a) first repetition, (b) second repetition, (c) third repetition, (d) fourth repetition.*

*Table 18. Type 1- Al-Si-Mg specimens tensile tests mean values results.*

| **Specimen** | **Tensile Strength (MPa)** | **Stress at Break (MPa)** | **Young's Modulus (GPa)** | **Elongation %** |
|---|---|---|---|---|
| 1_No | 325,49 | 260,39 | 3,43 | 14,31 |
| 1_Low | 33,48 | 2,33 | 2,09 | 10,80 |
| 1_Mid | 69,26 | 55,41 | 1,66 | 6,11 |
| 1_High | 121,25 | 97,00 | 2,70 | 7,96 |

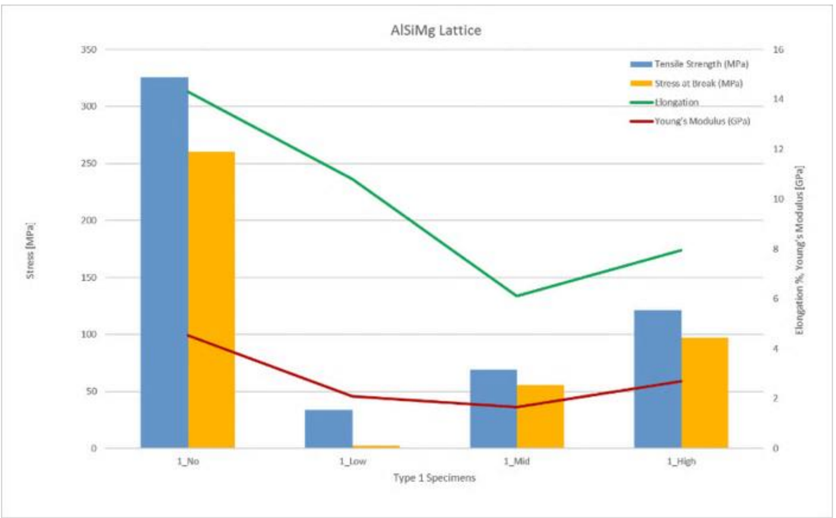

*Figure 35. Type 1- Al-Si-Mg specimen tensile tests results.*

Figure 36 and 37, with Table 19, display the data obtained from the tensile tests of Type 1 – Al-Cu specimens.

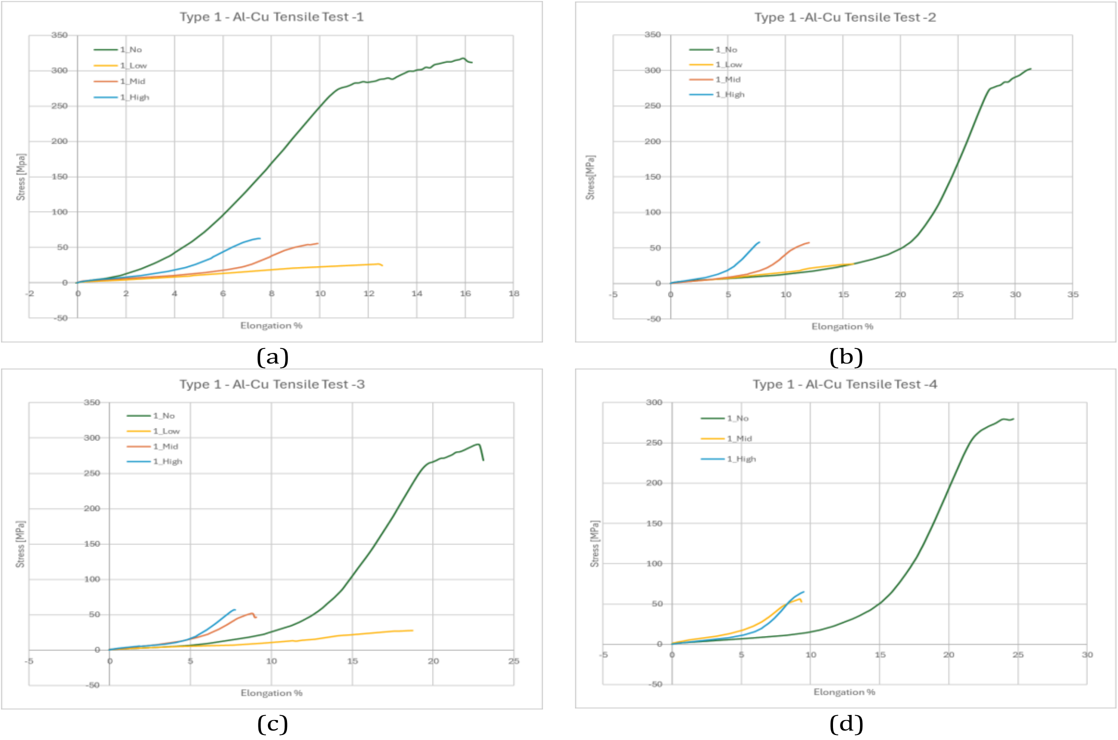

(a) (b)

(c) (d)

*Figure 36. Stress-Strain diagrams for Type 1 - Al-Cu specimens; (a) first repetition, (b) second repetition, (c) third repetition, (d) fourth repetition.*

*Table 19. Type 1- Al-Cu specimens tensile tests mean values results.*

| Specimen | Tensile Strength (MPa) | Stress at Break (MPa) | Young's Modulus (GPa) | Elongation % |
|---|---|---|---|---|
| 1_No | 298,29 | 238,64 | 4,05 | 24,03 |
| 1_Low | 27,45 | 21,96 | 0,66 | 15,84 |
| 1_Mid | 55,63 | 44,51 | 1,53 | 10,16 |
| 1_High | 61,12 | 48,89 | 1,93 | 8,16 |

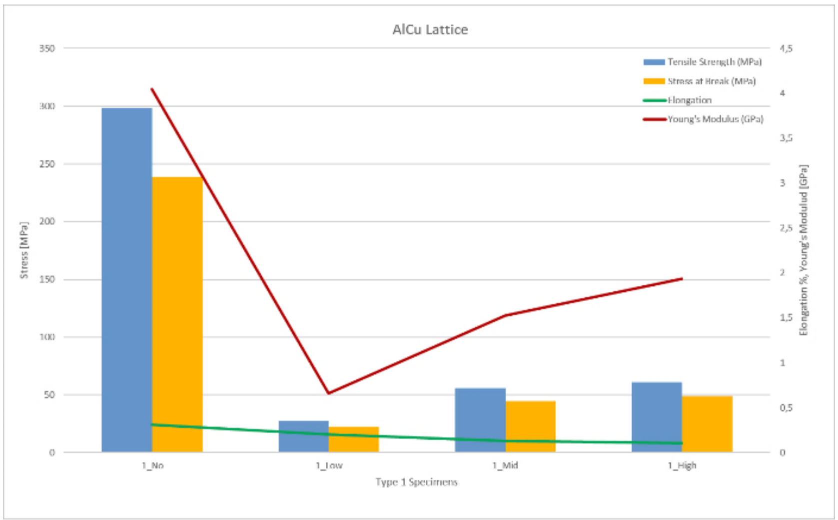

*Figure 37. Type 1- Al-Cu specimens tensile tests results.*

### 3.6.2 Analysis of Porosity

One of the key issues related to the L-PBF process for metals is the presence of internal porosity in the produced parts. The causes of porosity can be correlated with combinations of process parameters, impurities in powders and gas, and surface oxidation or contamination. Some emerging problems include lack of fusion, keyhole, gas entrapment, and balling. Quantifying porosity, expressed as a percentage of the analysed surface area, is essential for assessing the overall quality of metal AM components.

Optical microscope Side-On and Top-Down analyses have been conducted on Type 1 specimens. In the following subsections, parts of the figures and data of these analyses are reported. Figure 38 reports the images and data from the Optical microscope analyses of the Type1 Al-Si-Mg specimens.

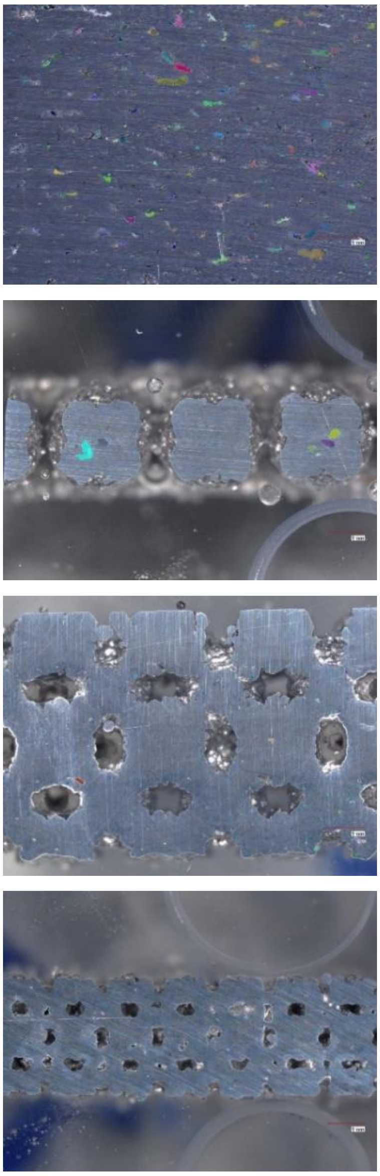

(a)

| **Specimen** | Al-Si-Mg, 1_No |
|---|---|
| **Analysis** | Side On |
| **Count** | 244 Pcs |
| **Area ratio** | 2,68 % |
| **Total region area** | 43,19 mm$^2$ |

(b)

| **Specimen** | Al-Si-Mg, 1_Low |
|---|---|
| **Analysis** | Top Down |
| **Count** | 10 Pcs |
| **Area ratio** | 0,4 % |
| **Total region area** | 77,24 mm$^2$ |

(c)

| **Specimen** | Al-Si-Mg, 1_Mid |
|---|---|
| **Analysis** | Side On |
| **Count** | 143 Pcs |
| **Area ratio** | 0,36 % |
| **Total region area** | 77,24 mm$^2$ |

(d)

| **Specimen** | Al-Si-Mg, 1_High |
|---|---|
| **Analysis** | Top Down |
| **Count** | 6 Pcs |
| **Area ratio** | 0,03 % |
| **Total region area** | 77,24 mm$^2$ |

*Figure 38. Optical microscope analyses of the Type1 Al-Si-Mg specimens: (a) 1_No, Side On; (b) 1_Low, Top Down; (c) 1_Mid, Side On; (d) 1_High, Top Down.*

Figure 39 reports the images and data analyses of the Type1 Al-Cu specimens.

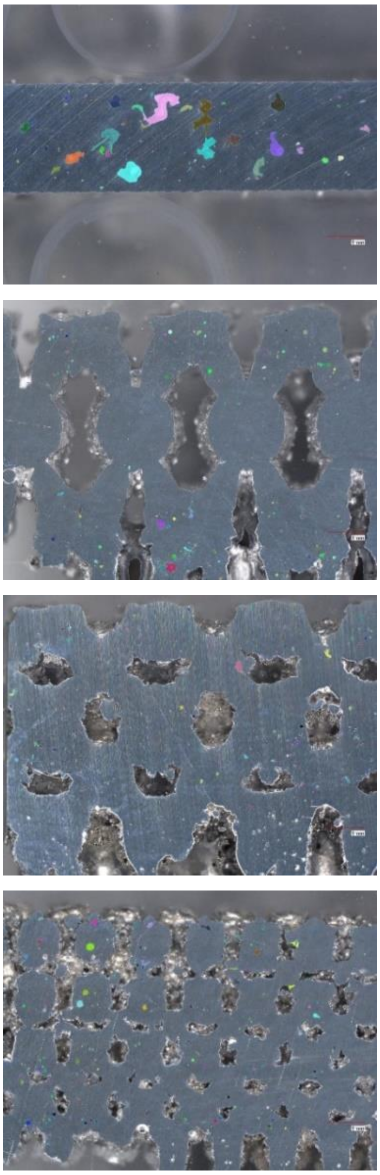

(a)

| Specimen | Al-Cu, 1_No |
|---|---|
| Analysis | Top Down |
| Count | 56 Pcs |
| Area ratio | 2,81 % |
| Total region area | 77,24 mm$^2$ |

(b)

| Specimen | Al-Cu, 1_No |
|---|---|
| Analysis | Side On |
| Count | 151 Pcs |
| Area ratio | 0,68 % |
| Total region area | 77,24 mm$^2$ |

(c)

| Specimen | Al-Cu, 1_Mid |
|---|---|
| Analysis | Top Down |
| Count | 173 Pcs |
| Area ratio | 0,44 % |
| Total region area | 77,24 mm$^2$ |

(d)

| Specimen | Al-Cu, 1_High |
|---|---|
| Analysis | Side On |
| Count | 320 Pcs |
| Area ratio | 1,05 % |
| Total region area | 77,24 mm$^2$ |

*Figure 39. Optical microscope analyses of the Type1 Al-Cu specimens: (a) 1_No, Top Down; (b) 1_Low, Side On; (c) 1_Mid, Top Down; (d) 1_High, Side On.*

Table 20 reports the mean values of measured internal porosity, taking the average of Side-On and Top-Down measurements for each specimen.

*Table 20. Mean values of measured internal porosity for each specimen.*

| Type 1 | Specimen | Mean Internal porosity | Type 1 | Specimen | Mean Internal porosity |
|---|---|---|---|---|---|
| Al-Si-Mg | 1_No | 2,73 | Al-Cu | 1_No | 1,41 |
| | 1_Low | 0,66 | | 1_Low | 0,51 |
| | 1_Mid | 0,68 | | 1_Mid | 0,47 |
| | 1_High | 0,76 | | 1_High | 0,53 |

## 3.7 Results and Discussions

This section analyses and discusses the analysis previously presented. The first part presents mechanical performance trends as a function of the SC, introducing a mechanical performance index to merge the mechanical results into a single metric, and evaluates the trends of this index with respect to SC. The second part introduces the measured internal porosity in the study and analyses how this parameter affects indices.

### 3.7.1 Mechanical Behaviour and Shape Complexity

Figure 40 plots the UTS, YS, and E% trends of Type 0 - Al-Si-Mg specimens; these samples have the same cross-section despite the increasing SC. Porosity measurements have not been conducted for these specimens.

The mechanical properties remain similar from No-Complexity (0_No) specimen to Low-complexity (0_Low) but rapidly decrease for High-complexity (0_High), arriving at a loss of 57% for UTS and 66% for E%. The YS presents the same trend, but the High-complexity loss is lower, about 38%. These values are reported in Section 3.6.1 (Table 17). As complexity increases, evaluated mechanical performance (UTS, YS, and E%) decreases, and the Al-Si-Mg material overall appears to become more brittle. The difference between UTS and YS values decreases, and the strain percentage also diminishes. Despite the SC increment not being so elevated (absence of lattice and complex surfaces), the loss in mechanical behaviour is relevant.

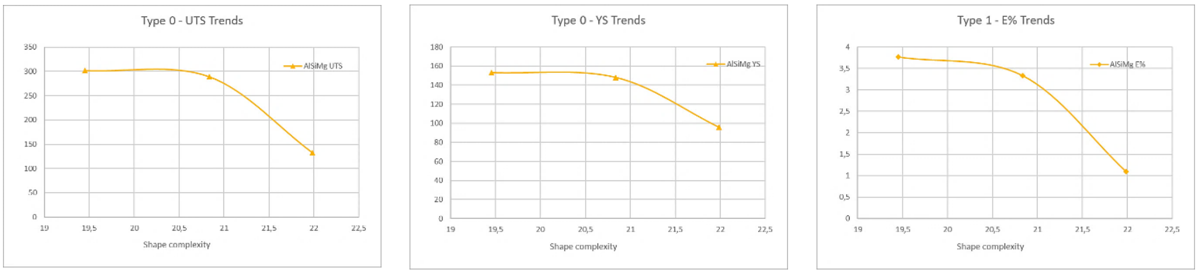

(a) (b) (c)

*Figure 40. Type 0 UTS, YS, and E% Trends as function of Shape Complexity: (a) UTS; (b) YS; (c) E%.*

Figure 41 shows the UTS, YS, and E% trends and the relative normalised trends with respect to the real cross-sections, obtained from the mean measured porosity. For the Type 1 lattice specimens, the UTS and YS trends exhibit the same behaviour, a rapid decrease from the No-complexity (1_No) to the Low-complexity (1_Low) and a slight increase for Mid-Complexity (1_Mid) and again for High-Complexity (1_High). Only the Al-Si-Mg YS has a decrease for Mid-complexity with respect to Low-complexity. The E% behaviour is quite different for each material at increasing complexity. The Al-Si-Mg E% decreases for Low and Mid-Complexity and increases slightly for High-Complexity. The Al-Cu E% decreases with increasing SC. Values are reported in Section 3.6.1 (Tables 18 and 19).

To better understand how geometries affect mechanical performance, normalised trends have been included. This involves dividing each value by its cross-sectional measurements. This approach allows for evaluating the effect of every single mm² of material at increasing SC. For the

Al-Si-Mg and Al-Cu Type 1 specimens, CAD and real-porosity normalised values are quite similar due to low numerical differences between these values; only the real ones are reported. Normalised UTS curves present quite similar patterns, a decrease for Low-complexity and a slight increase for Mid and High-Complexity. Similar trend is visible for Al-Cu YS; the Al-Si-Mg YS shows a relevant increase for Low-Complexity, even compared to No-Complexity. E% trends exhibit a starting increase value for Low-Complexity, a decreasing trend for Mid-Complexity, and again increasing for High-Complexity. Normalised values are reported in Table 29.

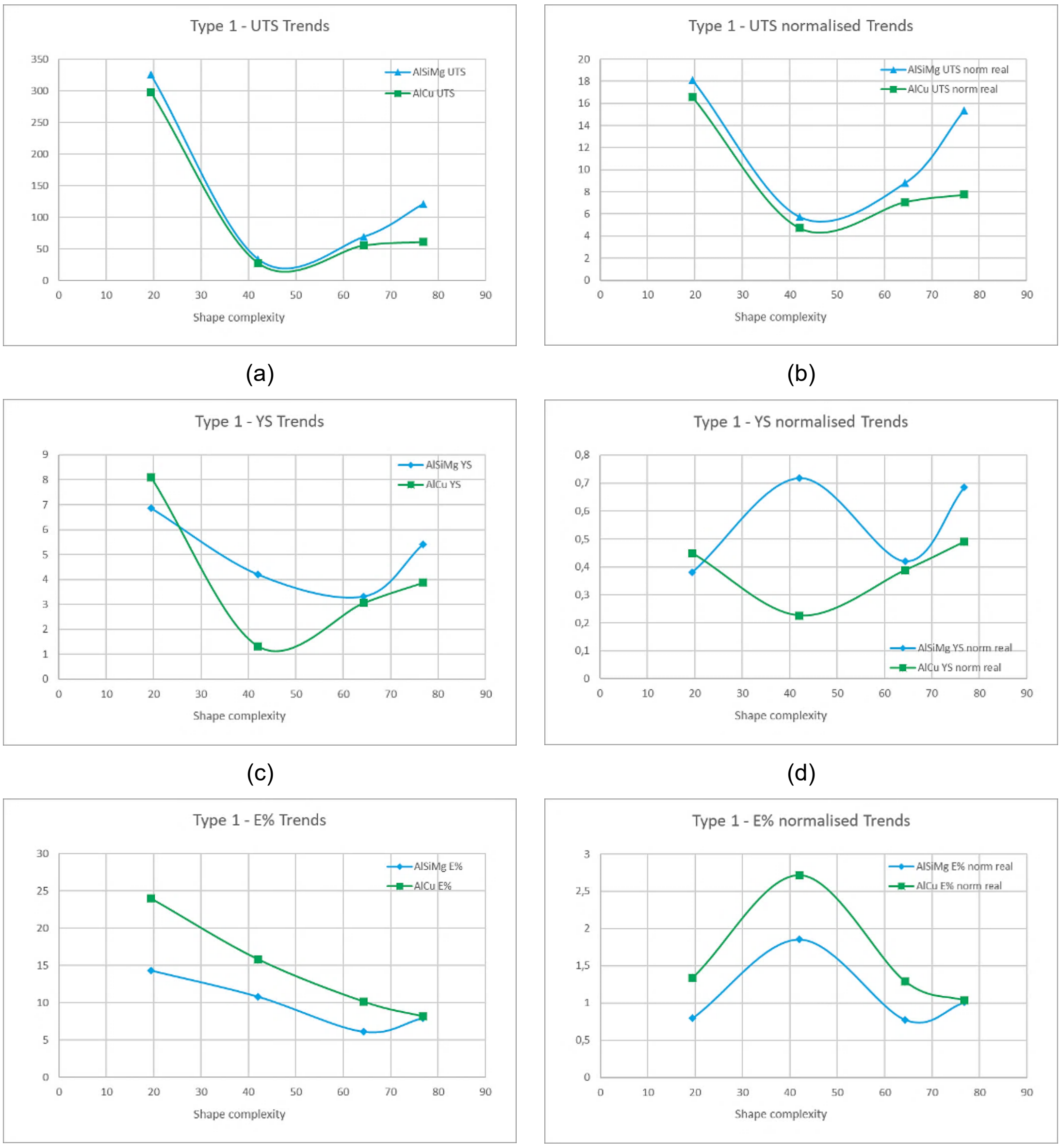

(a) (b)

(c) (d)

(e) (f)

*Figure 41 . Type 1 trends and normalised trends: (a) UTS; (b) UTS normalised; (c) YS; (d) YS normalised; (e)E%; (f) E% normalised.*

To establish a unique correlation between material performance and shape complexity, a Mechanical Performance Index (MPI) has been developed. The driving idea is to find a criterion to aggregate material information obtained from mechanical tests into a single index and to refer increasing SC specimens to the No-Complexity ones. Within the elastic domain, the YS can be estimated from the Young’s Modulus by assuming a limiting strain of 0.002, corresponding to the conventional 0.2% offset yield criterion. Equation 16 shows the MPI, where $UTS_i$, $YS_i$, and $E\%_i$ are respectively the ultimate tensile stress, the yield stress, and the elongation % of $i-th$ specimen. The subscript $No-comp$ refers to the no-complexity specimens, used as benchmarks for each single material and specimen type.

$$\begin{cases} MPI_i = w_1 \dfrac{UTS_i}{UTS_{No-Comp}} + w_2 \dfrac{YS_i}{YS_{No-Comp}} + w_3 \dfrac{E\%_i}{E\%_{No-Comp}} \\ \displaystyle\sum_{i=1}^{3} w_i = 1 \end{cases} \tag{16}$$

where $w_1 = 0{,}478$, $w_2 = 0{,}261$, and $w_3 = 0{,}261$ are constant normalizing indices, calculated through the Fuzzy Analytical Hierarchy process (FAHP), so that the MPI index for the benchmark materials (no-complexity) is always unitary.

The FAHP is an extension of the traditional Analytical Hierarchy Process that integrates fuzzy logic to handle uncertainty and vagueness in human judgments. While AHP relies on exact numerical comparisons to determine the relative importance of criteria and alternatives, FAHP allows the use of fuzzy numbers, described in Figure 42, to express subjective assessments, for this study reported in Table 21, such as “Moderate” or “very strong”. Fuzzy numbers are a trio of values $M = (l, m, u)$, where $l$ and $u$ are the lower and upper bound of the preference $m$ expressed by the decision maker.

This approach includes the imprecision of human opinion in evaluations. The process involves structuring the decision problem into a hierarchy, conducting pairwise comparisons using fuzzy scales, aggregating, and disaggregating the fuzzy judgments to obtain values, and finally deriving weights and rankings for the alternatives [228].

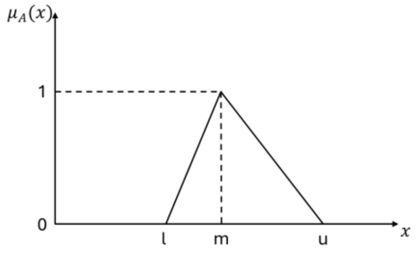

(a)

$$\mu_A(x) = \begin{cases} 0 & x < l \\ \dfrac{x-l}{m-l} & l \le x \le m \\ \dfrac{u-x}{u-l} & m \le x \le u \\ 0 & x > u \end{cases}$$

(b)

*Figure 42. Triangular Fuzzy numbers: graphical description (a), and mathematical description (b).*

*Table 21. Subjective assessments and correlated Fuzzy numbers.*

| Linguistic term | Fuzzy number (l, m, u) |
|---|---|
| Equal (E) | (1, 1, 1) |
| Moderate | (2, 3, 4) |
| Strong | (4, 5, 6) |
| Very Strong | (6, 7, 8) |
| Extreme | (8, 9, 10) |

The initial step involves analysing the correlation of the examined variables. A survey was created to facilitate this purpose; the questions are listed in Table 22, and Table 23 presents the results.

*Table 22. Survey to correlate mechanical properties importances.*

| | **Questions** |
|---|---|
| Q1 | How important is the UTS when compared with YS? |
| Q2 | How important is the UTS when compared with E%? |
| Q3 | How important is the YS when compared with E%? |

*Table 23. Survey results*

| | | **Importance (or) preference of one criterion over another** | | | | | | | | | |
|---|---|---|---|---|---|---|---|---|---|---|---|
| Q | **Crit.1** | Extreme | Very Strong | Strong | Moderate | Equal | Moderate | Strong | Very Strong | Extreme | **Crit. 2** |
| Q1 | UTS | | | | | | x | | | | YS |
| Q2 | UTS | | | | | | x | | | | E% |
| Q3 | YS | | | | | x | | | | | E% |

The second step regards the realisation of the crisp pair-wise comparison matrix, where the $n$ criteria are summarised in a $(n \times n)$ matrix in which the element $a_{ij}$ is the quotient of the weights of the criteria. Table 24 shows the crisp pair-wise comparison matrix of this study; colours are consistently used to improve readability across matrices.

*Table 24. Crisp pair-wise comparison matrix.*

| **Criteria** | **UTS** | **YS** | **E%** |
|---|---|---|---|
| **UTS** | (1,1,1) | (2,3,4) | (2,3,4) |
| **YS** | (1/4,1/3,1/2) | (1,1,1) | (1,1,1) |
| **E%** | (1/4,1/3,1/2) | (1,1,1) | (1,1,1) |

The third step involves the mathematical calculation to normalize and find the relative weights:

1. Calculate the fuzzy geometric mean for each criterion (Equation 17.1).

$$r_i = (\prod_{j=1}^{n} l_{ij})^{1/n}, (\prod_{j=1}^{n} m_{ij})^{1/n}, (\prod_{j=1}^{n} u_{ij})^{1/n} \tag{17.1}$$

2. Calculate the total fuzzy sum (Equation 17.2)

$$r_{sum} = \sum_{i=1}^{n} r_i \tag{17.2}$$

3. Calculate the normalized fuzzy weight dividing each fuzzy numbers by the total fuzzy sum, element by element (Equation 17.3)

$$w_i = r_i \otimes (r_{sum})^{-1} \tag{17.3}$$

4. Transform fuzzy numbers into a single number, to obtain a numerical weight, using the centroid method (Equation 17.4)

$$w_{c_i} = \frac{w_{l_i} + w_{m_i} + w_{u_i}}{3} \tag{17.4}$$

5. Normalize the obtained weights (Equation 17.5). These $W_i$ are the final weights of the criteria.

$$W_i = \frac{w_{c_i}}{\sum_i w_{c_i}} \tag{17.5}$$

Table 25 reports the calculation results, obtaining for this work $w_1 = 0{,}478$, $w_2 = 0{,}261$, and $w_3 = 0{,}261$.

*Table 25. FAHP calculation results.*

| **Criteria** | $r_l$ | $r_m$ | $r_u$ | $w_l$ | $w_m$ | $w_u$ | $w_{c_i}$ | $W_i$ |
|---|---|---|---|---|---|---|---|---|
| UTS | 1,587 | 2,080 | 0,630 | 0,500 | 0,600 | 0,333 | 0,478 | 0,478 |
| YS | 0,794 | 0,693 | 0,630 | 0,250 | 0,200 | 0,333 | 0,261 | 0,261 |
| E% | 0,794 | 0,693 | 0,630 | 0,250 | 0,200 | 0,333 | 0,261 | 0,261 |
| $r_{sum}$ | 3,175 | 3,467 | 1,890 | | | Σ | 1 | 1 |

Table 26 reports the value of MPI for Type 0 specimens. The increasing SC effect on the Rod-Specimens (Type 0) is shown in Figure 43. The No-Complexity specimens present an MPI of unit value, as the MPI has been constructed, and the MPI decreases with increasing SC.

*Table 26. Type 0 specimens MPI calculation.*

| **Type 0** | | **UTS** | **YS** | **Elongation** | **Shape Complexity** | **MPI** |
|---|---|---|---|---|---|---|
| Al-Si-Mg | 0_No | 301,44 | 153,00 | 3,77 | 19,454 | 1 |
| | 0_Low | 288,93 | 148,00 | 3,33 | 20,835 | 0,94 |
| | 0_High | 132,56 | 96,00 | 1,10 | 21,986 | 0,45 |

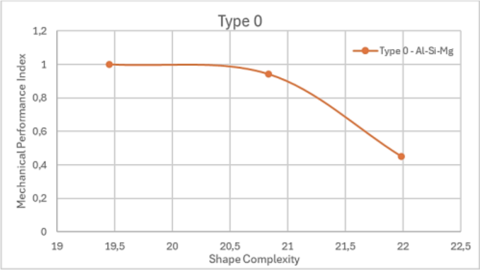

*Figure 43. Type 0 specimens MPI trends as a function of $SC\_total$.*

Table 27 reports the value of MPI for Lattice specimens (Type 1). Figure 44 shows the MPI trends as a function of the $SC\_total$ index.

*Table 27. Type 1 specimens MPI evaluation.*

| **Type 1** | | **UTS** | **YS** | **Elongation** | **Shape Complexity** | **MPI** |
|---|---|---|---|---|---|---|
| Al-Si-Mg | 1_No | 325,49 | 6,86 | 14,31 | 19,473 | 1 |
| | 1_Low | 33,48 | 4,19 | 10,80 | 42,072 | 0,41 |
| | 1_Mid | 69,26 | 3,31 | 6,11 | 64,330 | 0,34 |
| | 1_High | 121,25 | 5,41 | 7,96 | 76,831 | 0,53 |
| Al-Cu | 1_No | 298,29 | 8,09 | 24,03 | 19,473 | 1 |
| | 1_Low | 27,45 | 1,32 | 15,84 | 42,072 | 0,26 |
| | 1_Mid | 55,63 | 3,06 | 10,16 | 64,330 | 0,30 |
| | 1_High | 61,12 | 3,87 | 8,16 | 76,831 | 0,31 |

For the Type 1 – Al-Si-Mg specimens, starting from the No-Complexity, the plot shows a rapid decrease up to the Low-complexity, with a loss of about 60%; at the Mid-Complexity level, they present a further decrease and significantly increase at the High-Complexity level, reaching about 53% of material performance with respect to No-Complexity specimens. The Al-Cu trend shows a loss of 75% at the Low-Complexity level and an increase to about 30% with respect to No-Complexity specimens at the Mid and High-Complexity levels. These trends could lead to the conclusion that it is better, if designers want to introduce complexity into designs, to introduce a high complexity level rather than a low level.

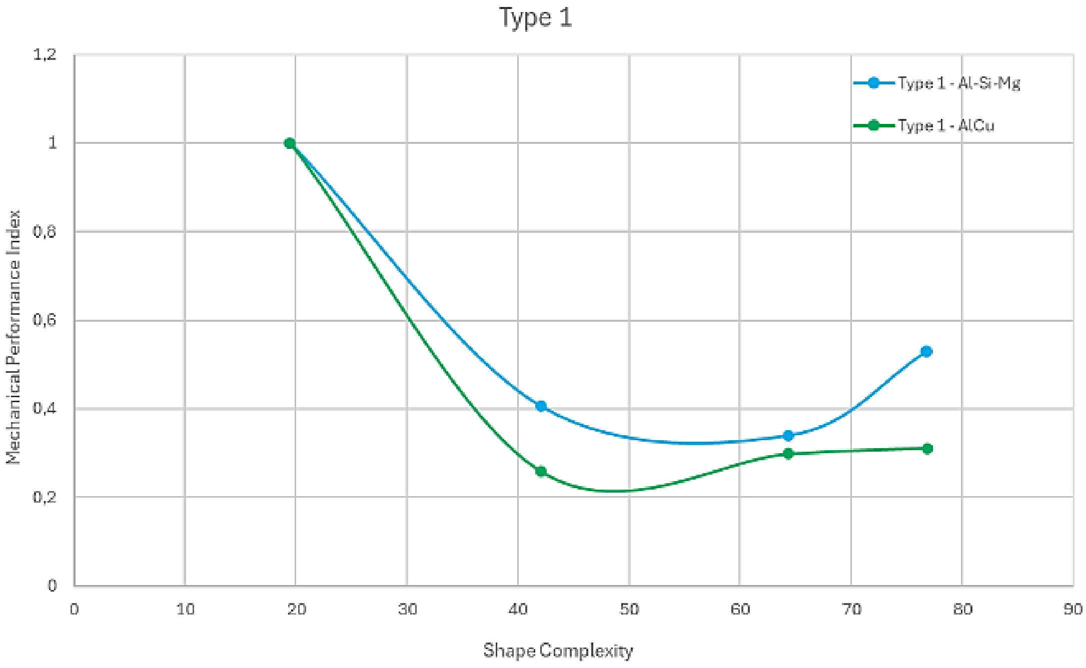

*Figure 44. Trends of MPI as a function of the $SC\_total$ Index.*

For tensile testing, a rod sample is ideal for determining mechanical properties. At the same time, a complex geometry is tested to study how a specific component behaves under load, simulating real-world operating conditions.

Figure 45 summarises the previously presented MPI trends by SCI and highlights the SC level for each specimen type analysed. The graph clearly shows how complexity affects different materials and geometries differently. The effect of complexity on mechanical properties is highly nonlinear. While the variation in complexity of Type 0 specimens is significantly smaller than that of Type 1 specimens, the Type 0 ones exhibit a greater loss in MPI values at the same SC levels. This behaviour may be related to geometries.

Type 0 geometry under tensile test is subjected only to traction behaviour, being made of rods only. On the contrary, Type 1 geometry (designed lattice) undergoes a complex combination of stresses having a complex geometry.

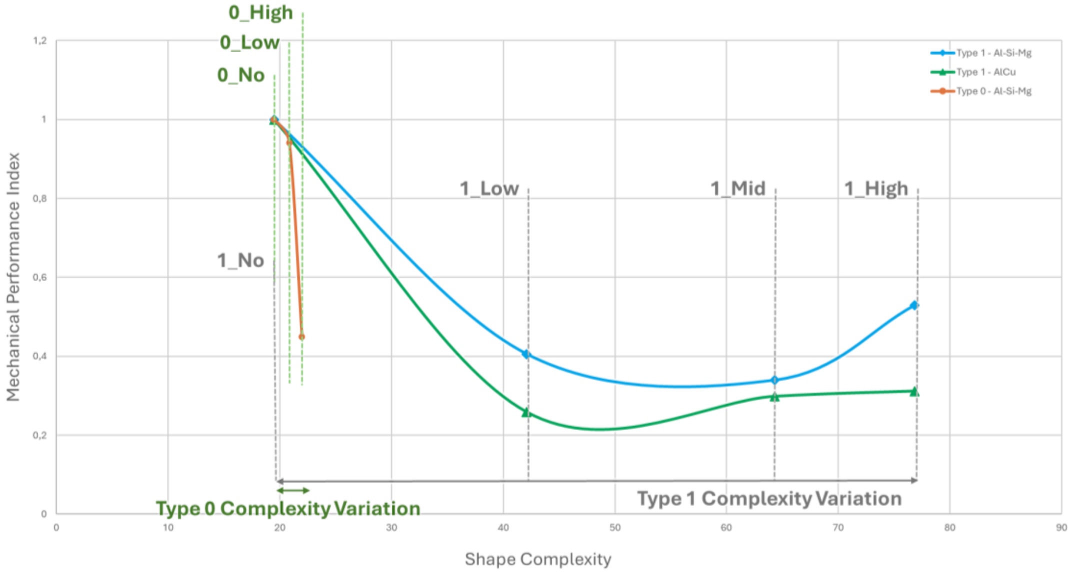

*Figure 45 Type 0 and Type 1 results comparison, highlighting different complexity variations.*

### 3.7.2 Internal Porosity and Shape Complexity

Internal porosity can significantly reduce mechanical performance by creating weak points inside a material. Pores act as stress concentrators, lowering strength, stiffness, and fatigue life. They can also promote crack initiation and growth, leading to earlier failure under load. The larger or more numerous the pores, the more severe the reduction in mechanical properties.

Table 28 reports the values of mean internal porosity for Type 1 metal specimens, including the real cross-section evaluated by removing from CAD cross-sections the percentage values of porosity. Despite the low precision in the realisation of exact geometries for Mid and High-Complexity specimens (as Figure 38 and 39 show), the internal porosity, which plays a crucial role in assessing the part quality, presents significantly lower values. The lattice geometries help in reducing the high thermal gradients between layers, improving quality in terms of internal porosity.

*Table 28. Measured mean internal porosity and real cross-section evaluation.*

| Type 1 | Specimen | CAD Cross Section | Mean Internal porosity % | Real Cross Section |
|---|---|---|---|---|
| Al-Si-Mg | 1_No | 18 | 2,73 | 17,97 |
| | 1_Low | 5,83 | 0,66 | 5,82 |
| | 1_Mid | 7,88 | 0,68 | 7,87 |
| | 1_High | 7,9 | 0,76 | 7,89 |
| Al-Cu | 1_No | 18 | 1,41 | 17,99 |
| | 1_Low | 5,83 | 0,51 | 5,82 |
| | 1_Mid | 7,88 | 0,47 | 7,88 |
| | 1_High | 7,9 | 0,53 | 7,89 |

Figure 46 illustrates the percentage of internal porosity for Type 1 – Al-Si-Mg and Al-Cu as a function of the SC. The Al-Si-Mg curve benefits more than the Al-Cu curve, starting from a higher value of internal porosity and reaching approximately the same values for Low, Mid, and High-Complexity. Analysing this graph, the increment of SC helps in reducing the internal porosity, diminishing part thicknesses, and helping dissipate high thermal gradients that arise in the bulk parts.

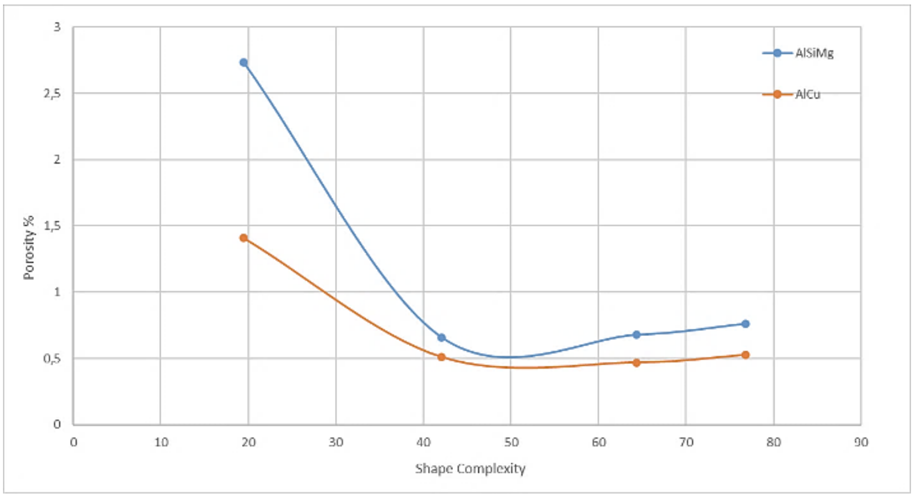

*Figure 46. Porosity trends as a function of the Shape complexity in Type 1 specimens.*

To correlate the results previously discussed with the measured internal porosity and understand the effect of this material quality property, Equation 18 has been formalised. This new MPI, called $MPI_{norm}$, normalises Equation 16, looking for a way to correlate tensile results to the real cross-section. The $MPI_{norm}$ wants to measure how each cross-section mm² contributes to the mechanical performance. Table 29 reports the normalised UTS, YS, E%, and $MPI_{norm}$.

$$\begin{cases} MPI_{norm_i} = w_1 \dfrac{\dfrac{UTS_i}{A_i}}{\dfrac{UTS_{No-Comp}}{A_{No-Comp}}} + w_2 \dfrac{\dfrac{YS_i}{A_i}}{\dfrac{YS_{No-Comp}}{A_{No-Comp}}} + w_3 \dfrac{\dfrac{E_i}{A_i}}{\dfrac{E_{No-Comp}}{A_{No-Comp}}} \\ \displaystyle\sum_{i=1}^{3} w_i = 1 \end{cases} \tag{18}$$

*Table 29. Metal Type 1 tensile test normalised in function of the measured cross-section.*

| **Type 1** | | $UTS_{norm}$ | $YS_{norm}$ | $E\%_{norm}$ | **Shape Complexity** | $MPI_{norm}$ |
|---|---|---|---|---|---|---|
| Al-Si-Mg | 1_No | 18,11 | 0,38 | 0,80 | 19,473 | 1 |
| | 1_Low | 5,75 | 0,72 | 1,85 | 42,072 | 1,25 |
| | 1_Mid | 8,80 | 0,42 | 0,78 | 64,330 | 0,77 |
| | 1_High | 15,36 | 0,69 | 1,01 | 76,831 | 1,21 |
| Al-Cu | 1_No | 16,58 | 0,45 | 1,34 | 19,473 | 1 |
| | 1_Low | 4,71 | 0,23 | 2,72 | 42,072 | 0,80 |
| | 1_Mid | 7,06 | 0,39 | 1,29 | 64,330 | 0,68 |
| | 1_High | 7,74 | 0,49 | 1,03 | 76,831 | 0,71 |

Figure 47 shows the $MPI_{norm}$ trends as a function of the $SC_{total}$ Index. While the Al-Cu curve presents an expected behaviour, with a reduction in performance of circa 20% at Low-Complexity, circa 32% at Mid-Complexity, and 30% at High-Complexity compared to the No-Complexity specimen, the Al-Si-Mg curve presents a complex behaviour. Despite UTS, YS, and E% values being significantly lower than the No-Complexity specimens, when mechanical properties are normalised with respect to the real cross-sections, they reveal oscillating results. For Low-Complexity and High-Complexity $MPI_{norm}$ results being respectively 125% and 120% compared to No-Complexity results, presenting values higher than the No-Complexity samples. $MPI_{norm}$ for Mid-Complexity is 77% of the No-Complexity one. These oscillating results suggest that more investigations are necessary.

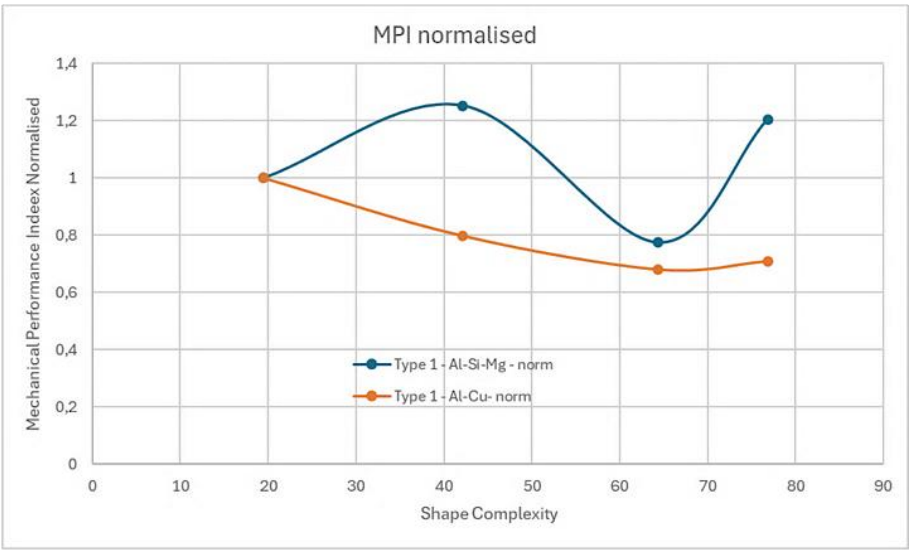

*Figure 47. Trends of $MPI_{norm}$ as a function of the $SC\_total$ Index.*

## 3.8 Conclusions

The overall aims of this thesis chapter are to: establish a correlation between mechanical performance and SC in Additively Manufactured HS-Al Components. Produced samples with Al-Si-Mg and Al-Cu at various levels of SC and analysed tensile strength, and internal porosity have been designed; and increase the sustainability and economic viability of HS-Al components produced via the L-PBF process, providing a sustainable alternative to composite materials for advanced lightweight applications.

This work is a preliminary study to determine how the SC can affect overall part quality and mechanical performance. Findings suggest that further research is needed to establish a definitive correlation between mechanical performance and shape complexity. Two classes of specimens with increasing SC have been designed: the Type 0 with rod structures, and the Type 1 with lattice structures. To identify a unique correlation between SC and mechanical performance, an index has been developed to group the results of tensile tests, considering the UTS, YS, and E%. This index aims to compare specimens with increasing SC to specimens with no complexity. The index has also been normalised with respect to the real specimens' cross-section, obtained from internal porosity measurements, only for metal Type 1 samples, to study the material strength correlated with shape complexity, of each mm² of real cross-section. The results of this work suggest that there might be a direct correlation between L-PBF part quality, measured using the resulting mechanical performance, and its SC. Results seem to suggest that components with no complexity present a higher percentage of internal porosity. Despite the samples with SC showing lower internal porosity, different to our initial assumptions, the same samples proved lower tensile strength. This seems to suggest that SC significantly reduces the tensile strength at parity of the volume of material and independently from the alloy. This might confirm that localised stress concentrations have a key role in affecting the mechanical performance. These results imply that engineers should carefully consider when and how to increase complexity since this might reduce the theoretical performance of materials. The Al-Si-Mg and Al-Cu lattice specimens present a loss in mechanical performance at low and mid complexity but gain it for high complexity. The Al-Cu lattice specimens appear to suffer more than Al-Si-Mg specimens at high complexity, presenting a higher reduction in mechanical performance. Regardless of the complexity of the shape, Al-Cu appears to offer slightly lower tensile strength compared to Al-Si-Mg. This result is quite remarkable given the significant difference in theoretical tensile strength. This might confirm the importance of defects (surface roughness, voids) and shape (complexity, design of the lattice) over intrinsic material properties in defining the mechanical properties of parts, together with a possible general improvement of the parts produced with an optimisation of the process parameters. Therefore, the sustainability and economic viability of complex geometry components realised in metal L-PBF and their adoption as an alternative to composite materials must be further established. The tensile strength of the tested Al-Cu specimens is significantly lower compared to theoretical values, with further decreases in value observed with increased SC. Since the rationale for L-PBF Al components is the exploitation of SC (e.g. lightweight components), future research will need to investigate how to improve the gap between real and theoretical mechanical properties.

# 4 Applications of the Design Optimization methods for L-PBF process

As described in the AM topology optimization methods Section (Section 1.5.2), different design optimization methods, especially based on algorithmic methods, are available to increase part performance, lightweighting, and reducing the number of components for a specific part usage. In this chapter, the thesis examines various design optimization methods as tools to enhance part performance. Some of them have been applied to enhance automotive components such as different connecting rods (1.6 L diesel, 100-cc racing kart, and 2.8 L diesel), and a lower arm of a McPherson suspension for a C-segment passenger car.

### 4.1.1 Connecting Rods

The main mechanism that allows Internal Combustion Engines (ICE) to work is the connecting rod-crank-piston system. This mechanism transforms the translational motion generated by the combustion inside the cylinder into rotary motion (Figure 48). Inertial forces play a fundamental role in the balance of forces and engine efficiency. By making these key parts lighter, it is possible to improve the overall performance of the ICE [229]. The connecting rod is an intermediary component connecting the piston and the crankshaft. Its main role involves transferring the push-pull action from the piston pin to the crankpin, converting the piston's reciprocating linear movement into the rotary motion of the crankshaft. This conventional design of the connecting rod is commonly observed within ICE [230]. The connecting rod is constantly subjected to alternating tension and compression stresses which vary in magnitude and direction during its operation. When the dimensions of the connecting rod are too large, it not only leads to the wastage of materials but also compromises the equilibrium of system motion, resulting in excessive noise during operation. As a result, the effectiveness and dependability of the connecting rod structure directly impact the smooth functioning of the ICE [231].

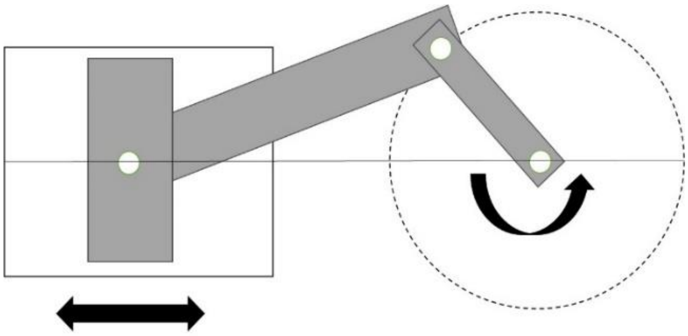

*Figure 48. Piston-Connecting Rod- Crank System.*

A connecting rod is a typical application of a mechanical component under load. In working conditions, the connecting rod moves in roto-translational cyclical motion and is subjected to fatigue load. The sizing of connecting rods is usually done by considering quasi-static loads in the moments in which the component is subjected to the highest loads, by calculating the maximum values. In particular, the moments to analyse are the compression load at the top dead centre after the combustion, the inertial load at the moment in which the crankshaft and the connecting rod form a 90° angle, and all the top and bottom dead centre points in which the contact point between the connecting rod and the piston pin or the crankshaft changes (in those last instances the loads are usually lower but is standard practice to check them due to shocks between shaft and hole).

#### *4.1.1.1.1 Topology Optimisation*

Figure 49 shows the proposed approach for applying a TO, combined with an AM printability check to validate the geometry obtained, to a mechanical component.

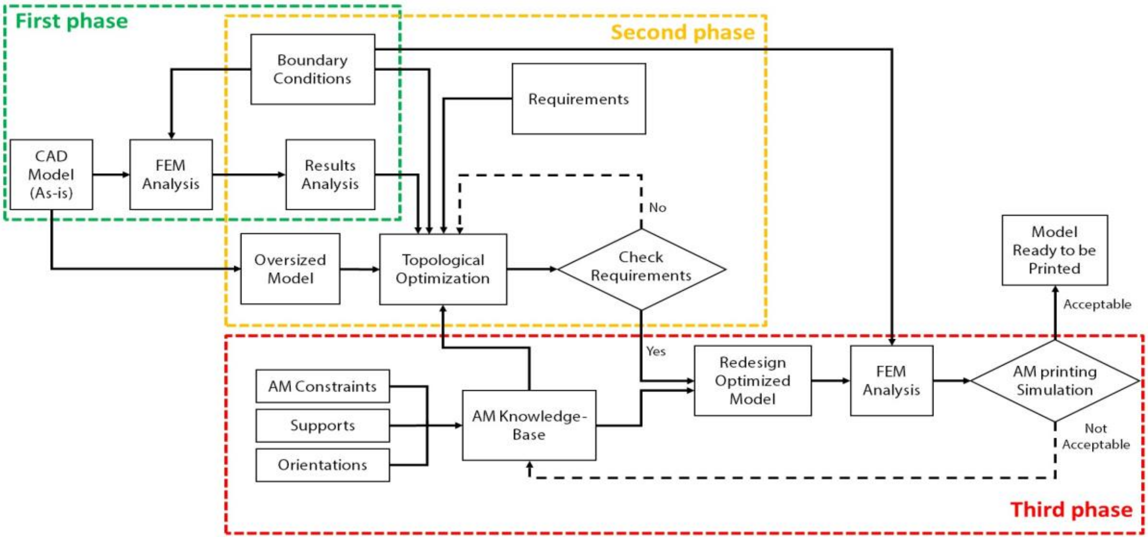

*Figure 49. Proposed approach for the TO usage in the AM field.*

The first phase begins with the CAD modelling (As-is model). This can be obtained through different techniques, such as Reverse Engineering. The original CAD model is imported into a Finite Element Method (FEM) system to study its mechanical behaviour under the boundary conditions. The second phase concerns the optimization of the geometry using the TO approach with an oversized CAD model as input. An oversized CAD model is used to limit the influence of the input model on the TO computation. To correctly apply the TO method, it is necessary to carefully choose the objective functions that drive the process, the constraints, and the geometric constraints (such as symmetries). This can be a long and iterative process. Moreover, the boundary conditions must be the same as the previous FEM analysis. The third phase regards the final CAD modelling, starting from the resulting geometry of the TO analysis. The objective is to arrive at a component that can be 3D printed. Therefore, it is necessary to consider the AM process constraints and evaluate the best trade-off between orientation and support structures. During this phase, the optimized model is redesigned considering all these factors. The FEM analysis is applied with the same boundary conditions to validate the final model. Finally, the AM printing simulation is applied to evaluate stress and deformation during and after manufacturing. If the result is acceptable, the part is ready to be printed; otherwise, something must be changed.

#### 4.1.1.1.1.1 Test Case

The proposed method has been applied to optimize the connecting rod of a 1.6-liter automotive diesel ICE, reducing the final weight, and considering manufacturing with the AM process. CAD software was used for the geometrical model of the connecting rod, and two different FEM tools were used for the structural simulations and the 3D printing analysis.

The starting CAD model (As-is) was realized by reproducing the geometry of the real component (Figure 50a). An oversized CAD model (Figure 50b) was used as input geometry for the TO phase, considering a greater volume to not affect the optimization result. The oversized model considers the limited operative dimensions of the analysed Piston-Connecting Rod-Crank system. This procedure allows the TO algorithm to be free as much as possible to remove material where it isn't necessary.

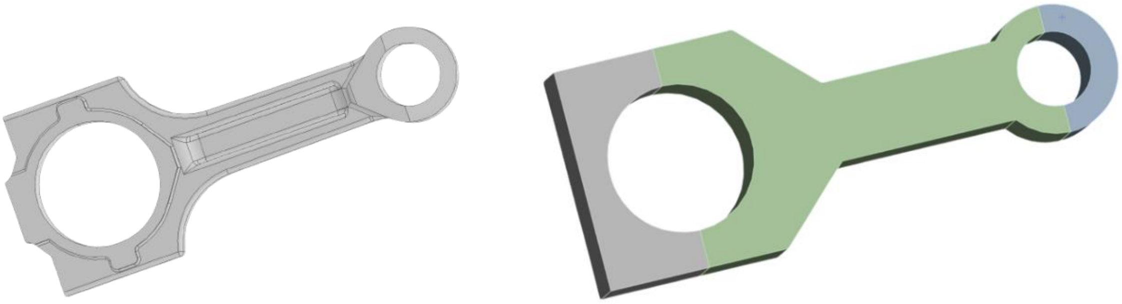
(a) (b)

*Figure 50. (a) CAD Model (As-is); (b) Oversized CAD Model used for the TO analysis.*

The loads acting on a connecting rod vary over time in direction and intensity. During the entire cycle, the connecting rod receives various tensile and compressive stresses. Five loading conditions (Table 30) were applied to the model to validate the component. To calculate the maximum compressive force, applied in the small end and the large one, a pressure of about 50 bar was considered in the combustion chamber at the top dead centre. On the other hand, the maximum tensile force was calculated considering the geometry of the Piston-Connecting Rod-Crank system and the maximum angular velocity. The tensile force was applied to the small and the large ends. A fifth load condition considers the case of inertia bending. This case condition is verified when the angle between the connecting rod and the crank is 90°. In this load case, the bending moment due to inertia forces is about $52{,}1\ Nm\ (M_{max})$ and it is combined with a residual compression force of $\mathrm{F_r} = 8000\ \mathrm{N}$, directed along the center of the crank rotation.

*Table 30. Load cases of the ICE connecting rod.*

| ID | Case | Applied loads |
|---|---|---|
| 1 | Compression force at small end | $\mathrm{F_{max}} = 25000\ \mathrm{N}$ |
| 2 | Tensile force at small end | $\mathrm{F}_t = 8842\ \mathrm{N}$ |
| 3 | Compression force at large end | $\mathrm{F_{max}} = 25000\ \mathrm{N}$ |
| 4 | Tensile force at large end | $\mathrm{F}_t = 8842\ \mathrm{N}$ |
| 5 | Inertia bending | $\mathrm{F_r} = 8000\ N;\ M_{max} = 52{,}1\ Nm$ |

Figure 51 shows the stress distribution for the load case ID 4, evaluated by FEM tools. This is the worst-case scenario between the five load cases considering the maximum Von-Mises Stress.

The most stressed area is on the small end. Table 31 shows the results of the FEM analysis for each load case.

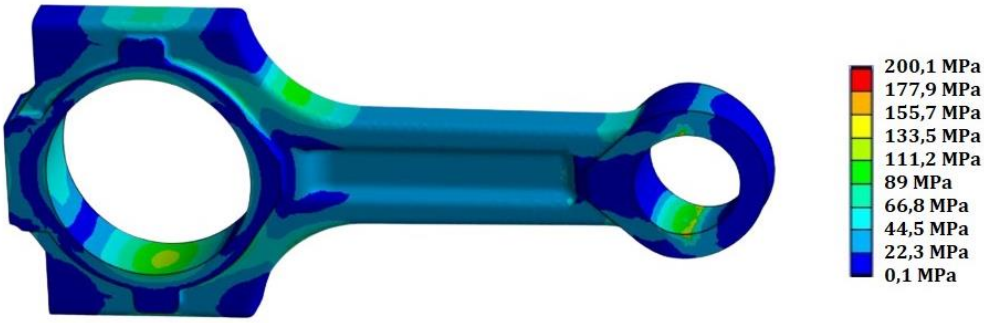

*Figure 51. Stress distribution report for the ID 4 case (worst-case scenario).*

*Table 31. Results of FEM Analysis.*

| Load ID | Equivalent von-Mises Stress [MPa] | Displacement [mm] |
|---|---|---|
| 1 | 165,8 | 0,045 |
| 2 | 177,1 | 0,049 |
| 3 | 175,9 | 0,061 |
| 4 | 200,1 | 0,062 |
| 5 | 41,6 | 0,006 |

Moreover, a modal analysis was performed to check the first natural frequency of the connecting rod. The first six modes of vibration are shown in Table 32.

*Table 32. Modes of vibration.*

| **Mode** | 1 | 2 | 3 | 4 | 5 | 6 |
|---|---|---|---|---|---|---|
| **Frequency [Hz]** | 648,74 | 1555,1 | 2409,1 | 4116,4 | 6415,5 | 9116,8 |

The SIMP method was used for the TO analysis. The optimization begins by defining the Design and Non-Design zones, which are the areas where the algorithm can act or not act due to coupling with other parts of the assembly. The selection of the design and non-design zones is extremely relevant for the success of the optimization in terms of the 3D printability of the component. This analysis also requires boundary conditions, optimization constraints, and optimization objectives. To achieve a lightweight and printable component the Ti6Al4V titanium alloy was chosen. The same loads applied to the FEM (As-is) analysis have been used. The chosen objective function is the minimization of the global compliance of the component due to all loads. The constraints chosen can be divided into two classes, the first one concerns the design constraints such as the symmetries of the connecting rod. The second regards the functional constraints related to stress and mass. The maximum stress was limited to 500 MPa, and the percentage of the final mass was between 15% and 20% of the input mode (oversized model). Figure 52 shows the result of the TO process after 56 iterations.

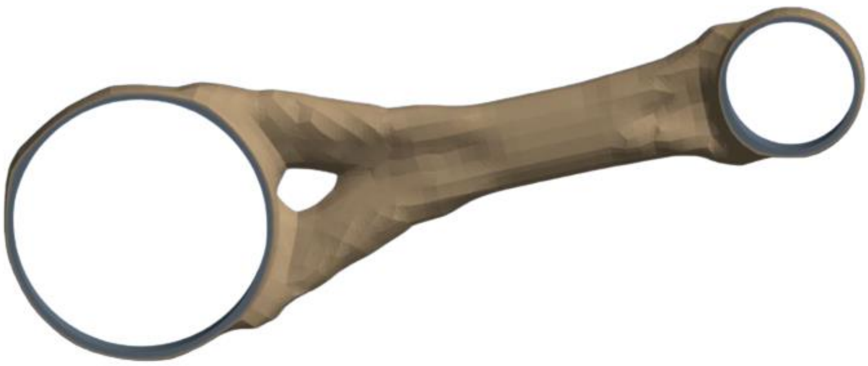

*Figure 52. Topology Optimisation Result.*

Following the proposed method to realize a lightweight component that can be easily printed, it is necessary to consider the AM knowledge base during the redesign phase. Considering all the AM parameters and constraints, and the geometry obtained from the TO analysis, it is now possible to obtain a lightened component. Figure 53a reports the result of the final redesign phase. To validate this optimized geometry is necessary to perform again the FEM Analysis. The previous boundary conditions were used, and the result of the worst load case (Load case 2) is shown in Figure 53b. Table 33 shows the results of the FEM analysis for each single load case. Table 34 shows the modes of vibration of the new connecting rod.

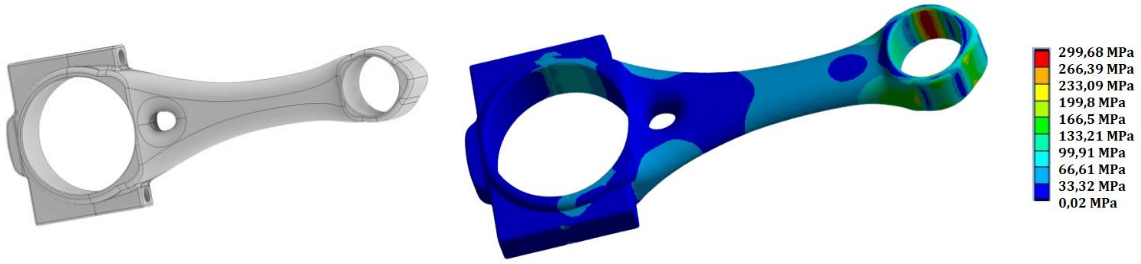

(a) (b)

*Figure 53. (a) Result of the redesign phase; (b) Stress distribution of the worst case (Load case 2).*

*Table 33. Results of FEM Analysis of the optimized geometry.*

| Load ID | Equivalent von-Mises Stress [MPa] |
|---|---|
| 1 | 156,2 |
| 2 | 299,7 |
| 3 | 111,5 |
| 4 | 239,5 |
| 5 | 39,8 |

*Table 34. Modes of vibration of the optimized geometry.*

| Mode | 1 | 2 | 3 | 4 | 5 | 6 |
|---|---|---|---|---|---|---|
| **Frequency [Hz]** | 744,72 | 1421,2 | 3930,1 | 4305,4 | 5400,9 | 8878,6 |

Figure 54 shows the results of the 3D printing simulation, reporting displacement (Figure 54a) and stress distribution (Figure 54b). The values of stress and deformation on the part can be considered acceptable. The connecting rod is now ready to be printed.

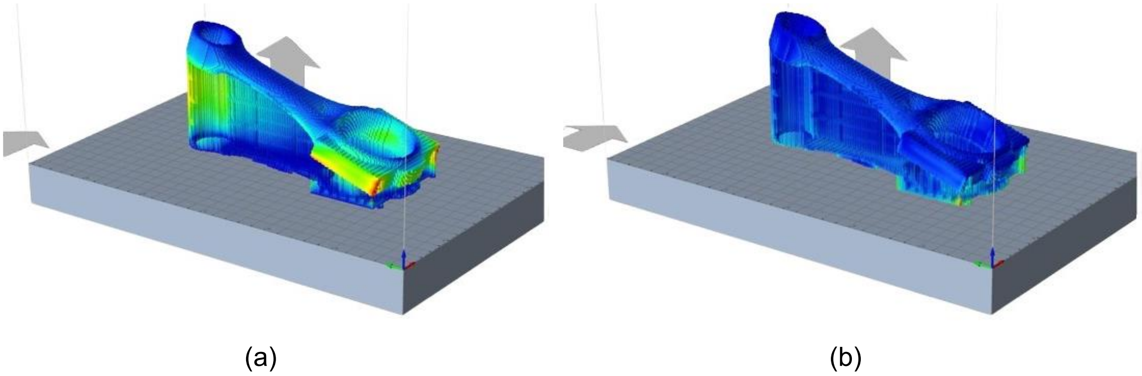
(a)
(b)

*Figure 54. (a) Displacement and (b) Von-Mises Stress trends obtained with the printing simulation of the optimized Connecting Rod.*

Table 35 shows how much the optimization of the geometry, and the change of the material affects the final weight of the component. The TO process and the use of a performing Titanium alloy (Ti-6AL-4V) reduce the volume by 21.8% and the overall weight of the connecting rod by 56,1%.

*Table 35. Volume and weight comparison.*

| **Model** | **Volume [$mm^3$]** | **Weight [Kg]** |
|---|---|---|
| As-is | 85.370 | 0,670 |
| Redesigned | 66775 | 0,294 |

#### 4.1.1.2 Lattice Structures

Figure 55 describes the proposed method to achieve the lightweight design of a kart connecting rod to be realized with the L-PBF techniques, starting from the geometry of a reference model. This method can be divided into three phases.

The first phase concerns the FEM analysis of the AS-IS CAD model. This CAD model can be obtained from existing models or by the 3D scanning of physical components. This simulation phase includes the knowledge of the employed materials and the boundary conditions. The results are useful for understanding the mechanical behaviour of the reference model and for evaluating the limitations of future optimizations. The second phase involves the use of lattice structures to reduce the weight of the component and the amount of the material used. To apply these structures, the designer must define several parameters, including material, the portion of volume to be replaced with lattice structures, type and thickness of the unit cell, cell distribution (uniform density or based on the FEM AS-IS analysis), etc. The third phase concerns the printability evaluation of the lightweight part, using AM simulations. The use of these simulations can help the designer identify the presence of geometric problems or problems that may arise during the 3D printing process. These problems can be due to the printing configuration such as the choice of orientation, supports, overhang limit angle, support types, etc. The proposed method considers two check conditions to evaluate whether to continue or to go back and modify geometries or parameters. The evaluation of these conditions is related to the designer's know-how and the results of the simulations.

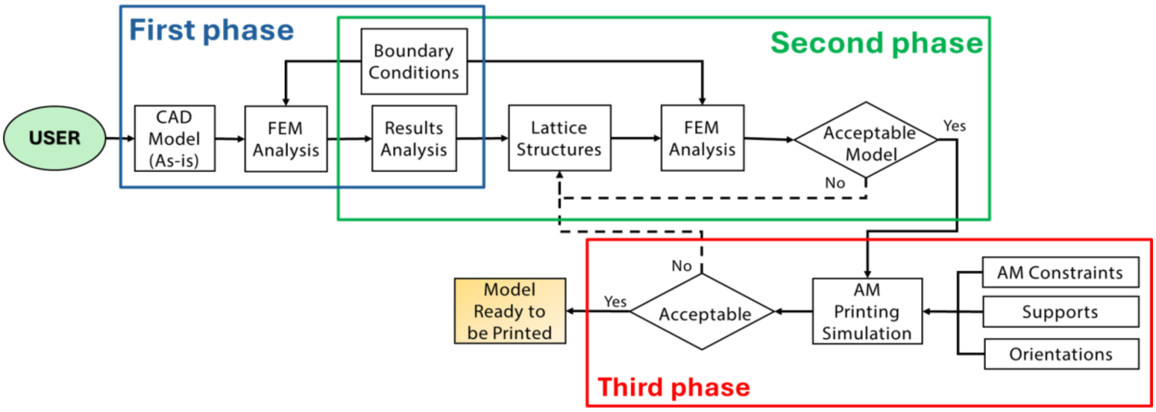

*Figure 55. Proposed Approach for the Lattice Application in the AM field.*

#### *4.1.1.2.1.1 Test Case*

The proposed method has been applied to lightweight the connecting rod of a 100-cc racing kart, considering the L-PBF use as the manufacturing process. Engine efficiency and force balance are significantly influenced by inertial forces. It is feasible to increase the ICE's overall performance by making components lighter [229] while providing the same mechanical behaviour under operation. Therefore, a racing connecting rod was chosen to validate the proposed method.

The software nTop was used for the geometrical modelling of the connecting rod, including the application of the lattice structure, and for the relative FEM analysis under the analysed boundary conditions. The software Altair® Inspire$^{TM}$ was used for simulating the L-PBF process of the optimized connecting rod.

Table 36 shows the main characteristics of the engine related to the analysed connecting rod. The direction and intensity of the loads acting on a connecting rod change with time. Five loading conditions were applied to the kart connecting rod to evaluate the structural performance and compare the results achieved with different CAD models (Figure 56).

*Table 36. Characteristics of the 100-cc Kart racing engine.*

| Description | Value | Description | Value |
|---|---|---|---|
| Displacement | 100 cc | Compression ratio | 10.5: 1 |
| Stroke | 2 | Maximum Power | 20 Hp at 9800 rpm |
| Bore | 48.20 mm | Maximum Torque | 1.4 Kgm at 9600 rpm |
| Stroke | 54 mm | Maximum Speed | 16000 rpm |
| Connecting rod c-to-c Distance | 102 mm | | |

A pressure of 30 bar was considered in the combustion chamber, at the top in the dead centre, to calculate the compressive force $F_c$. A pressure of about 1.2 bar was considered to estimate the residual force $F_r$, which is directed along the centre of the crank rotation.

ID 1) Compression force at small end
$F_c = 5474$ N

ID 2) Tensile force at small end
Ft = 1941 N

ID 3) Compression force at large end
Fc = 5474 N

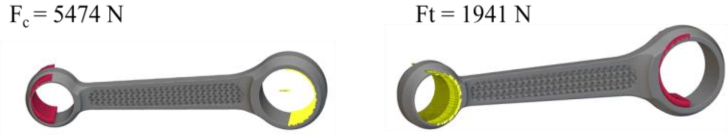

ID 4) Tensile force at large end
Ft = 1941 N

ID 5) Inertia Bending
$F_r = 220$ N; $M_f = 22$ Nm

*Figure 56. Load cases applied to the CAD model.*

Figure 57 shows the reference CAD model and the Equivalent von Mises Stress distribution obtained simulating the load case ID 1. For the simulation of the AS-IS model, the material considered was the 36NiCrMo4 steel, which is a steel used for connecting rods due to its good fatigue strength. The overall weight of the reference model is 0.086 Kg. All the described load conditions have been applied to the simulation model; the main results of the FEM analysis are reported in Table 37.

*Figure 57. a) Starting CAD model (AS-IS); b) FEM analysis of the CAD model (AS-IS): Load case ID 1, Von Mises Stress distribution.*

*Table 37. Results of the FEM analysis for the AS-IS CAD model.*

| Load ID | Equivalent Von Mises Stress [MPa] | Displacement [mm] |
|---|---|---|
| 1 | 200.9 | 0.042 |
| 2 | 124.5 | 0.023 |
| 3 | 200.9 | 0.042 |
| 4 | 124.5 | 0.023 |
| 5 | 207.1 | 0.092 |

The application of lattice structures allows the components to be lightened by replacing the full volume of material with a repetition of unit cells. For this case study the gyroid cell type was chosen to fill the rod of the component, using a unit cell size of 2.5 mm x 2.5 mm x 2.5 mm and a thickness value of 0.4 mm. The selection of the cell type, cell dimension, and thickness has been carried out following a Design of Experiments (DoE) approach, various tests have been conducted varying the geometrical parameters and evaluating results from FEM simulations.

Figure 58 shows the redesigned CAD model with the applications of the gyroid cells. The material used is the Ti6AL4V, which is a titanium alloy used in 3D printing. Combining lattice structure with gyroid and titanium alloy material, the model of the connecting rod achieved a final weight of 0.044 Kg.

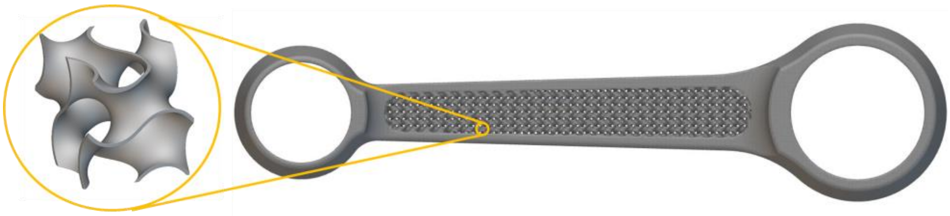

*Figure 58. Redesigned geometry of connecting rod, using gyroid unit cells for the lattice structure.*

The structural behaviour of the redesigned model was evaluated by FEM analysis, and the results are reported in Table 38. The computational time related to the reported FEM analysis was about 1 hour, using a computer with RAM 64 GB, CPU 13th generation INTEL i7 16 core, and GPU NVIDIA RTX 4060.

The presence of a lattice structure increased the stress distribution and displacement. However, Ti6AL4V allows higher stress values to be achieved. Figure 59 shows the Equivalent von Mises Stress distribution for the load case ID 1. While the yield stress for Ti6AL4V can arrive at 1000 MPa, the 36NiCrMo4 material is limited to 800 MPa.

*Table 38. FEM analysis results of the redesigned connecting rod with gyroid cells.*

| **Load ID** | **Equivalent Von Mises Stress [MPa]** | **Displacement [mm]** |
|---|---|---|
| 1 | 419.9 | 0.136 |
| 2 | 133.2 | 0.063 |
| 3 | 425.5 | 0.138 |
| 4 | 133.9 | 0.063 |
| 5 | 282.2 | 0.173 |

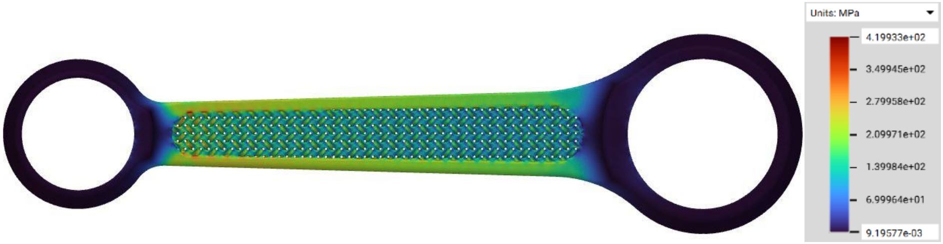

*Figure 59. FEM analysis of the latticed Connecting Rod: Load case ID 1, Von Mises Stress field.*

Analysing the AM job, Figure 60 shows some of the possible solutions studied for the part orientation to minimize the deformations in the printing phase (Figure 60a), to minimize the printing time (Figure 60b), to minimize the printing time while avoiding side supports on the gyroid cells (Figure 60c). This last configuration was here considered in the part orientation.

Table 39 highlights the setup used for the AM simulations. Figure 61 reports the displacement after the 3D printing phase, calculated through the simulation of the AM process. Table 40 compares the starting model (AS-IS) with the optimized one (Redesigned Connecting Rod) in terms of weight. With the use of a high-performance and low-density titanium alloy suitable for the L-PBF process, a weight reduction close to 50% was achieved.

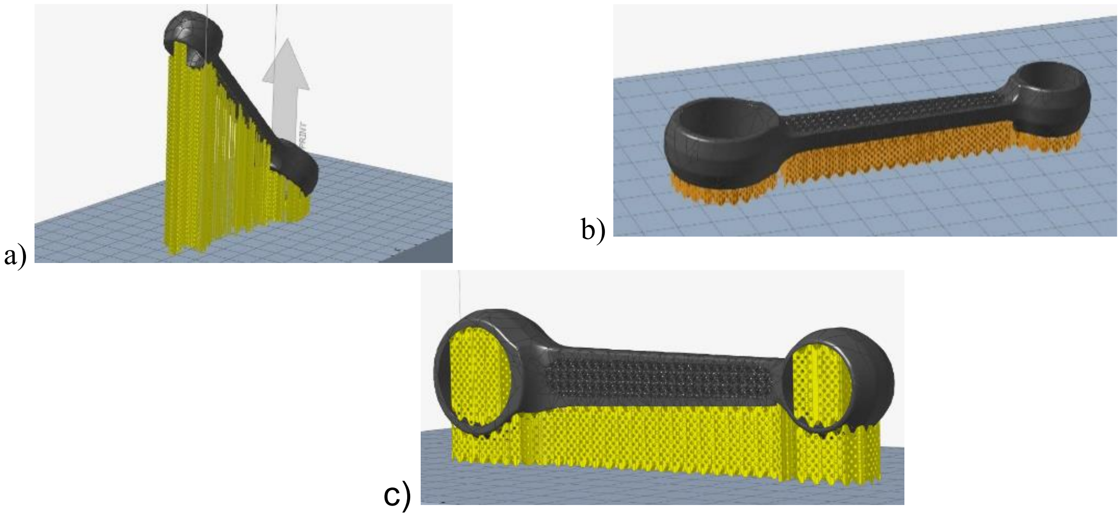

*Figure 60. Possible orientations for the 3D printing phase: a) minimum deformation setup; b) minimum deformation avoiding supports on cells setup; c) minimum printing time avoiding supports on cells setup.*

*Table 39. AM simulation Set-Up.*

| Parameter | Value | Parameter | Value |
|---|---|---|---|
| Build volume | 300 mm x 300 mm x 250 mm | Layer Thickness | 0.040 mm |
| Orientation strategy | Minimum printing time avoiding supports on gyroid cells | Deformation (calibration) | 0.15 mm |
| Distance from plate | 5 mm | Voxel Mesh average thickness | 1 mm |
| Support type | Block support | Simulation method | Inherent strain |
| Support thickness | 0.2 mm | | |

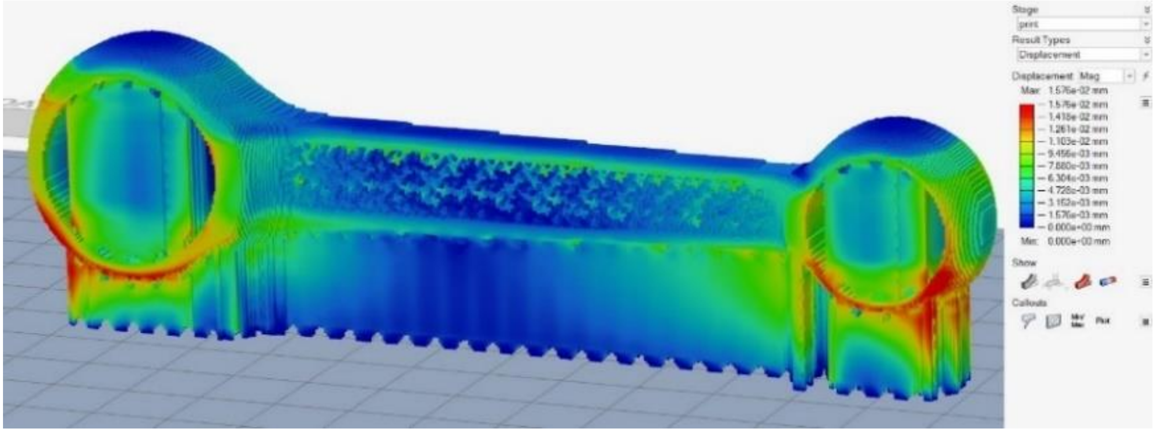

Stage: print

Result Types: Displacement

Displacement Mag

*Figure 61. AM simulation: the displacement during the printing process.*

*Table 40. Comparison between AS-IS and the Redesigned model.*

| Model | Material | Lattice Unit Cell | Weight |
|---|---|---|---|
| Reference model (AS-IS) | 36NiCrMo4 | - | 86 g |
| Redesigned Connecting Rod | Ti6AL4V | Gyroid | 44 g |

### *4.1.1.3* Parametric Optimisation trough Response Surfaces and Genetic Algorithm*s*

Figure 62 shows the applied flowchart used to identify the optimal solution for a lightweight design of a diesel ICE connecting rod. The proposed method can be divided into six sub-sections. The first step involves the CAD modelling of the connecting rod with the introduction of the TPMS lattice structures; the second step regards the definition of the DoE to explore possible combinations of solutions of cell parameters for the LS; the third step studies these experiments realising an FEM analysis of all the tests; the fourth step builds a surrogate model (Response Surface Method (RSM)) to approximate the simulation results in all the constrained solution space; the fifth step allows the solution space to be explored in a better resolution with the use of a genetic algorithm; the last step finds the Pareto front of the optimal solutions from which the designer can choice the final design in accordance with the goals of the study. Each step uses data from the previous one. For example, GA uses only the results of RSMs, trained with the results from the FEM analysis. GA is not directly connected with FEM analysis.

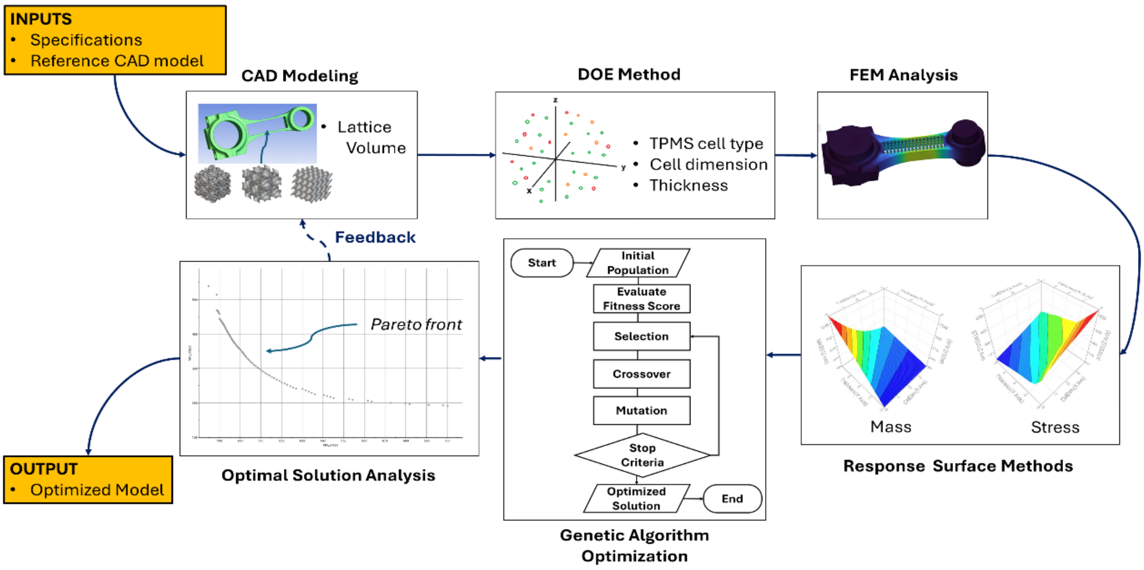

*Figure 62. Proposed approach to combine the Lattice application in the AM field with DoE methods used to construct a RSM and apply GA to select the best cell for the specific application.*

#### *4.1.1.3.1.1 Test case*

Figure 63 shows the CAD models realised to carry on the case study; Figure 63b describes the CAD model with the parametric cavity to insert the TPMS Lattice Structures (LS). The cavity has been designed parametric with a parallelepiped shape, limiting the minimum thickness of the residual material in the rod. Figure 63a shows the upper bound volume considered for the optimisation. The parallelepiped void is therefore infilled with cubic TPMS parametric LS, varying lattice type between Diamond, Gyroid, and SplitP, varying wall cell thickness, and varying cell dimensions. Only these three parameters are considered as variables for the case study.

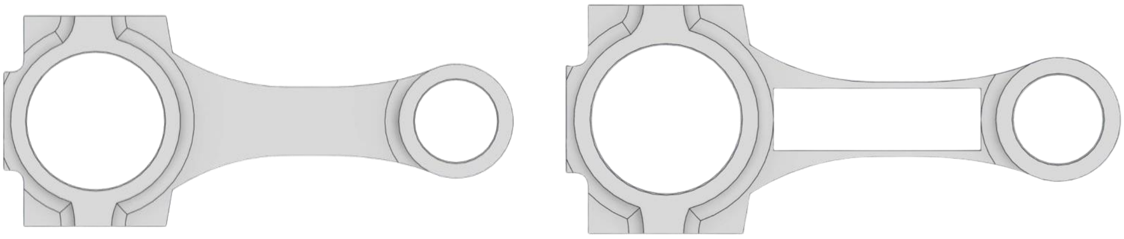

(a) (b)

*Figure 63. (a) The initial CAD model referred to the real connecting rod (b) CAD model with parametric volume for TPMS lattice structures.*

To explore the effect of possible parameter combinations, a virtual Design of Experiments (DoE) is defined. The DoE expects to assign a singular combination of parameters to each element. Starting from the 3-dimensional continue design space in which the parameters may vary, the elements are excluded by considering technological, practical, and geometrical constraints. This method allows the consideration of all the available design solutions, from which a sample of solutions is selected and analysed. The chosen criteria for sampling the solution space allow it to be divided into equidistant intervals; criteria and constraints for sampling are listed in Table 41.

*Table 41. Criteria and constraints for DoE sampling.*

| **Parameter** | **Constraint/Range** | | **Step** | **Note** |
|---|---|---|---|---|
| Cell type | Diamond | | - | - |
| | Gyroid | | - | - |
| | SplitP | | - | - |
| Cell dimension | < 18 mm | | 1,5 mm | Lower than cavity dimension |
| | > 3 mm | | | Difficult to be printed |
| Wall thickness | > 0.5 mm | | 0,5 mm | L-PBF Technological limit |
| Cell dimension/ Wall Thickness | < 20 | | - | Avoid buckling of slim elements |
| | Diamond | > 2,8 | - | Allow powder removal |
| | Gyroid | > 2,2 | - | Allow powder removal |
| | SplitP | > 4 | - | Allow powder removal |

Specifications and boundary conditions have been applied to the starting CAD model to understand the mechanical behaviour of the real component under its operating conditions. Then, the results of this analysis have been used as benchmarks to confront the following connecting rod mechanical behaviour.

Boundary conditions used to simulate the mechanical behaviour of the connecting rod through FEM analysis reflect the heaviest load on the connecting rod during its operating conditions, corresponding to the compression after the combustion phase. Bending and traction loads have been checked, resulting in less stress. Equation 19 describes the compressive force applied on a pin in the small end, using as maximum pressure a value of $P_{max} = 50\ \mathrm{bar}$, and a bore of $d = 94\ \mathrm{mm}$. To simulate the presence of the crankshaft, a fixed support constraint is applied on a pin in the big end. Figure 64 shows FEM analysis of the initial connecting rod used to identify the lower value of the possible stress, and FEM analysis of the upper value of the possible stress.

$$F = A \cdot P_{max} = \frac{\pi d^2}{4} \cdot P_{max} = 34681{,}3\ N \cong 35000\ N \tag{19}$$

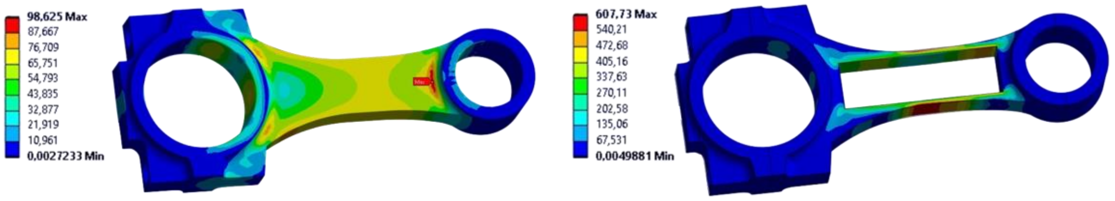

(a) (b)

*Figure 64. (a) FEM analysis of the initial connecting rod used to identify the lower value of the possible stress; (b) FEM analysis of the upper value of the possible stress.*

The LS infill procedure is realised with CAD/CAE software nTop [232]. Parameters from the DoE elements (cell type, cell dimensions, and wall thickness) are sent to nTop through a .csv file created and edited using Python code [233, 234]. Simulation results from nTop (a .csv file) are then analysed to find the von Mises maximum stress value and its coordinates through a second Python code that realises a dataset by updating the DoE starting file with results from simulations. A second set of nTop files, through Python, updates the .csv file with the mass of the connecting rod that corresponds to the DoE elements studied. Figure 65 describes the process of building the dataset.

*Figure 65. Workflow to update the dataset.*

The simulation of the mechanical behaviour of the LS can be realised by meshing all the domains as they are or using homogenisation techniques that model the LS behaviour, define a material with equivalent properties, and substitute the LS with a bulk volume with these material properties [235]. This method allows the creation of an equivalent model that is fast to be simulated without considering intensification stress factors. Figure 66 compares the classical FEM analysis (Figures 66a and 66b) with the Homogenization method (Figures 66c and 66d) of the DoE element previously described.

Due to the excessive underestimation of maximum stress in the homogenisation method, the classical FEM analysis has been considered valid results for the following stages of the approach. Moreover, the classical method may introduce higher values for the maximum stress due to meshing issues. To resolve this issue, mesh sizing could be reduced, increasing computational cost.

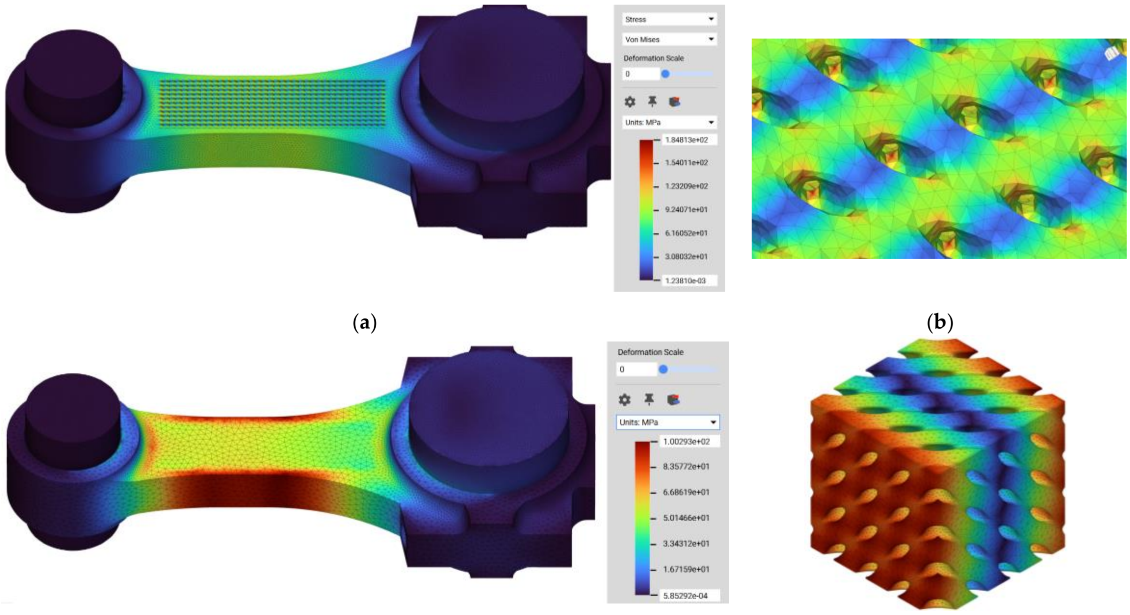

(**a**) (**b**)

(**c**) (**d**)

*Figure 66. Diamond cell (wall thickness: 1,5 mm; cell dimension: 4,5 mm): (a) Classical FEM analysis; (b) Classical FEM analysis detail of the cell; (c) Homogenization Method analysis; (d) Homogenization Method analysis detail of tensile test on the cells.*

At the end of the DoE, the data from the FEM simulations updates the .csv file. In this case study, the data analysis is conducted using the optimisation modeFRONTIER [236] by the company ESTECO and by converting the .csv file into a .xlsx file, which can be read by the program. Once the inputs, outputs, and objectives of the study are defined, the software uses different algorithms to construct RSMs. Since the calculations of the RSM do not require much computational effort, the RSM calculation process is done with every algorithm supported by the software (including Gaussian models, ML models, and genetic models) and is then chosen to analyse the data coming from the algorithm which model best fits the dataset. By comparing statistical metrics from the RSM generation, it is evident that Mass RSMs were all very accurate and Stress RSMs were less accurate (as shown in Table 42).

*Table 42. Accuracy parameters of best RSM used for training the GA.*

| **Cell Type** | **Response** | **RSM** | **MAE** | **MRE** | **$R^2$** |
|---|---|---|---|---|---|
| Diamond | Mass | Gaussian Process [237] | 0,4 g | 0,0006 | 0,99 |
| | Stress | Neural Network [238] | 17,3 MPa | 0,06 | 0,87 |
| Gyroid | Mass | Gaussian Process | 0,07 g | 0,0002 | 0,99 |
| | Stress | H2O AutoML [239] | 7 MPa | 0,02 | 0,91 |
| SplitP | Mass | Gaussian Process | 0,12 g | 0,0002 | 0,99 |
| | Stress | H2O AutoML | 21,4 MPa | 0,07 | 0,84 |

This can be attributed to stress concentration phenomena or meshing imperfections. RSM model files are then saved and can provide an account of input-output correlation on a continued domain of the input parameters. An example of RSM results of the method is reported in Figure 67.

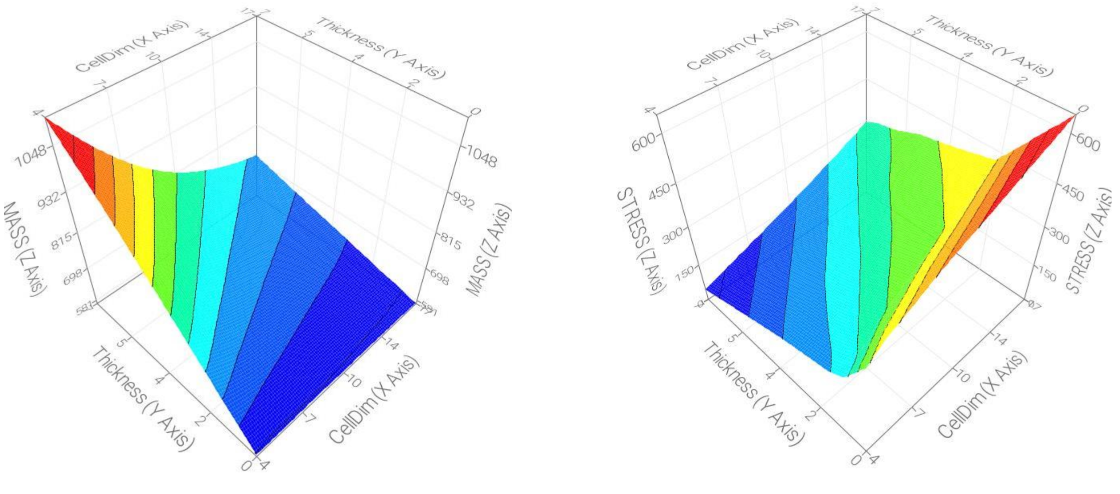

(**a**) (**b**)

*Figure 67. Surrogate models for Gyroid cell type: (a) gaussian - Mass (b) H2O AutoML – Stress.*

The optimisation process begins with analysing the RSM curves for mass and stress. These trained RSMs in the continuous domain are used to identify a discrete domain, allowing the selection of real design parameters. While possible solutions can be extracted directly from the RSM results, in this case study, the software modeFRONTIER was used to apply the Genetic Algorithm (MOGA-II) to find optimal solutions for the defined objectives efficiently. The input ranges of the algorithm are the same as the DoE. The number of evaluations for the MOGA-II is set at 3000 evaluations to correctly identify the Pareto front by finding enough points of the front. The objective functions that calculate the fitness score are based on the overall mass minimisation and maximum stress minimisation. This set of objective functions follows the criteria of conflicting goals necessary to obtain coherent results.

The optimisation process leads to the Pareto Optimum solutions highlighted in Figure 68. The Pareto Optimum solutions for each cell type are extracted from this dataset. To find a singular design choice in multi-objective optimisation, the designer often transforms an objective into a constraint. This allows us to lessen the variables to consider and make clearer choices. In this instance, the stress objective has been transformed into a constraint. The design choice for each cell type is the lighter one that does not reach 300 MPa of stress. This may be represented with a horizontal line that separates the feasible results from the unfeasible ones.

Table 43 shows the selected result for each cell type, from which the cell type Gyroid leads to a better lightweight. This step completes the case study, identifying the optimal design of lattice structure parameters and the cell type that guarantees lower weight by imposing a stress limit. The design choice is the cell type Gyroid with a wall thickness of 0,5 mm (corresponding to the L-PBF technological limit) and a cell dimension of 4,3 mm.

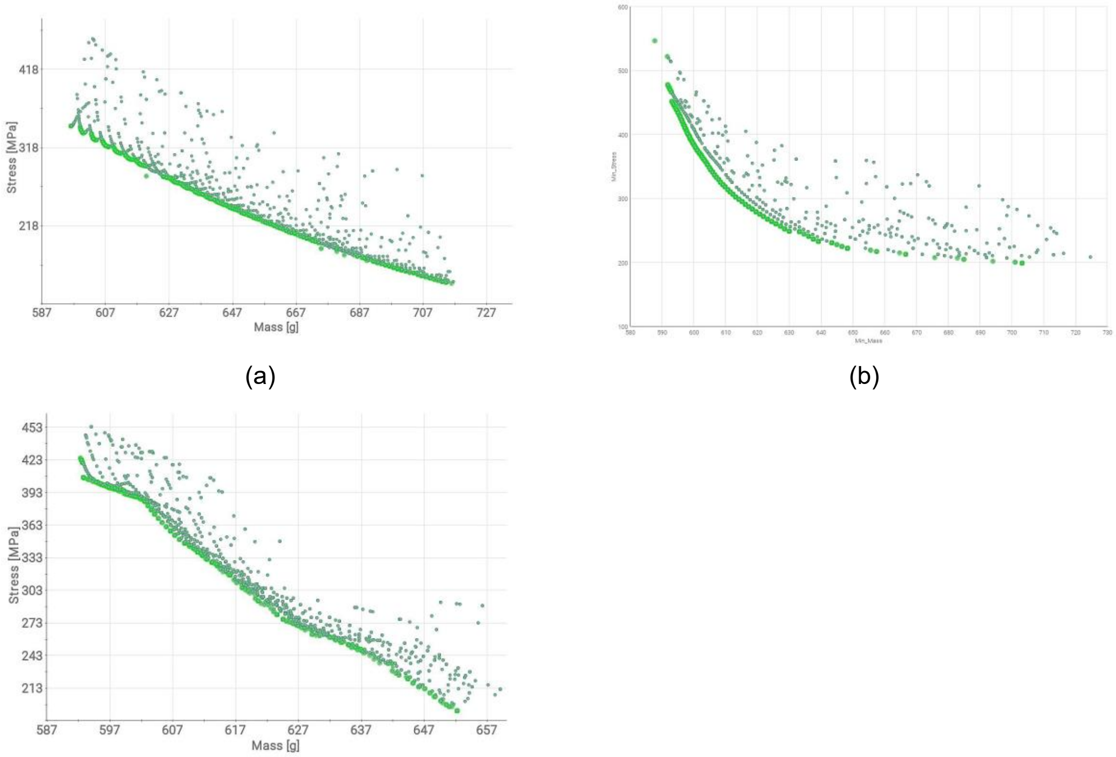

(a)

(b)

(c)

*Figure 68. Pareto Fronts: (a) Diamond, (b) Gyroid, (c) SplitP.*

*Table 43. Results of the optimal solution of the genetic algorithm for each cell type.*

| Cell type | ID | Cell dimension [mm] | Wall thickness [mm] | RSM mass [g] | RSM Stress [MPa] |
|---|---|---|---|---|---|
| SplitP | 355 | 9,6 | 1,3 | 620,1 | 295,8 |
| Diamond | 179 | 10,5 | 1,1 | 617,1 | 299,2 |
| Gyroid | 505 | 4,3 | 0,5 | 614,1 | 298,7 |

Figure 69 shows the selected final CAD (ID 505 of Table 43) model with the Gyroid cell type. The final mass of the connecting rod is 614 g (Ti6Al4V), achieving a mass reduction of 52% from the initial connecting rod of 1277,6 g (Chrome Molybdenum Steel).

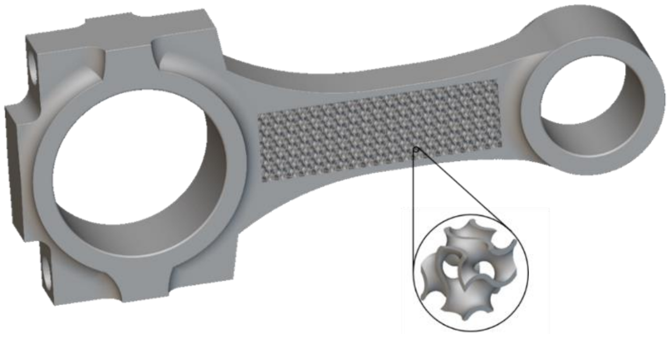

*Figure 69. Final connecting Rod with Gyroid cell detail.*

### 4.1.2 Lower Arm of a McPherson Suspension

The McPherson Suspension is the most used system for front axles of the B and C segments. The lower arm guides the wheel, and the guide is integral to the shock absorber. The first one is linked to the main body by two silent blocks, usually with different axis orientations, and the second one by the upper pivot. The lower arm is connected to the wheel strut through a spherical joint. This design is advantageous due to its simplicity, low cost, and compact transverse dimension [240, 241].

#### *4.1.2.1 Topology and Shape Optimisation*

Figure 70 describes the proposed approach for optimising a mechanical component to be realised by L-PBF, including the 3D modelling from the reference model. The proposed redesign approach begins with a technical analysis of the component under study, which includes examining its Environmental Operating Conditions (EOC) and focusing on specific scenarios for optimisation. The physical part is then designed using a CAD tool and then simulated to assess its mechanical behaviour. In this phase, simulations can be supported by real measurements to enhance the model's robustness. It is relevant to ensure the similarity between the physical component and its virtual counterpart in terms of shape, dimensions, and mechanical behaviour under the simulated operative conditions. However, minor geometrical simplifications are generally accepted to reduce the computational cost. The virtual part can then be virtually optimised using FEM tools, applying the EOC resulting from the first phase. Optimisation techniques can be applied in this phase. The optimisation techniques can be used individually, sequentially, or in combination, depending on the designer’s preference and the specific case study. The designers choose the optimisation method that best suits the case study, based on their experience, expertise, available resources, cost, and time constraints. The result of the optimization is a new CAD model that represents the redesign proposal. The suitability of the resulting model for the 3D printing process is checked considering the rules and constraints related to DfAM. This step is essential for ensuring part quality and preventing failures. If the review of the design proposal yields a positive outcome, the resulting model is printable.

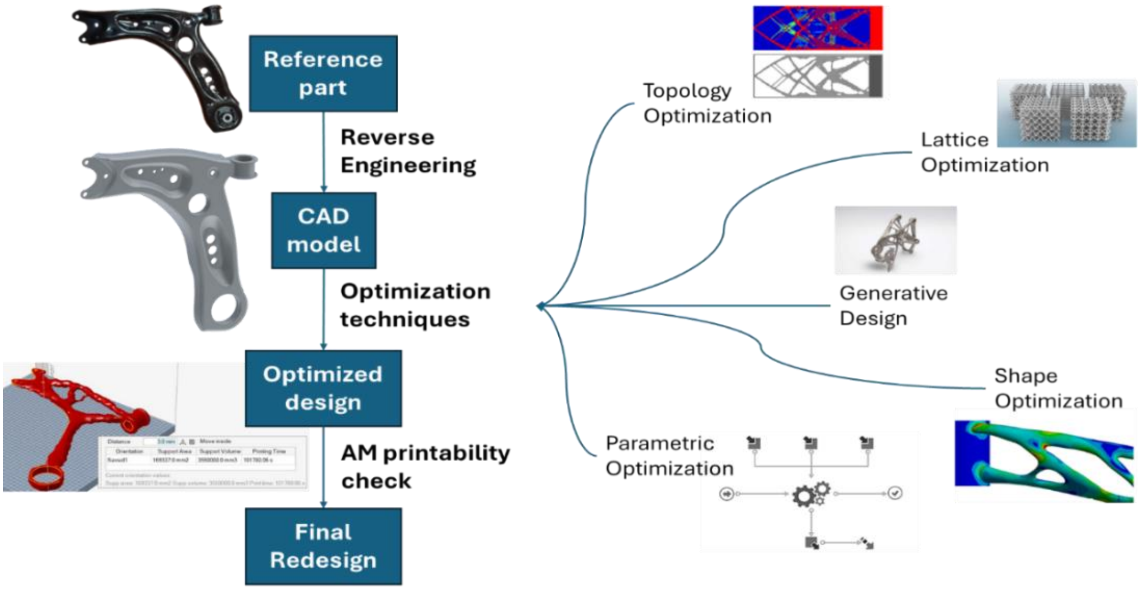

*Figure 70. Final Proposed approach for AM optimization, the optimization phase can regard a single optimization method or a combination of them.*

#### *4.1.2.2 Test Case*

The proposed approach has been applied to the redesign study of the lower arm of a McPherson suspension for a C-segment passenger car (Figure 71a).

The scope of the case study is to apply the optimisation approach to the arm and provide a suitable and optimised redesign for the suspension arm. The main idea is to redesign the suspension arm to be realised by L-PBF. In the optimisation phase, the high-specific-strength titanium alloy Ti6Al4V has been selected to maximise the overall performance.

The analysed C-segment passenger car has a gross vehicle weight of approximately 1800 kg, a wheelbase of 2630 mm, and a track width of 1530 mm, an estimated centre of gravity height of 510 mm, and a front-rear weight distribution of 54% – 46%. The analysed load cases are illustrated in Figure 71b, along with the CAD model of the analysed model, created using Autodesk Inventor. The analysed suspension arm is constrained by two bushings: one horizontal (Figure 71b, Point A) and one vertical (Figure 71b, Point B), and loaded with external forces (Figure 71b, Point C) in the XY plane. The starting mass of the part is 2,7 kg. The force intensity has been evaluated accordingly to [242], considering the maximum possible steering and braking conditions of the vehicle at full weight capacity, achieving these values: $Fx = 7930\ N$ and $Fy = 6980\ N$.

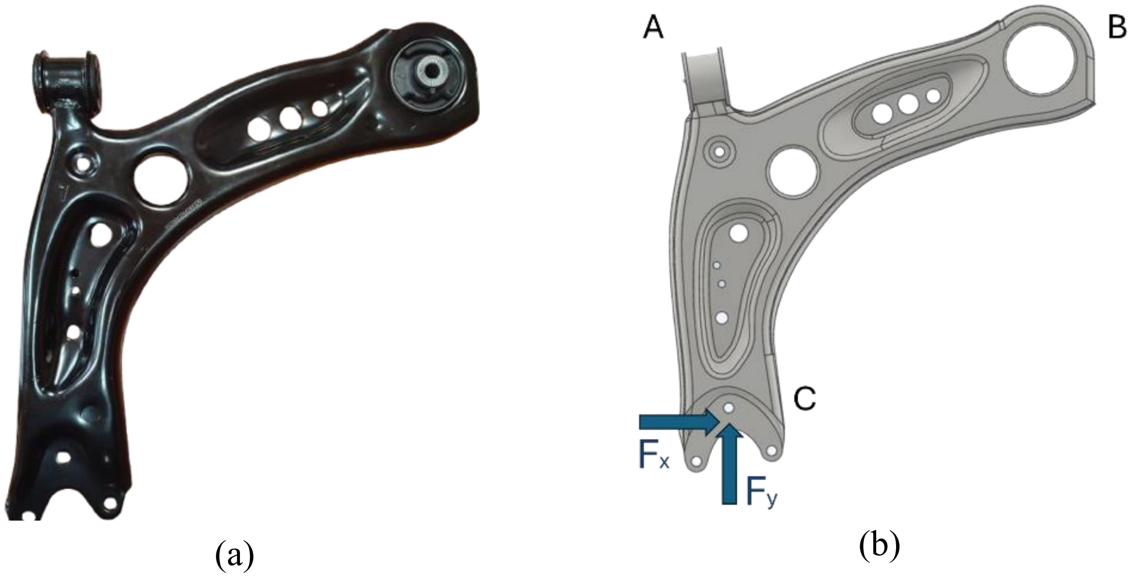

*Figure 71. Case study: Suspension Arm. (a) Photo of the physical reference part; (b) CAD model realised with load case highlighted.*

A static structural FEM analysis was conducted on the reference CAD model, utilising EOC, considering Carbon Steel as the initial material. These simulations and the following optimisation analysis were performed using Ansys® Mechanical Workbench, Student Version 2025 R1. Figure 72a and 72b show the results of displacement and equivalent von Mises stress. About displacement, a maximum of 0,704 mm was achieved near Point C (see Figure 72b). About equivalent von Mises stress, a maximum of approximately 182 MPa was registered along the component rib.

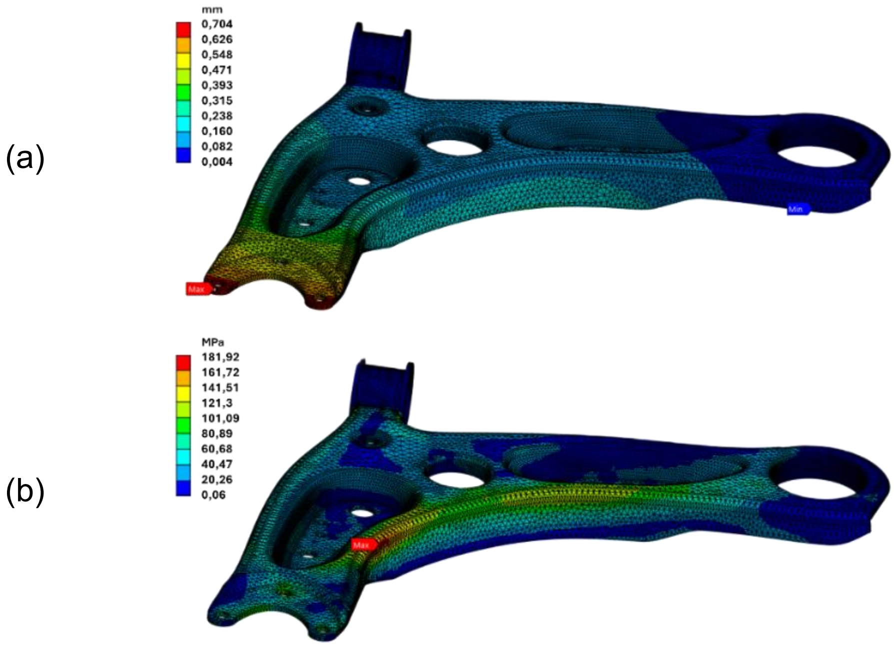

*Figure 72. Results in terms of contour maps of the FEM analysis of the reference CAD model: a) Displacement, b) Equivalent von Mises stress.*

As previously described, a mix of optimisation strategies can be applied to identify numerous possible new design solutions. In this case study, optimisation was performed in two steps using an FEM tool. The first step involves a TO based on the SIMP algorithm, applied to a simplified geometry (Figure 73a) of the suspension arm, which enables the algorithm to find unconventional solutions without relying on the real geometry as a starting reference. The second step involves an SO approach, performed on the result of the TO, to refine the obtained shape further. The material used in these optimisation steps is Ti6Al4V.

Figure 73b shows the TO result obtained with a 0,4-density threshold, 400 MPa for the maximum equivalent von Mises stress, 25% response mass constraint, and compliance minimisation. The result has been obtained with 22 iterations and a convergence accuracy of 0,1% of the combined objectives. To ensure component functionality, the constrained and loaded areas have been designated as a non-design zone; therefore, the algorithm cannot operate in these areas, maintaining the original geometry. The TO result must be redesigned for further application; in particular, the surface must be refined (removing sharp edges, intersections, and holes) and simplified to ensure reusability for subsequent meshes. Figure 74 shows the redesigned TO result after a first geometrical fixing, achieved using Ansys® SpaceClaim, Student Version 2025 R1.

To verify the findings of the TO process, a static structural FEM analysis was performed on the redesigned CAD model, using the same EOC and Ti6Al4V as material. Results are visible in Figure 75a and 75b. The maximum displacement has a value of approximately 0,7 mm, the maximum equivalent von Mises stress is about 93 MPa, and the resulting mass is 1,76 kg.


(a) (b)

Figure 73. a) Simplified CAD geometry used for the TO analysis, b) Result of TO with 0,4 density value as threshold.

*Figure 74. Redesign outcome of the TO analysis.*

To better exploit the material used in the component, a SO has been performed. It has been evaluated considering the same non-design zones described before. The selected objective function is to minimise the equivalent von Mises stress. The constraint of the SO regards the minimum compliance obtained with the TO. Figure 76 shows the redesigned result of the SO (same mesh fixing as before). The result has been obtained with 78 iterations and a convergence accuracy of 0,1% of the objective function.

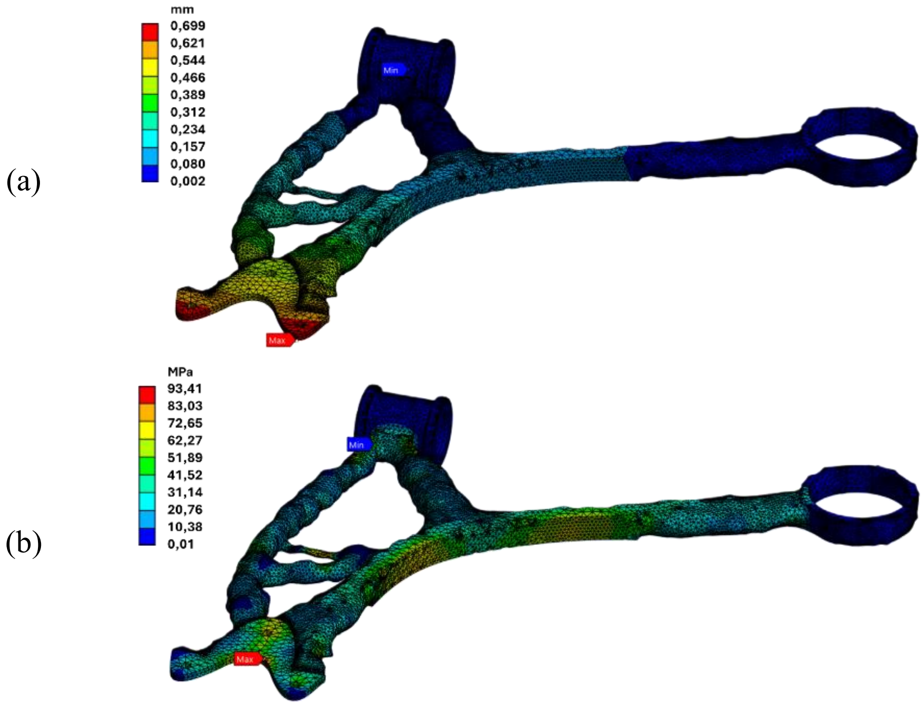

*Figure 75. Contour maps of the TO result redesign FEM analysis: a) Displacement, b) Equivalent von Mises stress.*

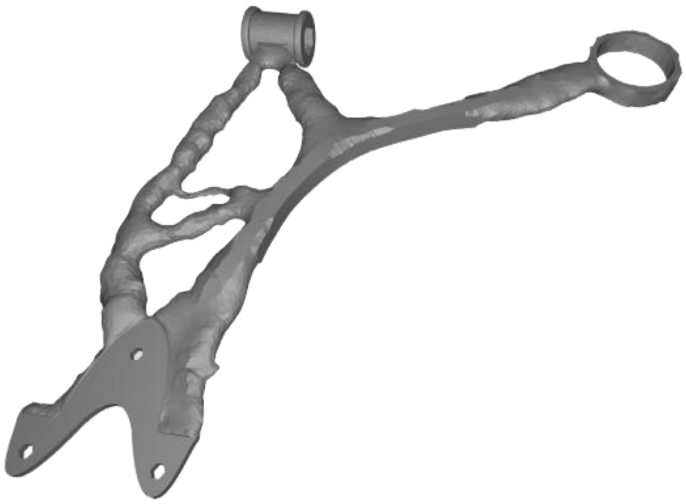

*Figure 76. Redesign outcome of the SO analysis.*

Figure 77a and 77b show the results of the static structural analysis performed on the SO result. While the maximum displacement of approximately 0,7 mm is confirmed, the maximum equivalent von Mises stress is about 78 MPa (less than the 93 MPa value achieved with the TO model). In general, the proposed optimisation process has improved material distribution and reduced the maximum stress from approximately 182 MPa to approximately 78 MPa, while maintaining similar maximum displacement values.

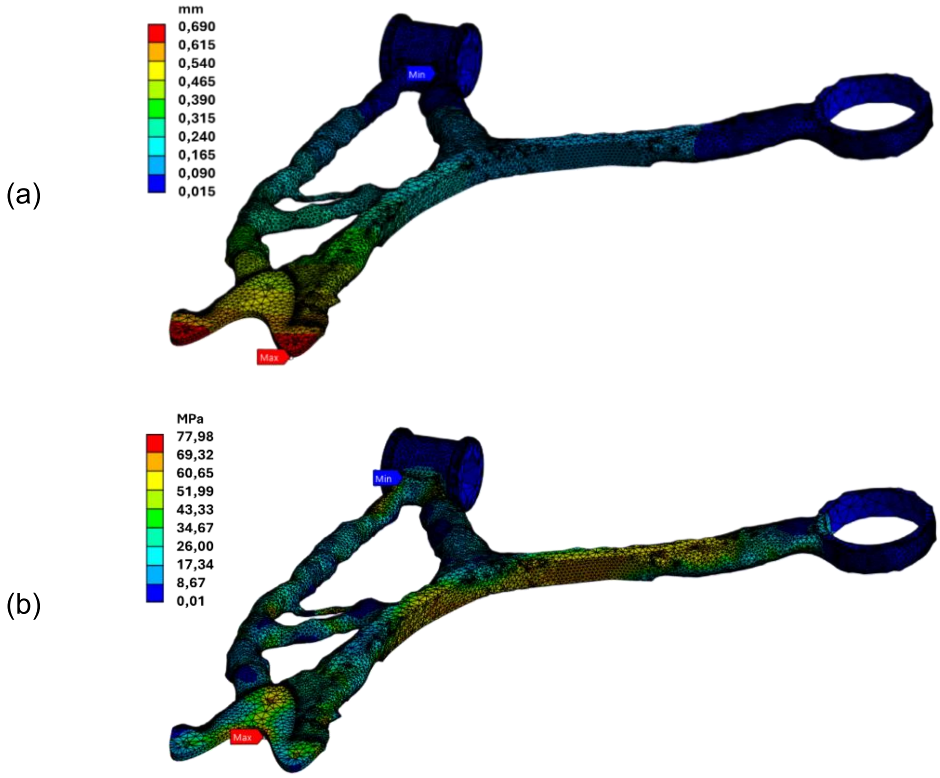

*Figure 77. Contour maps of the SO result redesign FEM analysis: a) Displacement, b) Equivalent von Mises stress.*

Due to the high production cost of 3D metal parts, it is common to perform an AM process simulation to ensure the part's 3D printability. In this case study, an inherent strain method simulation was performed using Altair® Inspire™ 2025.1 to simulate the L-PBF process. This method involves calibration for simulation by obtaining data from a real 3D-printed sample and applying the resulting tensor to all the geometry to be printed. To perform the simulation, it is necessary to select the printing orientation (Figure 78a) and the type and characteristics of the supporting structure (Figure 78b). These process parameters influence the 3D printing results in terms of cost and part quality and must be optimised accordingly. In this instance, part orientation has been chosen to minimise the maximum height from the build plate, considering a 3 mm minimum distance between the part and the plate.

Figure 79a and 79b present the displacement and the equivalent von Mises stress during the 3D printing phase. The maximum stress value achieved in the 3D printing simulation is 266 MPa, and it's located in the support structures. The value is lower than the critical range and therefore does not affect printability.  The maximum displacement value is circa 29 μm. Both values are suitable for the selected 3D printing process (L-PBF); thus, the geometry is correctly validated for the production phase.

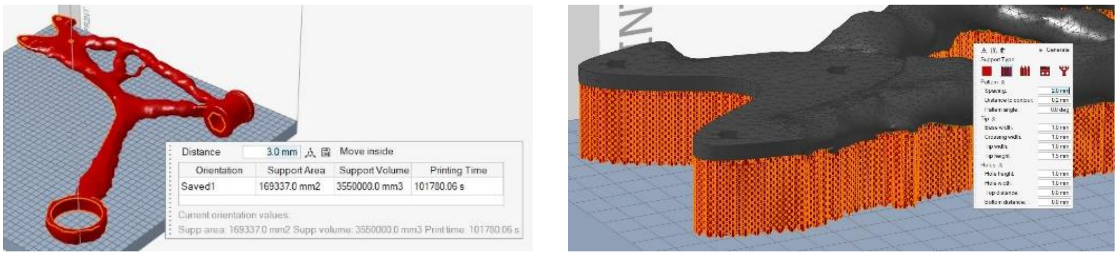

| Orientation | Support Area | Support Volume | Printing Time |
|---|---|---|---|
| Saved1 | 169337.0 mm2 | 3550000.0 mm3 | 101780.06 s |

Distance 3.0 mm Move inside

Current orientation values:

Supp area: 169337.0 mm2 Supp volume: 3550000.0 mm3 Print time: 101780.06 s

(a) (b)

*Figure 78. AM simulation setup: a) Part orientation; b) Support structures type and characteristics.*

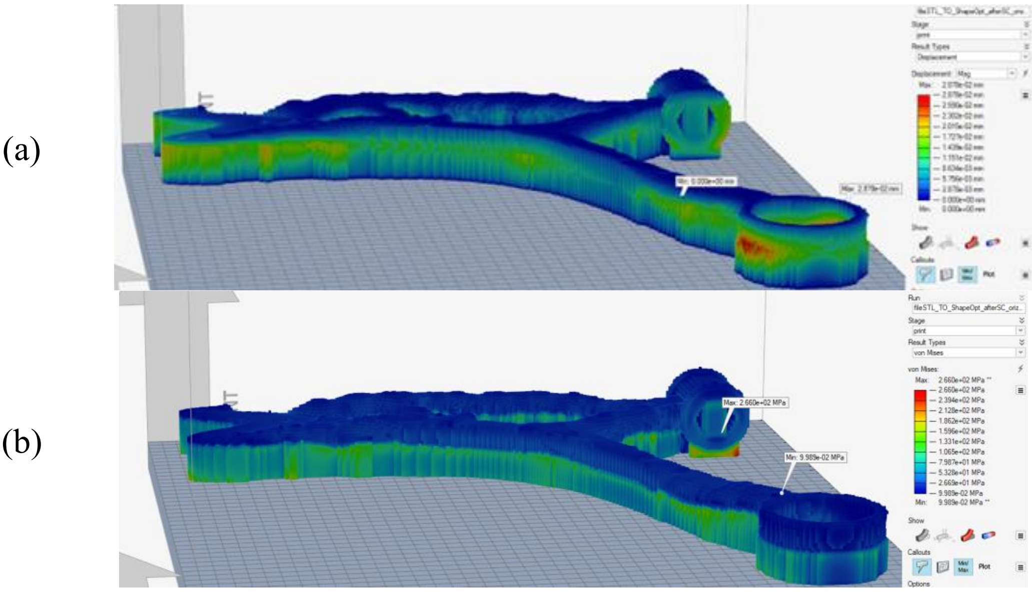

Figure 79. Contour maps of the inherent strain simulation during the 3D printing phase: a) Displacement; b) Equivalent von Mises stress.

Fatigue loading represents one of the most critical design constraints for components produced by L-PBF, particularly when these parts are used for structural or cyclically loaded applications. In contrast to traditionally manufactured alloys, the fatigue properties of L-PBF materials are strongly dependent on process-induced microstructural heterogeneity and defect populations, including lack-of-fusion pores, gas porosity, unmelted particles, surface roughness, and residual stresses. These features act as crack initiation sites, significantly reducing fatigue life, especially in the high-cycle regimes [243]. Moreover, the layer-wise fabrication strategy introduces anisotropy in both microstructure and mechanical response, meaning that fatigue resistance can vary substantially with build orientation and loading direction. Surface condition is also particularly influential in L-PBF parts, since the as-built roughness often amplifies local stress concentrations and accelerates crack nucleation [244]. Post-processing treatments such as machining, polishing, HIP, and stress-relief heat treatments improve fatigue behaviour, reducing surface defects, closing internal porosity, and mitigating residual stresses; however, their effectiveness depends on alloy, defect morphology, and the specific loading environment. Consequently, the fatigue assessment of L-PBF components cannot rely solely on nominal bulk material properties but must account for the combined effects of manufacturing defects, microstructural anisotropy, and post-processing history to ensure reliable structural performance [245].

# 5 Case Studies: ML Models for DfAM

This chapter describes the developed ML applications to support AM designers and the industry in making decisions and reducing errors. Three ML models have been realised for the analysis and evaluation of CAD models in the early design phases. Predicting relevant features, such as printing time, necessary support volumes dependent on the orientation of the part, cost, and printability of the part, can ease the feasibility study. The trained ML models are:

- A Decision Tree Classifier for Printability Prediction
- A Random Forest Regressor for Printing Time Prediction
- Three Neural Networks in cascade for Cost Estimation

All these models are SL models; they require a dataset with complete and numerous elements to provide suitable and usable results. Gathering enough data to train ML models can be expensive in terms of time and money; to overcome this problem, real data are often accompanied by numerical data obtained from simulations. For training these ML models, due to the absence of a suitable open-source dataset, a dataset of parametric flanges has been created. Although flanges are not the best example of L-PBF geometry, building a parametric dataset of simple models has allowed us to obtain a significant number of CAD models and their relative data. Figure 80 shows some examples of these parametric flanges. The variable parameters are thickness, height, diameters, and the number and diameters of holes.

To complete the dataset with the necessary information, different tools have been used, such as VB.NET code to extract geometrical data from CAD files, Python code to extract data from STL format files, and AM simulation software.

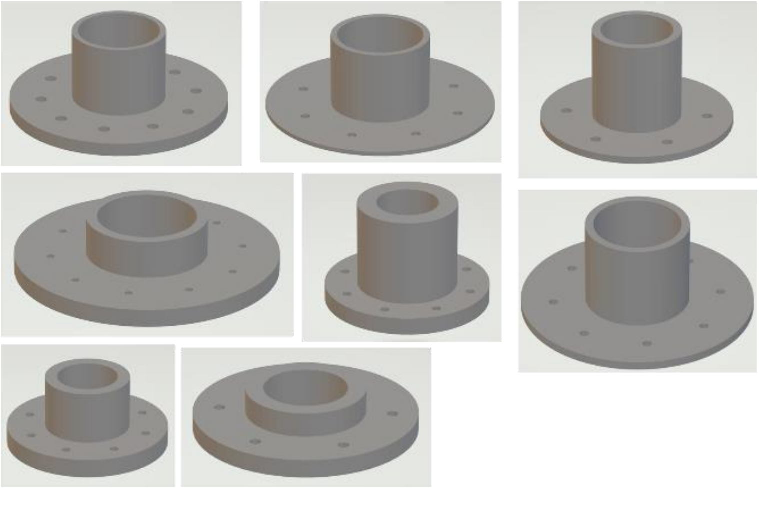

*Figure 80. Some examples of flanges used for training the ML models.*

With the AM simulation software usage, it is possible to evaluate, after an accurate calibration, print orientation, support volume dependent on orientations, printing time, and distortions and stress during and after the printing phase.

## 5.1 Printability Prediction

The first ML model aims to provide a tool for the early evaluation of the printability of a 3D model for metal L-PBF processes. This approach uses a Decision Tree (DT) Classifier with the CART algorithm. Figure 81 shows the Early Geometry Validation Method proposed to evaluate the 3D part printability. The validation method includes an Automatic Data Extraction (ADE) tool, which interacts with the CAD tool and Knowledge Base (KB). The KB module includes the rules to extract geometric and non-geometric data from a 3D CAD model.

The Decision Tree Evaluation (DTE) phase completes the workflow by predicting the printability of the part to be analysed. The DT is trained with virtual analysis. The training set preparation includes the definition of a list of CAD models to be simulated for the evaluation of the printability. These CAD models also required the automatic extraction of the data to be used as parameters in the training dataset.

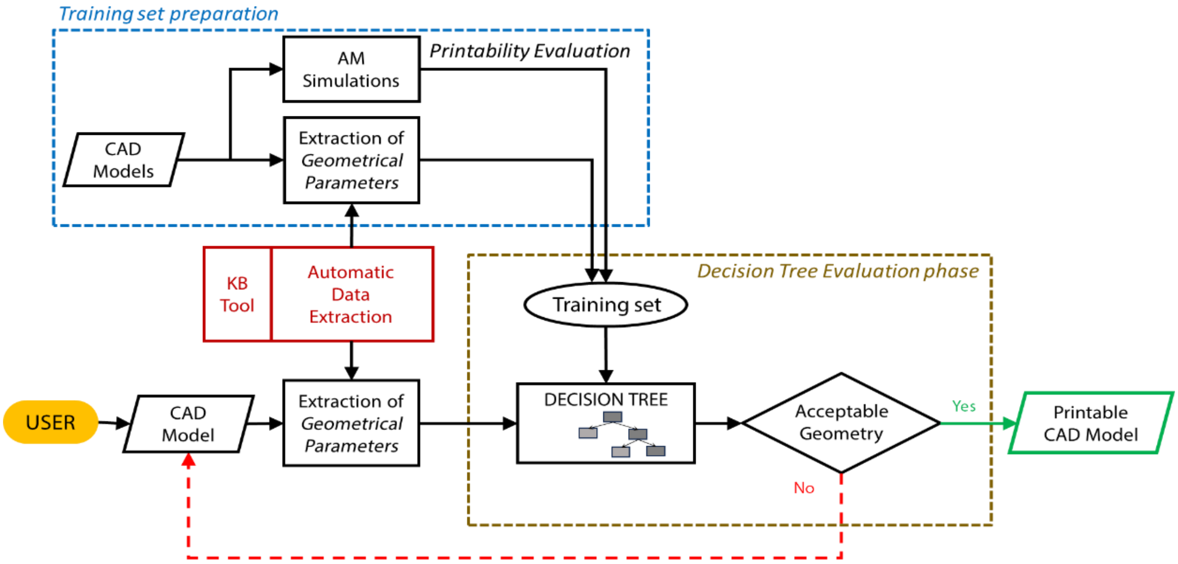

*Figure 81. Early Geometry Validation Method.*

### 5.1.1 Automatic Data Extraction Phase

The proposed approach starts with the 3D CAD modelling of the component to be evaluated. The first part of the method involves the use of the ADE tool. The ADE tool has been developed by the VB.NET programming language using the SDK (Software Development Kit) libraries for the connection to the CAD software used here, Autodesk Inventor®. This tool performs a connection with the CAD software to extract the data related to the B-Rep (Boundary Representation) of the model to be acquired. Among these parameters, some are geometric, such as volume, area, maximum extension, minimum thickness, etc., and others include non-geometric properties such as material, weight, object type, etc. The rules to manage these geometrical and non-geometrical parameters are managed by the Knowledge Base (KB) tool. These rules were defined in a pre-analysis activity during the study of the model.

The developed data structure considers classes such as bodies, faces, edges, points, vectors, features, etc. Inside these classes, methods were defined to extract the necessary parameters for further printability analysis. Some parameters are volume, area, weight, volume of the bounding box, etc. Only some parameter combinations were considered useful for training the DT. The parameters useful are ratios such as area/volume, area/bounding box volume, volume/ bounding box volume, minimum thickness/area, and minimum thickness/volume. These parameters are organised in an orderly structure before being exported. These ratios define the dataset with the labels and the targets for training the ML model.

### 5.1.2 Decision Tree Evaluation Phase

The DTE phase requires the previously defined dataset, which is necessary to train the ML technique chosen. This paper considers a DT method based on the CART algorithm, using Entropy as the node-impurity evaluation function. The training phase is performed using a dataset filled with the parameters extracted by the ADE tool and the results of the AM printing simulations. The output of the DTE phase is the evaluation of the component printability, analysing the input geometrical parameters extracted by the CAD model. The DT model, after training, provides a series of graphical rules useful to evaluate the model's printability.

The criteria to evaluate the printability of the parts used to train the DT method are related to the results of the AM simulations. The AM simulation tools allow residual stress and deformation to be estimated on the geometry of the 3D part. To define the parts' printability, threshold values were defined on the AM simulation results. The thickness of the metal powder layer was imposed as the maximum allowable deformation. Two-thirds of the maximum tensile strength of the chosen material was imposed as the maximum Von Mises stress allowable.

Using the Scikit-Learn libraries for Python, a code to realise a DT model, based on the CART algorithm, has been written. As for every supervised ML model, the dataset has been divided into training data and test data. The training data allows the model to be trained from itself, realising the classifier model. The test data are useful to evaluate the model, calculating the Accuracy parameter defined as the set of labels predicted for a sample that must exactly match the corresponding set of labels.

The Entropy function has been used to evaluate the purity of every single node of the DT. (Equation 20) describes the definition of Entropy for the $i^{th}$ node where the $p_{i,k}$ is the ratio of the class $k$ instances among the training instances in the $i^{th}$ node.

$$Entropy = -\sum_{\substack{K=1 \\ p_{i,k}\neq 0}}^{n} p_{i,k}\log_2(p_{i,k}) \tag{20}$$

### 5.1.3 Training Model

The test case is focused on flange parts to be realised by 3D metal printing, L-PBF process. A set of a hundred CAD models was created to obtain data to train the DT model. All the flanges used for training were generated from a parametric CAD model.

The selected material for this case study is Inconel 718, a niobium-modified precipitation hardening nickel-iron alloy, designed for strength, creep resistance, and good fatigue life at high temperatures of up to 700 °C. This alloy is one of the most frequently used alloys in metal AM, finding widespread application in gas turbines, turbocharger rotors, aircraft, and other corrosive and structural uses [246].

The printing simulations of the L-PBF process are a useful tool for evaluating the AM design; these simulations help to reduce the number of physical tests and the related cost and time. Altair ® Inspire™ software was used in this project to carry out the 3D printing simulations. The setup used for the simulations is shown in Table 44. An example of a 3D printing analysis is reported in Figure 82.

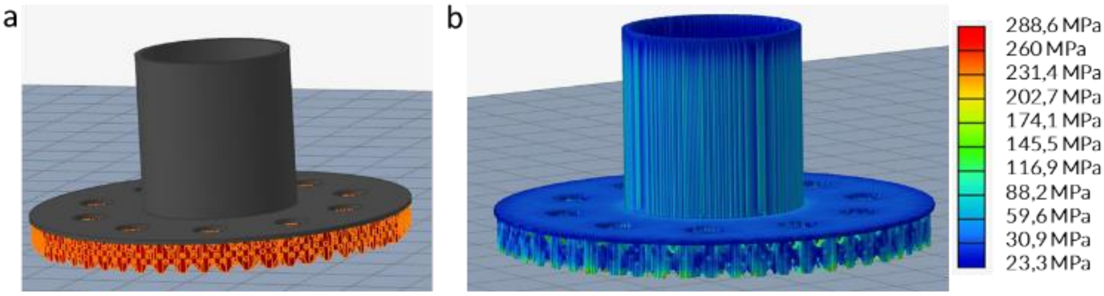

*Figure 82. (a) Support and orientation used for the AM simulation setup; (b) Example of Von Mises Stress distribution on the 3D model after 3D printing.*

Figure 83 shows the trained DT model used to evaluate the printability of new flange models with an accuracy of 0.91. About the limitations of this test case, the AM analysis only considers one type of support structure (block support). Moreover, the orientation is not a parameter in this early study. The orientation defined in the AM analysis is related to the minimum printing time strategy. The defined dataset considers just a family of CAD models and a type of material.

*Table 44. AM Simulation setup.*

| **Parameter** | **Value** |
|---|---|
| Build volume | 300 mm x 300 mm x 250 mm |
| Orientation strategy | Minimum printing time |
| Distance from plate | 5 mm |
| Support type | Block support |
| Support thickness | 0.2 mm |
| Layer Thickness | 0.040 mm |
| Deformation (calibration) | 0.15 mm |
| Voxel Mesh average thickness | From 1.5 to 5 mm |

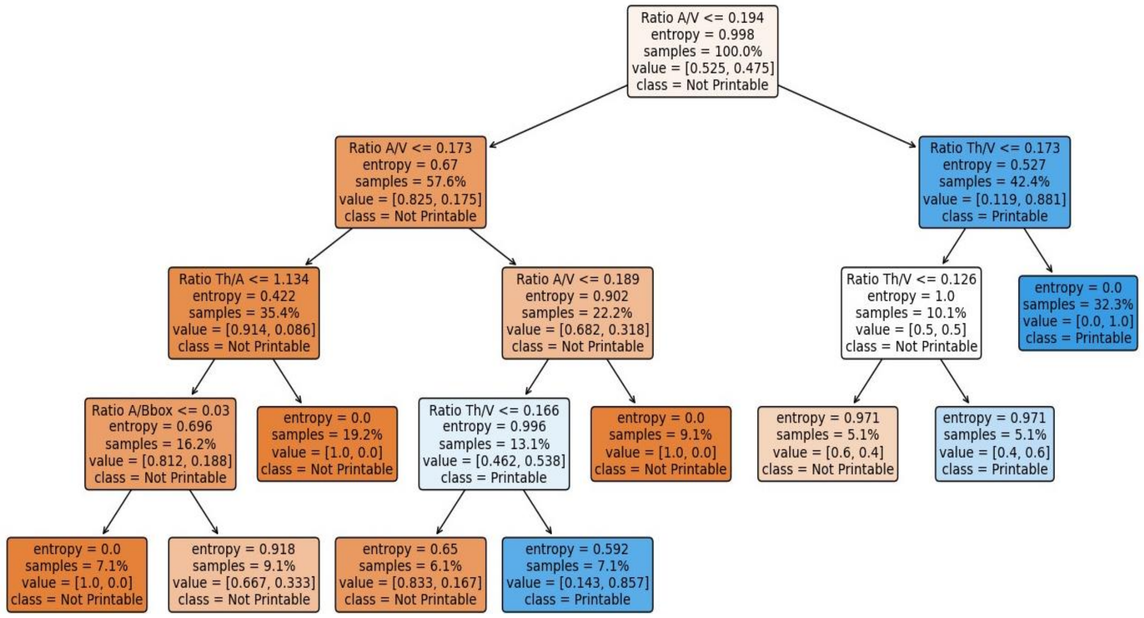

*Figure 83. The trained Decision Tree.*

## 5.2 Printing Time Prediction

The second ML model trained aims to predict printing time for the L-PBF component. The L-PBF is a relatively slow process, and evaluating orienting time can support the logistic process.

Figure 84 shows the proposed approach to estimate the 3D printing time of a metal part to be realised with the L-PBF process. The method can be divided into different phases. The first phase concerns the realisation of the dataset; the second phase regards the training and the tuning of the ML model, a Random Forest (RF) Regressor; and the third phase uses the trained model to predict the 3D printing time of a part.

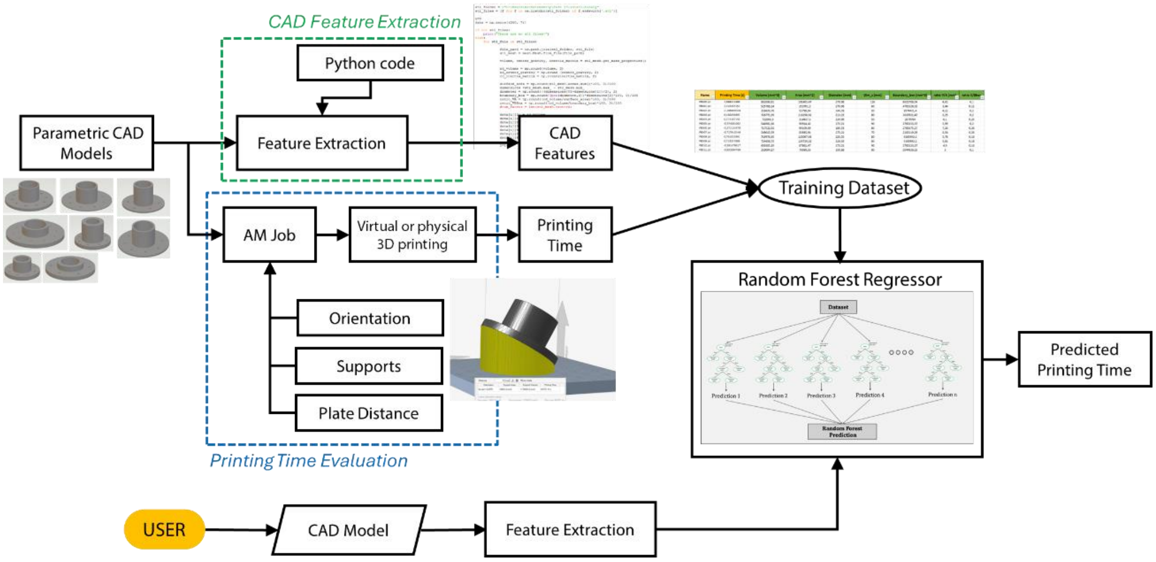

*Figure 84. Proposed Method for the printing time prediction.*

The dataset realisation phase can be further divided into two other sub-phases. The first sub-phase concerns extracting features from the STL models using Python code and subsequently writing the extracted features to a spreadsheet. The second sub-phase concerns the estimation of the 3D printing time associated with a CAD model. This estimation can be achieved by virtual or physical 3d printing. Using virtual data to build the dataset reduces cost and training time. On the other hand, using real data is expensive, but it provides more reliable results.

A standard file format used in CAD and 3D printing is a Stereolithography (STL) file. It represents three-dimensional models by dividing their surfaces into a series of triangular facets that together characterise the geometry and contour of the object. STL files can be stored in ASCII or binary forms; both represent the same 3D model but differ in how the data is stored and the file size [247]. Table 45 describes the main features and differences of the two formats. Since the STL format is the most used exchange format for CAD models, using the STL format as a starting file allows the model to interface with any software.

*Table 45. STL formats comparison.*

| Feature | ASCII STL | Binary STL |
|---|---|---|
| Human-readable | Yes | No |
| File size | Larger | Smaller |
| Editing | Can be edited in a text editor | Requires specialised software |
| Usage | Rarely used for large models | Preferred for 3D printing, CAM, etc. |

### 5.2.1 Random Forest Regressor

An RF model is an ensemble learning method used primarily for classification and regression tasks. This ML method works by creating many decision trees during the training phase and combining their outputs to produce a more accurate and stable prediction [248]. These phases, called bootstrap and aggregation phases, are essential steps that work together to create a robust predictive model. During the bootstrap phase, multiple samples of the original dataset are randomly generated. Each tree is trained on a random subset of the data and sees only a fraction of the total information, introducing variety among the trees, making the forest more resilient to overfitting, as each tree offers a slightly different perspective on the data. In the aggregation phase, the predictions from each tree are combined to produce the final model output. For a classification task, aggregation involves using a majority voting system, where the predicted class is the one chosen by the most trees. In regression, aggregation is realised by averaging the predictions from each tree, which results in a smoother, more accurate prediction [249].

Figure 85 shows the RF working scheme. Single trees in an RF are powerless learners, meaning each tree has limited predictive power. RF model is appreciated for its high performance, ease of use, and ability to handle large datasets and complex interactions among features. RF interpretability is also enhanced by feature importance scores, which indicate how much each feature contributes to predictions, making it a versatile choice for many practical applications.

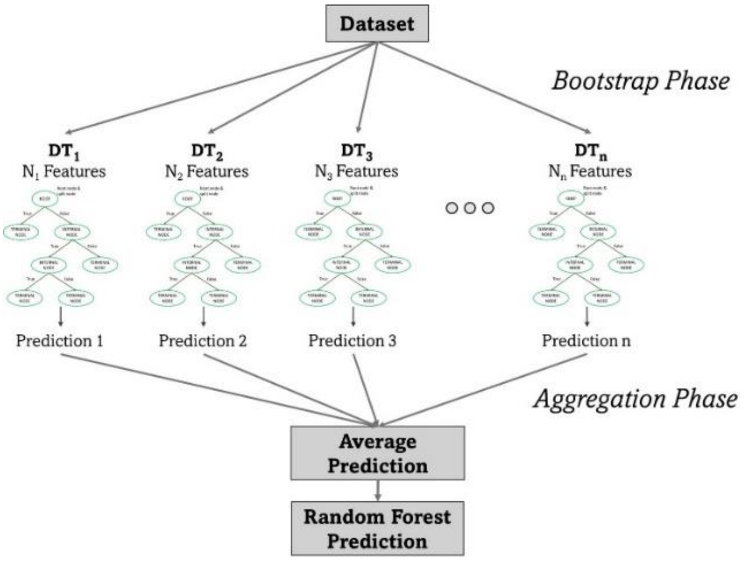

*Figure 85. Random Forest working scheme.*

Using the constructed dataset, the second phase trains and tunes the RF Regressor. The selection of the right hyperparameters and the choice of the features useful for training the model can be a lengthy process. Three different metrics have been used to evaluate and compare training results, such as the Mean Squared Error (MSE), the Mean Absolute Error (MAE), and the $R^2$ index, also known as the coefficient of determination. Equation 21 describes the $R^2$ index.

$$R^2 = 1 - \frac{\sum_{i=1}^{n}(y_i - \hat{y}_i)^2}{\sum_{i=1}^{n}(y_i - \overline{y_i})^2} \tag{21}$$

Where $y_i$ represents the actual value of the target variable for the $i-th$ observation; $\hat{y}_i$ is the predicted value from the model; $\overline{y_i}$ is the mean of all actual values $y_i$ in the dataset. $\sum_{i=1}^{n}(y_i - \hat{y}_i)^2$ is the Residual Sum of Squares, which measures the total squared prediction errors, $\sum_{i=1}^{n}(y_i - \overline{y_i})^2$ is the Total Sum of Squares, which measures the total variance in the actual values. $R^2$ describes the proportion of variance in the actual data that is explained by the model. It is important to compare the variance in the prediction errors to the variance in data values. Concluding, $R^2$ provides a mathematical interpretation of how well a model captures the variance in the actual values.

The final phase involves using the trained model to evaluate the printing time of a CAD model that was not included in the training set. A Python script has been created to extract features from this STL file and utilise the ML model, achieving the desired goal.

### 5.2.2 Training Model

To validate the proposed method, a set of two hundred parametric flange CAD models has been realised. Each flange's geometrical parameter, such as the number and diameter of holes, the thickness of the plate, the axial extension, the length of the axial extension, and internal and external diameters, can vary within its specific range. For example, the external diameter can vary from 35 mm to 115 mm with steps of 5 mm. The total number of possible combinations is about two million. A DoE Latin Hypercube method was used to select the two hundred CAD models for training the RF. The CAD models have been automatically generated using a VB.NET code previously developed (case study in section 5.1).

The flange is not a useful component to study for metal AM, but its ease of parameterisation allowed it to speed up the dataset creation times.

The parametric flanges' printing time was evaluated using the software Altair® Inspire™ 2024. The software uses the Inherent-Strain Simulation method [250] to simulate residual stresses and deformation during and after the printing process. Figure 86 shows an example of printing time evaluation with this software; this data has been used to complete the dataset. The setup used for evaluating these simulations includes a building volume of 300 mm x 300 mm x 250 mm, an orientation strategy of 30° from the building plate, and a distance from the plate of 5 mm. For each CAD model, the same printing setup has been used.

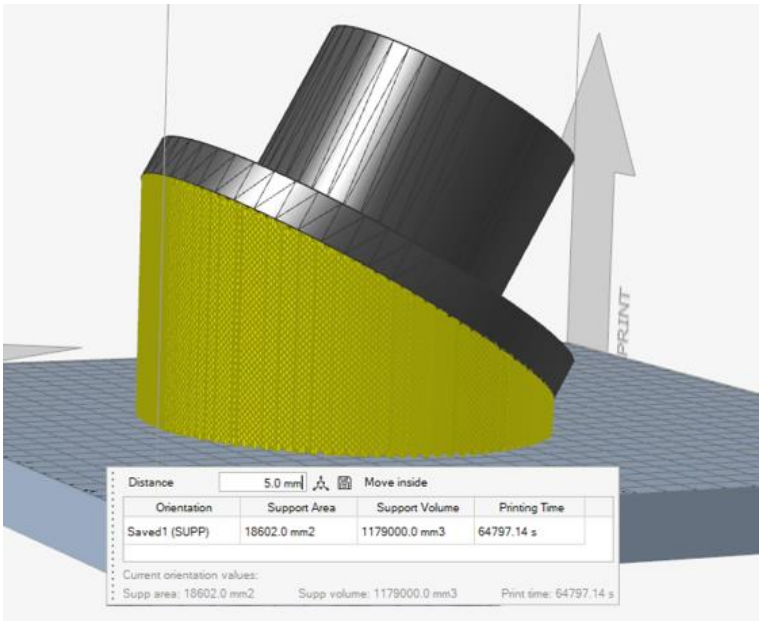

Distance 5.0 mm

| Orientation | Support Area | Support Volume | Printing Time |
|---|---|---|---|
| Saved1 (SUPP) | 18602.0 mm2 | 1179000.0 mm3 | 64797.14 s |

Current orientation values:
Supp area: 18602.0 mm2 Supp volume: 1179000.0 mm3 Print time: 64797.14 s

*Figure 86. 3D printing software Setup evaluated using the software Altair® Inspire™ 2024.*

#### 5.2.2.1 Data Preparation

The creation of the dataset involves three main steps: extracting data from STL CAD files, writing that data to a spreadsheet, and associating printing times with CAD models. The first two steps were accomplished using Python code, while the third step was completed manually.

Equation 22 shows the formula used to standardise each feature in the dataset. A standardised variable always has a mean of zero and a standard deviation of one. Standardisation allows the comparison of variables that have means and standard deviations measured on different units of measurement and orders of magnitude.

$$z = \frac{x - \mu}{\sigma} \tag{22}$$

Where z is the new value of the variable, $x$ is the starting value, $\mu$ is the mean of the feature, and $\sigma$ is the standard deviation of the feature.

#### *5.2.2.1.1 Tuning ML model*

Hyperparameters play a crucial role in tuning the ML model’s complexity, speed, and predictive accuracy. Table 46 shows the selected hyperparameters used to train the RF model in this study. The first one, the number of estimators (*n_estimators*), describes the number of parallel decision trees in the forest. A high value improves the model stability but increases the computation time. The second one (*max_depth*) characterises the maximum depth of each tree. Deeper trees can capture more detail but pose the risk of overfitting. The third one (*min_samples_split*) shows the minimum number of samples required to split an internal node; with high values, the node needs more samples to split, leading to less model complexity and reduced overfitting. The fourth one (*min_samples_leaf*) describes the minimum number of samples necessary to be at a leaf node. The last one (*max_features*) considers the maximum number of features considered for splitting each node. This hyperparameter controls how many features each tree considers for splits, balancing diversity and accuracy in the ensemble.

*Table 46. Hyperparameters for the trained Random Forest Regressor.*

| **Hyperparameter** | **Value** |
|---|---|
| n_estimators | 200 |
| max_depth | None |
| min_samples_split | 5 |
| min_samples_leaf | 2 |
| max_features | None |

## 5.2.3 Results

Table 47 shows the obtained results, listing the three metrics used to evaluate the trained RF model, such as MSE, MAE, and $R^2$. Each metric evaluates a specific aspect of the trained model. Low values of MSE indicate that the model's predictions are adjacent to the target values (0.0140 MSE was achieved; 0 is the perfect prediction). The values of MAE evaluate the average amplitude of errors without considering their positive or negative sign (0.0863 MAE was achieved; 0 is the perfect prediction). The $R^2$ score measures how the model's predictions match the data. $R^2$ values range from 0 to 1, the value 1 indicates perfect prediction, and 0 indicates no explanatory power. In this case, the $R^2$ score suggests that 98.51% of the variance in the target variable is explained by the model. This high $R^2$ score confirms that the model fits the data very well.

Figure 87 shows the comparison between the predicted printing time (red line) and test data (blue dots). Test data are fifteen percent of the dataset.

*Table 47. Evaluation metrics for the trained Random Forest Regressor.*

| **Metrics** | **Value** |
|---|---|
| Mean Squared Error (MSE) | 0.0140 |
| Mean Absolute Error (MAE) | 0.0863 |
| $R^2$ score Training | 0.9911 |
| $R^2$ score Test | 0.9851 |

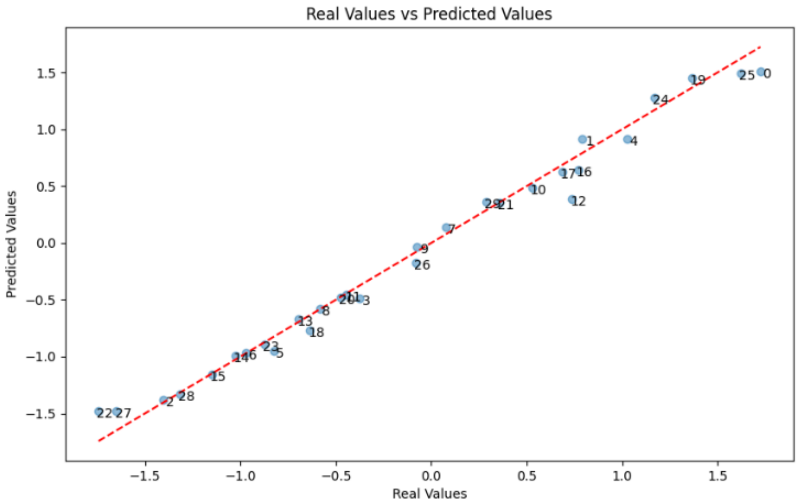

*Figure 87. Comparison between predicted values (red line) and real test values (blue dots).*

Table 48 lists the relevance of the obtained features of the trained RF Regressor. The Features relevance (or feature importance) represents how relevant each feature is in making predictions. RF models provide feature importance scores by evaluating each feature's contribution across all the trees in the forest.

*Table 48. Features relevance for the trained Random Forest Regressor.*

| **Feature Relevance** | **Value** |
|---|---|
| Volume | 0.0022 |
| Area | 0.5619 |
| Diameter | 0.4236 |
| Maximum Height | 0.0008 |
| Boundary Box | 0.0091 |
| ratio Volume/Area | 0.0011 |
| ratio Volume/Boundary Box | 0.0013 |

Currently, the proposed approach does not include the nesting technique, which involves filling the building chamber as much as possible to optimise time and costs.

## 5.3 Cost Estimation

The third ML model’s objective is to provide an ML-based web service platform that supports engineers in assessing Support Volume, 3D Printing Time, and Cost of metal parts realised by L-PBF. Figure 88 illustrates the proposed approach, highlighting three phases: Dataset Building, Machine Learning Web-Service Platform, and Use.

The first phase involves implementing the dataset through CAD models and virtual experiments. Physical prototypes can also be created, if possible, to reduce uncertainties resulting from software calculations. A code automatically extracts features from the geometry to acquire the necessary input data. The STL format was used for the CAD files.

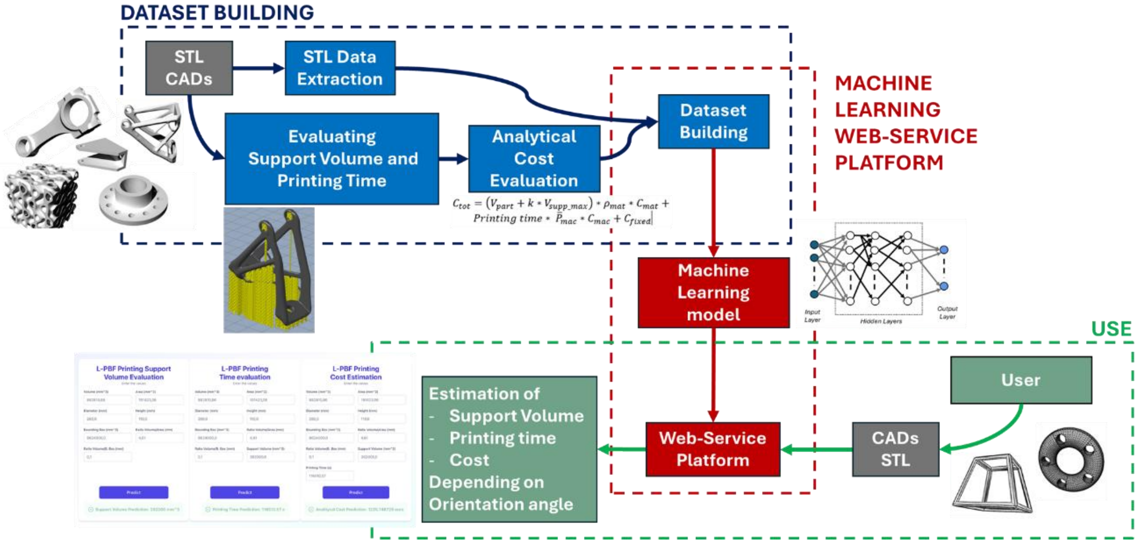

*Figure 88. The proposed approach includes the implementation of an ML-based tool trained using virtual and experimental data, as well as its use phase.*

This file format describes a three-dimensional model by splitting up its surfaces into numerous triangle facets that together characterise the geometry and contour of the object. At this point, the target values for *Support Volume*, *3D Printing Time*, and *Cost* are evaluated. While Support Volume and 3D Printing Time are evaluated using simulation software, the cost is analysed through an analytical approach. Equation 23 reports the formula used for the cost evaluation:

$$C_{tot} = \left(V_{part} + k * V_{supp\_max}\right) * \rho_{mat} * C_{mat} + \ Printing\ time * \ \bar{P}_{mac} * C_{mac} + C_{fixed} \qquad (23)$$

where $C_{tot}$ is the total cost evaluated in €, $V_{part}$ is the volume of the part to be printed (mm$^3$), *k* (dimensionless) is the ratio between the effective and maximum volume support $V_{supp\_max}$ (mm$^3$), and its value varies between 0 and 1, depending on the type of support structure used, the most common are lattice and block support structures [251] (Typical values for *k*: 0,2 – 0,5), $\rho_{mat}$ is the material density (kg/mm$^3$), $C_{mat}$ is the material cost(€/kg), $\bar{P}_{mac}$ is the average machine power (kW), and $C_{mac}$ is the specific energy cost (€/kWh), and $C_{fixed}$ is the fixed cost, such as machine depreciation, scheduled maintenance, human-related cost, etc. The scope of the methodology is restricted to the 3D printing process as it is, without considering post-processing or machining, therefore considering only net-shape components, optimal for AM production.

The second phase, related to the development of the web service, can be divided into two levels: defining the ML model and developing the web service platform, which is the Model Endpoint. The first level concerns the training and testing of the ML model to predict *Support Volume*, *3D Printing Time*, and *Cost* related to a CAD model to be printed. On the other hand, the second level regards the implementation of a web service platform that exploits the trained ML models inside an online system designed to streamline and support the technical users.

The use phase describes the workflow of input/output provided by the analysed web platform to predict the time and cost for a CAD model to be realised by L-PBF.

### 5.3.1 Training Model

This section describes the application of the previously proposed method to support the DfAM of Ti-6Al-4V flanges. The implemented ML system predicts the 3D printing time and printing cost of these components by analysing the specific geometrical features. The analysed parts were designed to be realised by L-PBF. The 3D printer used for reference is the EOS M400-4. This printer has a build volume of 400 x 400 x 400 mm, four 400 W fibre lasers, and a mean power consumption of 22 kW.

The ML training is based on virtual experiments. The CAD models employed were generated using a CAD automation tool that integrates VB.NET code with Autodesk Inventor®, using a CAD model template with geometrical parameters. These parameters regard diameters, thicknesses, the number of holes, height, and others.

A total of 235 CAD models (dataset samples) of parametric flanges have been produced using a DoE table of parameter combinations. Each CAD model was exported in STL format. To generate the dataset, labels and targets were extracted and calculated from the CAD models. The extracted labels regard the geometrical features, acquired by a Python code. The Python code uses the open-source library "*numpy-stl 3.2.0"* [252]. From this analysis, the following parameters were considered as geometrical labels: Volume, Area, Diameter, Height, Bounding box, Ratio Volume/Area, and Ratio Volume/Bounding Box. Support Volume, 3D Printing Time, and Cost have been considered as targets. Diameter and Height are calculated from the Bounding Box dimension extracted using the library; they are related only to this test case geometry. For more complex geometries, the features will be extracted accordingly from CAD models.

While Support Volume and 3D Printing Time have been obtained by performing 3D printing analysis with Altair® Inspire™ (Figure 89), the Cost label has been calculated using Equation 23. Fixed costs have not been included in this case study, being a constant of AM processes, depending on the company procedures on a case-by-case basis. The case study considers only the $C_{AM}$. For the final cost evaluation, post-processing, such as thermal treatment and finishing surfaces, must be considered. This test case focuses only on $C_{AM}$.

Considering the possibility of different part orientations, the dataset was built into two subsets: one considering 0° of part orientation on the 3D printing plate, and one considering 30° of part orientation. The 0° orientation refers to the solution that minimises the 3D Printing Time, and the 30° solution comes from the experience of simulations to lower residual stresses and deformations. The plate distance has always been considered 5 mm for the dataset realisation. Therefore, two parallel ML models were trained using NNs.

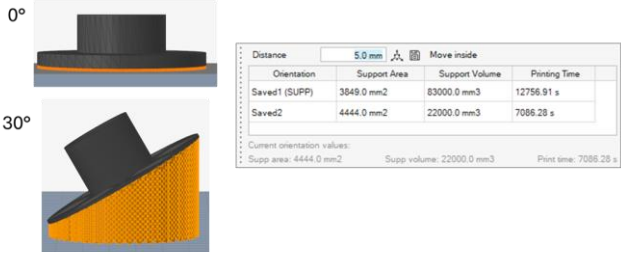

Distance 5.0 mm

| Orientation | Support Area | Support Volume | Printing Time |
|---|---|---|---|
| Saved1 (SUPP) | 3849.0 mm2 | 83000.0 mm3 | 12756.91 s |
| Saved2 | 4444.0 mm2 | 22000.0 mm3 | 7086.28 s |

Current orientation values:

Supp area: 4444.0 mm2 Supp volume: 22000.0 mm3 Print time: 7086.28 s

*Figure 89. Phase of the 3D printing analysis considering a part orientation of 0◦ and 30◦.*

Figure 90 illustrates the overall prediction model, which is divided into two channels (0° and 30°). Each channel consists of three NNs. Using three NNs for each channel instead of a single one allows the output of the first NN to be used as input for the second, and the output of the second to be used as input for the third.

Support Volume is predicted as a target in the first NN and used as a label in the second NN to predict 3D Printing Time. Similarly, Support Volume and 3D Printing Time are used as labels to predict the Cost in the third NN. With the data automatically extracted from the STL CAD models (geometrical labels), the first NN, called NN_1, has been trained to obtain the Support Volume at 0° and 30°, using the multi-output regressor technique. NN_2_0 and NN_2_30 use labels referring to the orientation of the study. NN_2_0 uses the geometrical labels and the "Support Volume 0°" to predict the 3D Printing Time. In the same manner, NN_3_0 and NN_3_30 are trained to predict the Cost of the 3D printing part, using STL data, support volume, and printing time as labels. All the trained NNs use the same hyperparameters, described in Table 49. The dataset has been divided into train and test samples, with a test size of 20%.

When dealing with a pipeline of NNs, it is important to consider the error propagation from earlier predictions to later ones. Understanding and managing error propagation is crucial in any pipeline, where predictions feed into future ones. Without mitigation, even small early mistakes can lead to significant degradation in performance, reducing the reliability of the entire system. For example, in this case, errors in Support Volume predictions can directly impact the inputs of Printing Time, in the same manner as Printing Time on Cost predictions.

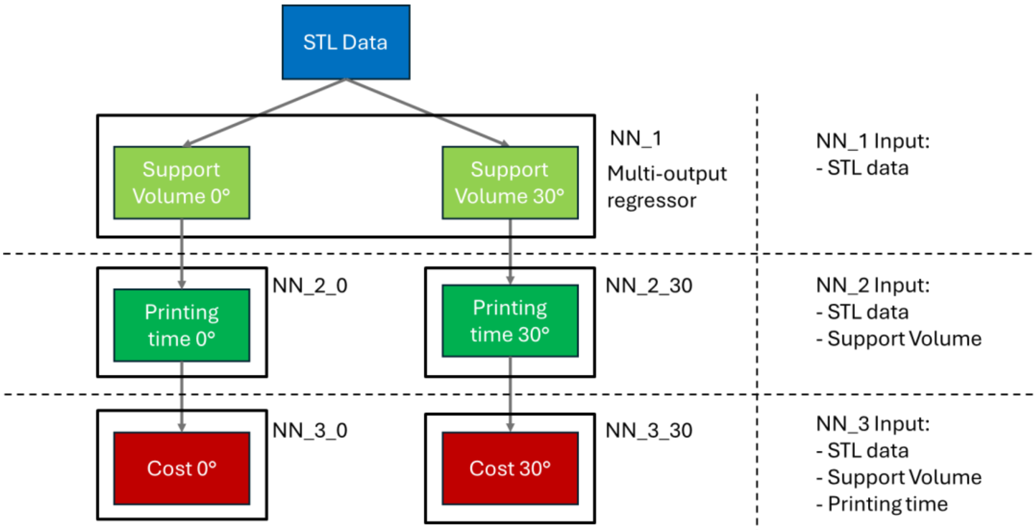

*Figure 90. Scheme of NNs trained, highlighting outputs on each NN.*

*Table 49. Hyperparameters used to train NNs.*

| **Hyperparameter** | **Value/Type** |
|---|---|
| Hidden layers | 5 |
| Neuron per hidden layer | 25, 50, 100, 50, 25 |
| Solver | Adam |
| Maximum iteration | 1000 |
| Activation function | ReLU |

The dataset normalisation allows the comparison of variables that have means and standard deviations measured on different units of measurement and orders of magnitude. In this paper, the open-source library “StandardScaler” [253]. Three different metrics have been adopted to evaluate and compare training and testing results, such as the MSE, MAE, and $R^2$ (coefficient of determination).

### 5.3.2 Training Results

Tables 50, 51, and 52 list the metrics obtained to evaluate the NN models, such as MSE, MAE, and $R^2$ for the train and test phases. Each metric evaluates a specific aspect of the trained model. Low MSE values imply that the model's predictions are close to the target values. MAE values measure the average amplitude of errors without considering their sign. The $R^2$ value indicates how well the model's predictions match the data. $R^2$ values vary from 0 to 1, with 1 representing perfect prediction and 0 indicating no predictive power.

Figures 91, 92, and 93 show the convergence trend, the Loss trend and the Validation score at each epoch, for the trained NN. The Loss function measures the difference between the network’s prediction and the actual target value using the MSE metric for regression problems. At each epoch, the prediction and the relative loss function are computed, gradients are computed using the chain rule, and the weights are updated, leading to new predictions and a new loss until convergence or early stopping.

*Table 50. Performance metrics of the NN_1 model.*

| **NN_1** | **Train metrics** | **Test metrics** |
|---|---|---|
| Support Volume 0° | $R^2$: 0.9975<br>MSE: 0.0022<br>MAE: 0.0338 | $R^2$: 0.9973<br>MSE: 0.0037<br>MAE: 0.0416 |
| Support Volume 30° | $R^2$: 0.9930<br>MSE: 0.0062<br>MAE: 0.0602 | $R^2$: 0.9912<br>MSE: 0.0125<br>MAE: 0.0704 |

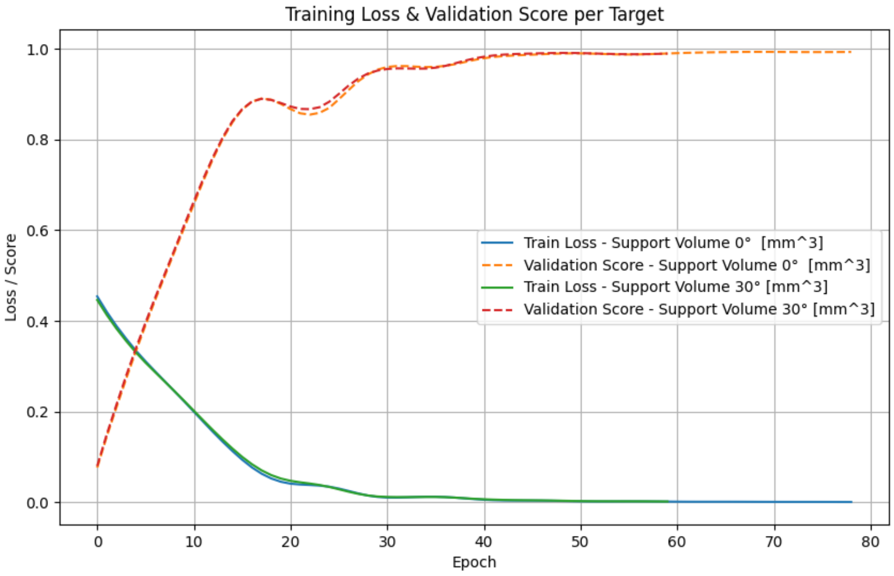

*Figure 91. The NN_1 convergence trends through epochs, evaluated by the Loss function and Validation score. These trends are reported for Support Volume 0◦ and Support Volume 30◦.*

*Table 51. Performance metrics of the NN_2_0 and NN_2_30 models.*

| **NN_2** | **Train metrics** | **Test metrics** |
|---|---|---|
| NN_2_0: Printing Time 0° | R²: 0.9799<br>MSE: 0.0191<br>MAE: 0.0992 | R²: 0.9864<br>MSE: 0.0163<br>MAE: 0.1036 |
| NN_2_30: Printing Time 30° | R²: 0.9865<br>MSE: 0.0122<br>MAE: 0.0811 | R²: 0. 9846<br>MSE: 0.0212<br>MAE: 0.1023 |

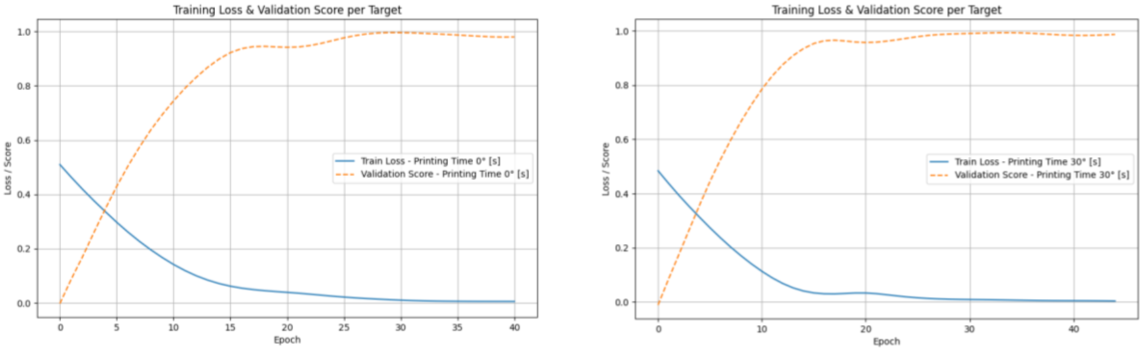

(**a**) (**b**)

*Figure 92. The convergence trend through epochs, evaluated by the Loss function and Validation score for (a) NN_2-0 Printing Time 0◦; (b) NN_2-30 Printing Time 30◦.*

*Table 52. Performance metrics of the NN_3_0 and NN_3_30 models.*

| **NN_3** | **Train metrics** | **Test metrics** |
|---|---|---|
| NN_3_0: Analytical Cost 0° | R²: 0. 9984<br>MSE: 0. 0015<br>MAE: 0. 0284 | R²: 0. 9965<br>MSE: 0.0044<br>MAE: 0.0457 |
| NN_3_30: Analytical Cost 30° | R²: 0.9983<br>MSE: 0.0015<br>MAE: 0.0295 | R²: 0.9937<br>MSE: 0.0044<br>MAE: 0.0527 |

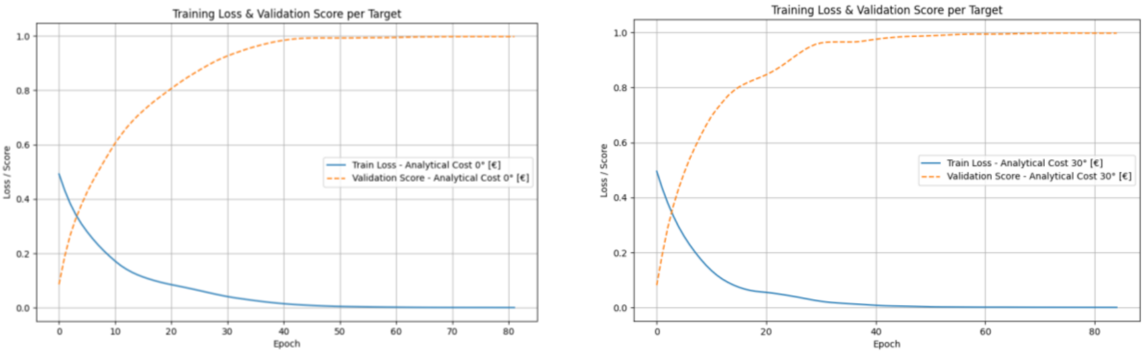

(**a**) (**b**)

*Figure 93. The convergence trend through epochs, evaluated by the Loss function and Validation score for (a) NN_3-0 Cost 0◦; (b) NN_3-30 Cost 30◦.*

Figure 94 illustrates the Web Interface Service Platform that utilises the three trained neural networks. By uploading an STL file to this online tool, it is now possible to predict the necessary support volume, printing time, and cost.

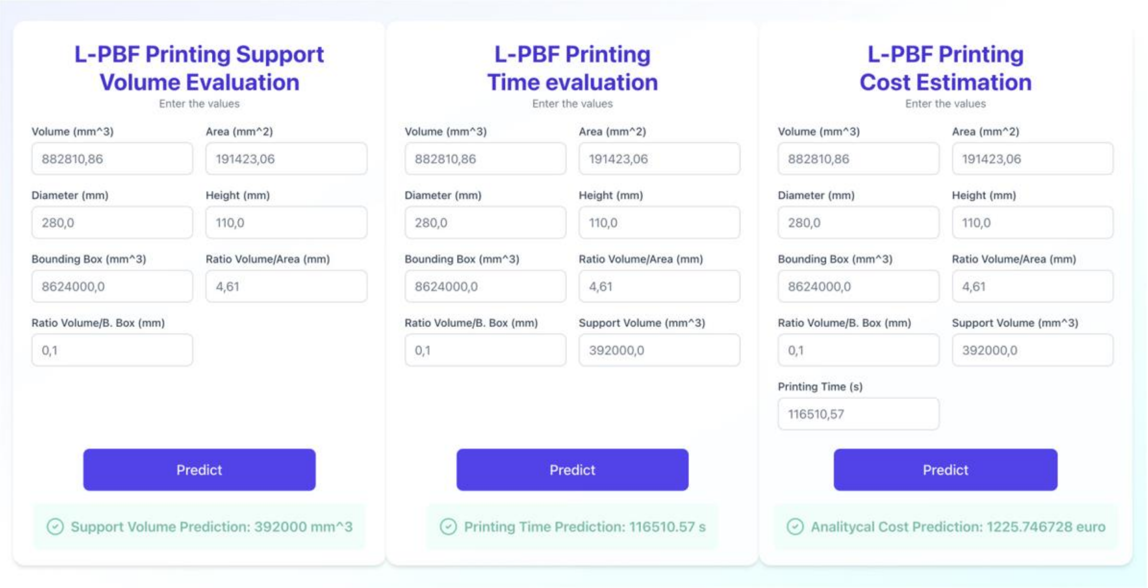

**L-PBF Printing Support Volume Evaluation**

Enter the values

Volume (mm^3): 882810,86
Area (mm^2): 191423,06
Diameter (mm): 280,0
Height (mm): 110,0
Bounding Box (mm^3): 8624000,0
Ratio Volume/Area (mm): 4,61
Ratio Volume/B. Box (mm): 0,1

Support Volume Prediction: 392000 mm^3

**L-PBF Printing Time evaluation**

Enter the values

Volume (mm^3): 882810,86
Area (mm^2): 191423,06
Diameter (mm): 280,0
Height (mm): 110,0
Bounding Box (mm^3): 8624000,0
Ratio Volume/Area (mm): 4,61
Ratio Volume/B. Box (mm): 0,1
Support Volume (mm^3): 392000,0

Printing Time Prediction: 116510.57 s

**L-PBF Printing Cost Estimation**

Enter the values

Volume (mm^3): 882810,86
Area (mm^2): 191423,06
Diameter (mm): 280,0
Height (mm): 110,0
Bounding Box (mm^3): 8624000,0
Ratio Volume/Area (mm): 4,61
Ratio Volume/B. Box (mm): 0,1
Support Volume (mm^3): 392000,0
Printing Time (s): 116510,57

Analitycal Cost Prediction: 1225.746728 euro

*Figure 94. Realised Web Interface Platform.*

The platform integrates these predictive models into a user-friendly environment, allowing users to quickly obtain key manufacturing insights without requiring in-depth technical expertise. Once the STL file is submitted, the system automatically processes the geometry, extracts relevant features, and feeds them into the neural networks. Each model then generates its prediction, which is presented to the user in a clear and structured format.

This approach significantly streamlines the pre-printing phase, enabling faster decision-making and improved resource planning. By providing early estimates of material usage, production time, and overall cost, the platform helps users optimise design choices, reduce trial-and-error iterations, and enhance the efficiency of the AM workflow.

# 6 Discussion and Conclusions

This thesis investigated design tools and methods for enhancing additive manufacturing integration in the industrial sector through virtual prototyping and artificial intelligence techniques.

The thesis initially analysed the state of the art of additive manufacturing techniques, with a particular focus on the laser-powder bed fusion process for metal parts, the design for additive manufacturing state of the art, posing attention on the topology optimisation techniques, and the state of the art of machine learning application in additive manufacturing and design for additive manufacturing for the laser-powder bed fusion process for metals.

A method is proposed to support designers in integrating machine learning models in the design for additive manufacturing workflows, combining the additive manufacturing design rules, such as technical constraints related to the chosen production process and optimisation techniques, with the training of a machine learning model for the defined objectives. Machine learning can be applied in many ways, and each application level calls for its own set of tools and algorithms. Typically, multiple tools and algorithms need to be combined to determine the approach that best meets the intended goals. Some machine learning applications for the metal laser-powder bed fusion process can already be found in the literature. These applications can be divided into different Levels, such as the geometrical design level, process configuration level, and process monitoring level.

To overcome the lack of supporting design tools to rapidly estimate a CAD model in the early design phases, three machine learning models for metal laser-powder bed fusion components have been developed and trained. The first model, a decision tree classifier, has been developed to predict printability from data extracted directly from the CAD models. The second model, a random forest regressor, was trained to estimate printing time directly from features extracted from the STL file. The last model, a cascade of three neural networks, has been built to predict, directly for the STL data, the necessary support volume, printing time and cost, depending on the part orientation.

Different design optimisation applications, related to the automotive sector, are also presented. These optimisations aim to identify lightweight geometries to exploit the best additive manufacturing benefit: the capacity of producing complex and intricate geometries that are impossible or difficult to manufacture with traditional manufacturing techniques. To lightweight automotive connecting rods, three different methods are presented: a topology optimisation, the application of lattice structures, and a parametric optimisation, supported by genetic algorithms and response surfaces, for exploring different solutions of lattice structures. The combination of a topology and a shape optimisation has been used to reduce the weight of an automotive lower arm. The laser-powder bed fusion manufacturability of all these designs has been checked with the support of the inherent strain method process simulation.

To understand the real mechanical behaviour of complex geometries obtainable with these algorithmic optimisation methods under loads, experimental data from tensile tests on increasing shape complexity Al-alloys specimens have been analysed. The findings of this study indicate a potential direct relationship between the quality of laser-powder bed fusion parts, assessed through their mechanical performance, and the complexity of their geometry.

Given the potentially unlimited amount of possible manufacturable geometries and objectives of a machine learning model, as future developments, studies on continual learning, that is, the possibility of updating a machine learning model without it forgetting the rules already learned, in the field of additive manufacturing, will be studied.

Future work could focus on several possible improvements to enhance the robustness, accuracy, and applicability of the proposed methodology. In the short term, increasing the size and diversity of training datasets, including different geometries, materials, and process parameters, could improve model generalisability and predictive performance. Additionally, integrating more advanced ML algorithms, such as ensemble methods, graph neural networks, or physics-informed models, could better capture complex relationships between geometry, process parameters, and part performance. In the medium term, embedding real-time process monitoring and sensor data into the design workflow would enable adaptive, feedback-driven optimisation, allowing machine learning models to update predictions based on actual production outcomes. Coupling this with multi-objective optimisation strategies could help designers balance trade-offs between weight, mechanical performance, manufacturability, and cost. Over the long term, the development of continual and lifelong learning frameworks will be critical, enabling models to evolve as new materials, processes, and design constraints emerge, without losing previously acquired knowledge. Ultimately, such advancements could support fully autonomous AM design pipelines, capable of generating highly optimised, complex industrial components while reducing development time, material waste, and overall production costs, thereby significantly accelerating the integration of AM in industrial applications.

# References

[1] Guo, D., Li, M., Lyu, Z., Kang, K., Wu, W., Zhong, R. Y., & Huang, G. Q. (2021). Synchroperation in industry 4.0 manufacturing. International Journal of Production Economics, 238, 108171. https://doi.org/10.1016/j.ijpe.2021.108171

[2] Dilberoglu, U. M., Gharehpapagh, B., Yaman, U., & Dolen, M. (2017). The Role of Additive Manufacturing in the Era of Industry 4.0. Procedia Manufacturing, 11, 545–554. https://doi.org/10.1016/j.promfg.2017.07.148

[3] ISO/ASTM 52900:2021; Additive Manufacturing—General Principles—Fundamentals and Vocabulary. ISO/ASTM International: Geneva, Switzerland, 2021.

[4] Gibson, I., Rosen, D. W., & Stucker, B. (2015). Additive Manufacturing Technologies (2nd ed.). Springer.

[5] Alogla, A. A., Baumers, M., Tuck, C., & Elmadih, W. (2021). The impact of additive manufacturing on the flexibility of a manufacturing supply chain. Applied Sciences, 11(8), 3707. https://doi.org/10.3390/app11083707

[6] Despeisse, M., & Ford, S. (2015). The role of additive manufacturing in improving resource efficiency and sustainability. In S. Umeda, M. Nakano, H. Mizuyama, H. Hibino, D. Kiritsis, & G. von Cieminski (Eds.), Advances in production management systems: Innovative production management towards sustainable growth (Vol. 460, pp. 129–136). Springer. https://doi.org/10.1007/978-3-319-22759-7_15

[7] McDermott, K. C., Winz, R. D., Hodgson, T. J., Kay, M. G., King, R. E., & McConnell, B. M. (2021). Performance tradeoffs for spare parts supply chains with additive manufacturing capability servicing intermittent demand. Journal of Defense Analytics and Logistics, 5(2), 179–213. https://doi.org/10.1108/JDAL-08-2020-0016

[8] Dalpadulo, E., Petruccioli, A., Gherardini, F., & Leali, F. (2022). A review of automotive spare-part reconstruction based on additive manufacturing. Journal of Manufacturing and Materials Processing, 6(6), 133. https://doi.org/10.3390/jmmp6060133

[9] Khan, N., & Riccio, A. (2024). A systematic review of design for additive manufacturing of aerospace lattice structures: Current trends and future directions. Progress in Aerospace Sciences, 149, 101021. https://doi.org/10.1016/j.paerosci.2024.101021

[10] Al Rashid, A., Ahmed, W., Khalid, M. Y., & Koç, M. (2021). Vat photopolymerization of polymers and polymer composites: Processes and applications. Additive Manufacturing, 47, 102279. https://doi.org/10.1016/j.addma.2021.102279

[11] DebRoy, T., Wei, H. L., Zuback, J. S., Mukherjee, T., Elmer, J. W., Milewski, J. O., Beese, A. M., Wilson-Heid, A., De, A., & Zhang, W. (2018). Additive manufacturing of metallic components – Process, structure and properties. Progress in Materials Science, 92, 112–224. https://doi.org/10.1016/j.pmatsci.2017.10.001

[12] Bourell, D., Kruth, J. P., Leu, M., Levy, G., Rosen, D., Beese, A. M., & Clare, A. (2017). Materials for additive manufacturing. CIRP Annals, 66(2), 659–681. https://doi.org/10.1016/j.cirp.2017.05.009

[13] Huang, R., Riddle, M. E., Graziano, D., Das, S., Nimbalkar, S., Cresko, J., & Masanet, E. (2017). Environmental and Economic Implications of Distributed Additive Manufacturing: The Case of Injection Mold Tooling. Journal of Industrial Ecology, 21(S1). Portico. https://doi.org/10.1111/jiec.12641

[14] Kunovjanek, M., Knofius, N., & Reiner, G. (2020). Additive manufacturing and supply chains – a systematic review. Production Planning &amp; Control, 33(13), 1231–1251. https://doi.org/10.1080/09537287.2020.1857874

[15] Gebler, M., Schoot Uiterkamp, A. J. M., & Visser, C. (2014). A global sustainability perspective on 3D printing technologies. Energy Policy, 74, 158–167. https://doi.org/10.1016/j.enpol.2014.08.03

[16] Weller, C., Kleer, R., & Piller, F. T. (2015). Economic implications of 3D printing: Market structure models in light of additive manufacturing revisited. International Journal of Production Economics, 164, 43–56. https://doi.org/10.1016/j.ijpe.2015.02.020

[17] Louvis, E., Fox, P., Sutcliffe, C. J. (2011). Selective laser melting of aluminium components. Journal of Materials Processing Technology, 211(2), 275–284. https://doi.org/10.1016/j.jmatprotec.2010.09.019

[18] Shanthar, R., Chen, K., Abeykoon, C. (2023). Powder-Based Additive Manufacturing: A Critical Review of Materials, Methods, Opportunities, and Challenges. Advanced Engineering Materials, 25(19). Portico. https://doi.org/10.1002/adem.202300375

[19] Mercelis, P., Kruth, J. (2006). Residual stresses in selective laser sintering and selective laser melting. Rapid Prototyping Journal, 12(5), 254–265. https://doi.org/10.1108/13552540610707013

[20] Stopyra, W., Gruber, K., Smolina, I., Kurzynowski, T., Kuźnicka, B. (2020). Laser powder bed fusion of AA7075 alloy: Influence of process parameters on porosity and hot cracking. Additive Manufacturing, 35, 101270. https://doi.org/10.1016/j.addma.2020.101270

[21] Yap, C. Y., Chua, C. K., Dong, Z. L., Liu, Z. H., Zhang, D. Q., Loh, L. E., Sing, S. L. (2015). Review of selective laser melting: Materials and applications. Applied Physics Reviews, 2(4). https://doi.org/10.1063/1.4935926

[22] King, W. E., Anderson, A. T., Ferencz, R. M., Hodge, N. E., Kamath, C., Khairallah, S. A., Rubenchik, A. M. (2015). Laser powder bed fusion additive manufacturing of metals; physics, computational, and materials challenges. Applied Physics Reviews, 2(4), 041304. https://doi.org/10.1063/1.4937809

[23] Fang, Z.-C., Wu, Z.-L., Huang, C.-G., Wu, C.-W. (2020). Review on residual stress in selective laser melting additive manufacturing of alloy parts. Optics &amp; Laser Technology, 129, 106283. https://doi.org/10.1016/j.optlastec.2020.106283

[24] Parry, L. A., Ashcroft, I. A., Wildman, R. D. (2019). Geometrical effects on residual stress in selective laser melting. Additive Manufacturing, 25, 166–175. https://doi.org/10.1016/j.addma.2018.09.026

[25] Zaeh, M. F., Branner, G. (2009). Investigations on residual stresses and deformations in selective laser melting. Production Engineering, 4(1), 35–45. https://doi.org/10.1007/s11740-009-0192-y

[26] Kotadia, H. R., Gibbons, G., Das, A., Howes, P. D. (2021). A review of Laser Powder Bed Fusion Additive Manufacturing of aluminium alloys: Microstructure and properties. Additive Manufacturing, 46, 102155. https://doi.org/10.1016/j.addma.2021.102155

[27] Rehman, M., Wang, Y., Ishfaq, K., Mushtaq, R. T., Kumar, M. S., & Yang, H. (2023). Potential assessment in laser powder bed fusion of bionic porous Ti scaffolds concerning compressive behavior, porosity, and surface roughness. Journal of Manufacturing Processes, 95, 461–478. https://doi.org/10.1016/j.jmapro.2023.04.030

[28] Rehman, M., Wang, Y., Ishfaq, K., Yang, H., Mushtaq, R. T., Kumar, M. S., & Ahmed, A. (2023). Manufacturability study in laser powder bed fusion of biomedical Ti alloys for orthopedic implants: an investigation of mechanical properties, process-induced porosity and surface roughness. Rapid Prototyping Journal, 29(6), 1299–1323. https://doi.org/10.1108/rpj-02-2022-0042

[29] Trovato, M., Belluomo, L., Bici, M., Prist, M., Campana, F., & Cicconi, P. (2025). Machine learning in design for additive manufacturing: A state-of-the-art discussion for a support tool in product design lifecycle. The International Journal of Advanced Manufacturing Technology, 137(5–6), 2157–2180. https://doi.org/10.1007/s00170-025-15273-9

[30] Trevisan, F., Calignano, F., Lorusso, M., Pakkanen, J., Aversa, A., Ambrosio, E. P., Lombardi, M., Fino, P., & Manfredi, D. (2017). On the Selective Laser Melting (SLM) of the AlSi10Mg Alloy: Process, Microstructure, and Mechanical Properties. Materials, 10(1), 76. https://doi.org/10.3390/ma10010076

[31] Li, C., Zhang, Q., Ren, Y., Chen, W., Li, W., Chen, J., & Zhou, L. (2024). Influence of energy density on the microstructure and property regulation of additive manufactured pure nickel. Advances in Mechanical Engineering, 16(2). https://doi.org/10.1177/16878132241230228

[32] Li, D., Zhang, X., Qin, R., Xu, J., Yue, D., & Chen, B. (2023). Influence of processing parameters on AlSi10Mg lattice structure during selective laser melting: Manufacturing defects, thermal behavior and compression properties. Optics &amp; Laser Technology, 161, 109182. https://doi.org/10.1016/j.optlastec.2023.109182

[33] Wycisk, E., Siddique, S., Herzog, D., Walther, F., & Emmelmann, C. (2015). Fatigue Performance of Laser Additive Manufactured Ti–6Al–4V in Very High Cycle Fatigue Regime up to 109 Cycles. Frontiers in Materials, 2. https://doi.org/10.3389/fmats.2015.00072

[34] Hovig, E. W., Azar, A. S., Grytten, F., Sørby, K., & Andreassen, E. (2018). Determination of Anisotropic Mechanical Properties for Materials Processed by Laser Powder Bed Fusion. Advances in Materials Science and Engineering, 2018(1). Portico. https://doi.org/10.1155/2018/7650303

[35] Kruth, J.-P., Levy, G., Klocke, F., & Childs, T. H. C. (2007). Consolidation phenomena in laser and powder-bed based layered manufacturing. CIRP Annals, 56(2), 730–759. https://doi.org/10.1016/j.cirp.2007.10.004

[36] du Plessis, A., Razavi, N., Benedetti, M., Murchio, S., Leary, M., Watson, M., Bhate, D., & Berto, F. (2022). Properties and applications of additively manufactured metallic cellular materials: A review. Progress in Materials Science, 125, 100918. https://doi.org/10.1016/j.pmatsci.2021.100918

[37] Bartolomeu, F., Gasik, M., Silva, F. S., & Miranda, G. (2022). Mechanical Properties of Ti6Al4V Fabricated by Laser Powder Bed Fusion: A Review Focused on the Processing and Microstructural Parameters Influence on the Final Properties. Metals, 12(6), 986. https://doi.org/10.3390/met12060986

[38] Wang, X., Gong, X., & Chou, K. (2015). Review on Powder-Bed Laser Additive Manufacturing of Inconel 718 Parts. Volume 1: Processing. https://doi.org/10.1115/msec2015-9322

[39] D’Andrea, D. (2023). Additive Manufacturing of AISI 316L Stainless Steel: A Review. Metals, 13(8), 1370. https://doi.org/10.3390/met13081370

[40] Zhao, L., Song, L., Santos Macías, J. G., Zhu, Y., Huang, M., Simar, A., & Li, Z. (2022). Review on the correlation between microstructure and mechanical performance for laser powder bed fusion AlSi10Mg. Additive Manufacturing, 56, 102914. https://doi.org/10.1016/j.addma.2022.102914

[41] Ozel, T., & Yang, L. (2021). Physics-based simulation models for digital twin development in laser powder bed fusion. International Journal of Mechatronics and Manufacturing Systems, 14(2), 1. https://doi.org/10.1504/ijmms.2021.10042371

[42] Körner, C., Bauereiß, A., & Attar, E. (2013). Fundamental consolidation mechanisms during selective beam melting of powders. Modelling and Simulation in Materials Science and Engineering, 21(8), 085011. https://doi.org/10.1088/0965-0393/21/8/085011

[43] Khairallah, S. A., & Anderson, A. (2014). Mesoscopic simulation model of selective laser melting of stainless steel powder. Journal of Materials Processing Technology, 214(11), 2627–2636. https://doi.org/10.1016/j.jmatprotec.2014.06.001

[44] Bugatti, M., & Semeraro, Q. (2018). Limitations of the inherent strain method in simulating powder bed fusion processes. Additive Manufacturing, 23, 329–346. https://doi.org/10.1016/j.addma.2018.05.041

[45] Bayat, M., Dong, W., Thorborg, J., To, A. C., & Hattel, J. H. (2021). A review of multi-scale and multi-physics simulations of metal additive manufacturing processes with focus on modeling strategies. Additive Manufacturing, 47, 102278. https://doi.org/10.1016/j.addma.2021.102278

[46] Setien, I., Chiumenti, M., van der Veen, S., San Sebastian, M., Garciandía, F., & Echeverría, A. (2019). Empirical methodology to determine inherent strains in additive manufacturing. Computers &amp; Mathematics with Applications, 78(7), 2282–2295. https://doi.org/10.1016/j.camwa.2018.05.015

[47] Bellet, M., Keumo Tematio, J., & Zhang, Y. (2023). The inherent strain method for simulation of additive manufacturing–A critical assessment based on a new variant of the method. International Journal for Numerical Methods in Engineering, 125(2). Portico. https://doi.org/10.1002/nme.7378

[48] Botha, H., Marais, D., & Kloppers, C. P. (2021). THE EFFICACY OF THE INHERENT STRAIN METHOD IN DETERMINING RESIDUAL STRESS IN IN718 SLM SPECIMENS. South African Journal of Industrial Engineering, 32(3). https://doi.org/10.7166/32-3-2662

[49] Adam, G. A. O., & Zimmer, D. (2015). On design for additive manufacturing: evaluating geometrical limitations. Rapid Prototyping Journal, 21(6), 662–670. https://doi.org/10.1108/rpj-06-2013-0060

[50] Hsu, W., & Woon, I. M. Y. (1998). Current research in the conceptual design of mechanical products. Computer-Aided Design, 30(5), 377–389. https://doi.org/10.1016/s0010-4485(97)00101-2

[51] Trovato, M., & Cicconi, P. (2023). Design tools for metal additive manufacturing: a critical and perspective overview. Procedia CIRP, 119, 1084–1090. https://doi.org/10.1016/j.procir.2023.03.151

[52] Kotadia, H. R., Gibbons, G., Das, A., & Howes, P. D. (2021). A review of Laser Powder Bed Fusion Additive Manufacturing of aluminium alloys: Microstructure and properties. Additive Manufacturing, 46, 102155. https://doi.org/10.1016/j.addma.2021.102155

[53] Gibson, I., Rosen, D. W., & Stucker, B. (2010). Additive manufacturing technologies: Rapid prototyping to direct digital manufacturing (1st ed.). Springer. https://doi.org/10.1007/978-1-4419-1120-9

[54] Zhang, B., Goel, A., Ghalsasi, O., & Anand, S. (2019). CAD-based design and pre-processing tools for additive manufacturing. Journal of Manufacturing Systems, 52, 227–241. https://doi.org/10.1016/j.jmsy.2019.03.005

[55] Gan, M. X., & Wong, C. H. (2016). Practical support structures for selective laser melting. Journal of Materials Processing Technology, 238, 474–484. https://doi.org/10.1016/j.jmatprotec.2016.08.006

[56] Cheng, B., & Chou, K. (2015). Geometric consideration of support structures in part overhang fabrications by electron beam additive manufacturing. Computer-Aided Design, 69, 102–111. https://doi.org/10.1016/j.cad.2015.06.007

[57] Jiang, J., Xu, X., & Stringer, J. (2018). Support structures for additive manufacturing: A review. Journal of Manufacturing and Materials Processing, 2(4), 64. https://doi.org/10.3390/jmmp2040064

[58] Nelaturi, S., Behandish, M., Mirzendehdel, A. M., & de Kleer, J. (2019). Automatic support removal for additive manufacturing post-processing. Computer-Aided Design, 115, 135–146. https://doi.org/10.1016/j.cad.2019.05.030

[59] Campana, F., & Germani, M. (2008). Datum identification for tolerances control on dense clouds of points. Computer-Aided Design & Applications, 5(1-4), 209–219. https://doi.org/10.3722/cadaps.2008.209-219

[60] Cicconi, P., Mandolini, M., Favi, C., Campi, F., & Germani, M. (2021). Metal additive manufacturing for the rapid prototyping of shaped parts: A case study. Computer-Aided Design & Applications, 18(5), 1061–1079. https://doi.org/10.14733/cadaps.2021.1061-1079

[61] Das, P., Chandran, R., Samant, R., & Anand, S. (2015). Optimum part build orientation in additive manufacturing for minimizing part errors and support structures. Procedia Manufacturing, 1, 343–354. https://doi.org/10.1016/j.promfg.2015.09.041

[62] Calignano, F. (2014). Design optimization of supports for overhanging structures in aluminum and titanium alloys by selective laser melting. Materials & Design, 64, 203–213. https://doi.org/10.1016/j.matdes.2014.07.043

[63] Redwood, B., Schöffer, F., & Garret, B. (2017). The 3D printing handbook: Technologies, design and applications. 3D Hubs B.V. ISBN 978-90-827485-0-5.

[64] Trovato, M., Vigna, A., Cicconi, P., Belluomo, L., Bici, M., & Campana, F. (2025). Analyzing Tools and Methods in Design for Additive Manufacturing: Workflow and Test Cases. Computer-Aided Design and Applications, 1125–1135. https://doi.org/10.14733/cadaps.2025.1125-1135

[65] Várady, T., Martin, R. R., & Cox, J. (1997). Reverse engineering of geometric models—an introduction. Computer-Aided Design, 29(4), 255–268. https://doi.org/10.1016/s0010-4485(96)00054-1

[66] Braga, D. F. O., Tavares, S. M. O., da Silva, L. F. M., Moreira, P. M. G. P., & de Castro, P. M. S. T. (2014). Advanced design for lightweight structures: Review and prospects. Progress in Aerospace Sciences, 69, 29–39. https://doi.org/10.1016/j.paerosci.2014.03.003

[67] Razvan, C. (2014). OVERVIEW OF STRUCTURAL TOPOLOGY OPTIMIZATION METHODS FOR PLANE AND SOLID STRUCTURES. ANNALS OF THE ORADEA UNIVERSITY. Fascicle of Management and Technological Engineering., XXIII (XIII), 2014/3(3). https://doi.org/10.15660/auofmte.2014-3.3043

[68] Rozvany, G. I. N. (2001). Aims, scope, methods, history and unified terminology of computer-aided topology optimization in structural mechanics. Structural and Multidisciplinary Optimization, 21(2), 90–108. https://doi.org/10.1007/s001580050174

[69] van Dijk, N. P., Maute, K., Langelaar, M., & van Keulen, F. (2013). Level-set methods for structural topology optimization: a review. Structural and Multidisciplinary Optimization, 48(3), 437–472. https://doi.org/10.1007/s00158-013-0912-y

[70] Leary, M., Mazur, M., Williams, H., Yang, E., Alghamdi, A., Lozanovski, B., Zhang, X., Shidid, D., Farahbod-Sternahl, L., Witt, G., Kelbassa, I., Choong, P., Qian, M., & Brandt, M. (2018). Inconel 625 lattice structures manufactured by selective laser melting (SLM): Mechanical properties, deformation and failure modes. Materials &amp; Design, 157, 179–199. https://doi.org/10.1016/j.matdes.2018.06.010

[71] Maconachie, T., Leary, M., Lozanovski, B., Zhang, X., Qian, M., Faruque, O., & Brandt, M. (2019). SLM lattice structures: Properties, performance, applications and challenges. Materials &amp; Design, 183, 108137. https://doi.org/10.1016/j.matdes.2019.108137

[72] Alomar, Z., & Concli, F. (2020). A Review of the Selective Laser Melting Lattice Structures and Their Numerical Models. Advanced Engineering Materials, 22(12). Portico. https://doi.org/10.1002/adem.202000611

[73] Gradišar, L., Klinc, R., Turk, Ž., & Dolenc, M. (2022). Generative Design Methodology and Framework Exploiting Designer-Algorithm Synergies. Buildings, 12(12), 2194. https://doi.org/10.3390/buildings12122194

[74] Jaisawal, R., & Agrawal, V. (2021). Generative Design Method (GDM) – A State of Art. IOP Conference Series: Materials Science and Engineering, 1104(1), 012036. https://doi.org/10.1088/1757-899x/1104/1/012036

[75] Chen, Q., Gao, Y., Ding, L., Zhou, C., Han, W., Zhou, Y., & Shi, Y. (2023). Genetic Algorithm–Based Multiobjective Optimization for 3D Printable Design of a Double-Shell Lunar Habitat Structure. Journal of Aerospace Engineering, 36(6). https://doi.org/10.1061/jaeeez.aseng-4755

[76] Albadr, M. A., Tiun, S., Ayob, M., & AL-Dhief, F. (2020). Genetic Algorithm Based on Natural Selection Theory for Optimization Problems. Symmetry, 12(11), 1758. https://doi.org/10.3390/sym12111758

[77] Allaire, G., Dapogny, C., & Jouve, F. (2021). Shape and topology optimization. Geometric Partial Differential Equations - Part II, 1–132. https://doi.org/10.1016/bs.hna.2020.10.004

[78] Aiza, I., Baldi, C., de la Vega, F. M., Sebastiani, S., Veronese, N. E., Yousefi, M., Mosallanejad, M. H., Maleki, E., Guagliano, M., Iuliano, L., Saboori, A., & Bagherifard, S. (2025). Effects of build orientation and inclined features on physical, microstructural and mechanical properties of powder bed fusion additively manufactured metallic parts. Progress in Materials Science, 147, 101357. https://doi.org/10.1016/j.pmatsci.2024.101357

[79] Javidrad, H. R., & Javidrad, F. (2023). Review of state-of-the-art research on the design and manufacturing of support structures for powder-bed fusion additive manufacturing. Progress in Additive Manufacturing, 8(6), 1517–1542. https://doi.org/10.1007/s40964-023-00419-6

[80] Bartsch, K., & Emmelmann, C. (2021). Enabling Cost-Based Support Structure Optimization in Laser Powder Bed Fusion of Metals. JOM, 74(3), 1126–1135. https://doi.org/10.1007/s11837-021-05055-5

[81] Awad, M., & Khanna, R. (2015). Machine Learning. Efficient Learning Machines, 1–18. https://doi.org/10.1007/978-1-4302-5990-9_1

[82] Kumar, S., Gopi, T., Harikeerthana, N., Gupta, M. K., Gaur, V., Krolczyk, G. M., Wu, C. (2022). Machine learning techniques in additive manufacturing: a state of the art review on design, processes and production control. Journal of Intelligent Manufacturing, 34(1), 21–55. https://doi.org/10.1007/s10845-022-02029-5

[83] Awad, M., Khanna, R. (2015). Machine Learning. Efficient Learning Machines, 1–18. https://doi.org/10.1007/978-1-4302-5990-9_1

[84] Trovato, M., Amicarelli, M., Prist, M., & Cicconi, P. (2025). A Neural Network-Based Approach to Estimate Printing Time and Cost in L-PBF Projects. Machines, 13(7), 550. https://doi.org/10.3390/machines13070550

[85] Cunningham, P., Cord, M., Delany, S. J. (n.d.). Supervised Learning. Cognitive Technologies, 21–49. https://doi.org/10.1007/978-3-540-75171-7_2

[86] Joshi, M., Flood, A., Sparks, T., & Liou, F. W. (2019, August). Applications of supervised machine learning algorithms in additive manufacturing: A review. In Proceedings of the 2019 International Solid Freeform Fabrication Symposium (University of Texas at Austin). Retrieved from https://repositories.lib.utexas.edu/items/ee152415-ab6b-4efb-b044-62872715a89c

[87] Zhang, Y., Safdar, M., Xie, J., Li, J., Sage, M., & Zhao, Y. F. (2022). A systematic review on data of additive manufacturing for machine learning applications: The data quality, type, preprocessing, and management. Journal of Intelligent Manufacturing, 34(8), 3305–3340. https://doi.org/10.1007/s10845-022-02017-9

[88] García-Moreno, A.-I., Alvarado-Orozco, J.-M., Ibarra-Medina, J., & Martínez-Franco, E. (2020). Image-based porosity classification in Al-alloys by laser metal deposition using random forests. The International Journal of Advanced Manufacturing Technology, 110(9), 2827–2845. https://doi.org/10.1007/s00170-020-05887-6

[89] Kumar, P., & Jain, N. K. (2022). Surface roughness prediction in micro-plasma transferred arc metal additive manufacturing process using K-nearest neighbors algorithm. The International Journal of Advanced Manufacturing Technology, 119(5–6), 2985–2997. https://doi.org/10.1007/s00170-021-08639-2

[90] Vandecasteele, M., Heylen, R., Iuso, D., Thanki, A., Philips, W., Witvrouw, A., Verhees, D., & Booth, B. G. (2023). Towards material and process agnostic features for the classification of pore types in metal additive manufacturing. Materials & Design, 227, 111757. https://doi.org/10.1016/j.matdes.2023.111757

[91] Banadaki, Y. M., Razaviarab, N., Fekrmandi, H., Li, G., Mensah, P., Bai, S., & Sharifi, S. (2022). Automated quality and process control for additive manufacturing using deep convolutional neural networks. Recent Progress in Materials, 4(1), Article 005. https://doi.org/10.21926/rpm.2201005

[92] Xiao, S., Li, J., Wang, Z., Chen, Y., & Tofighi, S. (2024). Advancing additive manufacturing through machine learning techniques: A state-of-the-art review. Future Internet, 16(11), 419. https://doi.org/10.3390/fi16110419

[93] Baturynska, I., Semeniuta, O., & Martinsen, K. (2018). Optimization of Process Parameters for Powder Bed Fusion Additive Manufacturing by Combination of Machine Learning and Finite Element Method: A Conceptual Framework. Procedia CIRP, 67, 227–232. https://doi.org/10.1016/j.procir.2017.12.204

[94] Mattera, G., Piscopo, G., Longobardi, M., Giacalone, M., & Nele, L. (2024). Improving the Interpretability of Data-Driven Models for Additive Manufacturing Processes Using Clusterwise Regression. Mathematics, 12(16), 2559. https://doi.org/10.3390/math12162559

[95] Song, L., Huang, W., Han, X., & Mazumder, J. (2017). Real-Time Composition Monitoring Using Support Vector Regression of Laser-Induced Plasma for Laser Additive Manufacturing. IEEE Transactions on Industrial Electronics, 64(1), 633–642. https://doi.org/10.1109/tie.2016.2608318

[96] Zhu, X., Jiang, F., Guo, C., Wang, Z., Dong, T., & Li, H. (2023). Prediction of melt pool shape in additive manufacturing based on machine learning methods. Optics & Laser Technology, 159, 108964. https://doi.org/10.1016/j.optlastec.2022.108964

[97] Equbal, M. A., Equbal, A., Khan, Z. A., & Badruddin, I. A. (2025). Machine learning in additive manufacturing: A comprehensive insight. International Journal of Lightweight Materials and Manufacture, 8(2), 264–284. https://doi.org/10.1016/j.ijlmm.2024.10.002

[98] Ciccone, F., Bacciaglia, A., & Ceruti, A. (2023). Optimization with artificial intelligence in additive manufacturing: a systematic review. Journal of the Brazilian Society of Mechanical Sciences and Engineering, 45(6). https://doi.org/10.1007/s40430-023-04200-2

[99] Gupta, N. (2013). Artificial Neural Network. Network and Complex Systems 3 (1).

[100] Zou, J., Han, Y., So, S.-S. (2008). Overview of Artificial Neural Networks. Artificial Neural Networks, 14–22. https://doi.org/10.1007/978-1-60327-101-1_2

[101] Dayan,P.: Unsupervised Learning. The MIT Encyclopedia of the Cognitive Sciences. Wilson, RA Keil, F, editors.

[102] Mahesh, B.: Machine Learning Algorithms - A Review. International Journal of Science and Research, 7426 (2018).

[103] Chua, A. E., Pfeifer, L. D., Sekera, E. R., Hummon, A. B., & Desaire, H. (2023). Workflow for evaluating normalization tools for omics data using supervised and unsupervised machine learning. Journal of the American Society for Mass Spectrometry, 34(12), 2775–2784. https://doi.org/10.1021/jasms.3c00295

[104] Naeem, S., Ali, A., Anam, S., & Ahmed, M. M. (2023). An unsupervised machine learning algorithm: Comprehensive review. International Journal of Computing and Digital Systems, 13(1), 911–921. https://doi.org/10.12785/ijcds/130172

[105] Sutton, R. S., & Barto, A. G. (2018). Reinforcement learning: An introduction (2nd ed.). MIT Press.

[106] Gupta, N. (2013). Artificial neural network. Network and Complex Systems, 3(1), 1–6.

[107] Arulkumaran, K., Deisenroth, M. P., Brundage, M., & Bharath, A. A. (2017). Deep Reinforcement Learning: A Brief Survey. IEEE Signal Processing Magazine, 34(6), 26–38. https://doi.org/10.1109/msp.2017.2743240

[108] Johnson, N. S., Vulimiri, P. S., To, A. C., Zhang, X., Brice, C. A., Kappes, B. B., & Stebner, A. P. (2020). Invited review: Machine learning for materials developments in metals additive manufacturing. Additive Manufacturing, 36, 101641. https://doi.org/10.1016/j.addma.2020.101641

[109] Jin, Z., Zhang, Z., Demir, K., & Gu, G. X. (2020). Machine Learning for Advanced Additive Manufacturing. Matter, 3(5), 1541–1556. https://doi.org/10.1016/j.matt.2020.08.023

[110] Hsiao, S.-W., Tsai, H.-C. (2005). Applying a hybrid approach based on fuzzy neural network and genetic algorithm to product form design. International Journal of Industrial Ergonomics, 35(5), 411–428. https://doi.org/10.1016/j.ergon.2004.10.007

[111] Jang, S., Yoo, S., Kang, N. (2022). Generative Design by Reinforcement Learning: Enhancing the Diversity of Topology Optimization Designs. Computer-Aided Design, 146, 103225. https://doi.org/10.1016/j.cad.2022.103225

[112] Bendsøe, M. P. (1989). Optimal shape design as a material distribution problem. Structural Optimization, 1(4), 193–202. https://doi.org/10.1007/bf01650949

[113] Sethian, J. A., Wiegmann, A. (2000). Structural Boundary Design via Level Set and Immersed Interface Methods. Journal of Computational Physics, 163(2), 489–528. https://doi.org/10.1006/jcph.2000.6581

[114] Shin, S., Shin, D., Kang, N. (2023). Topology optimization via machine learning and deep learning: a review. Journal of Computational Design and Engineering, 10(4), 1736–1766. https://doi.org/10.1093/jcde/qwad072

[115] Rawat, S., Shen, M. H. (2019). Application of Adversarial Networks for 3D Structural Topology Optimization. SAE Technical Paper Series. https://doi.org/10.4271/2019-01-0829

[116] Nie, Z., Lin, T., Jiang, H., Kara, L. B. (2021). TopologyGAN: Topology Optimization Using Generative Adversarial Networks Based on Physical Fields Over the Initial Domain. Journal of Mechanical Design, 143(3). https://doi.org/10.1115/1.4049533

[117] Lee, S., Kim, H., Lieu, Q. X., Lee, J. (2020). CNN-based image recognition for topology optimization. Knowledge-Based Systems, 198, 105887. https://doi.org/10.1016/j.knosys.2020.105887

[118] Deng, C., Wang, Y., Qin, C., Fu, Y., Lu, W. (2022). Self-directed online machine learning for topology optimization. Nature Communications, 13(1). https://doi.org/10.1038/s41467-021-27713-7

[119] Li, H., Kafka, O. L., Gao, J., Yu, C., Nie, Y., Zhang, L., Tajdari, M., Tang, S., Guo, X., Li, G., Tang, S., Cheng, G., Liu, W. K. (2019). Clustering discretization methods for generation of material performance databases in machine learning and design optimization. Computational Mechanics, 64(2), 281–305. https://doi.org/10.1007/s00466-019-01716-0

[120] Kallioras, N. Ath., Lagaros, N. D. (2021). MLGen: Generative Design Framework Based on Machine Learning and Topology Optimization. Applied Sciences, 11(24), 12044. https://doi.org/10.3390/app112412044

[121] Shabani, B., Dukovski, V. (2021). Integration of Reverse Engineering and Topology Optimization with Additive Manufacturing. Computer-Aided Design and Applications, 19(1), 164–175. https://doi.org/10.14733/cadaps.2022.164-175

[122] Trovato, M., Perquoti, F., & Cicconi, P. (2023). Topological Optimization for the Redesigning of Components in Additive Manufacturing: The Case Study of the Connecting Rod. Engineering Proceedings, 56(1), 131. https://doi.org/10.3390/ASEC2023-16638

[123] Ahmad, A., Elamana, S., Kazmierczak, A., Bici, M., & Campana, F. (2023). Lightweight Horse Saddletree Through Reverse Engineering and Lattice Structure Design. Computer-Aided Design and Applications, 923–935. https://doi.org/10.14733/cadaps.2023.923-935

[124] Ahmad, A., Bici, M., Campana, F. (2021). Guidelines for Topology Optimization as Concept Design Tool and Their Application for the Mechanical Design of the Inner Frame to Support an Ancient Bronze Statue. Applied Sciences, 11(17), 7834. https://doi.org/10.3390/app11177834

[125] ZHU, J., ZHOU, H., WANG, C., ZHOU, L., YUAN, S., ZHANG, W. (2021). A review of topology optimization for additive manufacturing: Status and challenges. Chinese Journal of Aeronautics, 34(1), 91–110. https://doi.org/10.1016/j.cja.2020.09.020

[126] YÜKSEL, N., EREN, O., BÖRKLÜ, H. R., SEZER, H. K. (2024). Mechanical properties of additively manufactured lattice structures designed by deep learning. Thin-Walled Structures, 196, 111475. https://doi.org/10.1016/j.tws.2023.111475

[127] Teawdeswan, L., Dong, G. (2024). Inverse design of multi-material gyroid structures made by additive manufacturing. International Journal of Mechanical Sciences, 262, 108734. https://doi.org/10.1016/j.ijmecsci.2023.108734

[128] Després, N., Cyr, E., Setoodeh, P., Mohammadi, M. (2020). Deep Learning and Design for Additive Manufacturing: A Framework for Microlattice Architecture. JOM, 72(6), 2408–2418. https://doi.org/10.1007/s11837-020-04131

[129] Alejandrino, J. D., Concepcion, R. S. I., Lauguico, S. C., Tobias, R. R., Venancio, L., Macasaet, D., Bandala, A. A., Dadios, E. P. (2020). A Machine Learning Approach of Lattice Infill Pattern for Increasing Material Efficiency in Additive Manufacturing Processes. International Journal of Mechanical Engineering and Robotics Research, 1253–1263. https://doi.org/10.18178/ijmerr.9.9.1253-1263

[130] Doodi, R., Gunji, B. M. (2023). Prediction and experimental validation approach to improve performance of novel hybrid bio-inspired 3D printed lattice structures using artificial neural networks. Scientific Reports, 13(1). https://doi.org/10.1038/s41598-023-33935-0

[131] Armanfar, A., Taşmektepligil, A. A., Ustundag, E., Lazoglu, I., Gunpinar, E. (2024). A mechanical property prediction system for G-Lattices via machine learning. Engineering Optimization, 1–19. https://doi.org/10.1080/0305215x.2023.2295353

[132] Han, T., Qi, D., Ma, J., Sun, C. (2024). Generative design and mechanical properties of the lattice structures for tensile and compressive loading conditions fabricated by selective laser melting. Mechanics of Materials, 188, 104840. https://doi.org/10.1016/j.mechmat.2023.104840

[133] Lee, S., Zhang, Z., Gu, G. X. (2022). Generative machine learning algorithm for lattice structures with superior mechanical properties. Materials Horizons, 9(3), 952–960. https://doi.org/10.1039/d1mh01792f

[134] Shen, C., Sheng, Q., Zhao, H. (2023). Predicting effective thermal conductivity of fibrous and particulate composite materials using convolutional neural network. Mechanics of Materials, 186, 104804. https://doi.org/10.1016/j.mechmat.2023.104804

[135] Kuszczak, I., Azam, F. I., Bessa, M. A., Tan, P. J., Bosi, F. (2023). Bayesian optimisation of hexagonal honeycomb metamaterial. Extreme Mechanics Letters, 64, 102078. https://doi.org/10.1016/j.eml.2023.102078

[136] Hooshmand, M. J., Sakib-Uz-Zaman, C., Khondoker, M. A. H. (2023). Machine Learning Algorithms for Predicting Mechanical Stiffness of Lattice Structure-Based Polymer Foam. Materials, 16(22), 7173. https://doi.org/10.3390/ma16227173

[137] Asami, K., Roth, S., Krukenberg, M., Röver, T., Herzog, D., Emmelmann, C. (2023). Predictive modeling of lattice structure design for 316L stainless steel using machine learning in the L-PBF process. Journal of Laser Applications, 35(4). https://doi.org/10.2351/7.0001174

[138] Li, H., Lachmayer, R. (2019). Automated Exploration of Design Solution Space Applying the Generative Design Approach. Proceedings of the Design Society: International Conference on Engineering Design, 1(1), 1085–1094. https://doi.org/10.1017/dsi.2019.114

[139] Vlah, D., Žavbi, R., Vukašinović, N. (2020). EVALUATION OF TOPOLOGY OPTIMIZATION AND GENERATIVE DESIGN TOOLS AS SUPPORT FOR CONCEPTUAL DESIGN. Proceedings of the Design Society: DESIGN Conference, 1, 451–460. https://doi.org/10.1017/dsd.2020.165

[140] Hatchuel, A., Le Masson, P., Thomas, M., Weil, B. (2021). WHAT IS GENERATIVE IN GENERATIVE DESIGN TOOLS? UNCOVERING TOPOLOGICAL GENERATIVITY WITH A C-K MODEL OF EVOLUTIONARY ALGORITHMS. Proceedings of the Design Society, 1, 3419–3430. https://doi.org/10.1017/pds.2021.603

[141] Jang, S., Yoo, S., Kang, N. (2022). Generative Design by Reinforcement Learning: Enhancing the Diversity of Topology Optimization Designs. Computer-Aided Design, 146, 103225. https://doi.org/10.1016/j.cad.2022.103225

[142] Oh, S., Jung, Y., Kim, S., Lee, I., Kang, N. (2019). Deep Generative Design: Integration of Topology Optimization and Generative Models. Journal of Mechanical Design, 141(11). https://doi.org/10.1115/1.4044229

[143] Mountstephens, J., Teo, J. (2020). Progress and Challenges in Generative Product Design: A Review of Systems. Computers, 9(4), 80. https://doi.org/10.3390/computers9040080

[144] Yoo, S., Lee, S., Kim, S., Hwang, K. H., Park, J. H., Kang, N. (2021). Integrating deep learning into CAD/CAE system: generative design and evaluation of 3D conceptual wheel. Structural and Multidisciplinary Optimization, 64(4), 2725–2747. https://doi.org/10.1007/s00158-021-02953-9

[145] Belluomo, L., Bici, M., Campana, F. (2022). A Generative Design Method for Cultural Heritage Applications: Design of Supporting Structures for Artefacts. Computer-Aided Design and Applications, 663–681. https://doi.org/10.14733/cadaps.2023.663-681

[146] Belluomo, L., Trovato, M., Bici, M., Cicconi, P., Campana, F. (2024). An Iterative Generative Design Approach for Multi-Material Components. Computer-Aided Design and Applications, 1089–1102. https://doi.org/10.14733/cadaps.2024.1089-1102

[147] Buonamici, F., Carfagni, M., Furferi, R., Volpe, Y., Governi, L. (2020). Generative Design: An Explorative Study. Computer-Aided Design and Applications, 18(1), 144–155. https://doi.org/10.14733/cadaps.2021.144-155

[148] Birosz, M. T., Bátorfi, J. G., Andó, M. (2023). Extending the usability of the force-flow based topology optimization to the process of generative design. Meccanica, 58(4), 607–618. https://doi.org/10.1007/s11012-023-01641-w

[149] Song, B., Dong, S., Zhang, B., Liao, H., Coddet, C. (2012). Effects of processing parameters on microstructure and mechanical property of selective laser melted Ti6Al4V. Materials amp; Design, 35, 120–125. https://doi.org/10.1016/j.matdes.2011.09.051

[150] Babu, S. S., Mourad, A.-H. I., Harib, K. H., Vijayavenkataraman, S. (2022). Recent developments in the application of machine-learning towards accelerated predictive multiscale design and additive manufacturing. Virtual and Physical Prototyping, 18(1). https://doi.org/10.1080/17452759.2022.2141653

[151] Zhang, W., Mehta, A., Desai, P.S., Higgs, C.F. III: Machine learning enabled powder spreading process map for metal additive manufacturing (AM). Proceedings of the 28th Annual International Solid Freeform Fabrication Symposium – An Additive Manufacturing Conference, 1235-1249 (2017).

[152] Xiong, Y., Tang, Y., Zhou, Q., Ma, Y., Rosen, D. W. (2022). Intelligent additive manufacturing and design: state of the art and future perspectives. Additive Manufacturing, 59, 103139. https://doi.org/10.1016/j.addma.2022.103139

[153] Cloots, M., Spierings, A.B., Wegener, K.: Assessing New Support Minimizing Strategies for the Additive Manufacturing Technology SLM, (2013).

[154] Günaydın, A. C., Yıldız, A. R., & Kaya, N. (2022). Multi-objective optimization of build orientation considering support structure volume and build time in laser powder bed fusion. Materials Testing, 64(3), 323–338. https://doi.org/10.1515/mt-2021-2075

[155] Tapia, G., Elwany, A. H., Sang, H. (2016). Prediction of porosity in metal-based additive manufacturing using spatial Gaussian process models. Additive Manufacturing, 12, 282–290. https://doi.org/10.1016/j.addma.2016.05.009

[156] Ren, Y., Wang, Q. (2021). Gaussian-process based modeling and optimal control of melt-pool geometry in laser powder bed fusion. Journal of Intelligent Manufacturing, 33(8), 2239–2256. https://doi.org/10.1007/s10845-021-01781-4

[157] Baldi, N., Giorgetti, A., Polidoro, A., Palladino, M., Giovannetti, I., Arcidiacono, G., & Citti, P. (2023). A Supervised Machine Learning Model for Regression to Predict Melt Pool Formation and Morphology in Laser Powder Bed Fusion. Applied Sciences, 14(1), 328. https://doi.org/10.3390/app14010328

[158] Gor, M., Dobriyal, A., Wankhede, V., Sahlot, P., Grzelak, K., Kluczyński, J., Łuszczek, J. (2022). Density Prediction in Powder Bed Fusion Additive Manufacturing: Machine Learning-Based Techniques. Applied Sciences, 12(14), 7271. https://doi.org/10.3390/app12147271

[159] Zhang, M., Sun, C.-N., Zhang, X., Goh, P. C., Wei, J., Hardacre, D., Li, H. (2019). High cycle fatigue life prediction of laser additive manufactured stainless steel: A machine learning approach. International Journal of Fatigue, 128, 105194. https://doi.org/10.1016/j.ijfatigue.2019.105194

[160] Kappes, B., Moorthy, S., Drake, D., Geerlings, H., Stebner, A. (2018). Machine Learning to Optimize Additive Manufacturing Parameters for Laser Powder Bed Fusion of Inconel 718. Proceedings of the 9th International Symposium on Superalloy 718 amp; Derivatives: Energy, Aerospace, and Industrial Applications, 595–610. https://doi.org/10.1007/978-3-319-89480-5_39

[161] Tapia, G., Khairallah, S., Matthews, M., King, W. E., Elwany, A. (2017). Gaussian process-based surrogate modeling framework for process planning in laser powder-bed fusion additive manufacturing of 316L stainless steel. The International Journal of Advanced Manufacturing Technology, 94(9–12), 3591–3603. https://doi.org/10.1007/s00170-017-1045-z

[162] Bao, H., Wu, S., Wu, Z., Kang, G., Peng, X., Withers, P. J. (2021). A machine-learning fatigue life prediction approach of additively manufactured metals. Engineering Fracture Mechanics, 242, 107508. https://doi.org/10.1016/j.engfracmech.2020.107508

[163] Zhan, Z., Li, H. (2021). Machine learning based fatigue life prediction with effects of additive manufacturing process parameters for printed SS 316L. International Journal of Fatigue, 142, 105941. https://doi.org/10.1016/j.ijfatigue.2020.105941

[164] Mythreyi, O. V., Srinivaas, M. R., Amit Kumar, T., Jayaganthan, R. (2021). Machine-Learning-Based Prediction of Corrosion Behavior in Additively Manufactured Inconel 718. Data, 6(8), 80. https://doi.org/10.3390/data6080080

[165] Kopf, R., Gottwald, J., Jacob, A., Brandt, M., Lanza, G. (2018). Cost-oriented planning of equipment for selective laser melting (SLM) in production lines. CIRP Annals, 67(1), 471–474. https://doi.org/10.1016/j.cirp.2018.04.032

[166] Manuguerra, L., Mandolini, M., Germani, M., Sartini, M. (2023). MACHINE LEARNING FOR PARAMETRIC COST ESTIMATION OF AXISYMMETRIC COMPONENTS. Proceedings of the Design Society, 3, 2485–2494. https://doi.org/10.1017/pds.2023.249

[167] Rudolph, J.-P., Emmelmann, C. (2018). Self-learning Calculation for Selective Laser Melting. Procedia CIRP, 67, 185–190. https://doi.org/10.1016/j.procir.2017.12.197

[168] Chan, S. L., Lu, Y., Wang, Y. (2018). Data-driven cost estimation for additive manufacturing in cybermanufacturing. Journal of Manufacturing Systems, 46, 115–126. https://doi.org/10.1016/j.jmsy.2017.12.001

[169] Sharma, F., Dixit, U. S. (2019). Fuzzy set based cost model of additive manufacturing with specific example of selective laser sintering. Journal of Mechanical Science and Technology, 33(9), 4439–4449. https://doi.org/10.1007/s12206-019-0840-x

[170] Jin, Z., Zhang, Z., Demir, K., Gu, G. X. (2020). Machine Learning for Advanced Additive Manufacturing. Matter, 3(5), 1541–1556. https://doi.org/10.1016/j.matt.2020.08.023

[171] Wang, C., Tan, X. P., Tor, S. B., Lim, C. S. (2020). Machine learning in additive manufacturing: State-of-the-art and perspectives. Additive Manufacturing, 36, 101538. https://doi.org/10.1016/j.addma.2020.101538

[172] Qin, J., Hu, F., Liu, Y., Witherell, P., Wang, C. C. L., Rosen, D. W., Simpson, T. W., Lu, Y., Tang, Q. (2022). Research and application of machine learning for additive manufacturing. Additive Manufacturing, 52, 102691. https://doi.org/10.1016/j.addma.2022.102691

[173] Caggiano, A., Zhang, J., Alfieri, V., Caiazzo, F., Gao, R., Teti, R. (2019). Machine learning-based image processing for on-line defect recognition in additive manufacturing. CIRP Annals, 68(1), 451–454. https://doi.org/10.1016/j.cirp.2019.03.021

[174] Zhang, Y., Hong, G. S., Ye, D., Zhu, K., Fuh, J. Y. H. (2018). Extraction and evaluation of melt pool, plume and spatter information for powder-bed fusion AM process monitoring. Materials amp; Design, 156, 458–469. https://doi.org/10.1016/j.matdes.2018.07.002

[175] Ye, D., Hsi Fuh, J. Y., Zhang, Y., Hong, G. S., Zhu, K. (2018). In situ monitoring of selective laser melting using plume and spatter signatures by deep belief networks. ISA Transactions, 81, 96–104. https://doi.org/10.1016/j.isatra.2018.07.021

[176] Ghayoomi Mohammadi, M., Mahmoud, D., Elbestawi, M. (2021). On the application of machine learning for defect detection in L-PBF additive manufacturing. Optics amp; Laser Technology, 143, 107338. https://doi.org/10.1016/j.optlastec.2021.107338

[177] Shevchik, S. A., Kenel, C., Leinenbach, C., Wasmer, K. (2018). Acoustic emission for in situ quality monitoring in additive manufacturing using spectral convolutional neural networks. Additive Manufacturing, 21, 598–604. https://doi.org/10.1016/j.addma.2017.11.012

[178] Taherkhani, K., Eischer, C., Toyserkani, E. (2022). An unsupervised machine learning algorithm for in-situ defect-detection in laser powder-bed fusion. Journal of Manufacturing Processes, 81, 476–489. https://doi.org/10.1016/j.jmapro.2022.06.074

[179] Clijsters, S., Craeghs, T., Buls, S., Kempen, K., Kruth, J.-P. (2014). In situ quality control of the selective laser melting process using a high-speed, real-time melt pool monitoring system. The International Journal of Advanced Manufacturing Technology, 75(5–8), 1089–1101. https://doi.org/10.1007/s00170-014-6214-8

[180] Pandiyan, V., Masinelli, G., Claire, N., Le-Quang, T., Hamidi-Nasab, M., de Formanoir, C., Esmaeilzadeh, R., Goel, S., Marone, F., Logé, R., Van Petegem, S., Wasmer, K. (2022). Deep learning-based monitoring of laser powder bed fusion process on variable time-scales using heterogeneous sensing and operando X-ray radiography guidance. Additive Manufacturing, 58, 103007. https://doi.org/10.1016/j.addma.2022.103007

[181] Drissi-Daoudi, R., Pandiyan, V., Logé, R., Shevchik, S., Masinelli, G., Ghasemi-Tabasi, H., Parrilli, A., Wasmer, K. (2022). Differentiation of materials and laser powder bed fusion processing regimes from airborne acoustic emission combined with machine learning. Virtual and Physical Prototyping, 17(2), 181–204. https://doi.org/10.1080/17452759.2022.2028380

[182] Ye, D., Hong, G. S., Zhang, Y., Zhu, K., Fuh, J. Y. H. (2018). Defect detection in selective laser melting technology by acoustic signals with deep belief networks. The International Journal of Advanced Manufacturing Technology, 96(5–8), 2791–2801. https://doi.org/10.1007/s00170-018-1728-0

[183] Jafari-Marandi, R., Khanzadeh, M., Tian, W., Smith, B., Bian, L. (2019). From in-situ monitoring toward high-throughput process control: cost-driven decision-making framework for laser-based additive manufacturing. Journal of Manufacturing Systems, 51, 29–41. https://doi.org/10.1016/j.jmsy.2019.02.005

[184] Okaro, I. A., Jayasinghe, S., Sutcliffe, C., Black, K., Paoletti, P., Green, P. L. (2019). Automatic fault detection for laser powder-bed fusion using semi-supervised machine learning. Additive Manufacturing, 27, 42–53. https://doi.org/10.1016/j.addma.2019.01.006

[185] Montazeri, M., Rao, P. (2018). Sensor-Based Build Condition Monitoring in Laser Powder Bed Fusion Additive Manufacturing Process Using a Spectral Graph Theoretic Approach. Journal of Manufacturing Science and Engineering, 140(9). https://doi.org/10.1115/1.4040264

[186] Gobert, C., Reutzel, E. W., Petrich, J., Nassar, A. R., Phoha, S. (2018). Application of supervised machine learning for defect detection during metallic powder bed fusion additive manufacturing using high resolution imaging. Additive Manufacturing, 21, 517–528. https://doi.org/10.1016/j.addma.2018.04.005

[187] Scime, L., Beuth, J. (2019). Using machine learning to identify in-situ melt pool signatures indicative of flaw formation in a laser powder bed fusion additive manufacturing process. Additive Manufacturing, 25, 151–165. https://doi.org/10.1016/j.addma.2018.11.010

[188] Kwon, O., Kim, H. G., Ham, M. J., Kim, W., Kim, G.-H., Cho, J.-H., Kim, N. I., Kim, K. (2018). A deep neural network for classification of melt-pool images in metal additive manufacturing. Journal of Intelligent Manufacturing, 31(2), 375–386. https://doi.org/10.1007/s10845-018-1451-6

[189] Giorgetti, A., Baldi, N., Palladino, M., Ceccanti, F., Arcidiacono, G., Citti, P. (2023). A Method to Optimize Parameters Development in L-PBF Based on Single and Multitracks Analysis: A Case Study on Inconel 718 Alloy. Metals, 13(2), 306. https://doi.org/10.3390/met13020306

[190] Magana-Carranza, R., Sutcliffe, C. J., Patterson, E. A. (2021). The effect of processing parameters and material properties on residual forces induced in Laser Powder Bed Fusion (L-PBF). Additive Manufacturing, 46, 102192. https://doi.org/10.1016/j.addma.2021.102192

[191] Di Angelo, L., Di Stefano, P., Guardiani, E. (2020). Search for the Optimal Build Direction in Additive Manufacturing Technologies: A Review. Journal of Manufacturing and Materials Processing, 4(3), 71. https://doi.org/10.3390/jmmp4030071

[192] Jayapal, J., Kumaraguru, S., Varadarajan, S. (2023). Evaluation of computationally optimized design variants for additive manufacturing using a fuzzy multi-criterion decision-making approach. The International Journal of Advanced Manufacturing Technology, 129(11–12), 5199–5218. https://doi.org/10.1007/s00170-023-12641-1

[193] Qin, Y., Qi, Q., Shi, P., Scott, P. J., Jiang, X. (2020). Automatic generation of alternative build orientations for laser powder bed fusion based on facet clustering. Virtual and Physical Prototyping, 15(3), 307–324. https://doi.org/10.1080/17452759.2020.175608

[194] Huang, S. H., Liu, P., Mokasdar, A., & Hou, L. (2012). Additive manufacturing and its societal impact: a literature review. The International Journal of Advanced Manufacturing Technology, 67(5–8), 1191–1203. https://doi.org/10.1007/s00170-012-4558-5

[195] Andriankaja, H., Penot, J.-D., Chaudron, R., & Hleiss, R. (2026). A comparative environmental assessment of an automotive component processed by laser powder bed fusion (LPBF) versus CNC machining, with steel powder reuse impact analysis. Cleaner Engineering and Technology, 30, 101137. https://doi.org/10.1016/j.clet.2025.101137

[196] Valentan, B., Brajlih, T., Drstvenšek, I., & Balič, J. (2011). Development of a Part-Complexity Evaluation Model for Application in Additive Fabrication Technologies. Strojniški Vestnik – Journal of Mechanical Engineering, 57(10), 709–718. https://doi.org/10.5545/sv-jme.2010.057

[197] Pradel P, Bibb R, Zhu Z, Moultrie J (2017). Complexity is not for free: the impact of component complexity on additive manufacturing build time. The Conference on Rapid Design, Prototyping & Manufacturing (RDPM2017), Loughborough University, UK, April 27–28. https://hdl.handle.net/2134/24338

[198] Greco, A., Manco, P., Russo, M. B., & Gerbino, S. (2023). Complexity-driven product design: part 1—methodological framework and geometrical complexity index. International Journal on Interactive Design and Manufacturing (IJIDeM), 18(8), 5441–5456. https://doi.org/10.1007/s12008-023-01426-1

[199] Matoc, D. A., Maheta, N., Kanabar, B., & Sata, A. (2025). Hybrid framework for assessing additive manufacturing complexity index: integration of analytical hierarchy process and machine learning for VAT photopolymerization. Progress in Additive Manufacturing. https://doi.org/10.1007/s40964-025-01220-3

[200] Ben Slama, M., Chatti, S., & Louhichi, B. (2024). Novel method for shape complexity evaluation: a threshold from machining to additive manufacturing in the early design phase. Research in Engineering Design, 35(2), 191–214. https://doi.org/10.1007/s00163-023-00429-z

[201] Alsalla, H., Hao, L., & Smith, C. (2016). Fracture toughness and tensile strength of 316L stainless steel cellular lattice structures manufactured using the selective laser melting technique. Materials Science and Engineering: A, 669, 1–6. https://doi.org/10.1016/j.msea.2016.05.075

[202] Carrozza, A., Bircher, B. A., Aversa, A., & Biamino, S. (2023). Investigating Complex Geometrical Features in LPBF-Produced Parts: A Material-Based Comparison Between Different Titanium Alloys. Metals and Materials International, 29(12), 3697–3714. https://doi.org/10.1007/s12540-023-01460-4

[203] Bushra, J., Budinoff, H. D., Luna Falcon, P., & Latypov, M. (2023). Enhancing Design Guidelines for Metal Powder Bed Fusion: Analyzing Geometric Features to Improve Part Quality. Volume 5: 28th Design for Manufacturing and the Life Cycle Conference (DFMLC). https://doi.org/10.1115/detc2023-117019

[204] Deep, A., Miri Beidokhti, M., & Piili, H. (2025). Preliminary manufacturability evaluation of complex geometrical parts based on layer thickness in the metal powder bed fusion process. Progress in Additive Manufacturing, 10(11), 8941–8961. https://doi.org/10.1007/s40964-025-01202-5

[205] Al-Alimi, S., Yusuf, N. K., Ghaleb, A. M., Lajis, M. A., Shamsudin, S., Zhou, W., Altharan, Y. M., Abdulwahab, H. S., Saif, Y., Didane, D. H., S T T, I., & Adam, A. (2024). Recycling aluminium for sustainable development: A review of different processing technologies in green manufacturing. Results in Engineering, 23, 102566. https://doi.org/10.1016/j.rineng.2024.102566

[206] Sverdrup, H. U., Ragnarsdottir, K. V., & Koca, D. (2015). Aluminium for the future: Modelling the global production, market supply, demand, price and long term development of the global reserves. Resources, Conservation and Recycling, 103, 139–154. https://doi.org/10.1016/j.resconrec.2015.06.008

[207] Kotadia, H. R., Gibbons, G., Das, A., & Howes, P. D. (2021). A review of Laser Powder Bed Fusion Additive Manufacturing of aluminium alloys: Microstructure and properties. Additive Manufacturing, 46, 102155. https://doi.org/10.1016/j.addma.2021.102155

[208] Kenevisi, M. S., Yu, Y., & Lin, F. (2021). A review on additive manufacturing of Al–Cu (2xxx) aluminium alloys, processes and defects. Materials Science and Technology, 37(9), 805–829. https://doi.org/10.1080/02670836.2021.1958487

[209] Kan, W. H., Chiu, L. N. S., Lim, C. V. S., Zhu, Y., Tian, Y., Jiang, D., & Huang, A. (2022). A critical review on the effects of process-induced porosity on the mechanical properties of alloys fabricated by laser powder bed fusion. Journal of Materials Science, 57(21), 9818–9865. https://doi.org/10.1007/s10853-022-06990-7

[210] Koutiri, I., Pessard, E., Peyre, P., Amlou, O., & De Terris, T. (2018). Influence of SLM process parameters on the surface finish, porosity rate and fatigue behavior of as-built Inconel 625 parts. Journal of Materials Processing Technology, 255, 536–546. https://doi.org/10.1016/j.jmatprotec.2017.12.043

[211] Park, T.-H., Baek, M.-S., Hyer, H., Sohn, Y., & Lee, K.-A. (2021). Effect of direct aging on the microstructure and tensile properties of AlSi10Mg alloy manufactured by selective laser melting process. Materials Characterization, 176, 111113. https://doi.org/10.1016/j.matchar.2021.111113

[212] Shakil, S. I., Hadadzadeh, A., Shalchi Amirkhiz, B., Pirgazi, H., Mohammadi, M., & Haghshenas, M. (2021). Additive manufactured versus cast AlSi10Mg alloy: Microstructure and micromechanics. Results in Materials, 10, 100178. https://doi.org/10.1016/j.rinma.2021.100178

[213] Li, Z., Kuai, Z., Bai, P., Nie, Y., Fu, G., Liu, W., & Yang, S. (2019). Microstructure and Tensile Properties of AlSi10Mg Alloy Manufactured by Multi-Laser Beam Selective Laser Melting (SLM). Metals, 9(12), 1337. https://doi.org/10.3390/met9121337

[214] Wei, P., Wei, Z., Chen, Z., Du, J., He, Y., Li, J., & Zhou, Y. (2017). The AlSi10Mg samples produced by selective laser melting: single track, densification, microstructure and mechanical behavior. Applied Surface Science, 408, 38–50. https://doi.org/10.1016/j.apsusc.2017.02.215

[215] Park, T.-H., Baek, M.-S., Hyer, H., Sohn, Y., & Lee, K.-A. (2021). Effect of direct aging on the microstructure and tensile properties of AlSi10Mg alloy manufactured by selective laser melting process. Materials Characterization, 176, 111113. https://doi.org/10.1016/j.matchar.2021.111113

[216] Kempen, K., Thijs, L., Van Humbeeck, J., & Kruth, J.-P. (2012). Mechanical Properties of AlSi10Mg Produced by Selective Laser Melting. Physics Procedia, 39, 439–446. https://doi.org/10.1016/j.phpro.2012.10.059

[217] Uzan, N. E., Shneck, R., Yeheskel, O., & Frage, N. (2018). High-temperature mechanical properties of AlSi10Mg specimens fabricated by additive manufacturing using selective laser melting technologies (AM-SLM). Additive Manufacturing, 24, 257–263. https://doi.org/10.1016/j.addma.2018.09.033

[218] Tradowsky, U., White, J., Ward, R. M., Read, N., Reimers, W., & Attallah, M. M. (2016). Selective laser melting of AlSi10Mg: Influence of post-processing on the microstructural and tensile properties development. Materials &amp; Design, 105, 212–222. https://doi.org/10.1016/j.matdes.2016.05.066

[219] Cui, L., Liu, K., & Chen, X.-G. (2025). Recent advances in cost-effective aluminum alloys with enhanced mechanical performance for high-temperature applications: A review. Materials &amp; Design, 253, 113869. https://doi.org/10.1016/j.matdes.2025.113869

[220] Li, S.-S., Yue, X., Li, Q.-Y., Peng, H.-L., Dong, B.-X., Liu, T.-S., Yang, H.-Y., Fan, J., Shu, S.-L., Qiu, F., & Jiang, Q.-C. (2023). Development and applications of aluminum alloys for aerospace industry. Journal of Materials Research and Technology, 27, 944–983. https://doi.org/10.1016/j.jmrt.2023.09.274

[221] Zhang, J., Gao, J., Song, B., Zhang, L., Han, C., Cai, C., Zhou, K., & Shi, Y. (2021). A novel crack-free Ti-modified Al-Cu-Mg alloy designed for selective laser melting. Additive Manufacturing, 38, 101829. https://doi.org/10.1016/j.addma.2020.101829

[222] Yin, J., Zhang, W., Ke, L., Wei, H., Wang, D., Yang, L., Zhu, H., Dong, P., Wang, G., & Zeng, X. (2021). Vaporization of alloying elements and explosion behavior during laser powder bed fusion of Cu–10Zn alloy. International Journal of Machine Tools and Manufacture, 161, 103686. https://doi.org/10.1016/j.ijmachtools.2020.103686

[223] Huang, B., Tang, H., Huang, J., Jia, Y., Liao, L., Pang, S., Zheng, X., & Chen, Z. (2024). Influence of Laser-Based Powder Bed Fusion of Metals Process Parameters on the Formation of Defects in Al-Zn-Mg-Cu Alloy Using Path Analysis. Micromachines, 15(9), 1121. https://doi.org/10.3390/mi15091121

[224] Ashby, M. F. (2011). Materials selection in mechanical design (4th ed.). Butterworth–Heinemann. https://doi.org/10.1016/C2009-0-25539-5

[225] Rao, R. V. (2006). A material selection model using graph theory and matrix approach. Materials Science and Engineering: A, 431(1–2), 248–255. https://doi.org/10.1016/j.msea.2006.06.006

[226] Chatterjee, P., Athawale, V. M., & Chakraborty, S. (2009). Selection of materials using compromise ranking and outranking methods. Materials &amp; Design, 30(10), 4043–4053. https://doi.org/10.1016/j.matdes.2009.05.016

[227] Jahan, A., Mustapha, F., Ismail, M. Y., Sapuan, S. M., & Bahraminasab, M. (2011). A comprehensive VIKOR method for material selection. Materials &amp; Design, 32(3), 1215–1221. https://doi.org/10.1016/j.matdes.2010.10.015

[228] Anojkumar, L., Ilangkumaran, M., & Sasirekha, V. (2014). Comparative analysis of MCDM methods for pipe material selection in sugar industry. Expert Systems with Applications, 41(6), 2964–2980. https://doi.org/10.1016/j.eswa.2013.10.028

[229] Ibhadode, O. (2023). Structural Design Strategies for the Production of Internal Combustion Engine Components by Additive Manufacturing: A Case Study of a Connecting Rod. Renewable Energy - Recent Advances. https://doi.org/10.5772/intechopen.110371

[230] Gopal, G., Suresh Kumar, L., Vijaya Bahskar Reddy, K., Uma Maheshwara Rao, M., & Srinivasulu, G. (2017). Analysis of Piston, Connecting rod and Crank shaft assembly. Materials Today: Proceedings, 4(8), 7810–7819. https://doi.org/10.1016/j.matpr.2017.07.116

[231] Cecchel, S., Razavi, N., Mega, F., Cornacchia, G., Avanzini, A., Battini, D., & Berto, F. (2022). Fatigue testing and end of life investigation of a topology optimized connecting rod fabricated via selective laser melting. International Journal of Fatigue, 164, 107134. https://doi.org/10.1016/j.ijfatigue.2022.107134

[232] nTop. (2025, January 9). Innovate. Iterate. Create. https://www.ntop.com/

[233] Python Software Foundation. (2025, February 4). Python™. https://www.python.org

[234] Tierney, G. (2025). A Python-Based Automation Script to Mark Computer-Aided Design Assessments. Applied Sciences, 15(3), 1203. https://doi.org/10.3390/app15031203

[235] LI, T. (2009). Meshing Method of High Precision FEM in Structural Simulations. Journal of Mechanical Engineering, 45(06), 304. https://doi.org/10.3901/jme.2009.06.304

[236] ESTECO Engineering. (2025, January 9). Design better products faster. https://engineering.esteco.com/modefrontier/

[237] Hu, B., Su, G., Jiang, J., & Xiao, Y. (2019). Gaussian Process-Based Response Surface Method for Slope Reliability Analysis. Advances in Civil Engineering, 2019(1). Portico. https://doi.org/10.1155/2019/9185756

[238] Zhang, S., Li, K., Wang, S., Li, J., Pang, Y., & Song, X. (2023). Recursive surrogate model based on generalized regression neural network. Applied Soft Computing, 145, 110576. https://doi.org/10.1016/j.asoc.2023.110576

[239] H2O.ai. (2025, January 9). H2O AutoML documentation. https://docs.h2o.ai/h2o/latest-stable/h2o-docs/automl.html

[240] Reimpell, J., Stoll, H., & Betzler, J. W. (2001). Tyres and wheels. The Automotive Chassis, 86–148. https://doi.org/10.1016/b978-075065054-0/50002-x

[241] Genta, G., & Morello, L. (2019). Suspensions. The Automotive Chassis, 133–242. https://doi.org/10.1007/978-3-030-35635-4_3

[242] Melaika, M., Nagurnas, S., Pečeliūnas, R., Višniakov, N., & Garbinčius, G. (2014). Investigation on distribution of stresses in steel and aluminium alloy arms of a car suspension system. Mechanics, 19(6). https://doi.org/10.5755/j01.mech.19.6.5987

[243] Afroz, L., Das, R., Qian, M., Easton, M., & Brandt, M. (2022). Fatigue behaviour of laser powder bed fusion (L-PBF) Ti–6Al–4V, Al–Si–Mg and stainless steels: a brief overview. International Journal of Fracture, 235(1), 3–46. https://doi.org/10.1007/s10704-022-00641-3

[244] Li, Z., & Affolter, C. (2024). High-Cycle Fatigue Performance of Laser Powder Bed Fusion Ti-6Al-4V Alloy with Inherent Internal Defects: A Critical Literature Review. Metals, 14(9), 972. https://doi.org/10.3390/met14090972

[245] Elangeswaran, C., Cutolo, A., Muralidharan, G. K., de Formanoir, C., Berto, F., Vanmeensel, K., & Van Hooreweder, B. (2019). Effect of post-treatments on the fatigue behaviour of 316L stainless steel manufactured by laser powder bed fusion. International Journal of Fatigue, 123, 31–39. https://doi.org/10.1016/j.ijfatigue.2019.01.013

[246] Hosseini, E., & Popovich, V. A. (2019). A review of mechanical properties of additively manufactured Inconel 718. Additive Manufacturing, 30, 100877. https://doi.org/10.1016/j.addma.2019.100877

[247] Wu, T., & Cheung, E. H. M. (2006). Enhanced STL. The International Journal of Advanced Manufacturing Technology, 32(3–4), 422–422. https://doi.org/10.1007/s00170-006-0881-z

[248] Genuer, R., Poggi, J.-M., Tuleau-Malot, C., & Villa-Vialaneix, N. (2017). Random Forests for Big Data. Big Data Research, 9, 28–46. https://doi.org/10.1016/j.bdr.2017.07.003

[249] Mohammadtaheri, H., Sedaghati, R., & Molavi-Zarandi, M. (2022). Inherent strain approach to estimate residual stress and deformation in the laser powder bed fusion process for metal additive manufacturing—a state-of-the-art review. The International Journal of Advanced Manufacturing Technology, 122(5–6), 2187–2202. https://doi.org/10.1007/s00170-022-10052-2

[250] Fawagreh, K., Gaber, M. M., & Elyan, E. (2014). Random forests: from early developments to recent advancements. Systems Science &amp; Control Engineering, 2(1), 602–609. https://doi.org/10.1080/21642583.2014.956265

[251] Su, J., Mo, Y., Shangguan, P., Panwisawas, C., Jiang, F., & Sing, S. L. (2025). Additive manufacturing-by-design for support structures: a critical review. International Journal of Extreme Manufacturing, 7(5), 052002. https://doi.org/10.1088/2631-7990/add4d2

[252] Numpy-stl 3.2.0. Available online: https://pypi.org/project/numpy-stl/Numpystl (accessed on 11 May 2025).

[253] StandardScaler. Scikit-Learn Documentation. Available online: https://scikit-learn.org/stable/modules/generated/sklearn. preprocessing.StandardScaler.html# (accessed on 11 May 2025).

# Publications and Conferences

## List of publications:

1. Trovato, M., & Cicconi, P. (2023). Design tools for metal additive manufacturing: a critical and perspective overview. Procedia CIRP, 119, 1084–1090. https://doi.org/10.1016/j.procir.2023.03.151
2. Belluomo, L., Trovato, M., Bici, M., Cicconi, P., & Campana, F. (2024). An Iterative Generative Design Approach for Multi-Material Components. Computer-Aided Design and Applications, 1089–1102. https://doi.org/10.14733/cadaps.2024.1089-1102
3. Cicconi, P., Trovato, M., & Caputo, A. C. (2023). A CAD-Based Tool to Support the Configuration of Parts Storage Shelving in Assembly Workstations. ASEC 2023, 74. https://doi.org/10.3390/asec2023-15303
4. Trovato, M., Perquoti, F., & Cicconi, P. (2023). Topological Optimization for the Redesigning of Components in Additive Manufacturing: The Case Study of the Connecting Rod. The 4th International Electronic Conference on Applied Sciences, 131. https://doi.org/10.3390/asec2023-16638
5. Trovato, M., Belluomo, L., Bici, M., Campana, F., & Cicconi, P. (2024). Machine Learning Trends in Design for Additive Manufacturing. Design Tools and Methods in Industrial Engineering III, 109–117. https://doi.org/10.1007/978-3-031-52075-4_14
6. Trovato, M., & Cicconi, P. (2024). A Decision Tree approach for an early evaluation of 3D models in Design for Additive Manufacturing. Procedia CIRP, 128, 96–101. https://doi.org/10.1016/j.procir.2024.06.009
7. Trovato, M., Vigna, A., Cicconi, P., Belluomo, L., Bici, M., & Campana, F. (2025). Analyzing Tools and Methods in Design for Additive Manufacturing: Workflow and Test Cases. Computer-Aided Design and Applications, 1125–1135. https://doi.org/10.14733/cadaps.2025.1125-1135
8. Cicconi, P., Gatta, G., Menon, F., Paradiso, S., Trovato, M., & Bue, N. (2024). Configuration and Optimization in the Early Design Phases of Offshore Buoys: A Test Case. Computer-Aided Design and Applications, 673–684. https://doi.org/10.14733/cadaps.2025.673-684
9. Cicconi, P., Trovato, M., Donati, L., & Caputo, A.C. (2024). Defining the configuration of storage shelving in assembly workstations: an ergonomic tool for a parametric optimization. Ergonomics In Design. https://doi.org/10.54941/ahfe1004807
10. Ferrara, D., Cicconi, P., Minotti, A., Trovato, M., & Caputo, A.C. (2024). The Role of the Design Structure Matrix in a Streamlined Innovative Product Design Approach. 26th International dependency and structure modeling conference, DSM 2024. https://www.designsociety.org/publication/47709/the_role_of_the_design_structure_matrix_in_a_streamlined_innovative_product_design_approach
11. Ferrara, D., Cicconi, P., Minotti, A., Trovato, M., Amicarelli, M., & Caputo, A. C. (2025). A design framework for the development of an innovative water-electrolysis space propulsion system. Procedia CIRP, 136, 856–861. https://doi.org/10.1016/j.procir.2025.08.146
12. Amicarelli, M., Trovato, M., Ferrara, D., & Cicconi, P. (2025). Recycled powders: an Eco-Design approach for Laser-Powder Bed Fusion. Procedia CIRP, 136, 677–682. https://doi.org/10.1016/j.procir.2025.08.116
13. Trovato, M., Amicarelli, M., Ferrara, D., Prist, M., & Cicconi, P. (2025). A machine learning method to predict printing time for the L-PBF process. Procedia CIRP, 136, 671–676. https://doi.org/10.1016/j.procir.2025.08.115

14. Trovato, M., & Cicconi, P. (2025). Lightweighting of a Kart Connecting Rod in Additive Manufacturing. Design Tools and Methods in Industrial Engineering IV, 47–56. https://doi.org/10.1007/978-3-031-76597-1_6
15. Amicarelli, M., Trovato, M., & Cicconi, P. (2025). Lightweight Design of a Connecting Rod Using Lattice-Structure Parameter Optimisation: A Test Case for L-PBF. Machines, 13(3), 171. https://doi.org/10.3390/machines13030171
16. Trovato, M., Belluomo, L., Bici, M., Prist, M., Campana, F., & Cicconi, P. (2025). Machine learning in design for additive manufacturing: A state-of-the-art discussion for a support tool in product design lifecycle. The International Journal of Advanced Manufacturing Technology, 137(5–6), 2157–2180. https://doi.org/10.1007/s00170-025-15273-9
17. Trovato, M., Amicarelli, M., Prist, M., & Cicconi, P. (2025). A Neural Network-Based Approach to Estimate Printing Time and Cost in L-PBF Projects. Machines, 13(7), 550. https://doi.org/10.3390/machines13070550
18. Ferrara, D., Cicconi, P., Minotti, A., Trovato, M., & Caputo, A. C. (2025). New Space Engineering Design: Characterization of Key Drivers. Applied Sciences, 15(15), 8138. https://doi.org/10.3390/app15158138
19. Trovato, M., Amicarelli, M., Ripiccini, A., Ferrara, D., & Cicconi, P. (2026). From Redesign to Additive Manufacturing: Approaches and Case Study in Automotive. In: Berselli, G., Andrisano, A.O., Di Stefano, P., Rizzi, C., Gherardini, F. (eds) Design Tools and Methods in Industrial Engineering V. ADM 2025. Lecture Notes in Mechanical Engineering. Springer, Cham. https://doi.org/10.1007/978-3-032-14953-4_11
20. Trovato, M., Prist, M., Cicconi, P., Bonci, A., Pompei, G., & Longarini, L. (2026). A continual learning framework for defect recognition in additive manufacturing using a progressive online ridge regression approach. The International Journal of Advanced Manufacturing Technology. https://doi.org/10.1007/s00170-026-18080-y
21. Trovato, M., Pal, S., Drstvenšek, I., White, J., Cicconi, P. & Pradel, P. The impact of shape complexity on Al-alloy and polymer specimens. Under Review.

## Participation as a speaker at conferences:

1) CIRP Design Conference 2023, University of New South Wales, Sydney, Australia. May 17th to 19th, 2023. Presenting a paper: “Design tools for metal additive manufacturing: a critical and perspective overview”.
2) ADM 2023 International Conference, Florence, Italy. September 6th to 9th. Presenting a paper: “Machine Learning Trends in Design for Additive Manufacturing”.
3) CAD'24 - Eger, Hungary. July 8th to 10th 2024. (Online). Presenting two papers: “Analyzing Tools and Methods in Design for Additive Manufacturing: Workflow and Test Cases”, and “Configuration and Optimization in the Early Design Phases of Offshore Buoys: A Test Case”.
4) CIRP Design Conference 2024, Cranfield University, Cranfield, United Kingdom. June 3rd – 5th 2024. Presenting a paper: “A Decision Tree approach for an early evaluation of 3D models in Design for Additive Manufacturing”.
5) ADM 2024 International Conference, Palermo, Italy. September 11th to 13th. Presenting a paper: “Lightweighting of a Kart Connecting Rod in Additive Manufacturing”.
6) CIRP Design Conference 2025, Patras, Greece. April 2nd to 4th. Presenting a paper: “A machine learning method to predict printing time for the L-PBF process”.
7) ADM 2025 International Conference, Genova, Italy. September 3rd to 5th. Presenting a paper: “From Redesign to Additive Manufacturing: Approaches and Case Study in Automotive”.

## Acknowledgement

Project ECS 0000024 Rome Technopole, Concession Decree No. 1051 of 23 June 2022 adopted by the Italian Ministry of University and Research, CUP B83C22002820006, Rome Technopole.